Do defects in the nematic ordering of cancer-associated fibroblasts influence cancer cell invasion ?

Cécile Jacques

Université Paris Cité

Ecole Doctorale 474 Frontières de l'Innovation en Recherche et Education

Institut Curie, UMR 144, Cell biology and Cancer

DMV lab, Cell migration & invasion

Do defects in the nematic ordering of cancer-associated fibroblasts influence cancer invasion?

Par Cécile Jacques

Thèse de doctorat de Biologie moléculaire et structurale et Biochimie, Biophysique moléculaire

Dirigée par Danijela Matic Vignjevic

Présentée et soutenue publiquement le 14/10/2022

Devant un jury composé de :

Audrey Ferrand, *CR-HDR, Université de Toulouse, Rapporteur*

Aurélien Roux, *Professor, Université de Genève, Rapporteur*

Benoît Ladoux, *DR, Université de Paris, Examinateur*

Raphaël Voituriez, *DR, Sorbonne Université, Examinateur*

Danijela Vignjevic, *DR, Sorbonne Université, Directrice de Thèse*

Résumé détaillé

L'invasion cancéreuse

Le cancer est une maladie intrinsèque aux êtres vivants liée à une croissance cellulaire anormale au sein de l'organisme (Mattiuzzi and Lippi, 2019). C'est la deuxième cause de décès dans le monde et devrait devenir la première d'ici quelques décennies. Cependant, les nouvelles thérapies ciblées venant de la recherche, la détection précoce et la prévention contre les facteurs de risque pourraient réduire leur mortalité.

Le cancer apparaît dans un organe et s'y développe en une tumeur avec un microenvironnement comprenant différents types de cellules cancéreuses (Hanahan, 2011). De plus, le microenvironnement tumoral possède également des cellules endothéliales, des péricytes, des cellules immuno-inflammatoires et des fibroblastes associés au cancer (CAFs). La matrice extracellulaire (ECM) est aussi présente comme la membrane basale et les fibres de collagène I et de fibronectine.

Les cellules normales subissent une série de transformations pour devenir cancéreuses. Ces changements sont classés dans les caractéristique du cancer (Hanahan, 2022; Hanahan and Weinberg, 2000). Ces caractéristiques comprennent entre autre la capacité à se multiplier indéfiniment, à échapper à l'apoptose et au système immunitaire, et à modifier son phénotype. Outre la modification des cellules, la tumeur subit également des transformations physiques comme son durcissement.

La cascade métastatique correspond à l'évasion des cellules cancéreuses de la tumeur primaire pour générer des tumeurs secondaires (Welch and Hurst, 2020). L'apparition de métastases entraînent le décès du patient dans 90% des cas. L'invasion cancéreuse est la première étape de la cascade métastatique. Elle correspond à l'évasion des cellules cancéreuses de la tumeur primaire pour rejoindre les vaisseaux sanguins. Les cellules cancéreuses franchissent la membrane basale entourant la tumeur primaire et migrent à dans le stroma (Clark, 2015). Pour traverser l'ECM, les cellules cancéreuses peuvent la remodeler en utilisant des stratégies chimiques ou physiques, seules ou avec l'aide de cellules de leur microenvironnement tel que les fibroblastes associés au cancer.

Les fibroblastes associés au cancer et leur rôle dans l'invasion cancéreuse

Les fibroblastes associés au cancer ont des origines multiples, la principale étant les fibroblastes résidants dans le stroma (LeBleu and Kalluri, 2018). Cependant, les cellules souches mésenchymes, les adipocytes, les cellules stellaires et les cellules épithéliales et endothéliales contribuent aussi à la génération de CAFs (Kalluri, 2016). Plusieurs déclencheurs, tels que les facteurs sécrétés par les cellules

cancéreuses ou les propriétés physiques du microenvironnement, conduisent à l'activation de ces cellules en CAFs.

Les CAFs ont de multiples fonctions à l'intérieur du microenvironnement tumoral (Sahai et al., 2020). Ils produisent et remodèlent l'ECM, favorisant ou prévenant l'invasion cancéreuse. Les CAFs peuvent également favoriser la croissance tumorale en améliorant la prolifération, la caractéristique cellule souche et la résistance au traitement des cellules cancéreuses (Park, 2020). De plus, les CAFs interagissent avec les autres cellules du microenvironnement tumoral en stimulant l'angiogenèse et en modulant les réponses immunitaires pouvant être pro- ou anti-tumorigénique. Enfin, les CAFs favorisent l'apparition de métastases en préparant des niche pré-métastatiques.

Il existe de nombreuses preuves que les CAFs stimulent l'invasion cancéreuse de diverses façons (Attieh, 2016). Premièrement, ils peuvent améliorer le caractère invasif et les capacités migratoires des cellules cancéreuses via la sécrétion de plusieurs facteurs, le remodelage et le durcissement de l'ECM (Dumont et al., 2013; Wei et al., 2015). Ensuite, ils peuvent mécaniquement générer des trous dans la membrane basale pour que les cellules cancéreuses s'y faufilent (Glentis, 2017). Ils peuvent également favoriser la migration des cellules cancéreuses à travers le stroma en remodelant les fibres de collagène I pour créer des routes avec des fibres de fibronectine (Attieh et al., 2017; Erdogan et al., 2017). Enfin, ils peuvent directement diriger la migration des cellules cancéreuses via des jonctions hétérotopiques avec elles (Gaggioli et al., 2007; Labernadie et al., 2017).

Cependant, des preuves montrent que les CAFs peuvent également prévenir l'invasion cancéreuse (Özdemir et al., 2014; Rhim, 2014), même si ce rôle a été moins étudié. La production de collagène I des CAF peut former des barrières physiques limitant l'invasion (Bhattacharjee et al., 2021). Ils peuvent également limiter l'EMT et le caractère invasif des cellules cancéreuses via la sécrétion de plusieurs facteurs (Maris et al., 2015).

Enfin, l'organisation de l'ECM et des CAFs autour de la tumeur peut être classée en différentes signatures du collagène associées à la tumeur (TACS) en fonction de leur orientation par rapport au bord de la tumeur (Barbazán, 2019). Une orientation perpendiculaire est corrélée avec des régions invasives, tandis qu'une orientation parallèle est corrélée avec des régions non invasives. Les CAFs forment une couche autour de la tumeur et sont connus pour générer un ordre nématique. Cette organisation particulière pourrait avoir un impact sur le rôle des CAFs dans l'invasion cancéreuse.

L’ordre nématique

L'ordre nématique apparait dans des ensembles d'objets à la forme allongée (Doostmohammadi et al., 2018). Les objets s'alignent selon leur grand axe, conduisant à la génération de zones alignées selon une direction appelée directeur ***n***. Plusieurs zones alignées avec des directeurs ***n*** différents peuvent exister dans le même système. Les points où ces différentes zones alignées se rencontrent sont appelés des défauts topologiques (Gennes and Prost, 1993). Les défauts sont des points où l'orientation des objets change continuellement d'un directeur à l'autre. Il existe différents types de défauts qui sont définis par le sens et la fraction de rotation nécessaire autour d'eux pour passer d'un directeur à l'autre. Les défauts peuvent aussi être considérés comme des charges topologiques, la charge topologique globales étant la somme des charges de tous les défauts. Pour apparaître ou disparaître, les défauts doivent respecter la règle de neutralité des charges : la somme des charges des défauts impliqués doit être nulle. A l'équilibre, le système tend à neutraliser sa charge globale. Les deux défauts les plus courants en 2D sont les +1/2 ressemblant à des comètes et les -1/2 ressemblant à des triangles. Deux paramètres caractérisent l'ordre nématique : le paramètre d'ordre ***Q*** et la longueur de corrélation ***ξ*** (Duclos et al., 2014; Mottram and Newton, 2014). Le paramètre d'ordre ***Q*** quantifie le degré d'ordre d'une zone donnée. La longueur de corrélation ***ξ*** mesure la taille moyenne des régions alignées dans l'ordre nématique.

Dans les systèmes biologiques, l'équilibre ne peut pas être atteint car de l’énergie est constamment ajoutée au système (Saw et al., 2018). L'ordre nématique est alors appelé nématique actif : des défauts peuvent apparaître, disparaître et se déplacer, générant des contraintes mécaniques. Il existe deux types de nématiques actifs : extensibles et contractiles. Le nématique extensible se caractérise par des objets poussant sur leur grand axe et des défauts +1/2 se déplaçant de la queue à la tête de la comète. Le nématique contractile se caractérise par des objets se contractant sur leur grand axe et des défauts +1/2 se déplaçant de la tête à la queue de la comète. L'équilibre entre les contraintes intra et intercellulaires régit le type de nématique actif que le système forme (Balasubramaniam et al., 2021).

Pour étudier une organisation spécifique ou un défaut spécifique de l'ordre nématique, il est possible de façonner l'ordre nématique dans l'organisation ou le défaut d'intérêt. Un moyen simple de le faire est d'imposer des bords au système (Bade et al., 2018; Duclos et al., 2017). Les objets détecteront physiquement les bords et aligneront leur axe long le long d'eux, propageant ensuite cet alignement à l'intérieur du système. La taille et la géométrie des motifs générés par les bords ont un impact sur la façon dont l'ordre nématique s'organise dans le motif. Les motifs avec une taille inférieure ou similaire à la longueur de corrélation ***ξ*** de l'ordre nématique peuvent générer soit un défaut spécifique, soit un nématique parfaitement aligné avec le bord. Cependant, les motifs dont la taille est supérieure à la

longueur de corrélation ξ génèrent un ordre nématique avec plusieurs défauts et des zones alignées. Les bords génèrent des interactions entre eux et les objets. Aux bords, les objets ont tendance à être plus allongés et à se déplacer plus rapidement le long du bord qu'à l'intérieur du système (Duclos et al., 2018).

De nombreux systèmes biologiques s'organisent en ordre nématique, posant la question de leur utilité biologique. Dans un système biologique, les défauts présentent des motifs de déplacement des cellules et des contraintes mécaniques spécifiques. De tels motifs peuvent avoir un impact sur l'homogénéité, la différenciation des cellules, la régulation et morphogenèse des tissus et leur organisation spatiale. Dans certains systèmes extensibles, les cellules s'accumulent aux défauts +1/2 et s'échappent des défauts -1/2 (Kawaguchi, 2017). Dans les tissus épithéliaux nématiquement extensibles, la compression des défauts +1/2 conduisent à la mort et l'extrusion cellulaire. Dans certains tissus contractiles, la compression dans les défauts +1 génèrent une différenciation localisée. Lorsque la différenciation est inhibée, le mouvement en spirale des cellules génère des protubérances aux défauts +1 (Guillamat et al., 2022). Dans des organismes recouverts entièrement de nématiques extensibles, les défauts se positionnent à chaque caractéristique morphologique (Maroudas-Sacks et al., 2020).

Objectifs

Au stade pré-invasif, la tumeur est séparée du stroma adjacent par la membrane basale. Juste en dessous, se trouve un réseau de fibroblastes associés au cancer (CAF), les principaux producteurs et remodeleurs de la matrice extracellulaire (ECM). En enveloppant la tumeur, les CAFs créent une barrière physique empêchant l'invasion cancéreuses. Cependant, les CAFs aident également l'invasion cancéreuse en remodelant mécaniquement l'ECM. De par leur forme allongée, les CAF s'alignent spontanément le long de leur grand axe dans un ordre nématique. L'ordre nématique est intrinsèquement lié aux défauts topologiques, là où des régions alignées dans différentes directions se rencontrent. Les défauts les plus courants sont les +1/2 ressemblant à des comètes et les -1/2 ressemblant à des triangles. Nous supposons que, alors que les CAFs ordonnés nématiquement forment une capsule empêchant l'invasion cancéreuse, les défauts dans l'ordre nématique peuvent représenter des points faibles d'où les cellules cancéreuses s'échappent. Pour tester cette hypothèse, les objectifs spécifiques de ma thèse sont :

1. Caractériser les probabilités de défauts d'être des points faibles dans la capsule

2. Déterminer par quel mécanisme les défauts pourraient favoriser l'invasion du cancer

3. Déterminer les sites d'invasion du cancer à l'intérieur de la couche CAF

Résultats

Dans cette étude, nous avons essayé de comprendre le rôle des défauts dans l'ordre nématique de la couche de CAF vis-à-vis de l'invasion des cellules cancéreuses. Tout d'abord, nous avons étudié la couche CAF et trouvé des indices suggérant que des défauts pourraient favoriser l'invasion des cellules cancéreuses et que des régions alignées pourraient l'empêcher.

Pour les défauts favorisant l'invasion des cellules cancéreuses, nous avons trouvé :

- Les défauts étaient suffisamment grands et fréquents pour stimuler l'invasion cancéreuses

La taille et la fréquence des défauts peuvent impacter leur capacité à stimuler l'invasion cancéreuse. Une fréquence de défauts élevée donnera plus de possibilité d'invasion. Une grande taille de défauts stimulera davantage de cellules cancéreuses. Pour connaitre ces valeurs dans ce système, j'ai généré des couches de CAFs nématiquement ordonnées que j'ai ensuite photographié dans leur ensemble. L'analyse des images m'a permis de mesurer la densité et la tailles de chaque défaut. Les comètes et les triangles avaient des densités similaires d'environ 1.5 défauts/mm² et mesuraient environ 400 µm. Cette fréquence et cette taille les rendaient donc susceptibles d'être les points de départ de l'invasion.

- Les défauts présentaient moins de densité cellulaire et de dépôt de fibronectine, ce qui en faisait une barrière plus fine à franchir par rapport aux régions alignées

Nous supposons que les CAFs forment une barrière physique autour de la tumeur. Les défauts pourraient donc stimuler l'invasion cancéreuse en étant des points où la barrière est plus facile à briser. La barrière pourrait être plus fine par exemple avec moins de cellules et d'ECM. Pour observer l'état de la couche de CAFs aux défauts, j'ai généré des couches de CAFs nématiquement ordonnées que j'ai ensuite colorées pour l'ADN et la fibronectine. J'ai ensuite compté les nombres de cellules et la quantité de fibronectine dans chaque type de défauts et les régions alignées. Cette quantification à montrer qu'il y avait moins de CAFs et de fibronectine dans les défauts que dans les régions alignées. La couche de CAFs était donc plus fragile aux défauts soit plus simple à franchir pour les cellules cancéreuses.

- Les défauts étaient stationnaires, laissant suffisamment de temps pour que l'invasion des cellules cancéreuses se produise

L'invasion cancéreuse a besoin de temps pour se faire. Les mouvements des défauts dans l'ordre nématique peuvent donc influencer leur capacité à stimuler l'invasion cancéreuse. Des défauts trop mobiles empêcheraient l'invasion cancéreuse d'avoir lieu à leur niveau. Pour connaître leur déplacement, j'ai filmé les défauts dans la couche de CAFs ordonnée nématiquement et j'ai

quantifié la trajectoire de chaque défaut. J'ai constaté que les défauts ne bougeaient pas de leur position initiale. De même, les CAFs non plus ne bougeaient pas dans la couche. Ainsi, la stabilité des défauts rendrait possible l'invasion cancéreuse à leur niveau.

- Les défauts possédaient des forces de traction plus élevées avec des motifs de force spécifiques qui pourraient soit générer de l'extrusion des CAFs (défaut +1/2 en comète) soit un pincement de la tumeur en dessous (défaut -1/2 en triangle)

L'une des caractéristiques majeures des CAFs est leur forte contractilité. Les CAFs sont en effet capable de générer des forces mécaniques sur leur environnement et remodeler l'ECM. Les défauts étant des points particuliers dans l'ordre nématique, ils pourraient être des places où les CAFs exercent plus de forces ou dans une organisation spécifique. Pour caractériser les forces générées par les CAFs, j'ai réalisé des microcopies à forces de traction de contraintes internes de la couche de CAFs. J'ai trouvé que les défauts possédaient plus de forces avec des motifs spécifiques. Les comètes avaient un pic de force et étaient compressées à leur tête ce qui pourrait suggérait l'extrusion des CAFs pour créer des routes dans l'ECM aux comètes. Les triangles avaient des pics de forces à chaque sommet et étaient tendus ce qui pourrait suggérait le pincement de la tumeur sous-jacente pour percer la couche de CAFs aux triangles. Ces deux potentiels conséquences des forces aux défauts pourraient favoriser l'invasion.

Pour les zones alignées empêchant l'invasion des cellules cancéreuses, nous avons trouvé :

- Les zones alignées présentaient une densité cellulaire et un dépôt de fibronectine plus élevés, ce qui en faisait une barrière plus épaisse à franchir par rapport aux défauts

Nous supposons que les CAFs forment une barrière physique autour de la tumeur. Au plus cette barrière est épaisse, au mieux elle préviendra l'invasion. La colorisation de l'ADN et la fibronectine réalisée avant a montré que la densité cellulaire et de fibronectine étaient plus importante dans les régions alignées que les défauts. Les régions alignées formaient donc des barrières plus épaisses pouvant davantage empêcher l'invasion cancéreuse.

- Les zones alignées forment des unités supra cellulaires avec de longues fibres de F-actine parcourant plusieurs cellules jointe par de la fibronectine, ce qui les rend compacts et solides, difficiles à pénétrer

Les régions alignées possédaient déjà une densité cellulaire et de fibronectine plus importante qu'au défauts en faisant des barrières plus épaisses. Une cohésion entre les CAFs pourrait cependant accentuer l'efficacité de la barrière en la solidifiant. Pour savoir si les CAFs se coordonnent dans les régions alignées, j'ai généré des couches de CAFs nématiquement ordonnées que j'ai ensuite colorées

pour la F-actine, la principale protéines d'adhésion entre cellules N-cadhérine, une protéine d'adhésion entre cellules et substrat vinculine, et la fibronectine. Ces colorations ont montré que la F-actine formaient de longues fibres sur plusieurs CAFs formant des unités supra cellulaire. La vinculine et la N-cadhérine n'étaient pas présentes entre les CAFs alignés et ne participaient donc pas à la formation de ces blocs. Cependant, la fibronectine se trouvaient entre les CAFs et participaient à la formation des unités supra cellulaire en joignant les CAFs entre eux. Ces unités supra cellulaires formaient des blocs compacts et solides dans les régions alignées ce qui pourraient prévenir l'invasion.

- Les zones alignées présentaient de faibles forces de traction sans motif spécifique

L'un des principaux mode d'action des CAFs est les forces qu'ils exercent sur leur environnement de par leur contractilité. La faible présence de forces de traction dans une zone signifierait que les CAFs agissent moins sur la tumeur sous-jacente à cet endroit, ne stimulant donc pas l'invasion à cet endroit. La microscopie à force de traction réalisée avant a montré qu'il y avait peu de forces dans les régions alignées et sans motifs particulier. Les régions alignées ne seraient donc pas des lieux facilitant l'invasion. Cependant, les CAFs pourraient tout de même générer des forces en les transmettant, non pas au substrat, mais entre eux à travers les unités supra cellulaires présentes dans les régions alignées et jusqu'aux défauts.

Nous avons également souligné l'importance de la fibronectine dans le système. Le dépôt de fibronectine fixait la couche de CAF dans son organisation initiale. Ainsi, les défauts et les CAF ne bougeaient pas. La fibronectine était également responsable de la formation des unités supra cellulaires en liant les CAFs entre eux.

La fibronectine était à la fois présente sous les CAFs pour former une barrière physique et entre les CAFs pour former les unités supra cellulaire. De plus, les colorations de la couche de CAFs pour la F-actine et la fibronectine ont montré que les fibres de fibronectine suivaient l'ordre nématique de la couche de CAFs. Ce dépôt suivant l'ordre nématique pourrait être l'origine de la stabilité des défauts : Les CAFs nématiquement ordonnées déposeraient la fibronectine suivant leur alignement puis, sentant l'organisation des fibres de fibronectines, s'ordonneraient dessus conservant ainsi l'ordre nématique initial. Pour vérifier cette hypothèse, j'ai laissé des CAFs générer des ordres nématiques et déposer de la fibronectine suivant ces ordres. Je les ai ensuite enlevés, puis coloré la fibronectine avant d'ajouter de nouveaux CAFs. J'ai ensuite fixé le système, coloré la F-actin des CAFs et comparé l'ordre nématique des nouveaux CAFs et la couche de fibronectine crée par les anciens. J'ai constaté que les nouveaux CAFs s'alignent sur l'ordre nématique de la fibronectine. De plus, j'ai privé les CAFs de fibronectine et utilisé ces CAFs sans fibronectine pour refaire les expériences précédentes. J'ai constaté que sans

fibronectine, les défauts et les CAFs bougeaient dans l'ordre nématique. Les forces de tractions sont aussi réduites. En rajoutant de la fibronectine nématiquement ordonnée au CAFs privé de fibronectine, les défauts et les CAFs ne bougeaient plus mais les forces restaient réduites. Ainsi, le dépôt de fibronectine par les CAFs servaient à fixer l'ordre nématique de la couche de CAFs, dont les défauts, tandis que la fibronectine entre les CAFs servaient à former des unités supra cellulaire pour transmettre les forces dans la couche.

Enfin, les données préliminaires des tests d'invasion ont révélé la formation de structures 3D ressemblant à des volcans aux comètes. Ils ont également suggéré que la présence de défauts pourrait stimuler l'invasion des cellules cancéreuses. L'invasion des cellules cancéreuses commencerait aux défauts. Le processus d'invasion perturberait la couche CAF et permettrait ainsi une invasion dans le reste de celle-ci.

La caractérisation de la couche de CAFs a montré que les défauts pourraient favoriser l'invasion cancéreuse. Pour savoir si l'invasion cancéreuse se fait effectivement au niveau des défauts, j'ai cultivé des CAFs et des cellules cancéreuses de chaque côté d'une membrane basale, venant d'un mésentère dé-cellularisé de souris. J'ai laissé le système évoluer plusieurs jours pour permettre aux cellules cancéreuses d'envahir la couche de CAFs puis j'ai fixé et observé cette invasion. J'ai constaté que plus il y avait des défauts dans la couche de CAFs, au plus il y avait d'invasion cancéreuse. J'ai de plus trouvé que l'invasion cancéreuse se faisaient préférentiellement au niveau des défauts. Enfin, j'ai remarqué qu'au plus il y avait de l'invasion cancéreuse, au plus celle-ci se faisait dans toute la couche de CAFs. L'invasion cancéreuse se faisait donc tout d'abord au niveau des défauts, cette invasion perturberait la couche de CAFs permettant aux cellules cancéreuses d'également envahir les régions alignées.

Acknowledgment

There I am, finally writing the acknowledgment of my thesis. It's been quite a journey! Let me tell you all about it! It all started at my birth… Nah, just kidding, you already have enough to read, no need to add more… But still, my thesis has been quite an adventure as has been the road that brought me to it. Now that this period is reaching its end, I can only look back at all the people I met on my way and who help me be where and how I am today.

First, I would like to thank Audrey Ferrand and Aurélien Roux for accepting to be the reporters on my jury and I am grateful for the corrections they provide to my manuscript. Then, I would also like to thank Benoît Ladoux and Raphaël Voituriez for being part of my jury too as the examinators. I hope you all have a great time at my defense and enjoy the scientific discussion we have together.

My next thanks go to Danijela, my thesis director. I am forever grateful for the opportunity you gave me to do my Ph.D. in your lab. I don't think I have the words to express all my gratitude towards you but I hope those would fill this purpose. You are a great mentor, you adapt yourself to your student so you can help them in the best way they need to be guided. You always take time to listen to us and give us good advice on both scientific and life matters. You treat us all as equal and are always careful to gather a good and caring team in your lab. Being part of the DMV lab during these years has made me grow both scientifically and humanly. I know that, as I leave, I will take with me lessons that make me a better scientist and human and I will cherish them and pass them on for the rest of my journey. So thank you for everything and please continue to rock this way, you take the best out of everyone!

The DMV lab would be nothing without all its members! I want to thank you all for being such a great and welcoming team. I do enjoy being part of this lab, and I spent so many good times with you all. You always have been there to support me, talk with me, and have fun together playing darts or having a drink. Without you to brighten the days, things won't have been so nice. Let's name you all because you all deserve it! First, I like to thank Andy who supervised me during the internship I did before joining the lab as a Ph.D., it was pleasant to work together on your project as your intern first and then as your colleague. My thank then go to Jorge and Rali who showed me around when I came back to my thesis and taught me most of the technics I use. I learned from you more than only science and you have been real supports to me. Thank Fati and Denis for your wisdom and advice that was always what I just needed to hear. I would like to then thanks Ram and Sacha for all the good laughs and discussion. We always had good times together and your sharing of your experience help me a lot during my thesis. These were the former lab members who are gone now, but some are still there, and new ones came! First, thank you Sophie for your presence, you're always here to help and have some fun, it's very nice being around you. I would then like to thank Carlos who hosted me when I visited his lab in

Barcelona and then pursued to help and supported me when he joined our lab. You have been one of my best support in the lab, one with whom I could easily talk about anything. Then, of course, Olivier whose experience was always interesting to hear and learn from. Thanks for all the good chats and laughs as well as for restarting the dart game, we had so many good times playing. It's always a pleasure discussing with you. Who says darts says Reda also! Thank you for always being so eager to chat, play or have a laugh, you're bringing the lab together and make to make everybody have a good time here and I enjoy discussing with you. I then would like to thank Louisiane who always knows what to say to support you or just make you have a good time around a drink, I love discussing with you and learning from you and your experience. The same goes for Neta, you're always here to listen to me and support me, your wisdom is always inspiring and you know how to find positivity in everything, thank you for all your attention and support. Thank you Neda for always being ready to have a good time, I enjoyed spending time with you while supporting each other. We had good laughs together and I like how we can talk about everything. I would also like to thank Meryem, your sharing of your experience is always interesting and I enjoy listening to you. You know how to be supportive and motivate people. Finally, thank you Jieun for brightening the office, your kindness and sweet discussion are always appreciated. Also Thank you Florence for joining the lab soon, I saw that you have the DMV spirit and will perfectly fit in the lab, we already have great times altogether thanks to you.

My thanks also go to Damien and Clément, the two interns I supervised during my thesis. Thank you for your help in my project and the opportunity you gave me to learn student management.

In addition, I would also like to thank all the other members of the second floor. My experience there has been incredible also thanks to your presence and the good atmosphere on the floor. Thank you, Céline and Anthony, for being so supportive and kind, I enjoy all the time I spent chatting with and laughing with you. Thank you, Veronique, Richard, Clarisse, Manon, Laure, Alix, and all the other ones for making the second floor, the floor to be to have the best time during a thesis!

En plus des gens au sein de Curie, j'aimerais également remercier mon entourage personnel. Pour commencer, j'aimerais remercier ma famille, dont mes parents et ma sœur. Merci d'avoir été là durant toutes ces années pour m'apporter confort et soutien. Je ne serais pas là où j'en suis désormais sans vous pour m'épauler et m'aiguiller. Votre support sans faille m'aide à avancer au jour le jour et à toujours chercher à aller plus loin et oser de nouvelles expériences.

Je voudrais aussi remercier mon cœur Théo pour m'avoir soutenue tout au long de ma thèse. Ce n'est pas toujours facile d'être avec quelqu'un en thèse, mais tu as toujours réussi à être là pour me soutenir et me réconforter. Ta simple présence a été un gros plus pour moi et simplement passer du temps m'a toujours remonté le moral. Merci pour tout.

J’aimerais également remercier tous mes amis qui m’ont toujours épauler durant toutes ces années et prêter une oreille attentive et surtout permis de vivre des chouettes moments inoubliables. Je voudrais commencer par remercier mes amis de prépa. Merci Valentin, Madleen, Vianney, Camille, Corentin, Marie-Anne et Thomas. Entre rires et discussions enflammées, j’ai toujours passé de bons moments avec vous et je chérie énormément notre amitié. Vous m’avez beaucoup apporté depuis qu’on se connaît. Vous savez toujours trouver les mots justes pour me soutenir, me faire rire, me conseiller. Vous êtes un support sans faille et j’apprécie tous les moments que je passe avec vous et je souhaite que cela dure pour toujours.

Je voudrais aussi remercier mes amis de l’ESPCI. Merci Audrey, Alice, Maxence, Sylvain, Donatien, Agathe, Pierre-Alain, Victoria, Antoine, Marie, Thomas, Victor, et tant d’autres. Votre amitié m’est aussi tout aussi précieuse. Depuis que l’on se connait, on a toujours pu compter les uns sur les autres. Vous avez toujours été là pour moi pour me soutenir, me conseiller ou simplement passer de bons moments ensemble. C’est toujours un plaisir de pouvoir passer du temps tant on s’amuse et parle de choses intéressantes et variées. Je sais que je peux toujours compter sur vous en cas de soucis, car vous répondrez présents. Merci pour cette amitié sans faille.

Je souhaiterais aussi adresser quelques mots à Becky, mon chat-chat que j’ai adopté durant ma thèse. Elle n’est malheureusement plus là pour me voir soutenir, mais son amour et ses câlins m’ont été d’un énorme soutien durant ma thèse. Cette petite boule de poil toute mignonne m’a été d’un grand réconfort. Merci à toi. J’aimerais aussi remercier Michu, mon nouveau chat adopté durant ma rédaction. Sa fougue et ses câlins m’ont apporté soutien et amusement durant les derniers moments d’écriture. Merci Chouchou et puisses-tu rester longtemps avec moi.

I would like to take the time to NOT thank the covid for all the confinements and restrictions towards working in the lab it generated. My thesis, as well as many other things, would have been way better without it. Let’s just hope it will leave us alone now.

Didn’t I say I was going to be short? Well… Guess I lied! Sorry, but I had too many people to thank, too many people to be grateful for. I am pretty sure I could think of even more people and sorry if I miss some. You all contributed to making me the woman and scientist I am today and I can just thank you for that. Your kindness, your support, your humor, your experiences, your love, and your friendship… you give me all these without restrictions.

Thank you all for everything!

Table of content

Abbreviations list

BISM	Bayesian inversion stress microscopy
CAFs	Cancer-associated fibroblasts
CRC	Colorectal cancer
CTC	Circulating tumor cell
CTGF	Cognitive tissue growth factor
CTLs	Cytotoxic lymphocytes
CXCL12	Stromal cell-derived factor 1
ECM	Extracellular matrix
EMT	Epithelial to mesenchymal transition
FAP	Fibroblast activation protein
FGF	Fibroblast growth factor
FN	Fibronectin
HGF	Hepatocyte growth factor
IL	Interleukin
LOX	Lysyl oxidase
MDCK	Madine-Darby canine kidney
MET	Mesenchymal to epithelial transition
MMP	Matrix metalloproteinase
MSC	Mesenchymal stem cell
MyHC	Myosin heavy chain
NAFs	Normal-associated fibroblasts
NK	Natural killer
NPC	Neural progenitor cell
PAA	Polyacrylamide

PDAC	Pancreatic ductal adenocarcinoma
PDGF	Platelet-derived growth factor
PDGFR	Platelet-derived growth factor receptor
PIV	Particle image velocity
REP	Retinal pigment epithelial
SASP	Senescence-associated secretory phenotype
SF/HGF	Scatter factor/Hepatocyte growth factor
Shh	Sonic hedgehog
TACS	Tumor-associated collagen signature
TGFβ	Transforming growth factor β
VEGF	Vascular endothelial growth factor
YAP	Yes-associated protein
α-SMA	α Smooth muscle actin

Chapter I: Cancer invasion

Cancer as a world health issue

Cancer evidence can be found inside fossils and other remains at all stages of living history, specifically human history. The first description of cancer disease has been traced back to 1600 BC in ancient Egypt inside the Edwin Smith Papyrus, which describes breast cancer, among other injuries. The name cancer for this disease was given by Hippocrates (460 BC – 370 BC) in ancient Greece. It comes from the Greek karkinos, which means crab or spider crab, as first observations of tumors noticed their resemblance with a crab or a spider crab: a solid tumorous body from which long veins arise (Hajdu, 2011). Cancer is a disease intrinsic to living beings as it comes from the deregulation and the hijacking of the cellular machinery inside organs. Cancerous cells generate malignant tumors that do not participate anymore in the system homeostasis as they do not execute anymore the functions they were initially dedicated to. The malignant tumors often grow exponentially and disseminate throughout the body leading to death.

Cancer is the second cause of mortality in the world behind ischemic heart disease and is expected to become the leading cause of mortality worldwide by 2060. In 2020, around 19 million new cases were discovered, and about 10 million patients died of cancer. The risk of developing cancer before 74 years old is 20,2 %. The most common cancers are breast, lung, and colorectal cancers (“Cancer Today,” 2020) (Figure 1). However, lung, colorectal, and liver cancers cumulate the most deaths, as the death ratio varies for each cancer. Colorectal cancer has a death ratio of about 50% (Mattiuzzi and Lippi, 2019). It is estimated that between 30% and 50% of cancers could be avoided by limiting risk factors and using prevention strategies. The main risk factors for cancer development are tobacco, unhealthy diet, lack of physical activity, alcohol, and air pollution.

Early detection of cancer and a better treatment choice also reduces death risk as the chance of survival for the patients is high when cancer is tackled down early and with the most appropriate treatment. Early cancer detection mainly relies on political involvement to improve cancer prevention and quick medical access. Early detection can also be enhanced by improving detection strategies by developing more efficient and less invasive diagnosis technologies such as liquid biopsy. Cancer treatment often relies on surgery, radiotherapy, and systemic therapy such as chemotherapy. Those different options can be heavy for patients and have strong side effects. Thus, the treatment strategy chosen depends on the type of cancer, its progression stage, and the patient's well-being. In the case of advanced-stage cancer with a poor chance of cure, palliative care is proposed instead, as the benefits/risks balance for the curative treatment is not favorable for the patients. Thanks to recent advances in cancer research, new curative treatment strategies such as immunotherapy and targeted therapies are being developed (Krzyszczyk et al., 2018; Zhang and Chen, 2018). These new curative

treatment strategies target tumor cells more precisely due to better knowledge of cancer mechanisms and patient specificity. Being more personalized, such treatments are more efficient with fewer or minor side effects improving survival as well as the well-being of the patients. These new curative treatments coupled with better preventive strategies of avoiding risk factors and improving early detection could help limit the burden cancer represents worldwide as well as the evolution of this burden in the future.

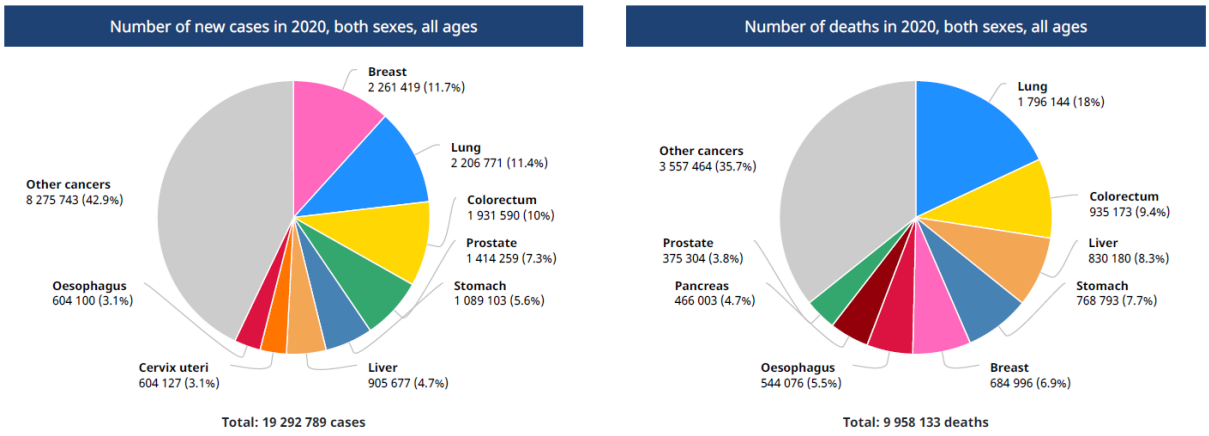

Figure 1. Cancer statistics of 2020.
Repartition of worldwide new cases in 2020 per each type of cancer (left) and repartition of worldwide deaths in 2020 per each type of cancer (right).
Taken from Globocan ("Cancer Today," 2020).

The tumor microenvironment

Most cancers generate solid tumors with a surrounding tumor microenvironment (Hanahan, 2022, 2011; Hanahan and Weinberg, 2000). The tumor microenvironment comprises the tumor itself and its immediate surroundings under the tumor's influence, which thus participates, in one way or another, in the tumor evolution. The tumor microenvironment is generally considered an organ because of its complexity in terms of organization, types of cells, and their interactions between them and with the extracellular matrix (ECM). Inside the tumor microenvironment, various kinds of cells co-exist (Figure 2). The tumor microenvironment evolves in terms of heterogeneity of cell types depending on its position in the dissemination process. Each cell type exhibits different characteristics and functions that lead to tumor development.

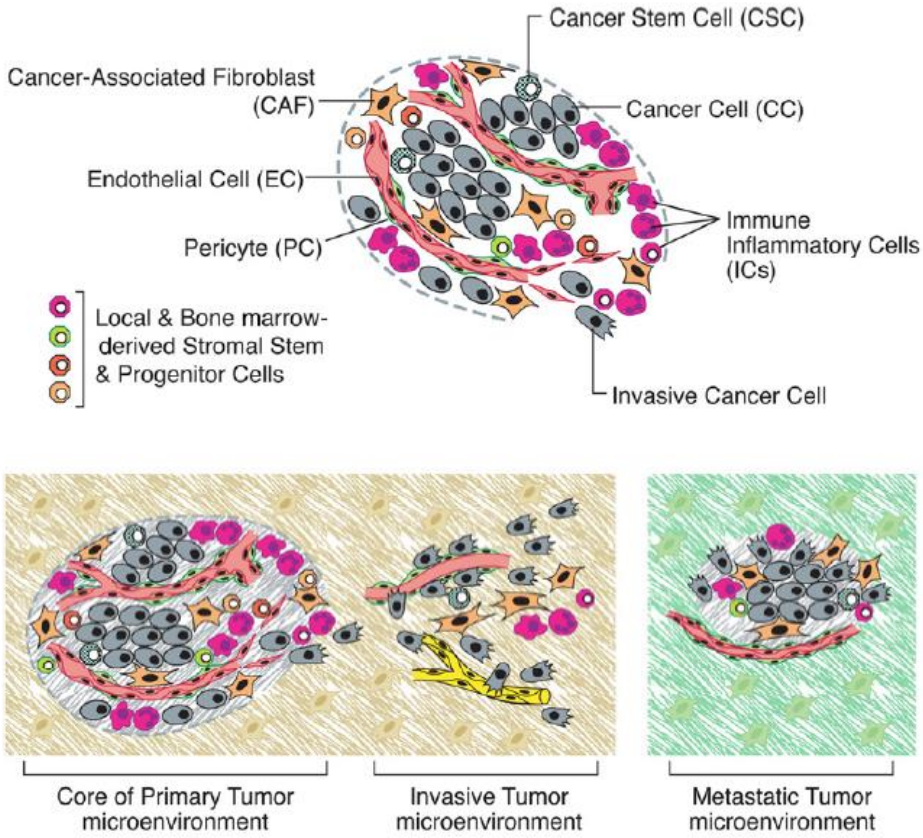

Figure 2. The tumor microenvironment.
Schemes describe the different cell types in the tumor microenvironment and the difference in the tumor microenvironment at different steps of cancer dissemination and metastasis.
Taken from Hanahan, 2011.

The most abundant cell type in cancer is cancer cells. Cancer cells are at the origin of the tumor as they possess the oncogenic mutations defining cancer. Cancer cells govern the tumor microenvironment evolution in primary tumors and during the different stages of metastasis. Indeed, after appearing, cancer cells recruit the other cell types or modify already present cells to promote tumor growth. Using signaling factors, cancer cells can attract other cell types and reprogram their already existing roles to their advantage (Egeblad et al., 2010a; Pietras and Ostman, 2010; Polyak and Weinberg, 2009). Earlier it was believed that cancer cells form a homogenous population of cells. However, in the last decade, it has become clear that cancer cells are heterogeneous. As a result of their genome instability, several cancer subpopulations appear that can cooperate or compete inside the tumor microenvironment (Al-Hajj et al., 2003; Yachida et al., 2010). Different subpopulations of cancer cells are defined by their expression level of differentiation, proliferation, angiogenesis, inflammatory, and invasiveness signals. Invasive cancer cells, for example, express a high level of invasive and motility genes and lead to the metastasis process. Cancer cells gain the invasive capacity and start migrating as collectives, or, through the process called epithelial to mesenchymal transition (EMT), they lose epithelial

characteristics and start migrating as individual cells. A portion of cancer cells consists of cancer stem cells. Cancer stem cells can efficiently create new tumors as they possess characteristics similar to stem cells in healthy tissues, such as self-renewal ability and the capacity to differentiate into different cell types (Cho and Clarke, 2008; Singh and Settleman, 2010). Moreover, cancer stem cells seem to have some form of tumor dormancy. This ability makes cancer stem cells resistant to treatment as they enter a latent state during treatment. Once treatments are stopped, cancer stem cells can return to an active state and recreate a tumor at any time (Morales-Valencia and David, 2022).

Besides cancer cells, the tumor microenvironment is rich in blood vessels made of endothelial cells and pericytes, immune cells, fibroblasts, and adipocytes (Hanahan, 2011; Park, 2020; Pietras and Ostman, 2010). Endothelial cells and pericytes are in charge of the vascularization of the tumor. Endothelial cells form every blood vessel in the body. Quiescent most of the time, they can be activated upon injury to repair the damaged vessels (Ahmed and Bicknell, 2009). Inside the tumor microenvironment, tumor-associated endothelial cells are permanently activated and thus generate new vessels to bring oxygen and nutrients inside the tumor to facilitate its growth (Carmeliet and Jain, 2000; Pasquale, 2010). Tumor-associated endothelial cells differ from normal activated endothelial cells by their gene expression profile and surface markers due to their recruitment and modification by cancer cells (Nagy et al., 2010; Ruoslahti et al., 2010). Pericytes are a mesenchymal cell type that wraps endothelial cells supporting the structure of blood vessels (Bergers and Song, 2005; Raza et al., 2010). Pericytes also cooperate with endothelial cells to generate the vascular basement membrane, reinforcing the blood vessels (Pietras and Ostman, 2010; Raza et al., 2010). Without pericytes, endothelial cells cannot develop fully functioning blood vessels (Gaengel et al., 2009; Gerhardt and Semb, 2008), thus the importance to recruit both endothelial cells and pericytes inside the tumor microenvironment.

Different types of infiltrating cells of the immune system are present in the tumor microenvironment (Hanahan, 2011; Park, 2020). Some of them come from already patrolling immune cells at the site of the tumor, whereas others are recruited there due to the inflammatory signals coming from the tumor (Grivennikov et al., 2010). In the tumor microenvironment, the role of the immune system is ambivalent as some types of immune cells have pro-tumorigenic functions, whereas other types of immune cells have anti-tumorigenic functions (DeNardo et al., 2010). On the one hand, some macrophage subtypes, mast cells, neutrophils, leukocytes, and some T and B lymphocytes promote tumor development by enhancing angiogenesis, proliferation, extracellular matrix degradation, and invasion of cancer cells (De Palma et al., 2007; DeNardo et al., 2010; Johansson et al., 2008; Murdoch et al., 2008). On the other hand, cytotoxic T lymphocytes (CTLs), natural killer (NK) cells, leukocytes, and some other T and B lymphocytes prevent tumor progression by trying to actively destroy the tumor with the tumor-killing response (DeNardo et al., 2010; Egeblad et al., 2010a; Johansson et al., 2008;

Pietras and Ostman, 2010). This dual role of the immune system can be explained by the way the immune system acts. First, the immune cells must find threats inside the body and destroy them with the appropriate immune response, and then, in the second phase, the immune cells support wound healing and clearing of the injury. Each of these phases is executed by different types or subtypes of the immune system and different means, such as killing response or angiogenesis promotion (Biswas and Mantovani, 2010; Grivennikov et al., 2010; Hanahan, 2011; Mantovani, 2010; Qian and Pollard, 2010). Thus, some of the immune cells can be recruited by the cancer cells to help the tumor development instead of preventing it.

Besides the cancer cells, cancer-associated fibroblasts (CAFs) are the main type of cells present in the tumor microenvironment. In normal tissues, fibroblasts are present inside the stroma in a quiescent state (Kalluri, 2016; LeBleu and Kalluri, 2018). Upon injury, fibroblasts get activated and participate to wound healing by producing and remodeling the extracellular matrix (ECM) (Bhowmick et al., 2004; Räsänen and Vaheri, 2010). Cancer cells recruit and reeducate fibroblasts inside the tumor microenvironment, maintaining them in an activated state. In this state, most CAFs are proliferative and keep producing and remodeling the ECM creating desmoplastic stroma. The role of CAFs inside the tumor microenvironment is also ambivalent. CAFs can either favor or prevent tumor development or even both simultaneously (Kalluri, 2016; Santi et al., 2017; Shimoda et al., 2010). Different CAFs subpopulations can also co-exist inside the tumor microenvironment, each having potentially different origins, characteristics, and roles concerning tumor development (Attieh, 2016; LeBleu and Kalluri, 2018; Park, 2020). The next chapter is dedicated explicitly to CAFs and their role in tumor development, particularly cancer invasion.

Finally, local and bone marrow-derived stromal stem and progenitor cells are also present in the tumor microenvironment. They are recruited by the cancer cells and serve mainly as a renewal pool for the other cell types (Bergfeld and DeClerck, 2010; Fang and Salven, 2011; Giaccia and Schipani, 2010; Lamagna and Bergers, 2006; Patenaude et al., 2010). Indeed, local and bone marrow-derived stromal stem and progenitor cells can differentiate into different stromal cells such as pericytes, immune cells, or CAFs. Their role is to promote tumor development by generating the cell types needed inside the tumor microenvironment as the tumor grows.

In addition to different cell types, the ECM is also present inside the tumor microenvironment. For example, in epithelial-derived cancers (carcinomas), a basement membrane surrounds the tumor separating it from the stroma. In the tumor microenvironment, fibronectin and collagen I fibers can also be found as they are produced by CAFs.

The hallmarks of cancer

Normal cells go through a multi-step process to acquire characteristics and capabilities, transforming them into cancer cells. These new characteristics mainly appear from spontaneous genetic mutations occurring one after the other. Each acquired feature enables the cells to escape the anticancer mechanism defense and generate a cancerous tumor until they reach their full cancer cells capabilities. There is no specific order for the apparition of each characteristic, even though some can appear simultaneously as they rely on the same type of mutation. In contrast, others can take several mutations to occur. The characteristics and capabilities cells need to acquire to become cancer cells have been classified as cancer's hallmarks (Hanahan, 2022, 2011; Hanahan and Weinberg, 2000). Each hallmark comprises all the features obtained by cells to enable one characteristic of cancer cells. There are currently fourteen hallmarks of cancer which are divided into two different types (Hanahan, 2022): the hallmarks' capabilities and the enabling characteristics. The hallmarks capabilities correspond to properties acquired to become cancer cells, whereas the enabling characteristics correspond to properties acquired to develop the hallmarks capabilities. All the current hallmarks of cancer are present in Figure 3 and are described below.

The first hallmark capability is sustaining proliferative signaling. This is one of the most important hallmark capabilities as sustaining proliferative signaling allows cancer cells to independently triggers their proliferation and thus multiply and potentially generate the other hallmarks. In normal tissue, proliferation is tightly controlled to keep with homeostasis, architecture, and function of the tissue, whereas inside a tumor, cancer cells are highly proliferative (Witsch et al., 2010). To proliferate, a cell needs to receive growth-promoting signals through receptors on the cell surface. However, in normal conditions, these growth factors are spatially and temporally controlled to generate new cells only where and when needed. By obtaining the sustained proliferative signaling hallmark capability, the cancer cells escape from this tissues-monitored proliferation system to an autonomous and permanent proliferation system. To do so, cancer cells can either secrete growth factors to which they respond or stimulate other cells present in the tumor microenvironment, such as CAFs, to generate growth factors(Cheng et al., 2008; Perona, 2006). In addition, cancer cells can increase the number of receptors at the cell surface to become hyper-responsive to growth signals.

Along with sustaining proliferative signaling, the following hallmark capability is evading growth suppressor. Indeed, in normal conditions, tissues not only express growth signals specifically when and where it is needed, but they also express anti-proliferative signals to keep the rest of the cells quiescent and thus ensure homeostasis. Cancer cells need to escape these anti-proliferative signals to proliferate rapidly and without restriction. Anti-proliferative signals can be transmitted by contact inhibition

between cells. Such inhibition does not affect cancer cells (Curto et al., 2007). However, most anti-proliferative signals are governed by tumor suppressor genes which generate proteins such as the retinoblastoma-associated protein RB or the TP53 (Burkhart and Sage, 2008; Sherr and McCormick, 2002). RB signaling is mainly responsible for receiving outside anti-proliferative signals and translating them by inhibiting cell division signals. TP53 signaling, on the other hand, is mainly in charge of dealing with anti-proliferative signals from inside the cells, such as the lack of good conditions for cells to divide. Losing one or several of these anti-proliferative signaling pathways allows cancer cells to obtain the evading growth suppressor hallmark capability and thus proliferate without restriction.

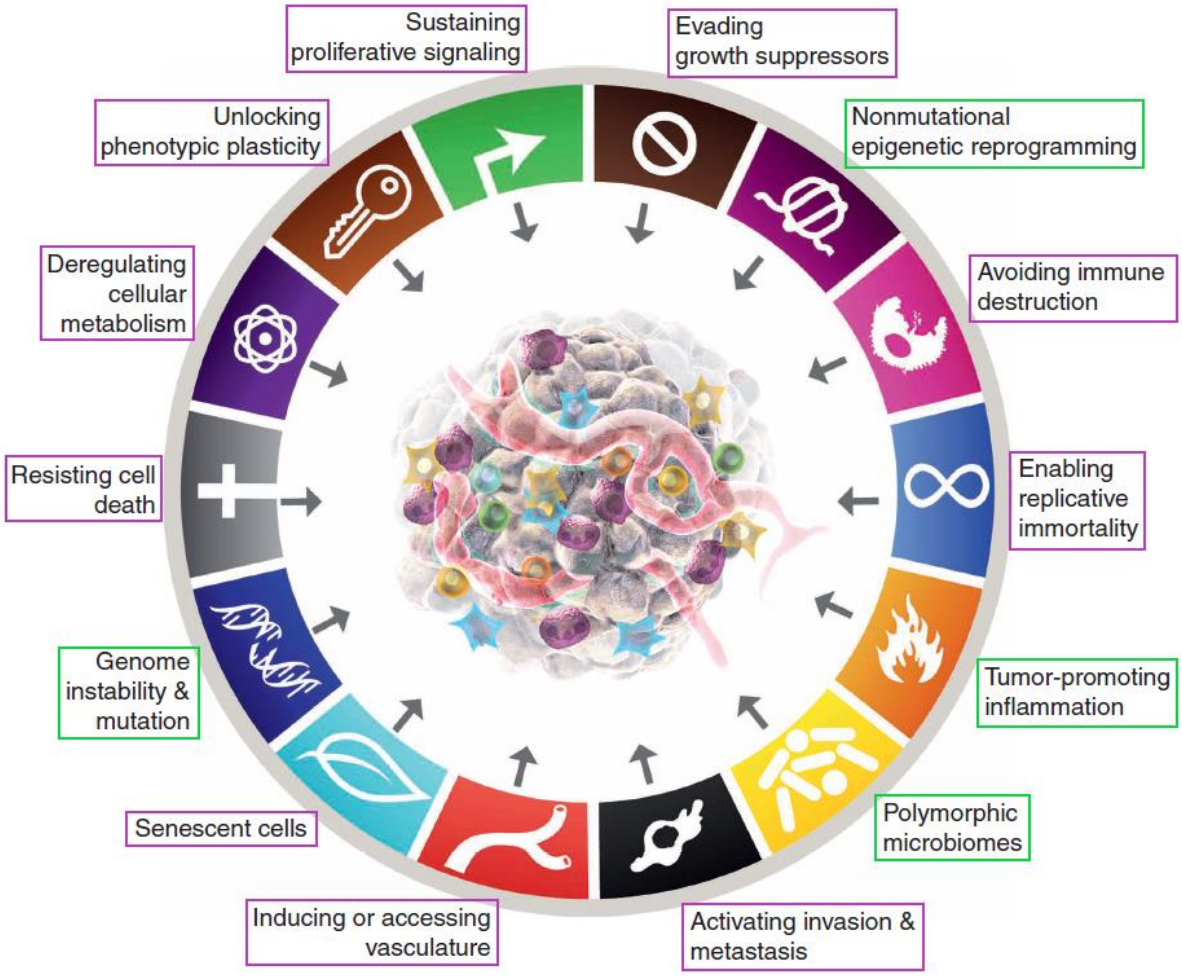

Figure 3. Hallmarks of cancer.
Scheme representing the fourteen hallmarks of cancer. In purple are the hallmarks capabilities, and in green are the hallmarks enabling characteristics.
Taken from Hanahan, 2022.

Being able to proliferate permanently and without restriction is not enough to generate and sustain a tumor, as cell death can still occur. Hence the next hallmark capability is resisting cell death. In normal conditions, cells have an apoptotic program that can be triggered from inside or outside the cells in

case of stress or detected abnormality such as DNA damage (Lowe et al., 2004). The apoptotic program comprises two parts: the regulators that monitor the outside and inside signaling to decipher whether or not to start the apoptosis process, and the effectors in charge of realizing the apoptosis process once cell death has been decided (Adams and Cory, 2007). Cancer cells can develop diverse strategies to avoid apoptosis, such as limiting their capacity to sense apoptosis signals or disturbing the communication between regulators and effectors. A common strategy found in many cancer cells is the loss of the TP53 tumor suppressor protein (Junttila and Evan, 2009) as it triggers apoptosis in many situations during tumor development, such as DNA damage or hypoxia. Cancer cells use different strategies to avoid apoptosis that can be used simultaneously to gain the resisting cell death hallmark capability.

Another death threat that cancer cells must overcome is the immune system. Indeed, in normal conditions, the immune system patrols the tissues to destroy any abnormality that could occur, such as the apparition of over proliferative cancer cells. Thus most tumors are killed from the start (Pagès et al., 2010). To develop into a tumor, cancer cells need to escape the immune system surveillance. Therefore, the next hallmark capability is avoiding immune destruction. To do so, cancer cells can impair the immune cell capacity to recognize them, for example, by secreting immunosuppressive factors. Secretion of TGFβ, for instance, can paralyze CTLs and NKs cells, thus preventing them from harming cancer cells (Yang et al., 2010). The secretion of immunosuppressive factors can be done by the cancer cells themselves, or it can be done by other cells under the control of the cancer cells. In addition, cancer cells can recruit and reformate inflammatory immune cells, such as regulatory T cells or myeloid-derived suppressor cells, to prevent CTLs actions thanks to their immunosuppressive capacity (Mougiakakos et al., 2010). This way, cancer cells not only escape the immune system but also hijack part of it to help them avoid the other part (Smyth et al., 2006). This gives rise to the avoiding immune destruction hallmark capability.

These four hallmarks allow cancer cells to proliferate autonomously and escape from programmed death, they are, however, still not sufficient for cancer cells to generate a tumor. Indeed, death can still occur, limiting the growth, and proliferation is limited by the number of replication cells can do. Once the limit is reached, cells stop multiplying and go either into senescence, a viable but irreversible non-proliferative state, or into a crisis phase that generally ends with cell death. Hence the aim of the next hallmark capability: enabling replicative immortality. In normal cells, proliferation limitation comes from the telomeres present at the end of each chromosome (Shay and Wright, 2000). Telomeres are parts of DNA present at each end of chromosomes that protect chromosomes from end-to-end fusion. At each replication, a short bit of telomeres is cut out at each end of chromosomes. This shortening of telomeres limits proliferation as cells either go into senescence before telomeres

get too short or continue until losing telomeres protection and go into a crisis state. To overcome this limitation, cancer cells generally start expressing telomerase (Artandi and DePinho, 2010; Blasco, 2005). Telomerase is a DNA polymerase that can continuously extend telomeres size, thus impeding telomeres shortening with division. This way, cancer cells obtain the enabling replicative immortality hallmark capability.

As cells become cancer cells, they gain new abilities and keep some properties from the type of cells they were before. Some of these properties are similar to functions cells used to have in healthy tissue. These functions go along with differentiation into specialized cells. However, the end of the cell differentiation pathway generally results in a quiescent anti-proliferative state. Hence, the next hallmark capability: unlocking the phenotypic plasticity. Through this hallmark, cancer cells can escape the terminal differentiation and go to the level of differentiation they need. Different pathways lead by different signaling are possible depending on the level of differentiation cancer cells exhibit (Yuan et al., 2019). Differentiated cancer cells can return to a dedifferentiated state, whereas progenitor cancer cells can either block differentiation or transdifferentiate (Merrell and Stanger, 2016; Saghafinia et al., 2021), meaning going through another differentiation than expected. Such phenotypic plasticity can give rise to cancer stem cells that can resist treatment by going into a dormant state and thus improve tumor survival. Cancer cells can also escape treatments targeting their lineage-specific markers by transdifferentiating into another lineage that does not express them (Mu et al., 2017). Finally, senescent cells can also escape from this quiescent non-proliferative state to return to a less differentiated state into which they can proliferate.

Senescence in the tumor microenvironment is generally seen as tumor inhibiting because senescence inactivates cells and thus proliferation. However, allowing the presence of senescent cells in the tumor microenvironment can, counterintuitively, be beneficial for tumor progression (Wang et al., 2020). Hence the next hallmark capability: senescence. Senescence is a dormancy state that can allow cancer cells to resist treatment aiming against proliferative capabilities. Because cancer cells develop the ability to escape from the senescent state by unlocking the phenotypic plasticity hallmark capability, cancer cells can use senescence to protect themselves from treatment (De Blander et al., 2021). Senescent cells also activate the senescence-associated secretory phenotype (SASP). Through SASP senescent cancer cells can contribute to proliferation, anti-apoptotic signals, angiogenesis, immunosuppressive and invading signaling in the tumor microenvironment (Faget et al., 2019). Finally, senescence can also occur in other cell types, such as CAFs. Senescent CAFs also express SASP and, as senescent cancer cells, contribute to several tumor-promoting signaling pathways (Ruhland et al., 2016). Senescent CAFs can also remodel the ECM to help local invasion and thus promote metastasis.

Cancer cells, like normal cells, need access to oxygen and nutrients to survive and function. With cancer cells' unlimited proliferation and tumor growth, proximity from blood vessel supply can be compromised, consequently limiting tumor growth. Hence the next hallmark capability: inducing or accessing vasculature. Blood vessels are formed and maintained by endothelial cells with the support of pericytes. In normal conditions, endothelial cells are kept quiescent to maintain tissue homeostasis. Upon injury, endothelial cells are activated to repair the damaged blood vessels through pro-angiogenesis signaling. To get vascularized, tumors start expressing pro-angiogenesis signaling such as vascular endothelial growth factor-A (VEGF-A) or fibroblast growth factor (FGF) (Baeriswyl and Christofori, 2009; Ferrara, 2009). These signals allow cancer cells to recruit and reformate endothelial cells and pericytes to generate vascularization inside the tumor (Bergers and Benjamin, 2003). Cancer cells can also recruit and reformate some immune cells and CAFs present in the tumor to express pro-angiogenesis signaling. Thus, endothelial cells and pericytes are always activated in the tumor microenvironment, generating new blood vessels to provide oxygen and nutrient for cancer cells.

Even with vascularization inside the tumor, cancer cells can still suffer from a lack of nutrients and particularly from a lack of oxygen, a condition called hypoxia. Moreover, proliferation is heavily energy-consuming. To have enough energy to keep multiplying in such conditions, cancer cells must obtain the next hallmark capability: deregulating cellular metabolism. In normal conditions, cells generate energy via glucose degradation using oxygen. Upon hypoxia, cells can switch to another metabolism pathway using glycolysis. However, the glycolysis pathway is eighteen-fold less efficient in generating energy than the glucose pathway. Hypoxia is frequent in the tumor microenvironment, so cancer cells switch to the glycolysis pathway to generate energy, even when oxygen is available (Hsu and Sabatini, 2008). To counter the lack of efficiency of this process, cancer cells gain the ability to increase the numbers of transporters, such as GLUT1, as well as several other enzymes involved in the glycolysis pathway (DeBerardinis et al., 2008; Jones and Thompson, 2009; Semenza, 2010). In doing so, cancer cells upregulate the glycolysis pathway and thus manage to produce enough energy to survive and proliferate at a high rate even under hypoxia.

As the tumor grows, resources and available places can still become a limiting development factor. To overcome this overpopulation issue, cancer cells obtain the last hallmark capability: activating invasion and metastasis. Cancer cells gain the ability to escape the tumor and invade new places to generate secondary tumors called metastasis. To do so, cancer cells develop invasive and migratory capacities, such as changing the adhesion molecules they use. In normal tissues, E-cadherin is the main adhesion molecule as it is a cell-cell junction molecule that helps maintain the architecture and homeostasis of the tissue. In certain cancer types, E-cadherin is downregulated in favor of N-cadherin, a cell-cell junction molecule found in mesenchymal cells, which is upregulated, favoring cancer cell migration

(Berx and van Roy, 2009). Another strategy generally used by cancer cells is the acquisition of the epithelial to mesenchymal transition (EMT). Cancer cells gain access to mesenchymal properties such as migration and invasion capacities as single cells (Klymkowsky and Savagner, 2009). Once in a new place, cancer cells can switch back to an epithelial phenotype, via mesenchymal to epithelial phenotype (MET), and start the colonization process. However, cancer cells can also migrate collectively without using EMT (Friedl and Wolf, 2010). Even more, thanks to the unlocking phenotypic plasticity hallmark capability, cancer cells can show different levels of epithelial to mesenchymal transition and thus benefit from both epithelial and mesenchymal properties simultaneously enhancing the metastasis process.

The first hallmark enabling characteristic is genome instability and mutations. In normal conditions, mutations are rare as there is an entire machinery constantly watching over the DNA integrity. This machinery reacts quickly to damage by repairing it or committing the cells to senescence or apoptosis. With genome protection, obtaining all the mutations needed for all the hallmarks capabilities won't be possible in a human lifespan. Hence the need for cancer cells to obtain genetic instability to facilitate the mutation process they go through. To do so, cancer cells deregulate the machinery watching over DNA to prevent it from either spotting damage, repairing it, or protecting DNA from potential harm (Berdasco and Esteller, 2010). Deregulating this machinery can be done by losing TP53 protein, a central protein in the DNA monitoring process, as in most cancers (Lane, 1992; Negrini et al., 2010). Without TP53 protein, cell division cannot be stopped anymore in case of DNA damage which generates genome instability facilitating the apparition of mutations.

The genome instability and mutations hallmark enabling characteristics are essential for cells to become cancer cells. However, not all characteristics of cancer cells are achieved through mutations, some can be obtained through reprogramming. Hence the next hallmark enabling characteristic is non-mutational epigenetic reprogramming. Indeed, cancer cells can be epigenetically reprogrammed to develop hallmark capabilities thanks to tumor microenvironment stimulus (Darwiche, 2020). Hypoxia, for example, enhances hypermethylation of DNA which can inactivate tumor suppressor genes (Thienpont, 2016), while ECM stiffening in the tumor enhances invasion (Mohammadi and Sahai, 2018). Moreover, cancer cells recruit and reprogram tumor-associated cells, such as CAFs, endothelial cells, pericytes, and immune cells, by inducing non-mutational epigenetic reprogramming through signaling inside the tumor microenvironment (Hanahan and Coussens, 2012). Thus, non-mutational epigenetic reprogramming facilitates tumor development and is a hallmark enabling characteristic.

The next enabling characteristic is tumor-promoting inflammation. Promoting inflammation in the tumor microenvironment could be detrimental for cancer cells as it attracts all different immune cells.

However, as discussed above, cancer cells can gain the ability to escape the immune system and, even more, can recruit and reprogram some immune cells for their benefit (Colotta et al., 2009; de Visser et al., 2006). Moreover, inflammation activates secretions of bioactive molecules that facilitate the acquisition of hallmark capabilities, such as favoring angiogenesis, promoting cell survival, enhancing cell proliferation, and ECM remodeling to help the invasion (DeNardo et al., 2010; Qian and Pollard, 2010). Finally, inflammatory cells can also facilitate mutations and thus the acquisition of new hallmark capabilities for cancer cells by releasing reactive oxygen species, molecules with mutagenic effects, inside the tumor microenvironment (Grivennikov et al., 2010). Therefore, tumor-promoting inflammation is an enabling characteristic.

The last enabling characteristic is the polymorphic microbiome. Several organs, such as the skin, the gut, the lungs, or the breast, are in contact with the outside environment through an epidermis or an internal mucosa. At these barriers, microbiota exists and develop themselves in symbiosis with the tissue to benefit from each other presence. Microbiota can thus interact with a tumor at the barrier and promote its growth (Dzutsev et al., 2017). In the gut, for example, some bacteria produce toxins that can enhance mutation inside cancer cells, while other bacteria can trigger cancer cell proliferation (Sears and Garrett, 2014). Moreover, for lung, breast, brain, bone, melanoma, pancreas, and ovary cancers, specific bacteria were found in cancer cells and the immune cells (Nejman et al., 2020). These different bacteria are associated with tumor-enhancing properties, such as inflammation promotion. Hence, the presence of polymorphic microbiomes in the tumor microenvironment can have, by different means, a positive effect on tumor development.

These hallmarks represent the characteristics that cancer cells should obtain to fully develop a tumor in the initial tissue and the capacity to disseminate and generate metastasis in other tissues. Most of these hallmarks, such as inflammation promotion, immune system survival signaling, angiogenesis promotion, or CAFs activation, also characterize injury repair mechanisms. Due to this resemblance, cancer is often referred to as the wound that never heals (Hanahan, 2011).

The physical hallmarks of cancer

The fourteen hallmarks described above correspond to biological aspects developed by cancer cells inside the tumor microenvironment. The role of the microenvironment in the tumor progression is described only through the biological properties of the other cell types present and some chemical conditions, such as hypoxia. However, physical abnormalities in the tumor microenvironment can also promote tumor development and enhance the hallmarks of cancer described above. Thus, it is important to also look at the physical traits of cancer inside the tumor microenvironment. Currently, there are four physical hallmarks of cancer described (Nia et al., 2021) (Figure 4).

The first physical hallmark is fluid pressure. In normal conditions, fluid presence inside tissues is maintained to the minimum required as blood stays inside the blood vessels and lymphatic vessels drain the excess fluid to maintain homeostasis with almost no fluid pressure. In the tumor microenvironment, angiogenesis-activated endothelial cells and outnumbered pericytes generate leaky blood vessels. In addition, blood and lymphatic vessels are often compressed, affecting their functioning. These conditions lead to an elevated interstitial fluid pressure inside the tumor. This higher pressure inside the tumor compared to the outside generates a gradient that drives fluids out of the tumor (Boucher et al., 1990). Once in normal tissues, fluids from the tumor are drained by lymphatic vessels. The directionality of this fluid flow towards the outside of the tumor can facilitate tumor spreading by driving cancer cells and growth factors to the border of the tumor (Polacheck et al., 2011). It can also enhance tumor resistance to drug treatments by evacuating drugs out of the tumor (Jain, 2013). Fluid flow also generates shear stress on the different cell types in the tumor microenvironment. Shear stress can, in return, activate CAFs, trigger invasion and migratory pathways in cancer cells, and modulate endothelial cell angiogenesis (Song and Munn, 2011), all of which promote tumor development.

The second physical hallmark is solid stress. By proliferating, cancer cells need more and more space, and thus, they push surrounding tissues, generating solid stress in the tumor. Nodular tumors, that grow cohesive systems generate higher solid stress than infiltrative tumors. Moreover, cancer cells and CAFs can contract and transmit their contraction to the ECM, further augmenting solid stress inside the tumor. Solid stress can impact tumor development. Under solid stress, blood vessels get compressed, leading to hypoxia, which can affect cancer cells' hallmarks capabilities, but also disturbance of drug delivery to the tumor, which can facilitate tumor resistance (Padera et al., 2004). Solid stress also enhances the invasiveness pathway in cancer cells (Tse et al., 2012). It activates mechanoresponsive factors such as yes-associated protein (YAP), which in turn promote cell proliferation and survival as well as activation of CAFs (Panciera et al., 2017). Finally, solid stress favors

cell competition inside the tumor and at the border between the tumor and the normal tissues, which promotes tumor growth and expansion inside the normal tissues (Merino et al., 2016).

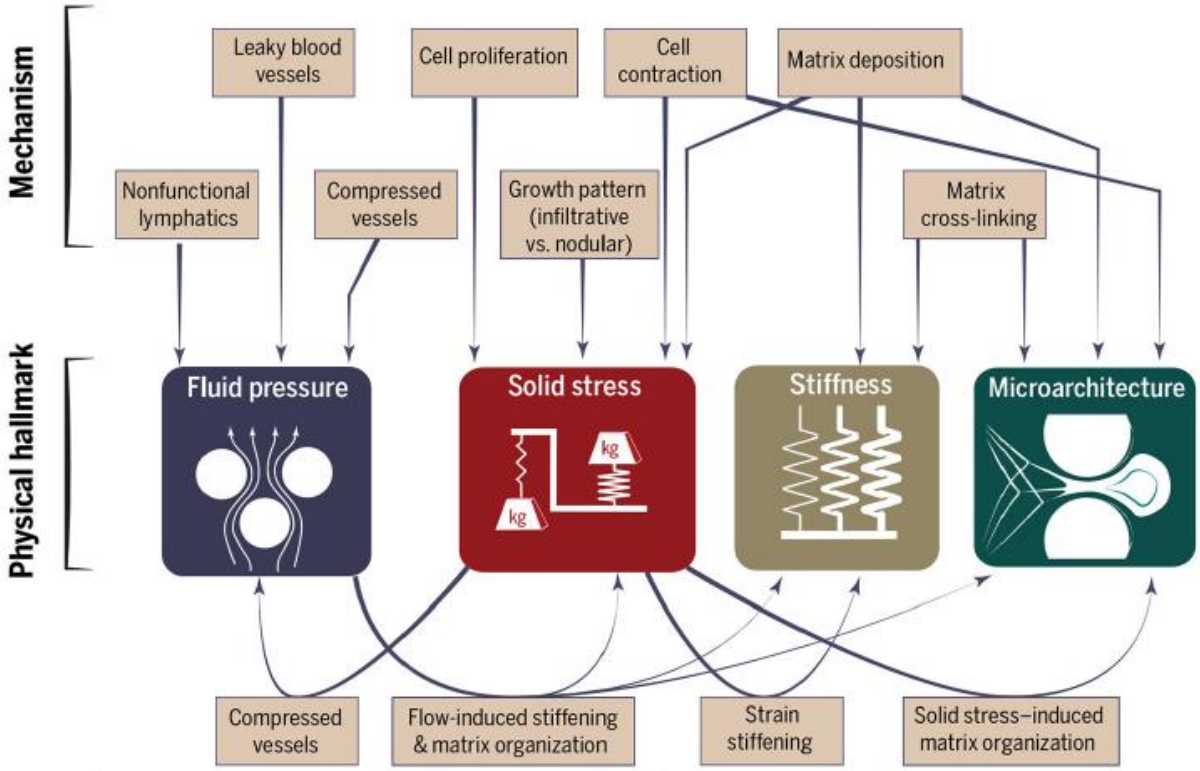

Figure 4. The physical hallmarks of cancers.
The scheme presents cancer's four physical hallmarks with associated mechanisms and interactions between them. Taken from Nia, 2020.

The third physical hallmark is stiffness. Stiffness corresponds to the quantity of elastic deformation a material undergoes when submitted to a force. The stiffer material is, the less it deforms. Stiffening of the tumor microenvironment occurs along the tumor development and is generally used to detect a tumor in a patient (Cochlin et al., 2002). Tissue stiffening is mainly due to the ECMs deposition, remodeling, and cross-linking realized by the CAFs under cancer cell activation. Solid stress inside the tumor microenvironment can also induce stiffening of the tumor microenvironment through strain-stiffening: stretching or compression of ECM fibers leads to their stiffening as an adaptation to the stress they feel (Storm et al., 2005). Moreover, stiffening of the ECM triggers CAFs to deposit and cross-link the ECM generating a positive feedback loop of the tumor microenvironment stiffening (Pickup et al., 2014). Stiffening, in return, promotes tumor growth by stimulating proliferation, angiogenesis, and growth factors secretion (Leight et al., 2012). It also enhances invasiveness and metastasis by

facilitating EMT, for example, and immune cell infiltration. Finally, stiffening also seems to provide treatment resistance.

The last physical hallmark is microarchitecture. In normal tissues, homeostasis is also maintained through the specific microarchitecture of each tissue, which promotes cell functions, efficiency, and tissue stability. Inside the tumor microenvironment, the initial microarchitecture is disturbed due to cell proliferation, solid stress deformation, and ECM deposition and cross-linking leading to a new microarchitecture specific to the tumor. Such new microarchitecture promotes tumor development. Specific arrangements of ECM can promote cell proliferation by imposing the cell shape, whereas aligned ECM enhances cancer cell migration (Provenzano et al., 2006). Invasiveness can also be promoted by microarchitecture through induction of EMT. The specific organization of the microarchitecture can also enhance genome instability and increase mutation rates. For example, forcing cancer cells to migrate through ECM pores smaller than their nucleus could induce their nuclear membrane rupture, thus DNA damage (Irianto et al., 2017). Finally, microarchitecture can also modify the diffusion of molecules in the tumor microenvironment and thus potentially promote tumor resistance to drug treatments (Stylianopoulos et al., 2010).

The metastasis cascade

One of the main issues with cancers nowadays is their capacity to metastasize - to generate secondary tumors in distant locations from the primary tumor. Indeed, the appearance of metastasis leads to a drastic decrease in survival rates in patients. To metastasize, cancer cells must exit the primary tumor and travel to the new location where they develop secondary tumors in a process called the metastasis cascade. Metastasis can occur at any time during tumor development, even before the tumor reaches its detectable size. The metastasis cascade is composed of several steps linked to the different environments cancer cells cross during their journey (Figure 5) (Welch and Hurst, 2020). It is a complex and selective process as only a few cancer cells which start the metastasis cascade manage to achieve it. To overcome all challenges of the metastasis cascade, cancer cells acquire several adaptive characteristics such as motility and invasion, modulation of the microenvironment, plasticity, and colonization. These characteristics have already been discussed in the above description of physical and biological hallmarks of cancer. They are further enhanced in cancer cells doing the metastasis cascade to promote their survival and actions, which generates a subpopulation of metastatic cancer cells.

Cancer cells generally move through the vascular system to reach the next location (Figure 5). Cancer cells, however, can also circulate through the lymphatic system, along the nerves, or outside of the

blood vessel (basal side of the endothelial cells) (Sleeman et al., 2011). The main use of the vascular system can explain the preferential metastatic sites for each cancer type by their immediate proximity in terms of blood circulation (Weiss, 1992). However, it does not explain all the preferential metastatic sites, especially the frequency of bone metastasis among all cancers. Hence the appearance of the "seed and soil" hypothesis (Fidler, 2002). This hypothesis stipulates that, while developing in the primary tumor, cancer cells acquire preferences for the microenvironments to grow in through signaling selection by the host tissue. The site of metastasis is thus chosen based on the crosstalk between cancer cells and potential new hosts to target those whose characteristics correspond to the cancer cells' preferences.

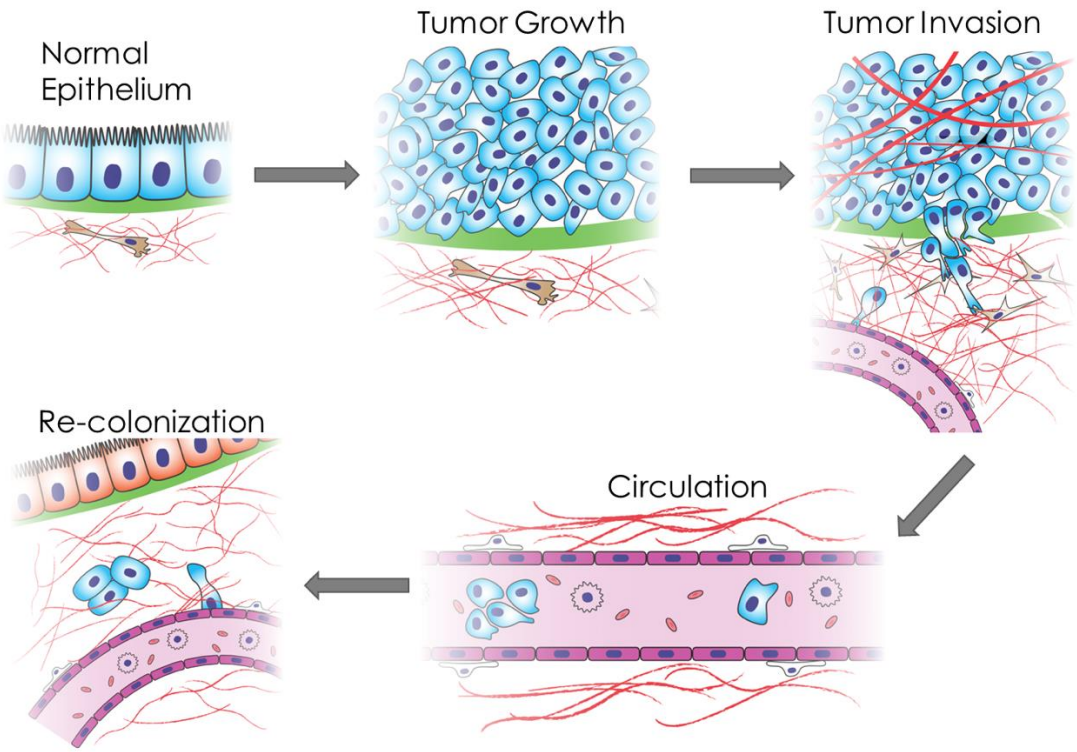

Figure 5. The metastatic cascade.
Scheme representing the different steps of the metastasis cascade.
Taken from Andrew Clark.

The metastasis cascade begins before cancer cells start their journey by establishing a pre-metastatic niche (Peinado et al., 2017). In the tumor microenvironment, soluble factors are secreted and transferred via blood vessels to the targeted sites for metastasis. At these sites, the soluble factors induce mesenchymal and hematopoietic stem cell activation to remodel the architecture of the microenvironment to suit the future metastases needs.

The first step of the metastasis cascade per se is the tumor invasion. During this step, cancer cells exit the tumor and start migrating inside the stroma to reach the vascular system. To be able to migrate

through the ECM, cancer cells gain the invasive and migratory capacities as well as the microenvironment modulation abilities discussed above. Different migration modes can be used, such as the EMT or amoeboid migration (Clark, 2015). Migration can also be done by single cells or groups of cells. Collective migration allows cancer cells with heterogeneous characteristics to cooperate and benefit from each other characteristics and thus gain efficiency. The type of migration depends on cancer cells' capacity to adhere to other cells and the ECM, and undergo deformation (Friedl et al., 2012). In carcinoma, a basement membrane separates the tumor and the stroma and is, thus, the first barrier cancer cells must breach to start the invasion. To overcome this barrier, cancer cells combine enzymatic matrix degradation and physical matrix remodeling by themselves or other tumor-associated cells to generate passage through the basement membrane (Bonnans et al., 2014; Schoumacher et al., 2011). Cancer cells then proceed inside the stroma using similar strategies. Finally, these disturbances of the microenvironment by the first migratory cancer cells leave tracks that the following cancer cells can use to facilitate their migration (Erdogan et al., 2017).

Once at a blood vessel, cancer cells enter the blood vessel via the intravasation process. Blood vessels are covered with a basement membrane. Thus, cancer cells first get through this basement membrane using their invasion strategy and then squeeze themselves between endothelial cell junctions to enter the blood vessel without damaging significantly the blood vessel integrity (Nicolson, 1982). Intravasation can also occur passively with cell proliferation pushing cells inside the blood vessel (Wong and Searson, 2017). Moreover, as blood vessels in the tumors are often leaky, the intravasation process is facilitated.

Upon entry inside the vascular system, the next step of the metastasis cascade is the dissemination and transport of cancer cells, also called circulation. During this step, cancer cells are called circulating tumor cells (CTC). Inside blood vessels, the microenvironment drastically differs from the tumor microenvironment leading to one of the biggest challenges: surviving (Butler and Gullino, 1975). Indeed, the sheer force and pressure from the fluid flow can rip cancer cells apart, especially in capillaries where the flow speed increases. CTCs also undergo huge deformations to squeeze through half their size capillaries. Such deformations can also tear them (Krog and Henry, 2018). Moreover, inside blood vessels, CTCs are more exposed to immune cells such as leukocytes that can kill them (Crissman et al., 1985). Consequently, many CTCs are destroyed while circulating inside the vascular system. Surviving CTCs possess enhanced deformability and the capacity to evade the immune system (Krog and Henry, 2018). This could be achieved by forming clusters, either with other CTCs or with fibrin, platelet, and immune cells, which improves CTCs' survival as being inside a cluster protect them from sheer and immune cells (Aceto et al., 2015). Finally, CTCs migration inside the blood vessel can

either be passive thanks to the flow of fluid pushing them or active via a migratory mechanism (Ito et al., 2001). In most cases, CTCs roll along the blood vessel walls.

The next step of the metastasis cascade is to exit the blood vessel at the chosen site: cellular arrest, vascular adhesion, and extravasation. Cells arrest either passively due to physical constraints, such as the diameter of the blood vessel, or actively due to CTCs adhering to specific places (Auerbach et al., 1987). Cancer cells can select where they stop inside the vasculature thanks to markers of endothelial cells at their surface. Indeed, endothelial cells express markers that specify where they are inside the body, like an address. Cancer cells can read these addresses and adhere selectively to the chosen ones (Pasqualini and Ruoslahti, 1996). Moreover, in case of inflammation inside the tissues, endothelial cells express specific markers to facilitate immune cells arriving at the site. Cancer cells can also feel these specific markers and adhere to them. Alternatively, cancer cells adhere to the ECM, such as fibronectin, produced by endothelial cells (Barbazán et al., 2017). Once attached to the endothelial cells, cancer cells induce endothelial cells' retraction, allowing access to the basement membrane below. Facing the basement membrane, cancer cells migrate through it using strategies similar to the intravasation process, finally entering the secondary organ.

Once arrived at the new location, the last step of the metastasis cascade starts: colonization. Colonization doesn’t necessarily begin as soon as cancer cells arrive at the location. Indeed, upon arrival, cancer cells can enter dormancy. In this dormancy state, cancer cells seem to be inactive and cannot be detected, which helps them escape treatment. Different possibilities can explain the entry into dormancy, such as lack of nutrients or immune surveillance (Gay and Malanchi, 2017). Upon stimulation, cancer cells can escape dormancy and go back to the colonization process. The colonization process at the new site can be facilitated as the environment is already modified to suit them thanks to the pre-metastatic niche established before cancer cells arrive (Kaplan et al., 2005). To generate a secondary tumor, cancer cells acquire the same characteristics as those that generate the primary tumor described before. Cancer cells that used EMT to migrate generally transition back to epithelial characteristics using MET to recapitulate their proliferative capacities (Hugo et al., 2007). Cancer cells, thus, start to proliferate again and generate a secondary tumor which will recapitulate the same characteristics as the primary tumor such as tumor microenvironment and hallmarks, as well as the capacity to metastasize. Hence, new metastasis can arise from secondary tumors using the metastasis cascade from the beginning.

Cancer invasion as the first step of the metastasis cascade

As described above and recapitulated in Figure 6, cancer invasion is the first step of the cancer cells' journey to form metastasis. This step comprises the escape from the primary tumor to the arrival at one blood vessel (Clark, 2015). In the case of carcinoma, cancer cells first need to breach the basement membrane separating the tumor from the stroma. Basement membranes are thin layers of ECM at the basal side of epithelium and endothelium, providing support for cell adhesion, cues for cell polarity, and compartmentalization (Glentis et al., 2014). Basement membranes are composed of two polymer networks, one made of collagen IV and the other of laminin, interconnected with nidogens and perlecan (Figure 7). Basement membranes are generated at the basal side of epithelial cells as the generation of the laminin network requires its adhesion to the cell receptor present there. The production of basement membranes is, however, a cooperated action between epithelial cells and mesenchymal cells, like fibroblasts or pericytes, as each type of cell secretes only a specific part of the proteins composing the basement membrane (Ekblom et al., 1994). Depending on their localization in the tissues, basement membranes vary in terms of chemical compositions as well as physical structures.

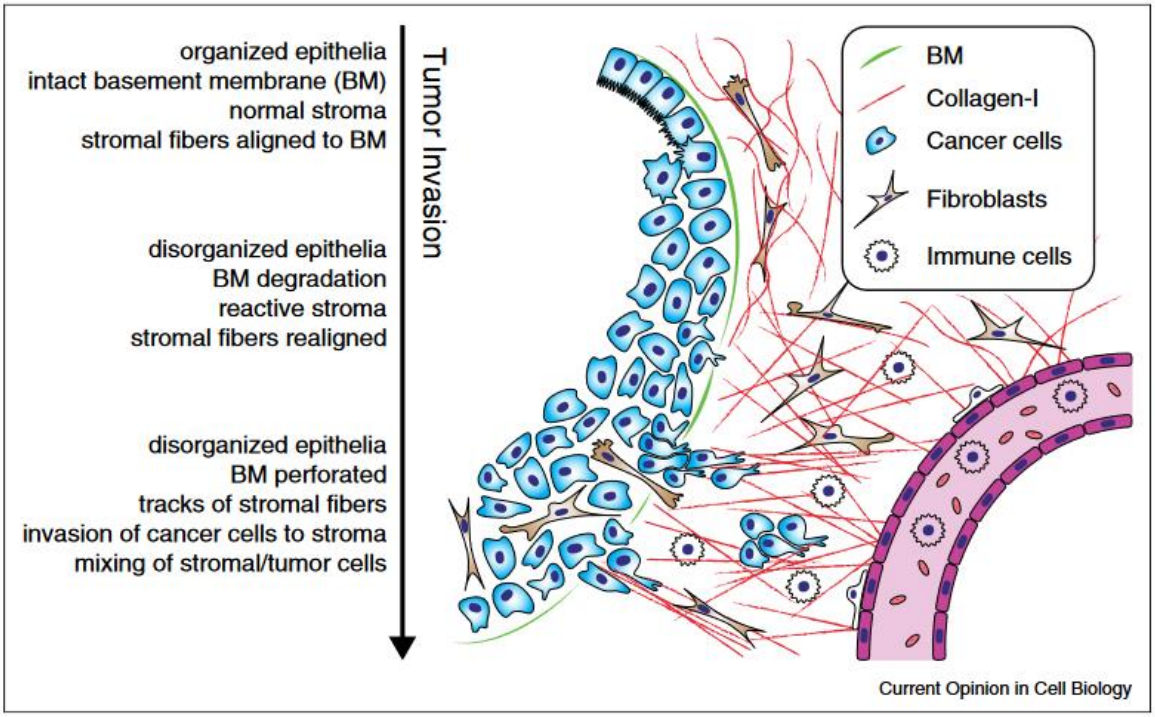

Figure 6. The tumor invasion process.
Scheme recapitulating the tumor invasion process.
Taken from Clark, 2015

To overcome the basement membrane, cancer cells develop several strategies. The first is to chemically deteriorate the matrix using matrix-degrading proteases such as matrix metalloproteinases (Poincloux et al., 2009). The second strategy is to physically make their way through the basement membrane using mechanical forces (Sahai and Marshall, 2003). Finally, the basement membrane barrier capacity could be reduced by decreasing the production of basement membrane components (Kang et al., 2013). These strategies can be combined to enhance invasiveness.

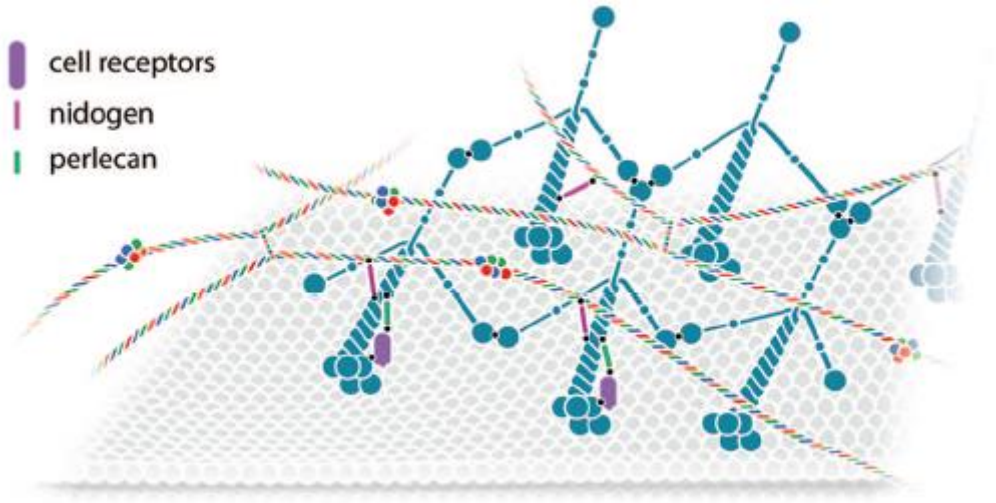

Figure 7. The basement membrane representation.
Scheme representing the two polymer networks composing the basement membrane: the laminin network (blue heterotrimers) and the collagen IV network (red, green, and blue fiber). The positions of the interconnectors, nidogen, and perlecan, and the position of cell receptors are also represented.
Taken from Glentis, 2014.

Once the basement membrane is breached, the next step for cancer cells during the tumor invasion is to modulate their way through the stroma to reach blood or lymphatic vessels. The stroma is mainly composed of a network of collagen I fibers that are curly and anisotropically oriented in healthy tissues. The growth of the primary tumor modifies the stroma around it by straightening and aligning the collagen I fiber parallel to the tumor (Egeblad et al., 2010b). Moreover, the stroma around the tumor also becomes stiffer over time due to remodeling and ECM deposition. This stiffening, parallel orientation, and excess of ECM can promote cancer cells' invasiveness characteristics as well as physically restrain the tumor growth and escape (Egeblad et al., 2010b). To invade the stroma, cancer cells develop strategies similar to the breaching of the basement membrane: stroma remodeling by chemical matrix disruption using proteases or physical fibers displacements with mechanical forces (Poincloux et al., 2009; Sahai and Marshall, 2003). This stroma remodeling during tumor invasion leads to a new organization of the collagen I fibers network around the tumor from parallel to the tumor to perpendicular to the tumor, creating highways that cancer cells follow to migrate out of the tumor and within the stroma (Conklin et al., 2011). Cancer cells migrate collectively as groups of cells or alone as

single cells using either amoeboid or mesenchymal migration. Collective migration can either be done by groups of cancer cells that maintain their cell-cell adhesion to move as a group with leaders and followers or by streams of cells following each other without being adhesive to each other (Bronsert et al., 2014; Clark, 2015). During the invasion, cancer cells exhibit one preferential type of migration depending on cell-cell and cell-ECM adhesion and contractile abilities as well as ECM density, stiffness, and reorganization. Upon changes in these properties, cancer cells can switch to another type of migration that fit better the new conditions they are facing to pursue cancer invasion (Weigelin et al., 2012).

Summary

Cancer is a disease intrinsic to living being linked to abnormal cell growth and migration inside the body. It is the second leading cause of death worldwide and is expected to become the first in a few decades. However, advanced cancer treatment coming from research, early detection, and prevention against the risk factors could reduce cancer mortality.

Cancer arises inside one organ and develops into a primary tumor whose microenvironment comprises cancer cells and other types of cells. Indeed, in addition to different types of cancer cells, the tumor microenvironment also possesses endothelial cells, pericytes, immune-inflammatory cells, and cancer-associated fibroblasts, as well as local and bone marrow-derived stromal stem and progenitor cells. The ECM, mostly composed of basement membranes, collagen I, and fibronectin fibers, is also present in the tumor microenvironment.

Normal cells undergo a series of transformations to acquire the cancer cells phenotype to become cancer cells. The characteristics needed to become cancerous are classified into the hallmarks of cancer. In addition to the biological modification of cells, the tumor microenvironment also undergoes physical transformation.

The metastasis cascade is the process through which cancer cells escape the primary tumor to disseminate into the body and generate secondary tumors. Apparition of metastasis is linked with poor survival prognostic as their apparitions lead to patient death in 90% of the cases. The cancer invasion is the first step of the cancer cells' journey during the metastasis cascade. It corresponds to the moment cancer cells escape the primary tumor to join blood or lymphatic vessels. During this step, cancer cells breach the basement membrane constraining the primary tumor and migrating inside the stroma. To overcome the ECM, cancer cells can remodel it using either chemical or physical strategies, alone or with the help of cells in their microenvironment.

Chapter II: Cancer-associated fibroblasts and their roles in cancer invasion

Origins of cancer-associated fibroblasts

Cancer-associated fibroblasts (CAFs) are the main component of the tumor microenvironment. They are characterized by their elongated spindle shape, mesenchymal phenotype, and contractile capacity (Kalluri, 2016; Sahai et al., 2020). Several markers are used to detect CAFs, such as α smooth muscle actin (αSMA), platelet-derived growth factor receptors (PDGFRα and PDGFRβ), fibroblast activation protein (FAP), vimentin, and desmin. However, none of these markers are exclusive to CAFs. CAFs can express all these markers or only some combinations (Santi et al., 2017). Thus, to identify CAFs, cell shape and the absence of markers specific to other cell types (epithelial, immune, and endothelial cells) must be combined with these markers. Such a lack of specific markers for CAFs and the plurality of markers used to detect them could be explained by the heterogeneous origins of CAFs inside the tumor microenvironment (LeBleu and Kalluri, 2018) (Figure 8).

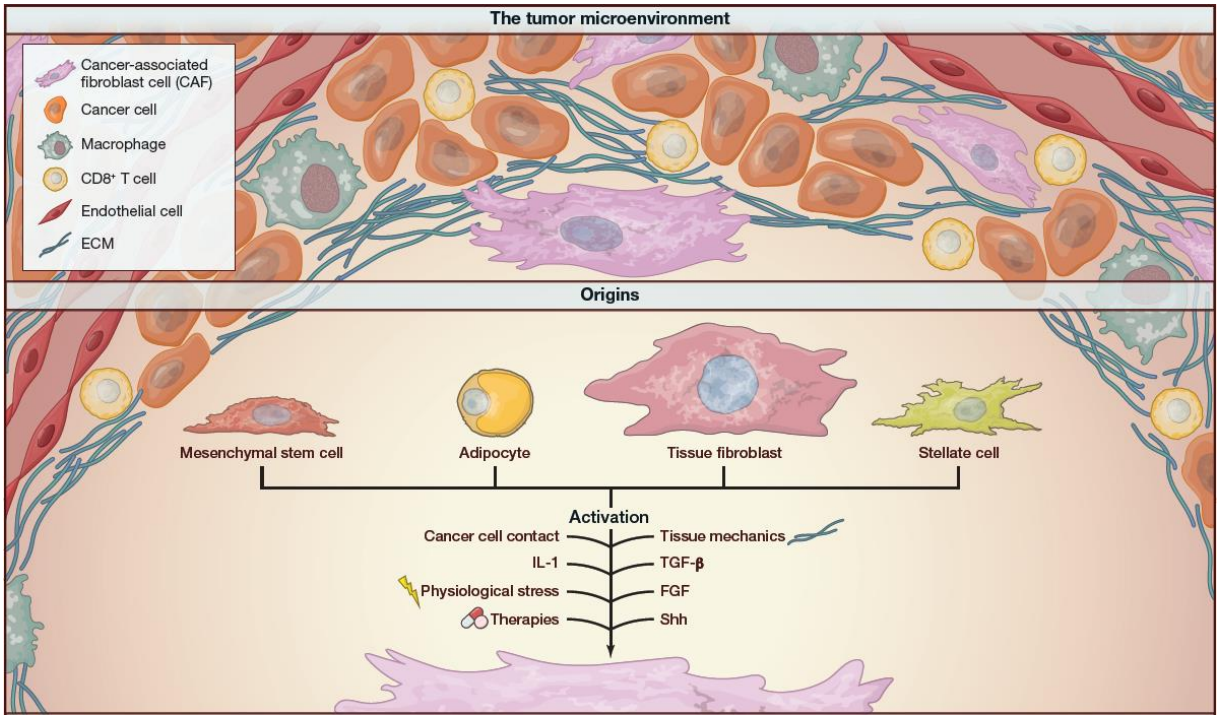

Figure 8. Cancer-associated fibroblasts (CAFs) inside the tumor microenvironment and their heterogeneous origins.
Scheme representing the different components of the tumor microenvironment (top) and different origins of CAFs with different triggers for their activation (bottom).
Taken from Park, 2020.

CAFs can arise from diverse origins (Sahai et al., 2020). The major contributors of CAFs are the resident fibroblasts already present in the healthy tissue (Arina et al., 2016). Resident fibroblasts emerge from the mesoderm during development, where they are particularly active in generating extracellular matrix for basement membranes, stroma, and other connective tissues. In adult tissues, resident fibroblasts are found inside the stroma as generally single cells in a resting and quiescent state. Upon

injury, resident fibroblasts get activated and gain contractile, proliferative, and migratory abilities to help repair the wound mainly through ECM production and remodeling as well as secretion of growth factors and cytokines (Tomasek et al., 2002). Once the wound is repaired, the resident fibroblasts either undergo apoptosis or revert to a resting and quiescent state to re-establish the homeostasis population and density. In case of tumor development, resident fibroblasts are first activated in response to the injury in the tissue caused by cancer cells before being permanently activated and transformed into CAFs (Beacham and Cukierman, 2005).

Another source of CAFs is the mesenchymal stem cells (MSCs) (Madar et al., 2013). MSCs are rare cells found inside interstitial tissue in a resting state. Resident MSCs serve as stem cells reservoir for mesenchymal cells as they can differentiate into several cell types such as adipocyte, chondrocyte, pericyte, or endothelial cells (Hematti, 2012). Upon activation by the tumor, resident MSCs can transform into CAFs. In addition to resident MSCs, MSCs can also be recruited from the bone marrow to join the tumor microenvironment as CAFs (Direkze and Alison, 2006).

Other potential sources of CAFs are different cell types present in the tissues, such as adipocytes (Bochet et al., 2013), stellate cells in the liver and pancreas, and smooth muscle cells, which, upon activation, transform into CAFs. Epithelial cells and endothelial cells can undergo epithelial to mesenchymal transition (EMT) or endothelial to mesenchymal transition to transform into CAFs (Radisky et al., 2007). Hence the plurality of origins of CAFs.

Multiple origins of CAFs are accompanied by multiple ways to activate and transform these diverse cells of origins into CAFs (Park, 2020). For example, cancer and immune cells secrete different growth factors, such as transforming growth factor β (TGF-β), platelet-derived growth factor (PDGF), fibroblast growth factor (FGF), interleukins (IL-1 and IL-6), and sonic hedgehog (Shh), that activate and permanently transform CAFs (Öhlund et al., 2014). Upon activation, CAFs also start secreting some of these growth factors, such as TGF-β, PDGF, or IL-6, to which they respond, resulting in the permanent activation feedback loop. The host tissue inflammatory reaction to the tumor also generates CAFs activation through physical stress or inflammatory secretions. CAFs could also be activated by directly contacting cancer cells using Notch signaling. In addition, hypoxia, oxidative stress, or mechanical stress can activate CAFs (Toullec et al., 2010). Further, CAFs could be activated by stiffened ECM. As a response, CAFs stiffen the ECM even more, leading to another permanent activation feedback loop (Calvo et al., 2013). Finally, the stress generated during therapy, such as radiation or chemotherapy, can also result in activation or reinforcement of activation for CAFs (De et al., 2021). Once activated, CAFs can maintain their activation state using different means described above and can be

epigenetically modified to assure their state. Thus, CAFs remain activated even when removed from the tumor microenvironment (Sahai et al., 2020).

Role of cancer-associated fibroblasts in the tumor microenvironment

Multiple origins and diversity of activation pathways of CAFs suggest a plurality of CAFs functions. However, it remains unknown if the functions of CAFs depend on their origin and/or the way they are activated. Each function either promotes or prevents tumor development. However, some functions, like ECM remodeling, can promote and prevent tumor development, depending on how they are used. Thus, CAFs are heterogeneous, and each subpopulation is defined by different origins, markers, activation pathways, and possible functions (Costa et al., 2018). Interestingly, it has been shown that CAFs' subpopulations can both stimulate and suppress tumor development and expansion following their functions. Moreover, CAFs can exhibit phenotype plasticity, allowing them to switch from one subtype to another depending on the local cues (Öhlund et al., 2017). CAFs subtypes are mainly classified between the secretory and immune modulatory subpopulations and the contractile and matrix-producing subpopulations (Figure 9).

CAFs are the major modifiers of the tumor microenvironment (Barbazán, 2019). First, they produce and deposit the ECM, particularly fibronectin and collagen I. They also remodel the ECM by different means (Attieh, 2016). For example, they can degrade the ECM by secreting matrix metalloproteinases (MMPs) using actin-rich protrusions, called invadopodia, which generate holes in the ECM, facilitating tumor growth and cancer cell invasion (Kessenbrock et al., 2010). CAFs can also create holes in the matrix using mechanical forces. Indeed, CAFs, particularly those expressing α-SMA, are highly contractile cells. By contracting and pulling on the ECM fibers, CAFs not only enlarge pre-existing gaps creating holes in the ECM but also align fibers creating highways perpendicular to the tumor boundaries that facilitate the cancer cell dissemination (Erdogan et al., 2017; Glentis, 2017). However, CAFs also aligned ECM fibers parallel to the tumor edge, in which CAFs and the ECM act as a barrier limiting cancer dissemination (Barbazan et al., 2021). This barrier also limits immune infiltration in the tumor. Finally, CAFs can also stiffen the ECM via strain stiffening due to their contractile activity and via cross-linking of the matrix by secreting amine-oxidase lysyl oxidase (LOX) (Cox et al., 2013). Matrix stiffening induces cancer cell invasion and metastasis (Mohammadi and Sahai, 2018). It activates CAFs via Yes-associated protein (YAP) translocation to the nucleus, further enhancing CAFs contractility, ECM remodeling, and stiffening, leading to a positive feedback loop (Calvo et al., 2013). In summary, force generation and ECM remodeling by CAFs contribute to the physical hallmarks of cancer described in the previous section with their pro- and anti-tumorigenic effects.

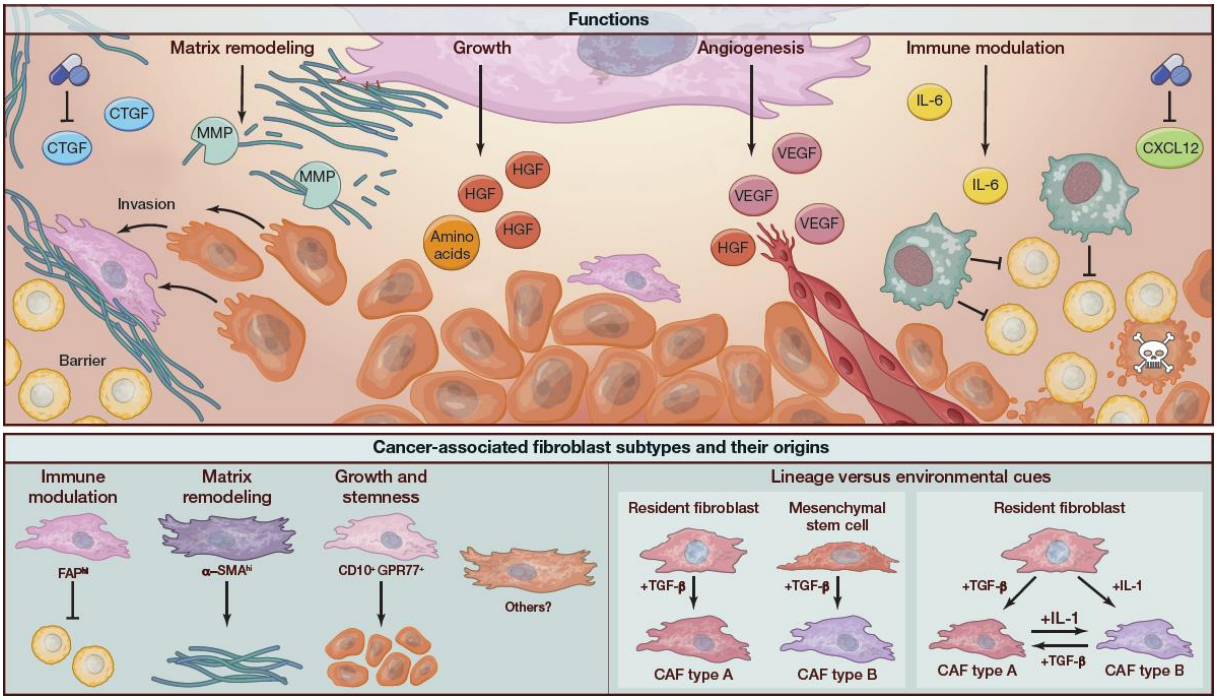

Figure 9. Functions and subtypes of cancer-associated fibroblasts (CAFs) in the tumor microenvironment.
Scheme of functions of CAFs and way of action for these functions on the tumor microenvironment (Top). Scheme of several subtypes of CAFs linked with different functions (bottom). Cells and matrix representations correspond to the same scheme in Figure 1.
Taken from Park, 2020.

CAFs also play a role in tumor development by secreting growth factors and cytokines that affect other cells in the tumor microenvironment (Gascard and Tlsty, 2016). First, CAFs enhance cancer cell survival, proliferation, resistance to therapies as well as cancer cell stemness and invasiveness through secretions of growth factors or cytokines such as TGFβ, PDGF, hepatocyte growth factor HGF, cognitive tissue growth factor CTGF, stromal cell-derived factor 1 CXCL12 and IL-6 (Calon et al., 2014; Tyan et al., 2011). CAFs also coordinate with cancer cells to reprogram their metabolisms, generating a metabolic symbiosis where each cell type benefits from metabolites produced by the other. CAFs can also pull cancer cells out of the tumor mass by establishing direct heterotypic contacts through N-Cadherin to E-Cadherin junctions (Labernadie et al., 2017). CAFs also interact with endothelial cells and pericytes to stimulate their recruitment and, thus, angiogenesis mainly through HGF, vascular endothelial growth factor (VEGF), IL-6, and CXCL12 (Fukumura et al., 1998). Finally, CAFs modulate the immune response in the tumor microenvironment. Indeed, secretions of IL-6, CXCL12, and TGFβ participate in generating an immunosuppressive environment via the recruitment of macrophages and the maturation of dendritic cells, which are pro-tumor development but can also have anti-tumor immune actions via the recruitment of natural killer cells and T lymphocytes which are anti-tumorigenic (Fearon, 2014; Flint et al., 2016).

In addition, CAFs participate in establishing the pre-metastatic niche via secretion of exosomes and can further participate in metastasis by following and protecting cancer cells along the metastasis cascade (De Wever et al., 2014; Duda et al., 2010).

Most of the CAFs functions are thought to be a reaction to the inflammatory environment in the tumor, to which CAFs respond similarly as in a never-ending wound healing process (Onfroy-Roy et al., 2021). As immune cells, CAFs' actions to support wound healing, such as secretions of angiogenesis, survival and proliferation factors, and perpendicular ECM remodeling, promote tumor development. However, CAFs' actions to destroy the injury, such as anti-tumor immune factors secretions and parallel ECM remodeling, prevent tumor development. Thus, CAFs can be both anti- or pro-tumorigenic leading to the development of therapies aiming either to inhibit their pro-tumorigenic functions, enhance their anti-tumorigenic functions or reprogram CAFs into a quiescent state.

Cancer-associated fibroblasts as a promoter of cancer invasion

CAFs promote the invasion of cancer cells by diverse mechanisms that are described below.

Before and during cancer cell invasion, CAFs can enhance cancer cells' migratory and invasiveness capacities by secreting factors. For example, the CAFs combined secretion of tenascin-C, an extracellular matrix glycoprotein, and SF/HGF (scatter factor/hepatocyte growth factor) promotes the invasiveness of colon cancer cells (De Wever et al., 2004). Indeed, CAFs' conditioned media promotes cancer cell invasion inside collagen I matrixes for several colon cancer cell lines. Tenascin-C and SF/HGF are found in CAFs' conditioned media, not cancer cells' conditioned media. Inhibition of one or the other blocks the CAFs' conditioned media-promoting effect on cancer cell invasion. Moreover, the direct addition of tenascin-C or/and SF/SHG to cancer cell invasion assays shows their combined need to promote invasion.

By secreting interleukin-11 (IL 11) CAFs also promote the invasion of colorectal cancer cells by triggering GP130/STAT3 signaling to promote their survival during the invasion (Calon et al., 2012). CAFs are the only producers of IL 11 in the tumor that activates GP130 receptors in cancer cells. GP130 depletion reduces STAT3 signaling in cancer cells and their capacity to initiate metastasis. Colorectal cancer cells engineered to express IL 11 can metastasize in mice despite CAFs' absence, while normal colorectal cancer cells can't. Thus, CAFs' IL 11 secretion promotes cancer cells' invasiveness. Moreover, in both cases, CAFs secretions are activated by TGFβ signaling in the tumor, highlighting TGFβ's major role in enhancing cancer cells' invasiveness.

In addition to secretions, CAFs can also enhance cancer cells' migratory and invasiveness capacities by modulating the tumor microenvironment and thus its signaling on cancer cells. CAFs' ECM deposition with an aligned and parallel topology in the tumor promotes mesenchymal phenotype in epithelial cancer cells and thus their dissemination (Dumont et al., 2013) (Figure 10). Human mammary cancer cells, which have an epithelial phenotype, exhibit a mesenchymal phenotype when co-cultured with CAFs (Figure 10A). This mesenchymal phenotype is assessed by a switch to mesenchymal morphology, an increase of N-cadherin and Thy-1 expression, two mesenchymal markers, and a decrease of an epithelial marker, EpCAM. The addition of collagenase, an enzyme that degrades collagen, prevents the cancer cells switch to this mesenchymal phenotype, highlighting CAFs' ECM deposition role as a trigger for the switch (Figure 10A). CAFs' ECM deposition differs from normal fibroblasts' ECM deposition: ECM fibers deposited by CAFs are aligned and linearized, while ECM deposited by normal fibroblasts are curly and meshed and random (Figure 10B, RMF146 matrix). Culturing cancer cells on ECM deposited by CAFs after CAFs removal is sufficient to induce a switch in cancer cells to the mesenchymal phenotype (Figure 10B).

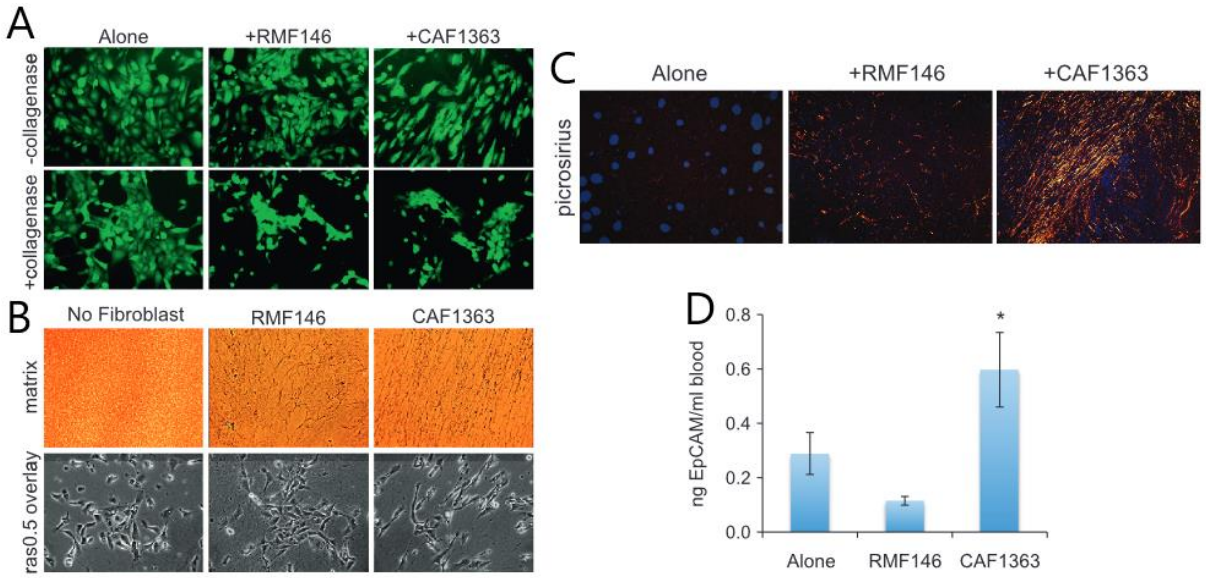

Figure 10. Cancer-associated fibroblasts (CAFs) promote cancer cells' mesenchymal phenotype and dissemination.
A) Human mammary epithelial cancer cells (green) cultured alone, with normal fibroblasts (RMF, reduction mammoplasty fibroblast), or with CAFs in the presence, or absence, of collagenase.
B) Pricrosirus staining of ECM deposition from either nothing, RMFs, or CAFs after cells' removal (top). Brightfields of cancer cells (ras0.5) on top of ECM deposition from either nothing, RMFs, or CAFs after cells' removal (bottom).
C) Pricrosirus staining of ECM deposition from in vivo tumor cancer cells injected with either nothing, RMFs, or CAFs.
D) Quantification of circulating tumor cells in mice blood, via qPCR analysis of EpCAM level, 8 weeks after injection of cancer cells with either nothing, RMFs, or CAFs.
Taken from Dumont, 2013.

Thus, the ECM deposited by CAFs promotes mesenchymal phenotype in epithelial cancer cells. This particular CAFs' ECM deposition is also present in vivo (Figure 10C). It is correlated with an increase in

the number of circulating tumor cells in the blood (Figure 10D), showing that CAFs' deposited ECM enhances the dissemination of cancer cells.

While aligning the ECM, CAFs stiffen the tumor microenvironment. This matrix stiffening also promotes cancer cells' invasiveness. For example, matrix stiffening promotes EMT and so metastasis in breast cancer cells via the TWIST1/G3BP2 mechanotransduction pathway (Figure 11) (Wei et al., 2015). On soft matrix, G3BP2 bonds TWIST1 in the cytoplasm. Upon matrix stiffening, G3BP2 releases TWIST1, which translocates to the nucleus, triggering EMT in cancer cells and invasion.

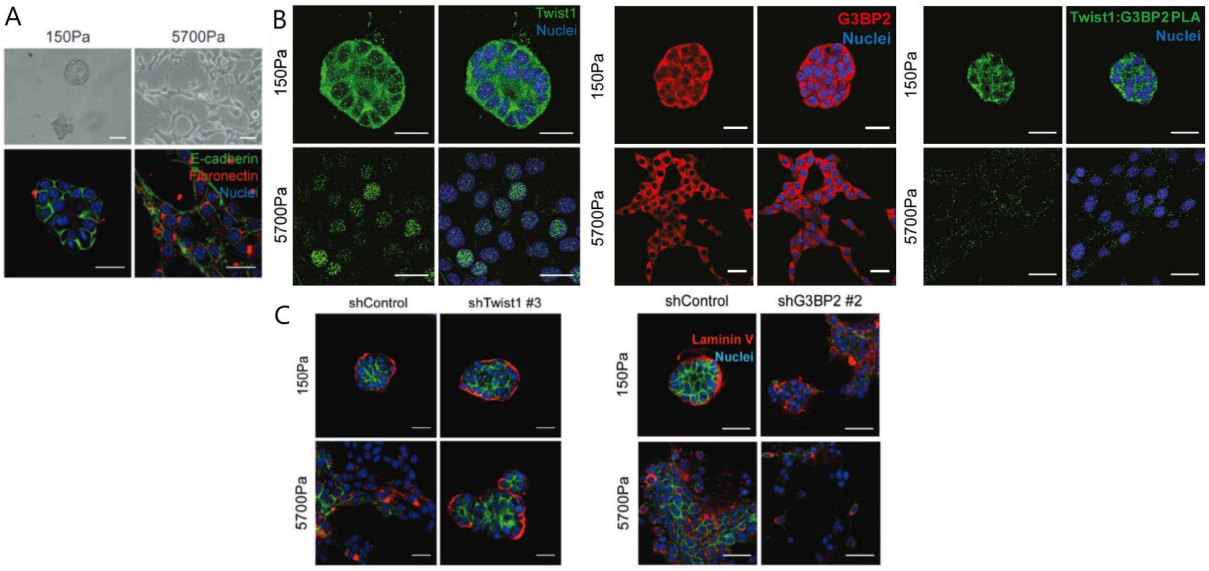

Figure 11. Matrix stiffening induces EMT in breast cancer cells leading to invasion via G3BP2/TWIST1 pathway.
A) Brightfield and staining of Eph4Ras, breast cancer cells, for E-cadherin (green), fibronectin (red), and DNA (blue) in soft (150 Pa) or stiff (5700 Pa) 3D polyacrylamide hydrogel. Scale bar: 25 µm.
B) Staining of Eph4Ras for DNA (blue) and either TWIST1 (green, left), G3BP2 (red, middle), or TWIST1/G3BP2 interaction (green, right) in soft (150 Pa) or stiff (5700 Pa) 3D polyacrylamide hydrogel. Scale bars: TWIST1 and TWIST1/G3BP2 interaction: 25 µm, G3BP2: 50 µm.
C) Staining of Eph4Ras for E-cadherin (green), laminin V (red), and DNA (blue) in soft (150 Pa) or stiff (5700 Pa) 3D polyacrylamide hydrogel upon depletion of either TWIST1 (shTwhist1, left) or G3BP2 (shG3BP2, right). Scale bar: TWIST1 depletion: 25 µm, G3BP2 depletion: 50µm.
Taken from Wei, 2015.

Indeed, breast cancer cells cultured in stiff matrixes exhibit a mesenchymal and invasive phenotype, whereas they exhibit an epithelial and non-invasive phenotype in soft matrixes (Figure 11A). The staining of TWIST1 and G3BP2 reveals the TWIST1 translocation to the nucleus in stiff matrixes while G3BP2 remains in the cytoplasm (Figure 11B). Moreover, TWIST1 and G43BP2 interact in soft matrixes while this interaction is lost in stiff matrixes due to TWIST1 translocation. Finally, TWIST1 depletion reverts cancer cells to the epithelial and non-invasive phenotype in stiff matrixes, while G3BP2 depletion switches cancer cells to the mesenchymal and invasive phenotype in soft matrixes (Figure 11C). This shows that the TWIST1 translocation is required to trigger EMT in stiff matrixes, and this translocation relies on the G3BP2 release of TWIST1 upon matrix stiffening.

Thus, CAFs can promote cancer cell invasion by enhancing their invasive and migratory capabilities via factors secretion or modification of the tumor microenvironment. However, CAFs can also promote cancer cell invasion by actively participating in helping cancer cells escape at each step of the cancer invasion process.

The first step of cancer invasion is breaching the basement membrane that allows cancer cells to access the surrounding stroma. Cancer cells and CAFs are present on the opposite sides of the basement membrane in carcinoma in situ. CAFs can help cancer cells to breach the basement membrane by secreting matrix metalloproteinases (MMPs) (Hotary et al., 2002) or by using mechanical forces to generate holes in the basement membrane that cancer cells use to go through (Glentis, 2017). The CAFs' mechanical generation of holes in the basement membrane doesn't rely on MMPs but CAFs' contractile ability (Figure 12). First, cancer cells contact CAFs on the other side of the basement membrane using protrusions. Later, CAFs pull on the basement membrane, expanding likely already existing holes in it. Finally, cancer cells squeeze through these holes and migrate to the other side of the basement membrane. Indeed, human colorectal cancer cells, HCT116, cultured on one side of de-cellularized mouse mesenteries, made of two superimposed basement membranes, breach and invade the basement membranes in the presence of human colorectal CAFs on the other side, but not in their absence (Figure 12A). CAFs' promotion of cancer cells' breaching doesn't rely on a cross-talk between CAF and cancer cells, as CAF's distant presence is not sufficient to induce breaching. Thus, CAFs' physical presence at the basement membrane is required to promote cancer cell invasion. Moreover, the holes in basement membranes are present only if cancer cells are cultured with CAFs (Figure 12B). MMPs inhibition doesn't affect CAFs' promotion of cancer cells' breaching, while the inhibition of CAFs' contractility does. Similarly, holes in the basement membrane are still present even after MMPs inhibition but they cannot be generated if contractility is inhibited, showing that CAFs generate holes by using mechanical properties. Live imaging further reveals that CAFs pull on the basement membrane to open holes that allow cancer cells to migrate on the opposite side (Figure 10C).

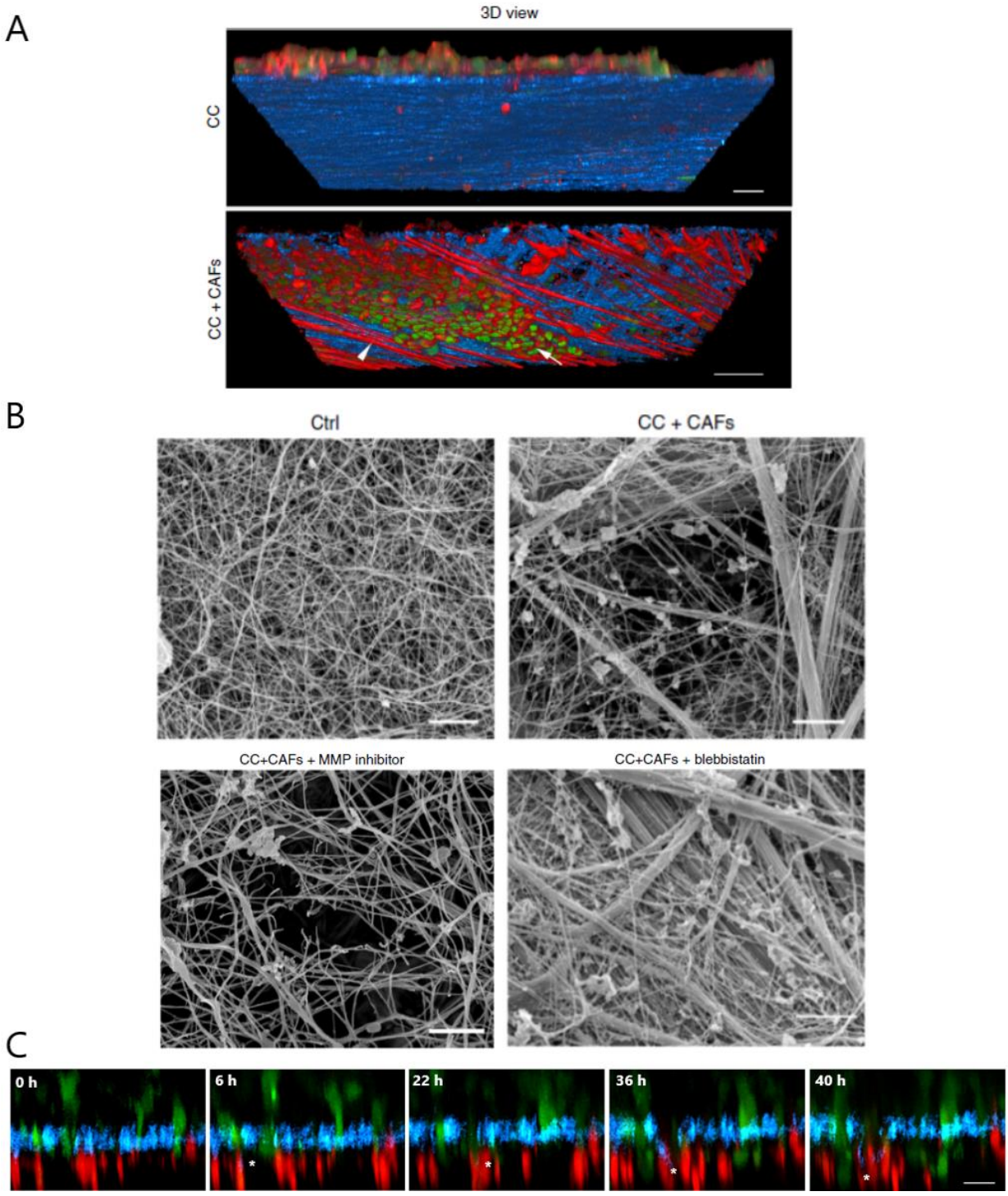

Figure 12. Cancer-associated fibroblasts (CAFs) generate holes in the basement membrane using contractile forces.
A) Invasion assay of colorectal cancer cells HCT116 through de-cellularized mouse mesentery in the presence or absence of CAFs. Actin (red), DNA (green), and the basement membrane (blue) are visualized. The arrow shows cancer cells, and the arrowhead shows CAFs. Scale bar: 20 µm.
B) Scanning electron micrographs of mesenteries after invasion assay in the presence or absence of CAFs, whether under treatment or not, with GM6001, MMP inhibitor, or blebbistatin, contractility inhibitor. Scale bar: 2 µm
C) Time-lapse imaging of an invasion assay. Cancer cells are green, CAFs are red, and mesentery is blue. White stars show CAFs pulling the basement membrane, followed by cancer cell migration. Scale bar: 20 µm.
Taken from Glentis, 2017.

After breaching the basement membrane, cancer cells migrate through the stroma mainly composed of collagen I matrix. CAFs facilitate cancer cells' migration in the stroma by aligning collagen I fibers perpendicular to the tumor and decorating them with similarly aligned fibronectin fibers (Attieh et al., 2017; Erdogan et al., 2017) (Figure 13). This anisotropic modification of the stroma promotes directional cancer cells' migration out of the tumor. CAFs perform such stroma remodeling and aligned fibronectin deposition using mechanical forces coupled with integrin-β3 and integrin-α5. Indeed, cancer cells embedded in a collagen I matrix poorly invade it. The addition of CAFs enhances cancer cell invasion and is correlated with a topological change of collagen I fibers toward a perpendicular orientation to the tumor (Figure 13A). However, the fibronectin depletion in CAFs prevents cancer cells' invasion, even though the perpendicular collagen I orientation remains. Thus, remodeling the stroma is not enough, and fibronectin deposition is needed to promote the invasion of cancer cells. The fibronectin deposition's orientation impacts cancer cells' migration: meshed fibers lead to random walk, whereas aligned fibers lead to directional migration with cancer cells following the fibers (Figure 13B).

Embedded in a collagen I matrix, CAFs' fibronectin deposition is on top of re-oriented collagen I fibers. Such fibronectin deposition relies on CAFs' contractility because if inhibited using blebbistatin, fibronectin is either not deposited or organized as meshed fibers (Figure 13C). Collagen I fiber re-orientation is also lost upon contractility inhibition. In addition to contractility, fibronectin deposition and assembly also rely on integrin-β3 and integrin-α5, since inhibiting each, using siRNA for β3 (Figure 13D) and P1D6 for α5 (Figure 13E), also leads to either no fibronectin deposition or meshed organization. Thus, in the stroma, CAFs can re-organize collagen I fibers perpendicular to the tumor using mechanical forces while deposing fibronectin on them using integrins β3 and α5. This CAFs' specific remodeling of the stroma promotes directional cancer cells' migration out of the tumor.

CAFs' fibronectin deposition to promote cancer cell invasion also relies on other CAFs' proteins such as Fibroblasts Activation Protein (FAP)(Lee et al., 2011) and Hic-5 (Goreczny et al., 2018, 2017). Indeed, in both cases, CAFs' depletion of either FAP or HIC-5 leads to lower and disorganized fibronectin deposition. Upon such altered fibronectin deposition and organization, cancer cells' migration is impaired, leading to a less invasive capacity of cancer cells. In these studies, cancer cells are let to migrate as single cells inside the fibronectin matrixes. However, CAFs' aligned fibronectin also guides cancer cells' collective invasion (Gopal et al., 2017).

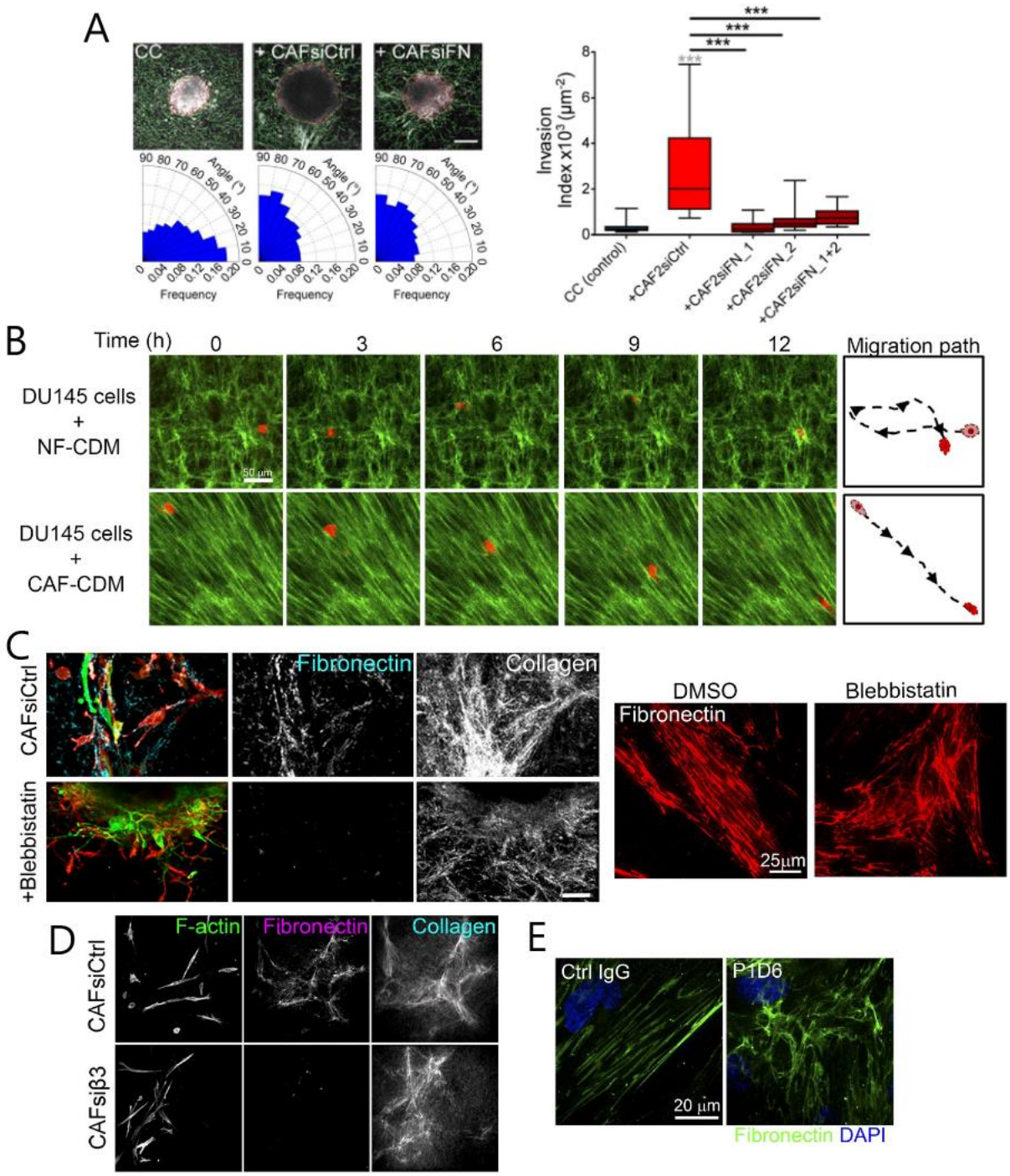

Figure 13. Cancer-associated fibroblasts (CAFs) stroma remodeling and aligned fibronectin promote cancer cells' directional migration and invasion.

A) Images of cancer cells CT29 spheroids embedded in collagen I matrixes by themselves, with CAFs, or fibronectin-depleted CAFs, and quantification of collagen fibers orientation towards the spheroid border (left). Associated quantification of cancer cells' invasion in the matrix (right). Scale bar: 100 µm.

B) Time-lapses of cancer cells DU145 (red) migration inside fibronectin matrixes (green) generated by normal fibroblasts (NF-CDM) or CAFs (CAF-CDM).

C) Staining of cancer cells CT29 and CAFs' spheroids embedded in collagen I matrixes treated or not with blebbistatin for cancer cells (green), F-actin (red), fibronectin (cyan), and collagen I (left). Staining of fibronectin (red) matrix generated by CAFs treated or not with blebbistatin.

D) Staining of cancer cells CT29 spheroids embedded in collagen I matrixes with CAFs, or integrin-β3 depleted CAFs for cancer cells (green), fibronectin (magenta), and collagen I (cyan).

E) Staining of matrixes generated by CAFs treated with IgG (control) or P1D6 for fibronectin (green) and DNA (DAPI, blue). Taken from Attieh, 2017 (A, C left, D) and Erdogan, 2017 (B, C right, E).

In addition to remodeling the stroma to promote directional cancer cells' migration, CAFs can directly lead the cancer cells' migration by pulling them out of the tumor via heterotypic E-cadherin/N-cadherin adhesions (Gaggioli et al., 2007; Labernadie et al., 2017) (Figure 14).

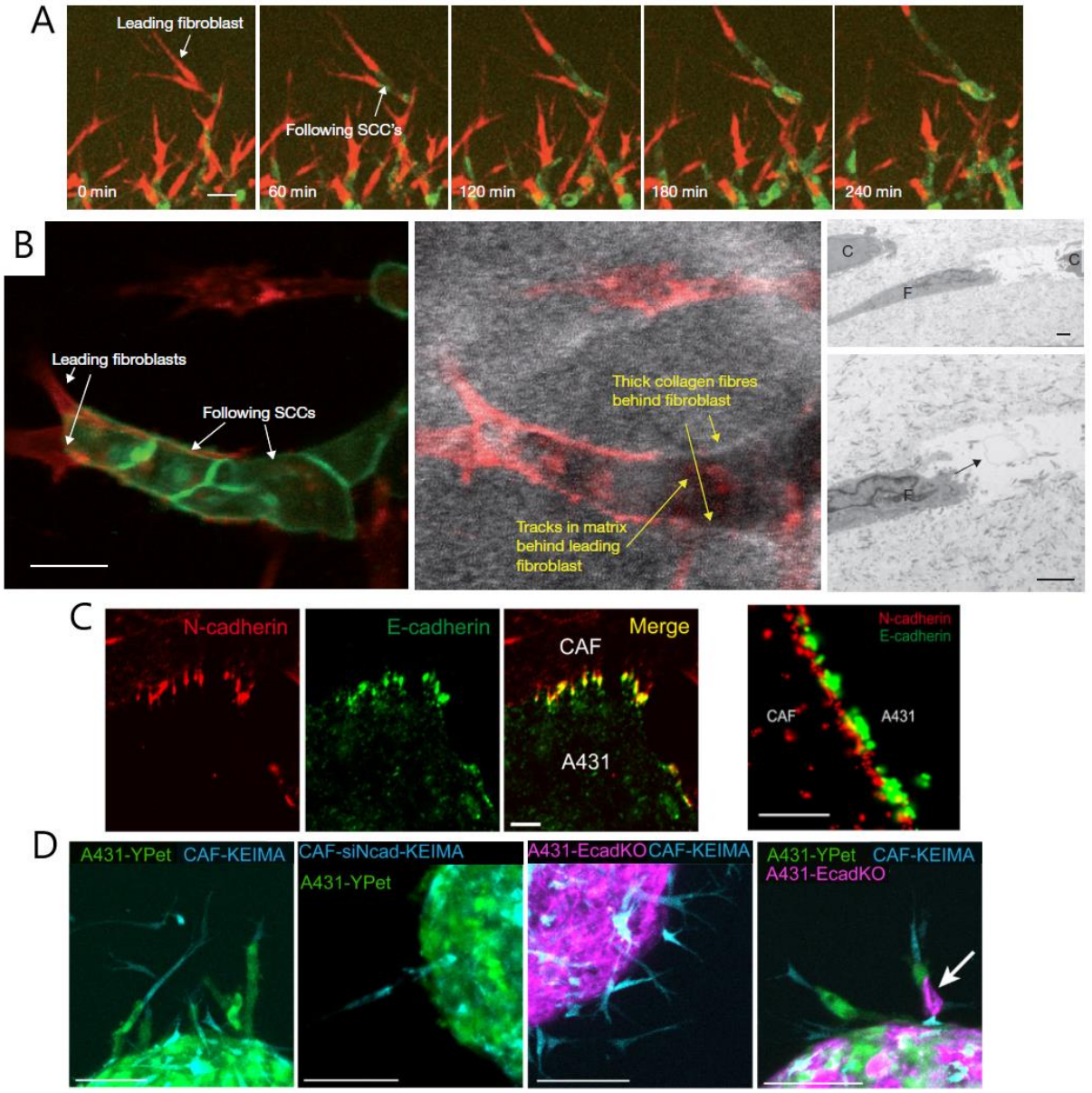

Figure 14. Cancer-associated fibroblasts (CAFs) pull cancer cells out of the tumor and lead their migration into the stroma via E-cadherin/N-cadherin adhesions.
A) Time-lapse imaging of cancer cells SCC12 (green) and CAFs (red) embedded in a collagen I matrix. Scale bar: 40 µm.
B) Invasion assays of cancer cells SCC12 (green) inside collagen I matrix (white) with CAFs (red) showing the tracks inside the matrix. Scale bar: 20 µm (left). Transmission electron microscopy of such invasion assay with CAFs (F), cancer cells SCC12 (C), and the tracks in the matrix (black arrow). Scale bar: 2 µm (right).
C) Confocal imaging (left) and STORM imaging (right) of cancer cells A431 and CAFs for N-cadherin (red) and E-cadherin (green). Scale bars: left, 5 µm; right, 500 nm.
D) Invasion of cancer cells A431 and CAF-KEIMAs' spheroids embedded in collagen I matrixes upon N-cadherin depletion in CAF (siNcad), total or partial E-cadherin depletion in cancer cells (EcadKO).
Taken from Gaggioli, 2007 (A, B) and Labernadie, 2017 (C, D).

Indeed, as seen above, spheroids of cancer cells and CAFs embedded in collagen I matrixes invade the surrounding matrix. The focus on their invasive portion reveals that CAFs adhere to cancer cells and lead them out of the tumor (Figure 14A). More precisely, collective groups of cancer cells are attached to leader fibroblasts while migrating. Such migration leaves tracks in the collagen I matrix that can be used by non-attached cancer cells to follow the invasion (Figure 14B). At the junctions between CAFs and cancer cells, CAFs display N-cadherin, whereas cancer cells display E-cadherin (Figure 14C). These heterotypic E-cadherin/N-cadherin adhesions are mechanosensitive and as strong as homotypic junctions. CAFs use these adhesions to transmit forces to cancer cells, thus pulling them out of the spheroids. Moreover, both E-cadherin depletion from cancer cells or N-cadherin depletion from CAFs prevents cancer cell invasion in the surrounding matrix (Figure 14D). However, the mix of normal cancer cells and E-cadherin-depleted cancer cells restores cancer cell invasion. Normal cancer cells adhere to fibroblasts while E-cadherin-depleted cancer cells are part of the following cancer cells. Thus, the heterotypic E-cadherin/N-cadherin junctions are required for cancer cell invasion led by CAFs.

Cancer-associated fibroblasts as inhibitors of cancer invasion

CAFs studies mainly focus on deciphering the mechanisms by which CAFs promote tumor development and invasiveness. However, there are reports that point toward CAFs' anti-tumorigenic functions, especially their capacity to promote the anti-tumor immune response (Harper and Sainson, 2014). Fewer studies also reveal that CAFs can inhibit cancer invasion (LeBleu and Kalluri, 2018). The mechanisms by which CAFs inhibit cancer invasion are described below.

One of CAFs' major roles is their capacity to remodel and deposit ECM. As seen above, this role mainly promotes tumor invasiveness. However, it has been suggested that CAFs' ECM alignment parallel to the tumor could act as a physical barrier preventing cancer invasion (Park, 2020). The CAFs' collagen I production can generate physical restrictions in the tumor, preventing cancer cells' invasion (Bhattacharjee et al., 2021) (Figure 15). Indeed, upon depletion of collagen I in CAFs in mice, metastasis size increases for both pancreatic ductal adenocarcinoma (PDAC) and colorectal cancers (CRC) (Figure 15A). Moreover, cancer cells' spheroids embedded in matrigel can invade their surrounding matrix, whereas such invasion is blocked upon the addition of collagen I in the matrigel (Figure 15B). Thus, ECM deposition and remodeling by CAFs can generate physical barriers constraining tumor invasion.

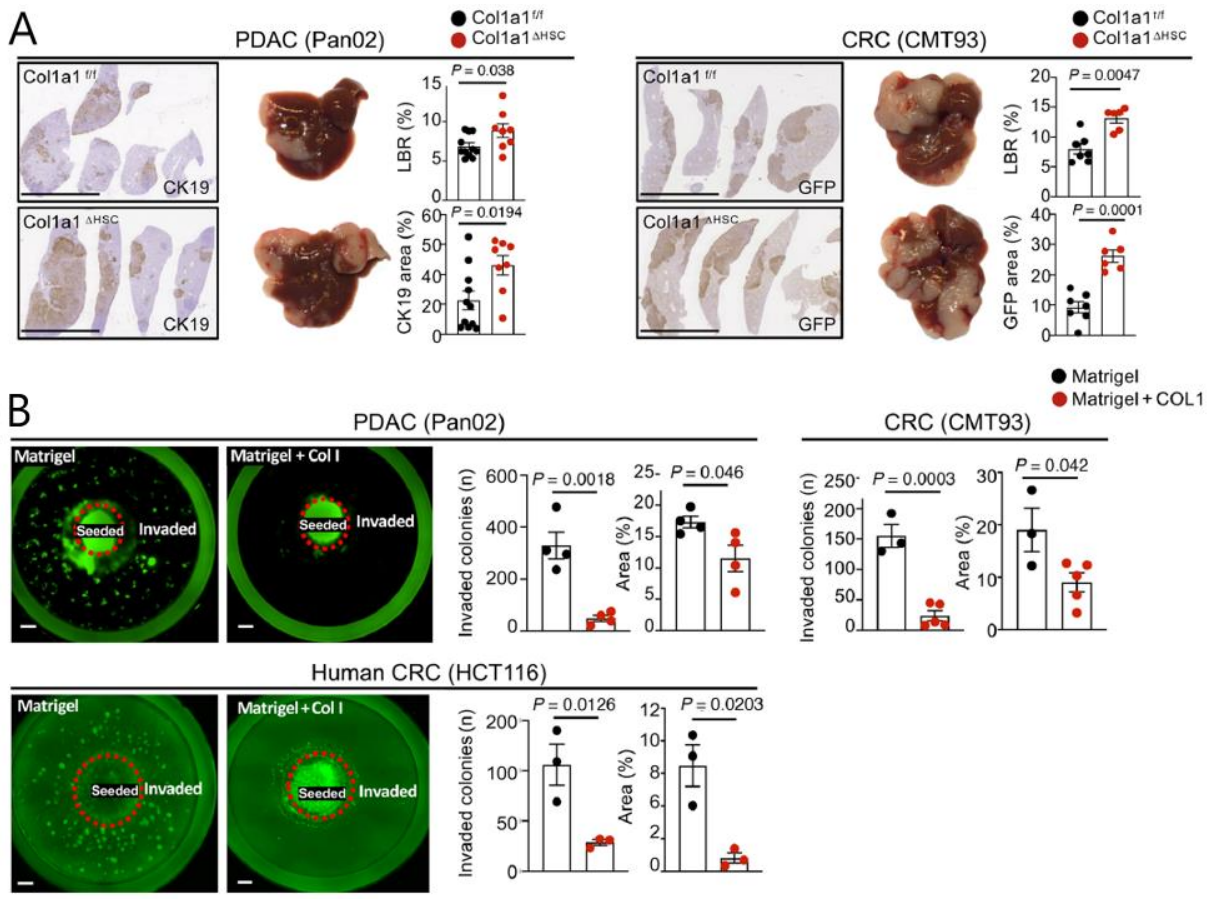

Figure 15. CAFs' collagen I production generates physical restrictions preventing cancer invasion.
A) Macroscopic images and IHC images of PDAC Pan02 and CRC CMT93 cancer cells metastasis in the liver for CAFs' collagen I depleted mice ($Col1a1^{\Delta HSC}$) and their control ($Col1a1^{f/f}$). Associated quantifications of the liver-to-body ratio (LBR) and the ratio of cancer cells' areas using CK19 and GFP as reporters for Pan02 and CMT93 cancer cells, respectively. Scale bar: 1cm. B) Invasion assays of cancer cells spheroids (green) from PDAC Pan02, CRC CMT93, and human CRC HCT116 in matrigel with or without the addition of collagen I and their associated quantifications of invaded colonies and area of invasion. Taken from Bhattacharjee, 2021.

Intriguingly and opposed to what has been seen before, CAFs can also prevent cancer invasion by limiting cancer cells' epithelial to mesenchymal transition (EMT) (Özdemir et al., 2014; Rhim, 2014). Indeed, in both studies, CAFs' depletion in PDAC leads to a decrease in mice survival. CAFs-depleted tumors present more undifferentiated and aggressive phenotypes than tumors with CAFs. In one case, (Özdemir et al., 2014), CAFs' depletion is correlated with reduced but more reorganized collagen I content in the tumor, promoting cancer invasion. Moreover, in both reports, cancer cells' invasiveness increases upon CAFs' depletion as more macrometastasis appears. In particular, CAFs' depletion enhances cancer cells' EMT. In addition, EMT transcription factors, such as TWIST, Slug, Snail, and Zeb1, increase by several folds. Thus, CAFs can inhibit cancer cell invasion by limiting their aggressiveness and cancer cells' EMT.

In some breast tumors, such CAFs' limitation of cancer cells' EMT and invasiveness is due to their secretion of Asporin, an ECM protein, upon TGFβ triggering (Maris et al., 2015). Indeed, cancer cells' conditioned media containing TGFβ, or the direct TGFβ addition, in CAFs culture triggers asporin secretion. However, such secretion is inhibited if cancer cells also express IL-1β. Asporin treatment of cancer cells inhibits TGFβ interactions with them, leading to a decrease in cancer cells' EMT and migratory capacity. Moreover, in vivo injections of highly metastatic cancer cells with CAFs forced to express asporin drastically reduce cancer cells' growth and metastatic ability. Thus, CAFs' asporin secretion can inhibit cancer cells' EMT and invasiveness.

In this last study, cancer cells' TGFβ secretion triggers CAFs to restrain cancer cells' invasiveness. This opposes the studies seen above in which cancer cells' TGFβ secretion triggers CAFs to promote invasion of cancer cells. Similarly, depletion of TGFβ type II receptor in CAFs' inhibits their responsiveness to TGFβ signaling (Cheng et al., 2005) enhancing cancer cells' growth, motility, and invasion in vivo and in vitro upon treatment with depleted-CAFs condition medium. Interestingly, secretion of HGF in CAFs increases upon depletion of TGFβ type II receptor, inhibiting this HGF secretion decreases cancer cells' invasiveness. Thus, CAFs' HGF secretion remains a promoter of cancer cells' invasiveness, and cancer cells' TGFβ secretion can limit its secretion and therefore restrain cancer cells' invasiveness. This highlights CAFs' capacity to modulate their secretion to restrain or promote cancer cells' invasiveness and the TGFβ signaling opposite action in both situations.

Finally, CAFs can also inhibit cancer cells' invasiveness by other factors' secretion. For example, CAFs' secretion of Slit2 activates Robbo1 receptors in cancer cells and restrains their invasive capacity (Chang et al., 2012). Indeed, breast cancer cell lines expressing Robbo1 fail to form colonies when cultured with CAFs, whereas breast cancer cell lines not expressing it form colonies when cultured with CAFs. Moreover, Robbo1 depletion in cancer cells restores their capacity to form colonies, whereas Robbo 1 forced expression in cancer cells blocks their ability to form colonies. The ligand associated with Robbo1, Slit2, is mainly expressed by CAFs. The addition of Slit2, instead of CAFs in cancer cells' culture, reproduces the above results. Similarly, Slit2 depletion in CAFs also enhances colonies' formation in cancer cells expressing Robbo1. Thus, CAFs' Slit2 secretion can target Robbo1-expressing cancer cells and restrain their invasiveness.

Extracellular matrix and cancer-associated fibroblasts' organization around the tumor

The ECM organization around the tumor can either promote or prevent cancer invasion (Conklin et al., 2011). During the tumor growth and stroma invasion, the ECM endorses massive transformations leading to drastic changes between its cancerous and normal topology (Provenzano et al., 2006). The classification of these different topologies leads to three categories of tumor-associated collagen signatures (TACS) associated with different patient prognoses (Figure 16) (Conklin et al., 2011; Provenzano et al., 2006).

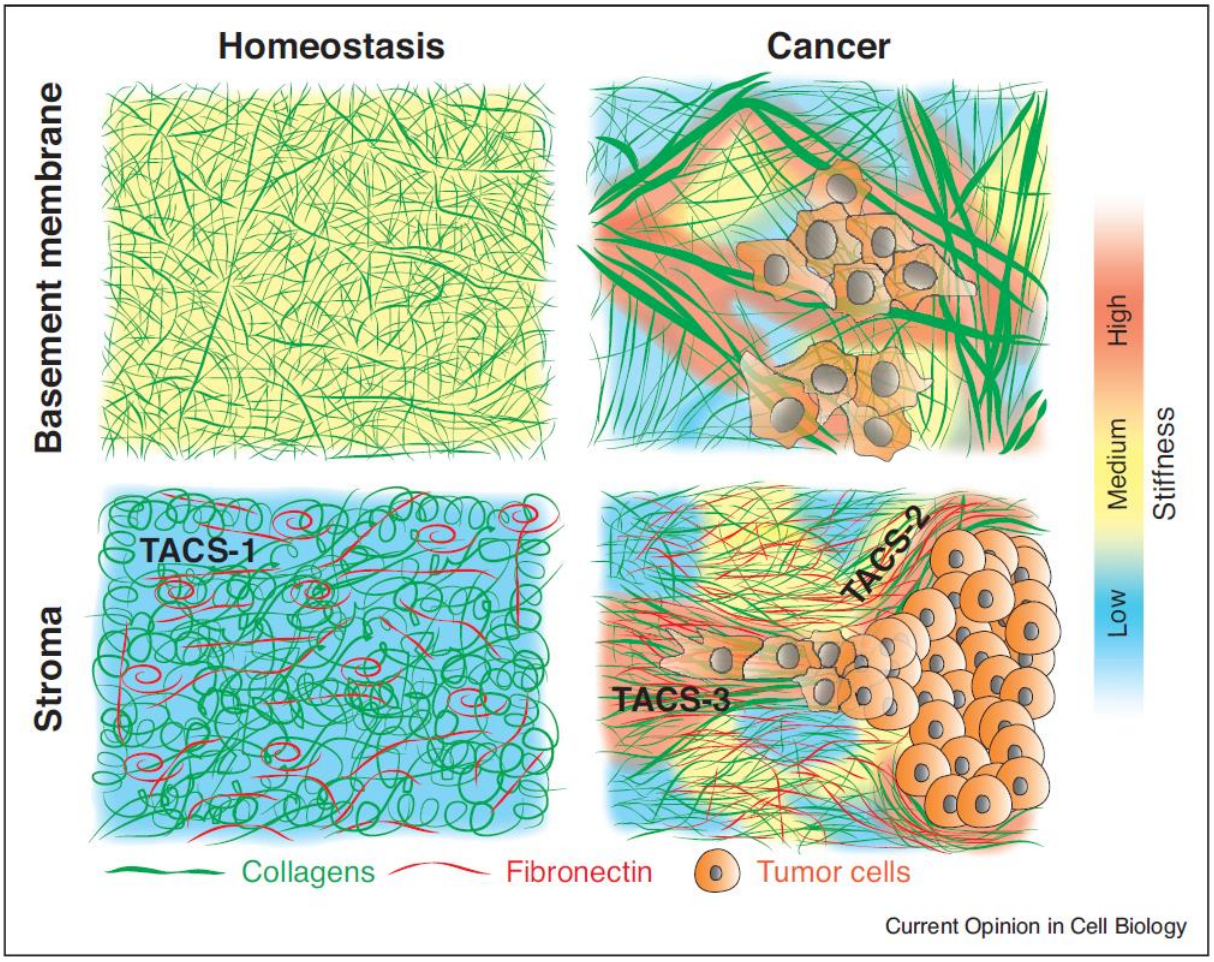

Figure 16. The different tumor-associated collagen signatures (TACS).
Scheme representing the different tumor-associated collagen signatures (TACS) in the basement membrane and the stroma. Taken from Barbazan, 2019.

TACS-1 is observed in normal tissue homeostasis. In this topology, ECM fibers are curly and randomly oriented, and ECM stiffness is homogeneous. TACS-2 and TACS-3 are observed in cancer topology. As cancer develops, ECM fibers get strengthened, aligned together, and locally stiffened. The ECM fibers' orientation toward the tumor edge differs between TACS-2 and TACS-3. TACS-2 has ECM fibers aligned parallel to the tumor edge and is associated with non-invasive tumors and a good prognosis. TACS-3

has ECM fibers aligned perpendicular to the tumor edge and is associated with invasive tumors and a bad prognosis. Both TACS-2 and TACS-3 can be found in the same tumor, the TACS-3 regions corresponding to the invasive region of the tumor. The proportion of TACS-3 topology in the tumor determines the patient's prognosis; the more TACS-3 regions, the worst the prognosis.

As seen above, CAFs are the main ECM remodelers and producers. Moreover, at the tumor's edge, CAFs form a layer around the tumor. Interestingly, CAFs are aligned with the ECM fibers for both TACS-2 and TACS-3, suggesting their role in the topologies switches between each TACS. In addition, the organization of the CAFs layer around the tumor could determine where TACS-3 regions appear. In particular, CAFs are known to align together into nematic ordering, generating heterogeneous orientations inside the layer (Saw et al., 2018).

Summary

Cancer-associated fibroblasts have multiple origins, primarily the resident quiescent fibroblasts. However, mesenchymal stem cells, adipocytes, stellate cells, and epithelial and endothelial cells can also contribute to CAFs. Several triggers, such as secreted factors from cancer cells or the microenvironment's physical properties, lead to the activation of fibroblasts and thus the generation of CAFs.

CAFs have multiple functions inside the tumor microenvironment. They produce and remodel the ECM that either enhances or prevents cancer invasion. CAFs can also help tumor growth by enhancing proliferation, stemness, and therapy resistance in cancer cells. In addition, CAFs interact with the other cells in the tumor microenvironment by enhancing angiogenesis and modulating immune responses that can be either pro- or anti-tumorigenic. Finally, CAFs stimulate metastasis by preparing pre-metastatic niches.

There is considerable evidence that CAFs stimulate cancer invasion. CAFs' ways to promote cancer invasion are diverse. First, they can enhance cancer cells' invasiveness and migratory abilities via several secreted factors, ECM remodeling, and stiffening. Then, they can use mechanical forces to generate holes in the basement membrane helping cancer cells to squeeze through. They can also promote cancer cell invasion through the stroma by remodeling collagen I fibers and generating tracks decorated with aligned fibronectin that cancer cells use to migrate. Finally, they can directly stimulate cancer cell migration by establishing heterotypic adhesions and pulling them.

However, evidence shows that CAFs can also prevent cancer invasion and metastasis, even though this role has been less studied. CAFs' collagen I production can form physical barriers constraining invasion. They can also limit cancer cells' EMT and invasiveness via several secreted factors.

Finally, ECM and CAFs organization around the tumor can be classified in different TACS depending on the orientation to the tumor edge. Perpendicular orientation correlates with invasive regions, whereas parallel orientation correlates with non-invasion areas. CAFs align with each other into nematic ordering and form a layer around the tumor. This particular organization could impact cancer invasion.

Chapter III: Nematic ordering

Definition

Ordering is defined by how a group of objects assembles to form a 2D or 3D structure. Different types of ordering are described by the rules that the objects follow and the assembly they include. One kind of ordering, the nematic ordering, is present in many different phenomena (Doostmohammadi et al., 2018). Nematic ordering can be found in passive materials, such as liquid crystals, or active materials, such as cells (Gennes and Prost, 1993). To be considered a nematic object, objects need to have an elongated shape with symmetry between both sides. When they are put together, nematic objects align along their long axis without any rule for their position towards each other. This means that the long axes of the objects are all in the same direction. However, objects can be placed anywhere along this main direction. This capacity to align in such a way is due to their elongated shape. The main direction of object ordering is usually termed the director ***n***. Since objects are not polarized, this director is not a vector, just a direction.

The alignment is, however, not perfect; different aligned areas often appear in the same system resulting in neighboring aligned areas of different directors. At the intersections of neighbor-aligned areas appear topological defects. Topological defects are points in the system that allow the transition between neighbor-aligned areas. Indeed, objects smoothly rotate from one to the other neighboring aligned area. The center of this symmetry rotation is the topological defect. Topological defects are characterized by the two parameters of the rotation needed to go from one aligned area to the neighbor one: the rotational direction and the fraction of a 360°C rotation done. Topological defects are named based on these characteristics. In two-dimensional nematic ordering, two types of topological defects are predominant (Figure 17): the +1/2 defect, corresponding to a +180°C rotation, and the -1/2 defect, corresponding to a -180°C rotation. Due to their resemblance to comets, +1/2 defects are also called comet defects, with the head of the comet at the core of the defect and the tail on one side. Due to their resemblance to triangles, -1/2 defects are named triangles, with the three vertexes around the core of the defect.

Topological defects can also be considered as topological charges of the system. The topological charge attributed to each defect corresponds to their definition: +1/2 for comet and -1/2 for triangle defect. The global topological charge of the system's nematic order is the sum of the charge of each defect. At the equilibrium, the system tries to neutralize as much as possible the global topological charge by having the fewest defects possible. Appearance and disappearance of defects in the system need to respect the rule of topological neutrality, meaning that the charges' sum of the defects involved must be zero: +1/2 and -1/2 defects appear in pairs before moving from each other and disappear in pairs by colliding. This helps to understand how a system with nematic order and its defects evolve.

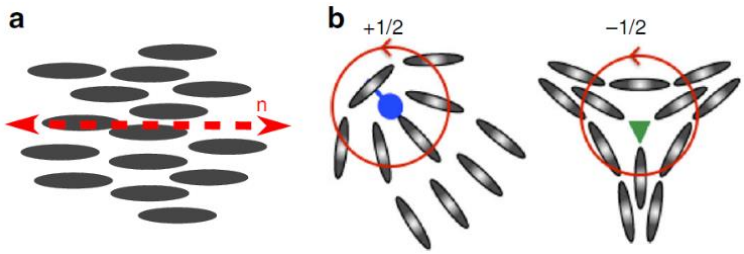

Figure 17. Schematic of nematic alignment.
a) aligned area for nematic objects with the director n.
b) comet-like or +1/2 defect (left) and triangle-like or -1/2 defect (right).
Taken from Doostmohammadi, 2018.

The nematic order parameter *Q* and the correlation length *ξ*

Describing the nematic ordering and creating tools helpful to compare different types of nematic ordering has been the main motivation for developing the theoretical aspect of nematic ordering. All these tools aim at quantifying the different aspects of nematic ordering. The first quantification of the nematic ordering can be done using the nematic order parameter ***Q*** (Mottram and Newton, 2014). The nematic order parameter ***Q*** compares the angle between a given direction and the mean of objects' long axis direction in a given area. As ***Q*** is calculated on a given site, it is space-dependent and can be used as a local or global parameter depending on the areas of calculation chosen. ***Q*** can be represented as a tensor or the scalar associated with it. The Q calculation also depends on the dimension in which the nematic ordering takes place. In two dimensions, with the use of Landau – de Gennes's theory of liquid crystal, the nematic order parameter ***Q*** is calculated as a scalar version by:

$$\boldsymbol{Q} = \sqrt{\langle \cos 2\theta \rangle^2 + \langle \sin 2\theta \rangle^2}$$

In this equation, θ represents the angle between each object's long axis and a chosen direction. θ can be calculated for each position in the system giving rise to an orientation map θ. For simplicity, the direction chosen to calculate θ generally corresponds to the system's x or y-axis. With this equation, ***Q*** varies between 1 and 0. ***Q*** = 1 corresponds to a perfect nematic ordering where long axes of all objects are in the same direction, while ***Q*** = 0 corresponds to a completely disordered state. Applied locally, this parameter helps find the defects in the system as near 0 values represent the place of a defect, and near 1 values represent ordered areas. Used globally, this parameter helps describe how much nematically ordered a system is and, that way, compares the nematic ordering of different systems.

Another parameter used to quantify the nematic order is the correlation length, ***ξ*** (Duclos et al., 2014). The correlation length ***ξ*** measures the mean size of aligned areas in the nematic ordering. ***ξ*** is calculated from the orientation map θ used to obtain ***Q***. Spatial autocorrelation of this orientation map θ is

realized, and the result is then fitted with a decreasing exponential fit from which the correlation length $\boldsymbol{\xi}$ is extracted (Figure 18). The correlation length $\boldsymbol{\xi}$ can also be used to compare the nematic ordering of different systems as it indicates how spread one orientation in the system is. However, this parameter is dependent on the objects' size. It is thus necessary to normalize $\boldsymbol{\xi}$ by the objects' size before comparing systems composed of objects of different sizes. The normalized $\boldsymbol{\xi}$ corresponds to how many objects one orientation can spread inside the system and compare the nematic capacity of a different system.

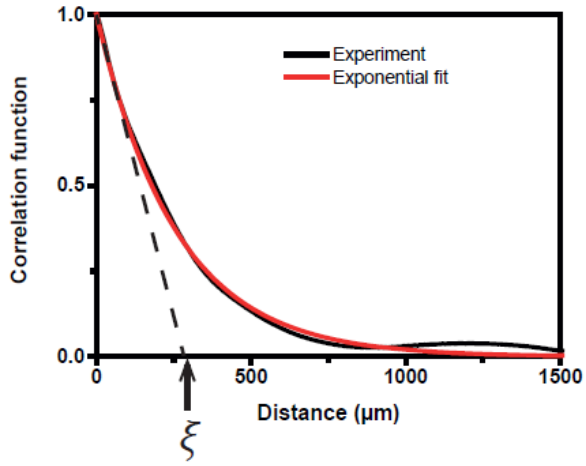

Figure 18. Extraction of the correlation length ξ from the spatial autocorrelation of the orientation map θ.
The autocorrelation curve of the orientation map of a nematic monolayer (black) is fitted with an exponential (red). The tangent at 0 of the exponential fit intersects the x-axis at the correlation length $\boldsymbol{\xi}$.
Taken from Duclos, 2014.

Nematic ordering in a 3D system

Nematic ordering in 3D systems could arise from either a 2D layer of nematically ordered objects in a 3D shape or a full 3D volume of nematically ordered objects. In the first case, the 2D layer of nematically ordered objects in a 3D shape presents the same type of ordering and defects as if they are on a 2D plane. The curved surface impacts the nematic ordering by placing defects at specific positions to adapt to the 3D shape. The 3D shape also facilitates the formation of +1 or -1 defects at the tips of the 3D shape. Finally, the curved surface can lead to the appearance of borders between aligned areas with almost the same director $\boldsymbol{n}$.

In the second case, nematic ordering inside a total 3D volume leads to the generation of 3D defects (Duclos et al., 2020). The 3D defects take the shape of lines or loops. Continuous change of object position and orientation happens in the perpendicular planes to the line. For each perpendicular plane, the line becomes a point around which a 2D-like defect is formed. However, it differs from 2D planar defects because, even if the position of the objects goes from +1/2 to -1/2 defects in the perpendicular

plane, the objects' orientation to the perpendicular plane can also vary along the line (Figure 19A). Loop defects are the most common defects in 3D. There are two types of loop defects: wedge-twist and pure-twist loops. For wedge-twist loop defects, the objects in the line's perpendicular planes rotate from parallel to perpendicular orientation to these planes along the line. For pure-twist loops, the objects in the line's perpendicular planes are always perpendicular to these planes (Figures 19 B and C).

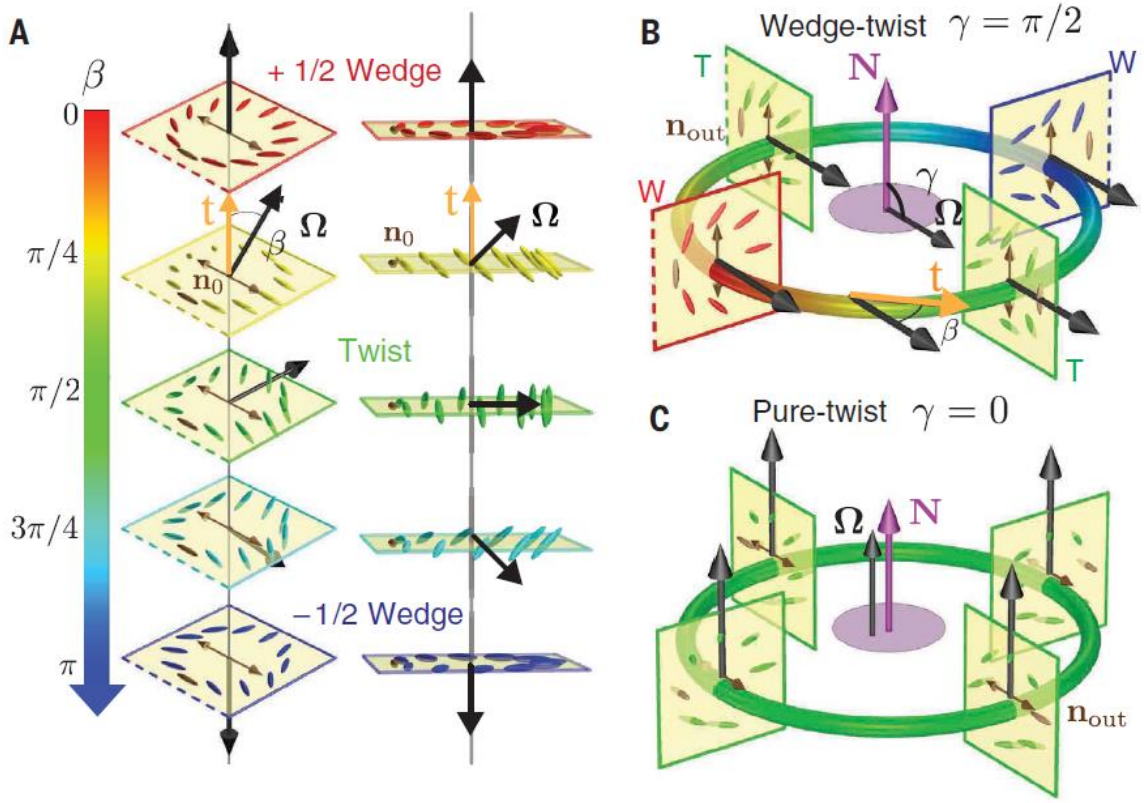

Figure 19. Schematic of line and loop defects in 3D.
A) Example of how a line defect goes from a +1/2 2D defect to a -1/2 2D defect while objects rotate along the perpendicular plane to the line. ***Ω*** *is the tangential vector of the object's orientation, and* ***β*** *is the angle between* ***Ω*** *and* ***t,*** *the tangential direction of the line, colors represent the value of* ***β****.*
B and C) Schematic showing the difference between a wedge-twist (B) and pure-twist loop (C). For wedge-twist, ***β*** *varies from 0 to π, whereas for pure-twist,* ***β*** *stays at π/2.* ***N*** *represents the tangential direction of the loop, while* ***γ*** *represents the angle between* ***N*** *and* ***Ω****. For wedge-twist loops,* ***γ*** *= π/2. For pure-twist loops,* ***γ*** *= 0.*
Taken from Duclos, 2020.

Both wedge-twist and pure-twist loops are topologically neutral as they continuously go from +1/2 to -1/2 2D-like defects. Being topologically neutral, loop defects can nucleate and annihilate themselves inside the 3D volume. When nucleating, loop defects grow and can merge with a line defect nearby, disconnecting the loop and resulting in a line defect. In the same process, line defects can interconnect, join both extremities and thus create loops.

Active nematics: extensile vs. contractile system

In passive nematics, once it is created, no additional energy is added to the system. The passive nematic is then let to evolve until it reaches an equilibrium where energy and the number of defects are minimized. In contrast to passive nematics, active nematics are out of the thermodynamic equilibrium (Doostmohammadi et al., 2018; Saw et al., 2018). The objects themselves or external factors constantly add energy to the system. This constant input of energy prevents the system from reaching its equilibrium: defects appear and disappear with the energy input and following the topological neutrality rule.

Moreover, objects, as well as the defects they form, move. Defects' appearance and disappearance and movement generate mechanical stress in the system. The mechanical stress generates two active systems: extensive and contractile (Figure 20).

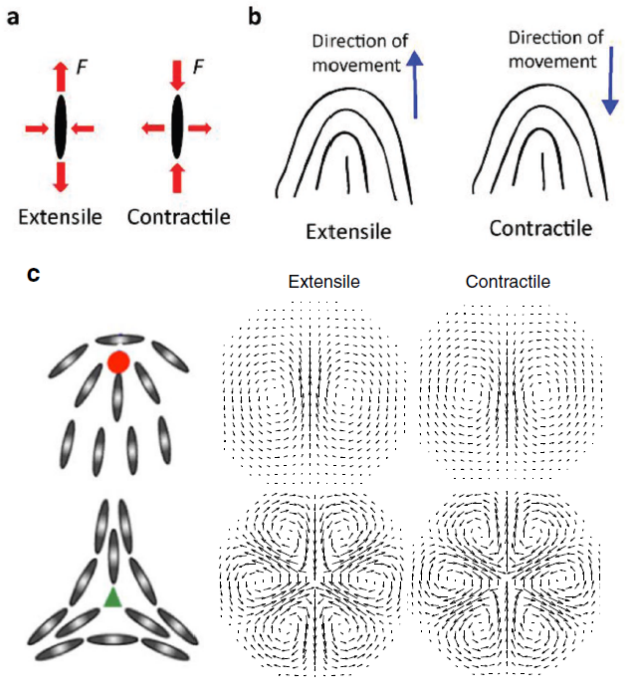

Figure 20. Schemes represent the differences between extensile and contractile systems.
a) Dipoles of forces along the object's small and long axis for each system.
b) Direction of movement for comet defect for each system.
c) Velocity fields around comet and triangle defects for each system.
Taken from Saw (a, b), 2018 and Doostmohammadi, 2018 (c).

In extensile systems, the objects contract along their smaller axis and push along their long axis. Comet defects move in a tail-to-head direction following the velocity field of objects. In contrast, in contractile systems, the objects push along their smaller axis and contract along their long axis. As a result, comet defects move in a head-to-tail direction following the velocity fields of objects. Biological objects generate active nematic ordering as they are generally active material or can be continuously

activated. Concerning cytoskeleton proteins, nematic systems using actin fibers as objects are largely contractile (Schuppler, 2016), whereas nematic systems using microtubules as objects are largely extensile (Sanchez, 2012). Cells are expected to form contractile nematic as single cells exhibit mechanical stresses comparable to contractile nematic objects. However, it has been observed that fibroblasts or myoblasts make a contractile nematic system, while epithelial cells (MDCK) or neural progenitor cells create an extensile nematic system. The system's contractile or extensile property depends on the cell monolayer's balance between intercellular and intracellular stresses (Figure 21) (Balasubramaniam et al., 2021).

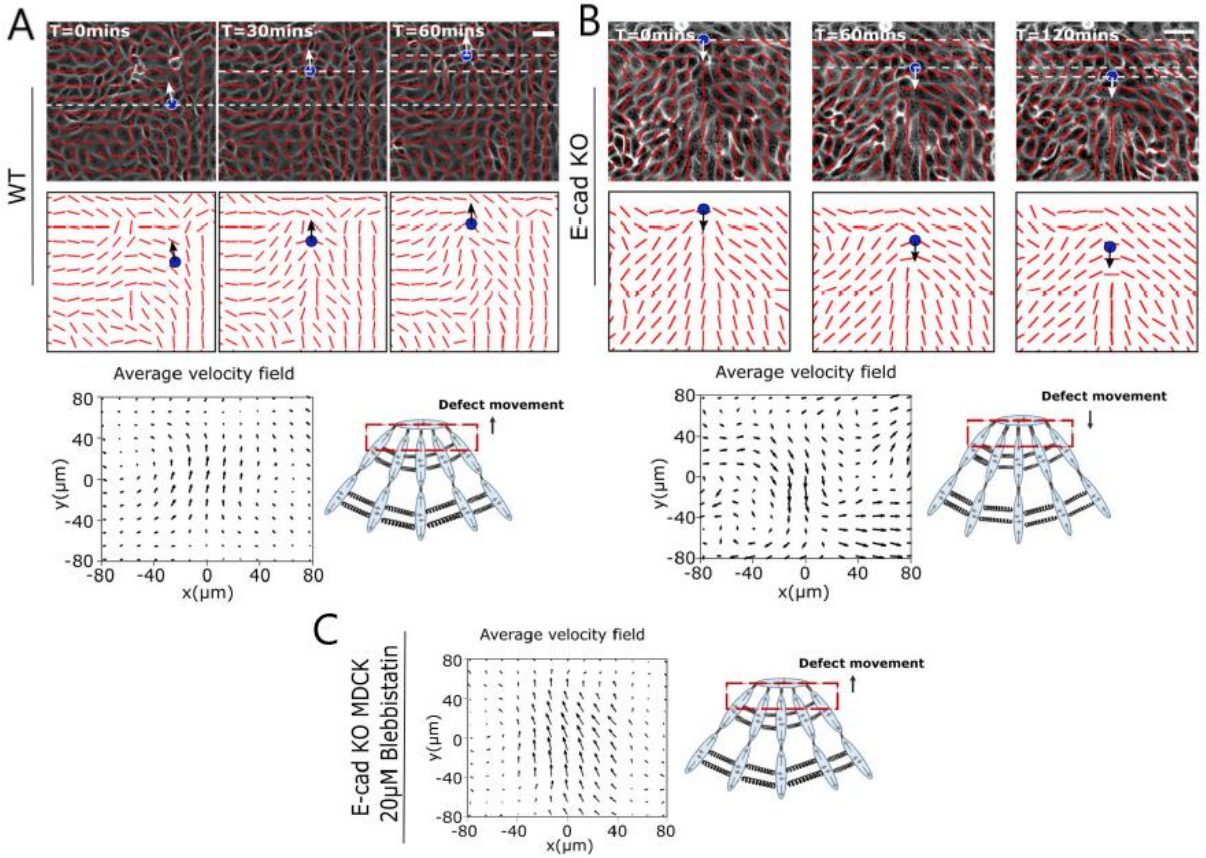

Figure 21. The balance between the cell monolayers' inter- and intracellular stresses governs the type of active nematic.
A and B) Time-lapse imaging of wild-type MDCK (A) or E-cadherin KO MDCK (B) monolayer showing a comet movement (blue point and arrow) on a bright field with local orientation (red line) (up). Associated average velocity field around comet and scheme showing comet movement direction (down).
C) Average velocity around comet and scheme showing comet movement direction for E-cadherin KO MDCK treater with 20 µM blebbistatin.
Taken from Balasubramaniam, 2021.

The cell-cell adhesions govern the intercellular stresses. The cell-substrate interactions and actomyosin machinery govern the intracellular stresses. Systems with predominant intercellular stresses are extensile, whereas systems with predominant intracellular stresses are contractile. Changes in the balance between inter and intracellular stresses lead to a switch from one type of active nematic to

the other one. For example, epithelial cells, like MDCK, are extensile thanks to their strong cell-cell junctions via E-cadherin. Depleting E-cadherin in MDCK switches the monolayer to a contractile nematic, visible by the change of the comet movement direction. Without E-cadherin cell-cell junctions, MDCK cells enhance their interaction with the substrate, leading to this change. However, the addition of blebbistatin, an inhibitor of the actomyosin machinery, switches back the monolayer to an extensile nematic. Indeed, blebbistatin reduced the actomyosin machinery, re-establishing the original balance. Thus, the balance between inter- and intracellular stresses determines the type of active nematic a cell monolayer is. Finally, active nematic ordering generated by cells can reach a steady state as their density rises with proliferation leading to a jamming system.

Shaping the nematic ordering

On a surface without constraint, nematic ordering is randomly created in terms of director of aligned areas, positions of defects, and their motions. However, it is feasible to shape the nematic ordering into an organization of interest using external clues. An easy way to force the nematic ordering into a particular alignment is to add edges on the surface within the system that can evolve. The objects physically sense the edges and consequently align their long axis along the edge. The ordering then spreads from the edge deeper into the system with the correlation length of the nematic system.

An example is represented in Figure 22. Fibroblasts forming nematic ordering with a correlation length $\boldsymbol{\xi}$ ~ 450 µm are confined between two long edges (Duclos et al., 2014). Such confinement is realized by making adhesive strips on a non-adhesive surface, edges are thus the borders between the adhesive and non-adhesive surface. When the width between the two edges is similar to or smaller than the correlation length, the system evolves to reach a perfectly aligned area with an order parameter $\boldsymbol{Q}$ ~ 1. However, when the width between the two edges gets above the correlation length, aligned areas of other directors $\boldsymbol{n}$ appear in the middle of the system, even if fibroblasts remain aligned along the edges. As a result, the order parameter $\boldsymbol{Q}$ decreases with the width of the confined area as more differently aligned areas appear.

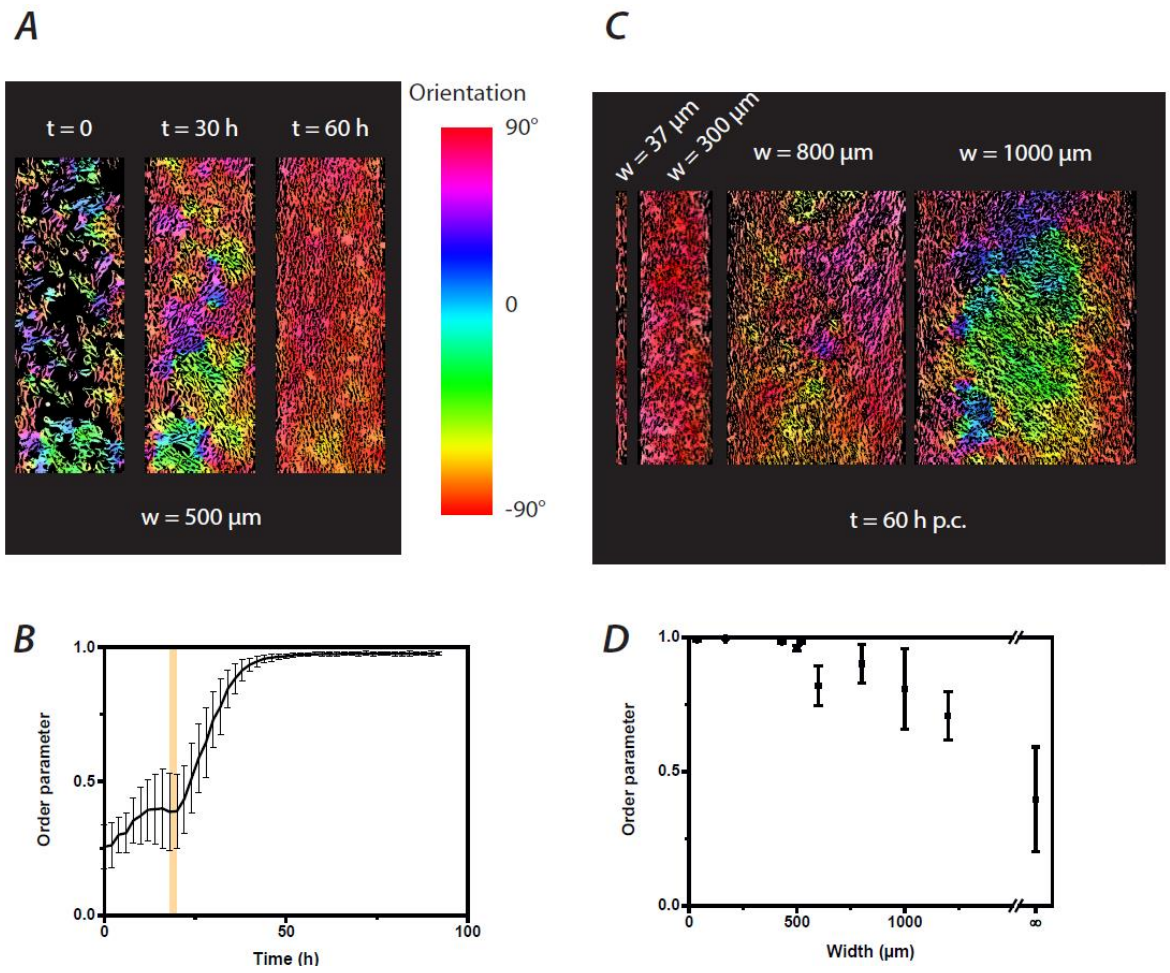

Figure 22. Confining nematic ordering between two long edges leads to ordering along these edges.
Experiments presented have been performed using NIH-3T3 fibroblasts.
A) Orientation maps of the nematic ordering on 500 µm width strips at different time points after seeding.
*B) Evolution over time of the global order parameter **Q** of (A), steady state of the system is reached around 60h, the orange line indicates system confluence.*
*C and D) Difference of the steady state (after 60h of evolution) of the nematic ordering on different strips width and corresponding order parameter **Q** (D).*
Colormap of (A) and (C) corresponds to the angles of the orientation map θ.
Taken from Duclos, 2014.

In the examples presented in Figure 22, edges are imposed only in one direction, while the others are left free. However, edges could be imposed in all directions leading to nematic ordering inside a pattern. In that case, the shape and size of the pattern determine what the nematic ordering looks like, which kind of defects can appear, and where. For example, vertical and horizontal edges on square patterns impose nematic ordering along their direction. These two different directors ***n*** meet at the corners leading to the appearance of -1/4 and +1/4 defects (Bade et al., 2018).

In the examples presented in Figure 23, mouse embryonic fibroblasts are seeded on a 1 mm x 1 mm square pattern and, after a particular time, give rise to -1/4 and +1/4 defects at the corners. These -1/4 and +1/4 defects differ by the fibroblasts' orientation and the movement flow around the corner.

For -1/4 defects, fibroblast flow follows the corner's curve by arriving at the corner from one edge and going away from the corner by the other edge. For +1/4 defects, fibroblast flows converge at the corner by arriving at the corner from both edges.

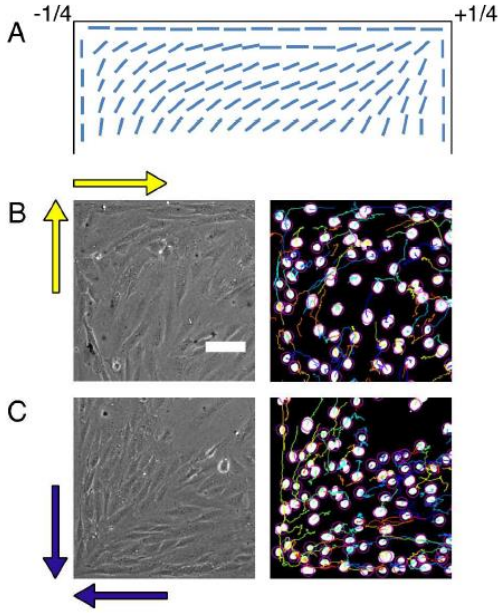

Figure 23. Square pattern leads to -1/4 and +1/4 defects at the corners.
Experiments are performed using mouse embryonic fibroblasts on a 1 mm x 1 mm square pattern.
A) Scheme representing the shape of -1/4 and +1/4 defects at the corners.
B and C) Focus on a corner with a -1/4 defect (B) and a corner with a +1/4 defect (C), a bright field is shown on the left, nuclei are shown on the right, and color lines represent nuclei trajectories over six hours. Yellow arrows (B) and blue arrows (C) represent the main direction of movement at the edges for each type of defect. Scale bar = 100 µm.
Taken from Bade, 2018.

Another possibility to generate a pattern from closed strips is to superpose vertical and horizontal stripes creating a cross pattern. Vertical and horizontal branches of the pattern can have the same or different widths. The widths of each branch and the difference between branches' widths impact the nematic ordering inside the cross pattern (Duclos et al., 2014). This could be illustrated with the following experiment. Fibroblasts forming nematic ordering with a correlation length ξ ~ 450 µm are confined in a cross pattern with varying vertical branches' widths, whereas the horizontal branches are kept constant at 200 µm (Figure 24). Because strips are closed, at the end of each branch, +1/4 and -1/4 defects appear. In each branch, the main orientation of the nematic ordering corresponds to the orientation of the branch. In the middle of the cross, where branches meet, the main orientation of the nematic ordering is imposed by the branch with the larger width as long as this width stays smaller or similar to the correlation length. If both branches have equal width, the main orientation in the middle of the cross evolves into the orientation of either branch with the same probability. Suppose the larger branch has a width above the correlation length. In that case, the smaller branch imposes its orientation in the middle of the cross as the nematic ordering inside this branch is one main aligned

area that spreads to the middle. However, because the center of the cross is also bigger than the correlation length, there is not only one big aligned area, thus a lower order parameter than in the other case.

Many other shapes can be generated using straight edges and then studied to see how they impact the nematic ordering. For example, a triangle pattern with the size of the correlation length could be used to create triangle defects. However, curved edges can also be used to shape the nematic ordering.

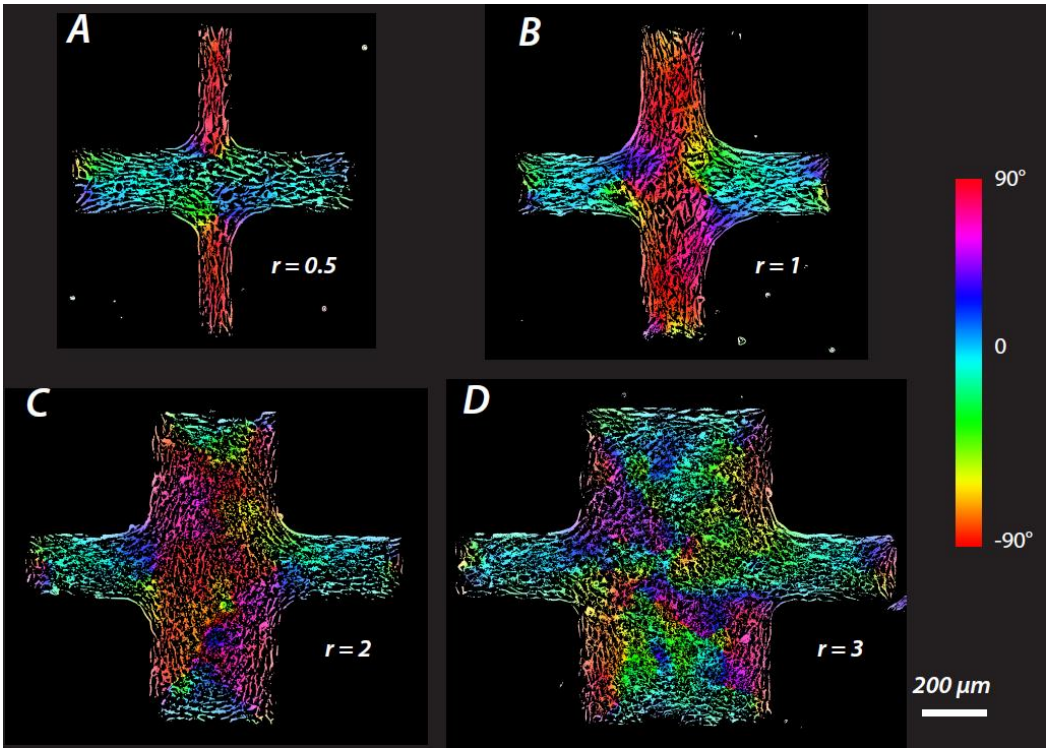

Figure 24. Nematic ordering on cross pattern with different vertical widths.
Experiments presented have been performed using NIH-3T3 fibroblasts. Colormap corresponds to the angles of the orientation map θ. For all crosses, the horizontal branch width is 200 µm, while the vertical branch width is either 100 µm (A), 200 µm (B), 400 µm (C), or 600 µm (D). The aspect ratio of the vertical to the horizontal branches is represented by ***r****.*
Taken from Duclos, 2014.

Using curved edges, it is possible to generate circular patterns. The size of the circular patterns compared to the correlation length of the system impacts the type of nematic ordering inside the circle and the type of defects generated inside the pattern. However, in both situations, the global topological charge of the circular pattern remains at +1. If the diameter of the circular pattern is above the correlation length ξ, objects align their long axis along the curvature of the circle at the border of the pattern. Inside the pattern, the nematic ordering gives rise to two comets, +1/2 defects, coupled by their tails (Duclos et al., 2017). This is illustrated with the following examples. Fibroblasts forming nematic ordering with a correlation length of $\xi \sim 450$ µm are confined in circular patterns with a diameter of 700 µm (Figures 25A, B). The two comets form a dipole positioned along one of the circle

diameters. Each comet is placed at a certain distance from the center, corresponding to 0.67 of the radius size. If the diameter of the circular pattern is similar to the correlation length ξ, objects generate a +1 defect at the center of the circle (Guillamat et al., 2022). In this circular pattern, +1 defects can take two different shapes: spiral shape, where objects swirl from the border to the center of the circle, or aster shape, where objects position perpendicularly from the border to the center of the circle (Figures 25C - F). In these examples, mouse myoblasts forming nematic ordering with a correlation length $\xi \sim 190$ µm are confined in circular patterns with a diameter of 200 µm. Spiral or aster shape +1 defects differ from each other in terms of objects' orientation and velocity patterns around the defect. The density of cells likely regulates the choice between spiral or aster shape +1 defect. At low density, cells generate spiral +1 defect with cells moving in the swirl. As density increases, spiral +1 defect transitions to +1 aster defect as cells orient more and more perpendicularly to the border, slowing down.

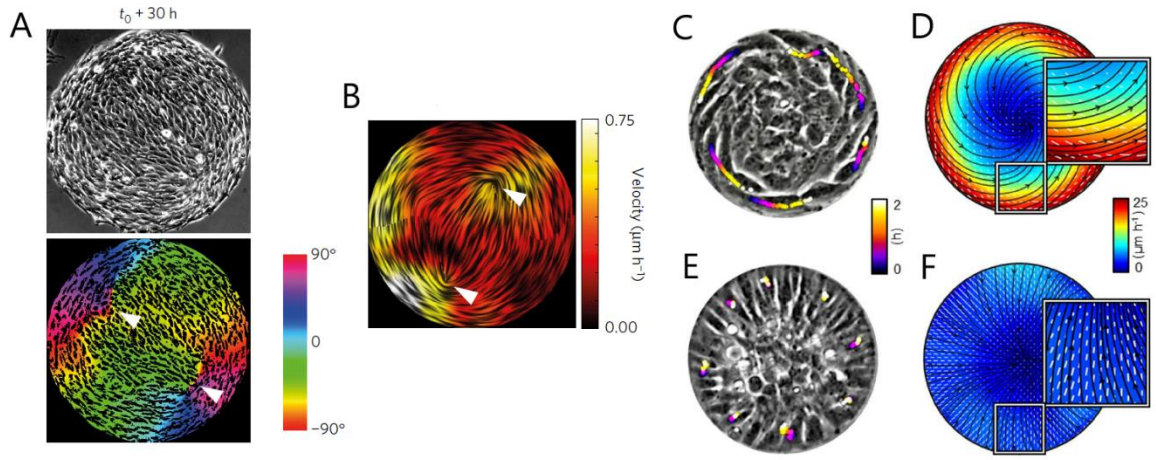

Figure 25. Nematic ordering on circular patterns with diameters above or similar to the correlation length of the system.
A and B) Nematic ordering of NIH-3T3 fibroblasts on a circular pattern with a diameter above the correlation length. White triangles indicate comet defects.
A) Bright field of the nematic ordering and its associated orientation map θ. Colormap corresponds to the angles of the orientation map θ.
B) Velocity field of the nematic ordering. Colormap corresponds to the cell velocity.
C, D, E, and F) Nematic ordering of C2C12 mouse myoblasts on a circular pattern with a diameter similar to the correlation length of the defect. Bright field of +1 defects inside the circular pattern shape either as a spiral (C) or aster (E) with a colored line showing cells movement over 2h and their corresponding orientation (black and white dash line) and velocity field (black line and colormap) for +1 spiral defect (D) and +1 aster defect (F).
Taken from Duclos, 2017 (A, B) and Guillamat, 2022 (C-F).

Using edges to shape the nematic ordering into the organization of interest also generates interactions between the edges and the objects in their proximity. In the case of active nematic with deformable objects, such as cells, objects move faster along the edge than inside the system. Specific examples demonstrating this are shown in Figure 26. For example, retinal Pigment Epithelial (RPE1) cells are confined on 500 µm wide stripes. On the velocity fields associated, a shear flow is present along the

edges, characterized by cells moving along the edge but in the opposite direction for each edge (Figure 26 A-E) (Duclos et al., 2018). This motion is lost in the middle of the stripe because the speed decreases with the distance from the edge. Another example is mouse embryonic fibroblasts confined on a 1 mm x 1 mm square pattern (Figure 26 G and J) (Bade et al., 2018). Close to the edges of the pattern, fibroblasts' trajectories are straight and parallel. In contrast, further away from the edges, the trajectories are less linear and persistent. Like for REP1 cells, fibroblasts' speed also decreases with the distance from the edge. This faster motion at the edge is also visible on the velocity fields (Figure 25).

Edges also impact the aspect ratio of cells. For example, fibroblasts are more elongated at the edges than in the center of the square (Figure 26 I) (Bade et al., 2018). Finally, as discussed above, edges impose the orientation of the cells in the vicinity. Cells orient themselves with a tilt that increases with the distance from the edge. The initial inclination between cells and the edge depends on the cell type (Figure 26 C - H) and correlates with different cells' movements at the edges (Duclos et al., 2018). For Figures 26 C and D, RPE1 cells are confined on stripes of 500 µm width. On their orientation maps θ, the initial tilt of cells decreases with the distance from the edge. The tilt orientation of REP1 cells is the same in 90% of the cases and is always associated with the same direction of shear flow: the side of the cell in contact with the edge leads the cell movement direction. In Figure 26 F, different cells are confined on stripes of 500 µm width.

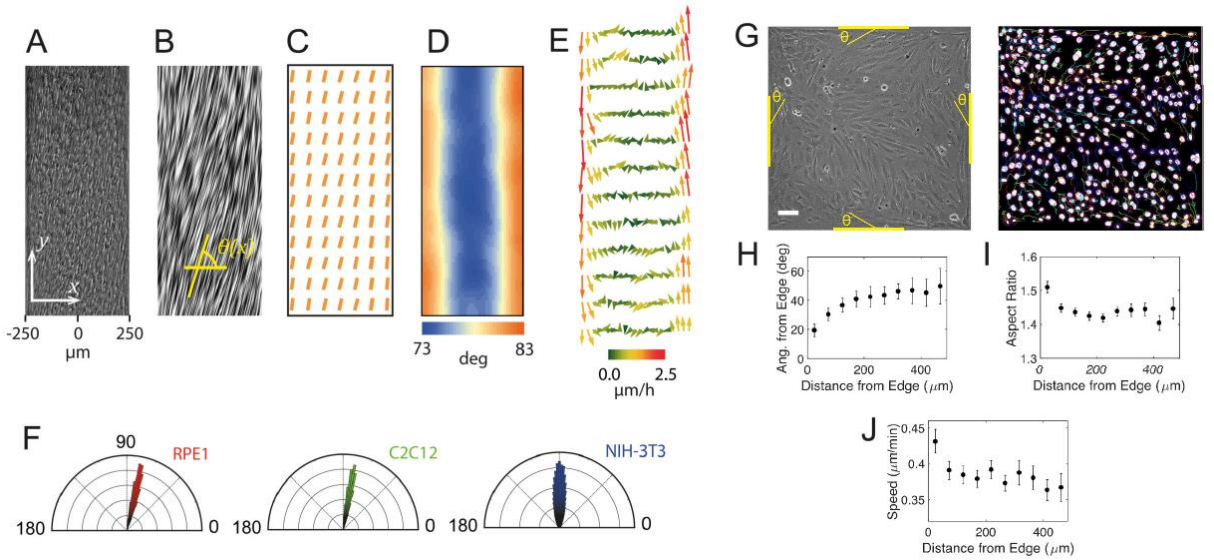

Figure 26. Proximity from the edges enhances elongation and speed of cells.
A, B, C, D, and E) Bright-field (A) of the nematic ordering of RPE1 cells on 500 µm-wide stripes and its image treatment with line integral convolution (B) from which the local director (C) and the orientation map θ (D) with its colormap are extracted. The velocity field (E) is represented with arrows to show the direction of movement and colors to represent the speed
F) Histogram of average cell orientation along 500 µm-wide stripes for different types of cells: RPE1 cells, C2C12 mouse myoblasts, and NIH-3T3 fibroblasts.
G, H, I, and J) Bright-field and nuclei (G) of the nematic ordering of mouse embryonic fibroblasts on 1 mm x 1 mm square patterns. Color lines on the nuclei field represent cell trajectories over six hours. Average of the angles from the edge (H), the aspect ratio (I), and the speed (J) over the distance of cells from the edge.
Taken from Duclos, 2018 (A-F) and Bade, 2018 (G-J).

The average tilting of cells compared to the edge over the stripe differs for each cell type. Interestingly, whereas C2C12 mouse myoblasts present a similar shear flow as REP1 cells with a similar tilt, NIH-3T3 fibroblasts, with no tilt, do not show any shear flow. Moreover, HT1080 sarcoma cells, with a tilt opposite to REP1 cells, present a shear flow in the opposite direction (not shown here). For Figure 9H, mouse embryonic fibroblasts are confined on a 1 mm x 1 mm square pattern. The average cell tilting relative to the edge increases as the distance from the edge increases (Bade et al., 2018). The direction of cell movement also corresponds to the tilt: the side of the cell in contact with the edge leads the cell movement direction. Thus, while cell tilting at the edge can be associated with cell movement, the tilt orientation gives the direction of cell movement.

Defects in the nematic ordering as biological tools

Active nematic ordering can be found in many biological systems, from gel cytoskeleton proteins such as actin fibers or microtubules to tissues composed of monolayers or multilayers of cells. The presence of nematic ordering across different biological scales questions their potential utility and function in the system they appear in. Defects are places with characteristic velocity fields and objects' orientations. The velocity fields around defects, however, depend on the type of active nematic, extensile, or contractile (Figure 20 C) (Saw et al., 2018). Thus, it is essential to consider the type of the active nematic when studying the function of defects in the tissues.

For extensile nematic and +1/2 defects, cells flow from the tail to the head of the comet, where velocity decreases. Such a pattern can lead to the accumulation of cells at +1/2 defect. For contractile nematic and +1/2 defects, cells flow in the opposite direction: from the head to the tail of the comet. Concerning the -1/2 defect, there is no preferential flow around the defect for neither extensile nor contractile nematic that can predict any particular behavior. Extensile and contractile nematic systems velocity fields can lead to different cell densities at defects compared to aligned areas (Figure 27) (Kawaguchi, 2017). For example, in murine Neural Progenitor Cells (NPCs), which create an extensile nematic system, cells accumulate at comet defects over time, forming three-dimensional formations and mounds, whereas cells escape at triangle defects. In contrast, in contractile nematics of C2C12 mouse myoblasts, cells neither accumulate nor escape defects. Also, in both cases, cell proliferation and differentiation do not change at defects. Thus, cell density change around defects for NPCs is mainly due to cell flow coupled with cell-cell and cell-substrate anisotropic friction arising from this flow.

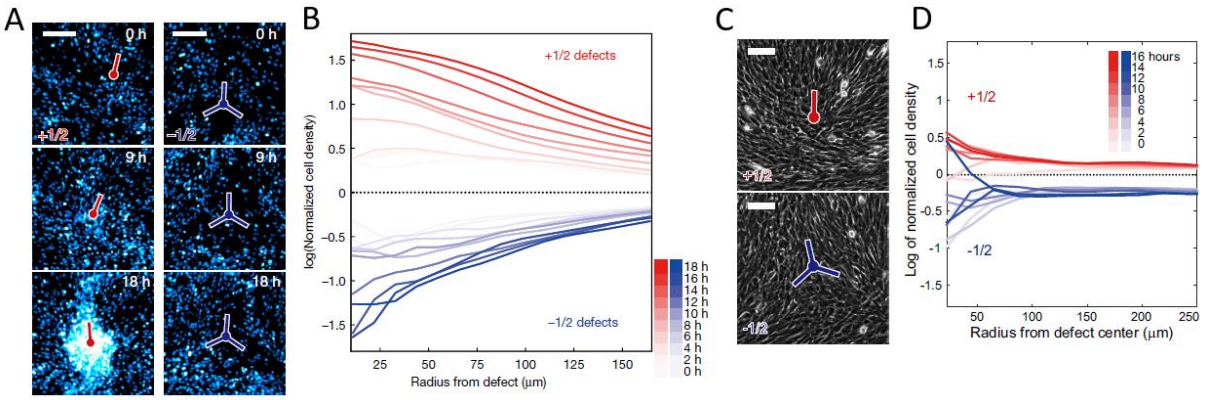

Figure 27. Extensile nematic can lead to cell accumulation at the defect and cell escape at the triangle.
A and B) Accumulation of murine NPCs cells at comet +1/2 defect (A left) and escape of cells at triangle -1/2 defect (A right) over time. Cell density over the distance from each defect (+1/2 defects in red, -1/2 defects in blue) for different time points (shade of colors) (B).
C and D) No accumulation of C2C12 mouse myoblasts at comet +1/2 defect (C up) and no escape of cells at triangle -1/2 defect (C down). Cell density over the distance from each defect (+1/2 defects in red, -1/2 defects in blue) for different time points (shade of colors) (D).
Taken from Kawaguchi, 2017.

However, cell accumulation at comet defects and cell escape at triangle defects do not appear in all extensile nematic systems (Saw et al., 2017). Other characteristics of active nematics, such as mechanical stress induced by the appearances and disappearances of defects, could also affect cell behavior. Indeed, mechanical stress around defects forms specific patterns compared to aligned areas (Doostmohammadi et al., 2018). Studying this particular pattern of mechanical stress in epithelial tissue led to deciphering the mechanism behind cell extrusion (Saw et al., 2017). Cell extrusion is linked with cell apoptosis and regulates the monolayer homeostasis, development, and removal of pathological cells from the epithelial tissue. Since most epithelial tissues generate active nematic ordering, the authors wonder if both phenomena could be linked. Thus, they compare cell extrusions and defects' positions. In epithelial tissues, extrusion mainly occurs around the comet head of +1/2 defects, a place with enhanced compressive stress. For example, such a phenomenon is visible in Madine Darby Canine Kidney (MDCK) epithelial monolayers, which generate extensile active nematic (Figure 28). In cells that will be extruded, the apoptotic signals, such as caspase-3 activation, are triggered. To assess if there is a link between cell extrusion and defects, the authors measured the distance between the extrusion zone (defined by the characteristic morphology of extruded cells and positive staining for cleaved caspase) and the closest +1/2 defect. They found that extrusion mainly occurs at or near comet defects in MDCK epithelial cells. This seems a standard feature for epithelial tissues as it also appears in other epithelial cell monolayers such as breast cell line MCF10a and human epithelial skin cells HaCaT (Saw et al., 2017).

Comet defects appear before cells extrusion and flow to the extrusion place. During displacement of the comets, mechanical stress induces compression at the head of the comet and tension inside the triangle. Such compressive stresses at the comet head of +1/2 defects increase until the comet reaches the extrusion site and extrusion happens. Based on these results, the mechanism underlying extrusion at the comet in epithelial defects is proposed: Cell movement inside the monolayer gives rise to +1/2 and -1/2 defects. +1/2 defects then move from the tail to the head of the comet. During comet movement, compressive stresses appear and increase at the comet head, triggering cell apoptosis. In the future extruded cell, apoptotic signals trigger cell extrusion at the +1/2 defect core. Most epithelial tissues act as extensile nematic, suggesting that this mechanism is common for most epithelial tissues and could be used to preserve tissue homeostasis by removing either excess cells or pathological cells, such as cancerous cells.

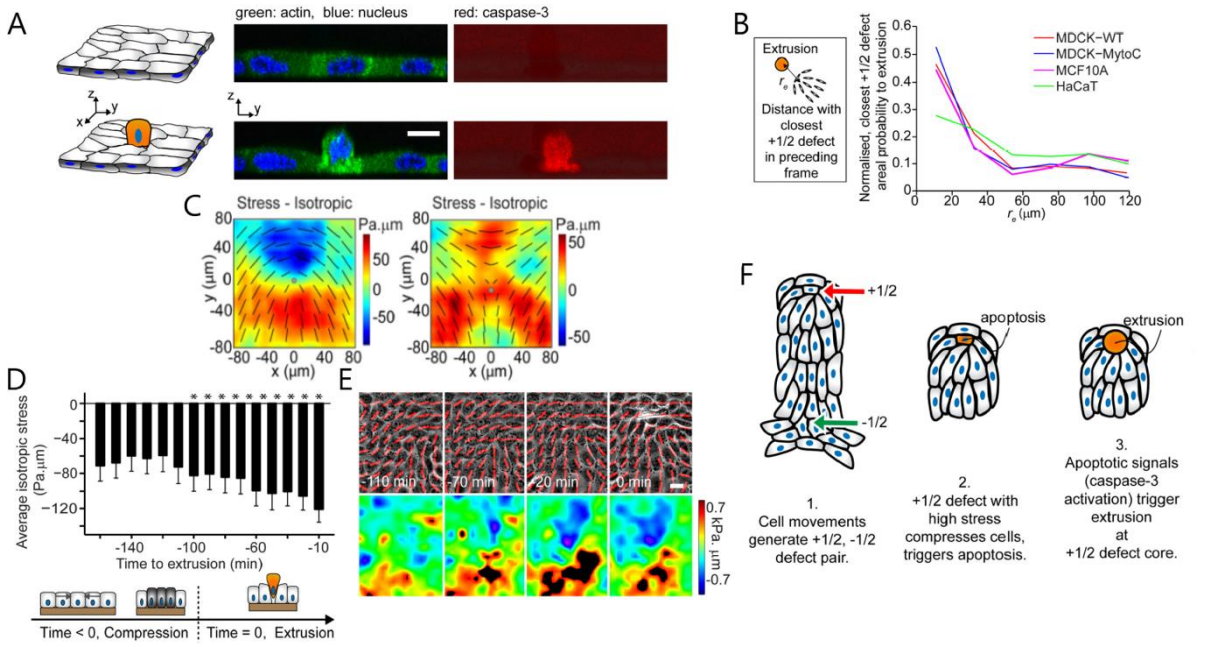

Figure 28. Compression at comet defect triggers cell apoptosis and extrusion.
Experiments presented in (A), (C), (D), and (E) have been performed using MDCK-WT.
A) Orthogonal view of cell extrusion with activation of caspase-3 in the extruded cell (right) and its corresponding scheme (left). Fluorescent images: blue: nucleus, green: actin, red: caspase-3, scale bar: 10 µm. Scheme: blue: nucleus, grey: cell body, orange: apoptotic extruded cell.
B) Normalised area probability to find the closest +1/2 defect from extrusion along r_e, the distance from the extruded cell, for different types of cells, the scheme on the left represents how r_e is measured.
C) Average map of isotropic stress of the tissues monolayer around +1/2 defects (left) and -1/2 defects (right). Cells' orientations around each defect are represented with a black dashed line. Color bar: negative values (blue) correspond to compression, and positive values (red) correspond to tension.
D) Average isotropic stress around the extruded cells over time before the extrusion.
E) Bright-field images with cell orientation in red dash line of a comet moving up to the extruded cell for different time points before the extrusion and their corresponding map of isotropic stress. Color bar: negative values (blue) correspond to compression, and positive values (red) correspond to tension. Scale bar: 10 µm.
F) Scheme representing the mechanism of extrusion at +1/2 defect.
Taken from Saw, 2017.

In extensile nematic, defects can lead to either change in cell density or compressive stresses, leading to, respectively, cell accumulation or escape, and cell extrusion. The Change in cell density and compressive stresses at defects can also combine leading to different biological functions. In the C2C12 mouse myoblasts monolayer, the transition of the +1 defect from spiral to aster generates cell mounds. Such transition generates compressive stresses and cell organization changes inside the cells' mound which cause either cell differentiation or steering morphogenesis (Guillamat et al., 2022). This is illustrated with the following example (Figure 29): C2C12 mouse myoblasts forming contractile nematic ordering with a correlation length $\xi \sim 190$ µm are confined in circular patterns with a diameter of 200 µm. In such circular patterns, cells create a +1 defect that transitions from spiral to aster shape as cell density increases (Figure 25). Even after an aster shape is obtained, cell density keeps on increasing and a cell mound appears and grows over time. At the base of this mound, cell density and nuclear volume differ depending on their position in the circular pattern. Nuclear volume decreases, and cell density increases as cells get closer to the center of the circular pattern. Theoretically, such variation in nuclear volume and cell density are linked with active internal stresses pointing toward the center and compressive stresses that increase from the border to the center of the circular pattern. Pillar constrictions inside the circular pattern confirm these theoretical predictions. C2C12 mouse myoblasts generate compressive stresses on the pillar that increase over time. The smaller the pillar is, the higher the compressive stresses exerted on it, which confirms that compressive stresses increase toward the center.

In addition to compressive stresses generated by the cells at the +1 defect, cells' orientation around the +1 defect inside the cell mound varies with the height. Cells organize as a +1 aster-shaped defect at the bottom of the mound whereas they organize as a +1 spiral-shaped defect at the top of it. The transition between aster and spiral shape appears by rising inside the cell mound. Both compressive stresses and changes in cells' organization inside the cell mound lead to two different evolutions of the system depending on the C2C12 myoblast's capacity to differentiate. C2C12 myoblasts are the precursors of skeletal muscle, and once differentiated, they can form myotubes by fusing. Differentiation can be triggered by mechanical stress, such as the compressive stresses found inside the +1 defect. Indeed, myosin heavy chain (MyHC), a marker of differentiation, is detected inside the cell mounds. MyHC intensity decreases as the distance from the center increase. Starvation can also lead to differentiation. Indeed starved C2C12 myoblasts' mounds also present MyHC. However, MyHC intensity in the starvation case is broader than in control conditions with 10 % FBS. Compressive stresses, thus, generate localized differentiation at the +1 defect. In a situation where differentiation is inhibited, for example during morphogenesis, the cell mound grows up to hundreds of microns. This

growth generates cylindrical vortices as cell organization from aster to spiral in a small mound is maintained, leading to the generation of a protrusion.

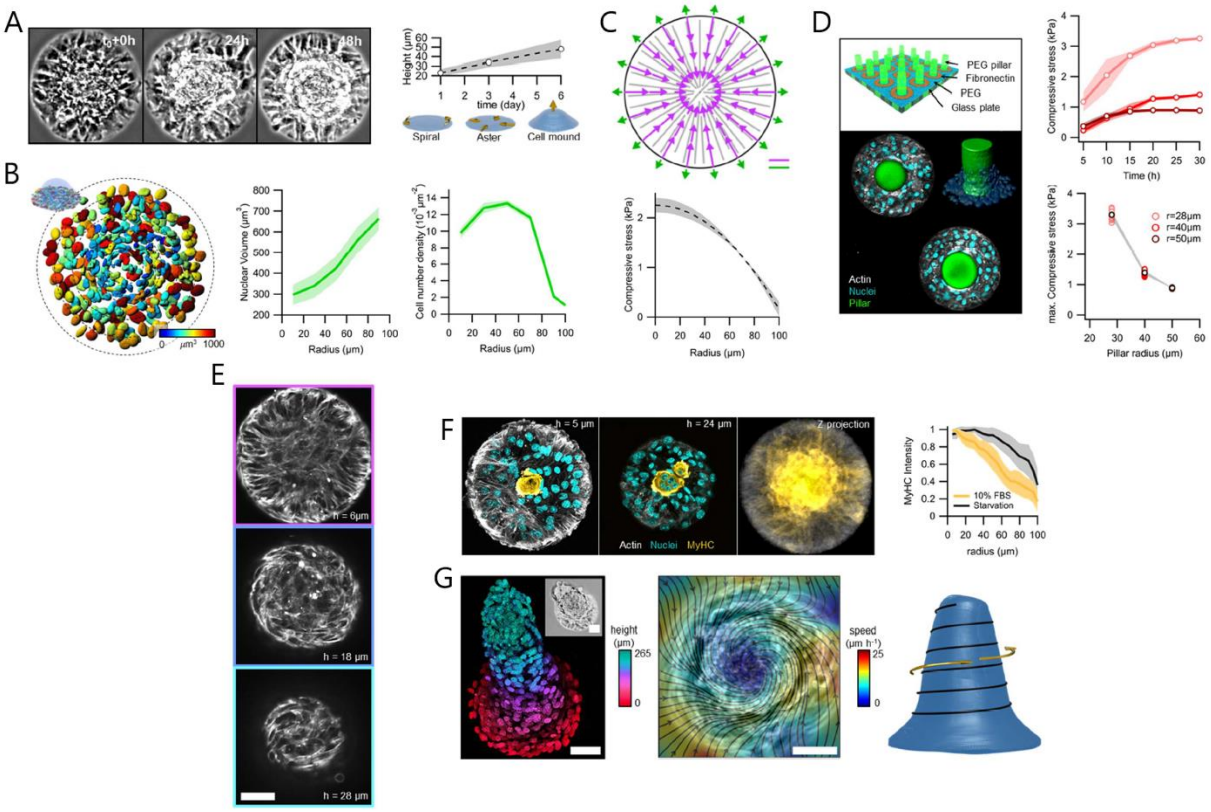

Figure 29. Aster +1 defects generate cell accumulation leading to cell differentiation or steering morphogenesis.
Experiments presented have been performed using C2C12 mouse myoblasts confined on a 200 µm diameter circular pattern.
A) Bright field of accumulation of cells inside +1 aster defects leading to cell mound over time (left). Quantification of cell mound height over time (right).
B) Position and volume of cells nuclei at the base of cell mound, color bar represents nuclear volume with its quantification of nuclear volume as well as cells density over the distance from the center of the circular pattern.
C) Theoretical prediction of active force, internal in purple and at the boundary in green, and theoretical prediction of compressive stress over the distance from the center of the pattern.
D) Pillar constriction to assess compressive stress inside aster defects: Scheme of the pillar with the 3D reconstruction of the pillar constriction, white: actin, cyan, nuclei, green, pillar. Quantification of compressive stress over time and the maximum compressive stress for the pillar of different radii.
E) Actin staining of cell mounds at different heights from the bottom (h = 6 µm, magenta border) to the top (h = 28 µm, cyan border) of the cell mound. Scale bar: 50 µm.
F) Disposition of myosin heavy chain (MyHC) expression inside the cell mound at the bottom (h = 5 µm) and middle (h = 24 µm) of the cell mound and overall (Z projection) (left). Quantification of MyHC expression over distance from the center of circular pattern for two different conditions. Scale bar: 50 µm
G) Nuclei staining of the cellular protrusion (left), color bar: height inside the cellular protrusion. Average velocity fluid for cellular protrusion (middle), color bar: velocity. Scheme representing orientation and flows of cells for cellular protrusions. Scale bar: 50 µm.
Taken from Guillamat, 2022.

The +1 defects are at the protrusion tip and generate the protrusion formation. Thus, defects in an active nematic ordering can allow the formation of morphological features as well as promote the morphogenesis of these morphological features. This is particularly visible in Hydra (Figure 30) (Maroudas-Sacks et al., 2020). Hydra is a small freshwater organism that has a tubular body with a

mouth at one end of the tube and a foot at the other. Several tentacles are present around the mouth. The Hydra's body is composed of two layers of epithelial cells. Inside each epithelial layer, long supra-cellular actin fibers coupled with myosin motors form an extensile nematic ordering covering the entire body. This nematic ordering has a long-range ordering along the body axis for the outer layer and perpendicular to it for the inner layer.

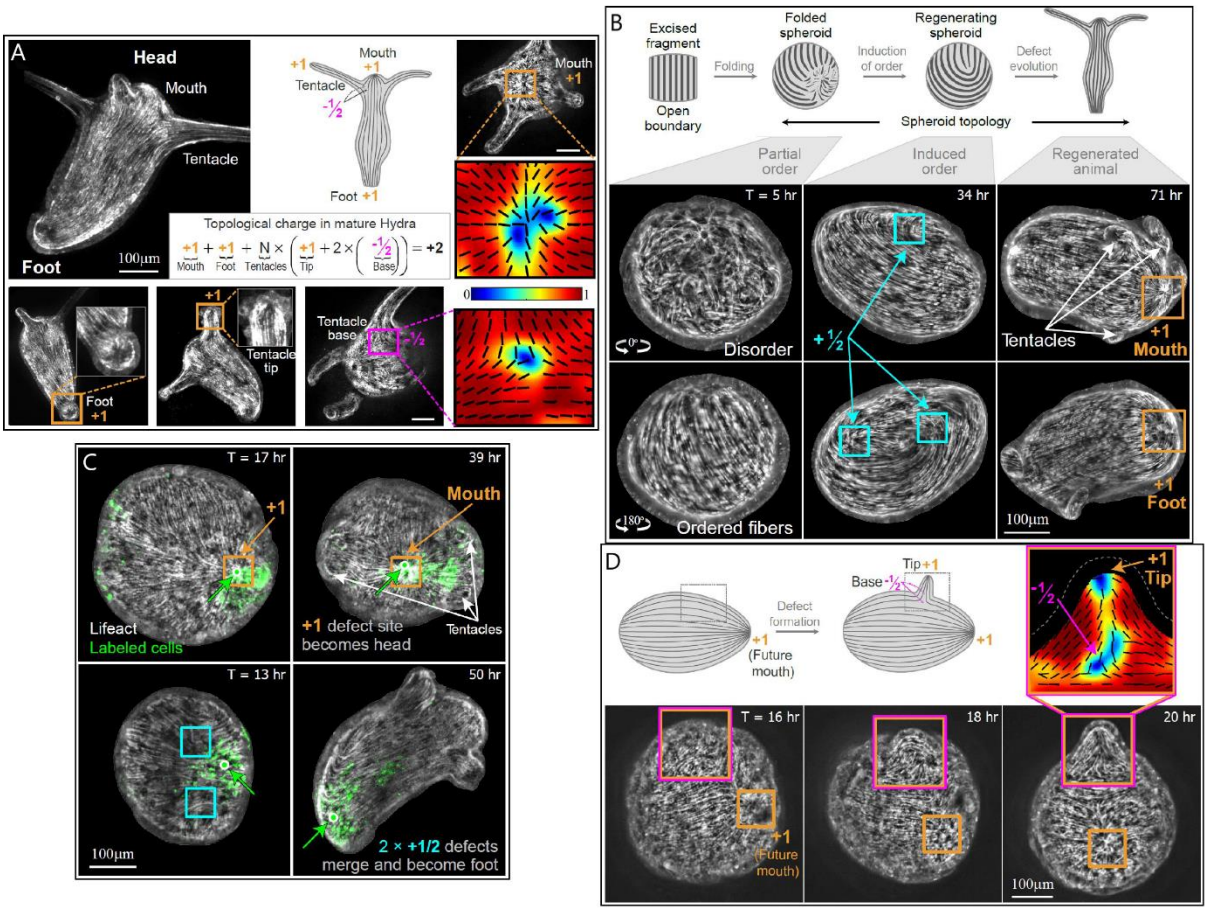

Figure 30. Defects in the nematic ordering of actin fibers map Hydra's spatial organization and drive the morphogenesis during regeneration.

Experiments presented have been performed on Hydra excised fragments.

*A) Spatial organization of defects inside the Hydra morphology. All images show the nematic actin fibers' organization. The image of the entire Hydra presents its morphological features and associated defects: mouth with +1 defect, foot with +1 defect, tentacle with +1 defect at the tip, and two -1/2 defects at the base. Close-up of each morphological feature and its associated defects. Local order parameter **Q** map (color bar) and actin orientation (black dash line) for +1 defect at the mouth and one -1/2 at the tentacle base.*

B) Change in the nematic organization during the regeneration process of Hydra from an excise fragment. Scheme representing the nematic organization of actin fiber at the different stages of the regeneration process of Hydra. Images of a regenerating hydra from two opposite sides at different time points represent each stage. Apparition of defects and each morphological feature of Hydra are spotted.

C) Focus on the generation of the mouth of Hydra at a +1 defect formed early stage during the regeneration process at an early and late time point (up). Focus on the generation of the foot of Hydra from merging two +1/2 defects during the regeneration process at early and late times.

*D) Focus on the generation of the tentacle of Hydra from the apparition of a +1 defect coupled with two -1/2 defects during the regeneration process at different time points. Scheme of the tentacle apparition process (up) with associated images (down). Defects are spotted during the tentacle apparition. Local order parameter **Q** map (color bar) and actin orientation (black dash line) of the newly formed tentacle at the last time point showed.*

Taken from Maroudas-Sacks, 2020.

Defects in nematic ordering are positioned at each morphological feature of Hydra's body. There is one +1 aster defect at the mouth and one +1 aster defect at the foot. For each tentacle, there are one +1 aster defect at the tip of the tentacle and two -1/2 triangle defects on the opposite side of the tentacle base. Each tentacle is topologically neutral. Thus, the global topological charge of a Hydra is +2, which is theoretically the global topological charge a 2D nematic ordering on a closed surface is supposed to have.

When damaged, Hydra can fully regenerate from an excised fragment. The regeneration process takes two to three days and goes through several stages. Each stage is linked with changes in the nematic ordering of the regenerating Hydra. At first, the excised fragment with full nematic ordering but open boundary folds into itself to create a spheroid. In this process, parts of the nematic ordering are lost for a disordered phase. The still ordered regions then spread into the disorder areas to induce order inside the full spheroid. In this process, defects appear, move inside the nematic ordering, and disappear. +1/2 defects, absent from the mature Hydra configuration, are prevalent at the beginning of the stage. The global topological charge of the spheroid reached +2 within about 24 h and remains stable as expected from a 2D nematic ordering on a closed surface. However, defects continue to evolve in the system, appearing and disappearing, until Hydra reaches its mature configuration. Each morphological feature of the mature Hydra is created by a different type of defect appearance and configuration. The mouth mainly arises from a +1 defect created early during the regenerative process, generally inside the disordered region, and remains stationary. The foot mainly arises from two +1/2 defects that move up to each other until merging with their comet heads facing each other, which creates a +1 defect. Tentacles emerge from the spontaneous apparition of a bump with a +1 defect at the tip and two -1/2 defects at the opposite side of the bump. It then protrudes to create the tentacle.

Summary

Nematic ordering arises from objects with an elongated shape. Objects align themselves along their long axis without having any precise position, leading to the generation of aligned areas along one direction called director ***n***. Several aligned areas with different directors ***n*** can exist in the same system. Places, where these different aligned areas meet, are called topological defects. Defects are points inside the nematic ordering where objects' orientation continuously changes from one director to another. Different types of defects exist, each defined by the direction and the fraction of rotation needed around them to go from one director to the other. Defects can also be seen as topological charges, the global topological charges being the sum of all defects charges. To appear or disappear, defects must respect the charges neutrality rule. At equilibrium, the system tends to have the most

neutralized global charge. The two most common defects in 2D are +1/2 defect looking like a comet and -1/2 defect looking like a triangle. The most common defect in 3D is loop defects with a neutral topological charge. Two parameters characterize nematic ordering: the order parameter $\boldsymbol{Q}$ and the correlation length $\boldsymbol{\xi}$. The order parameter $\boldsymbol{Q}$ quantifies how much ordered a given area in the system is. The correlation length $\boldsymbol{\xi}$ measures the mean size of the aligned regions inside the nematic ordering.

In active systems, such as biological systems, equilibrium cannot be reached as new energy is constantly added to the system. Nematic ordering from this active system is called active nematics. Defects can appear, disappear and move, generating mechanical stresses. There are two types of active nematic: extensile and contractile. Extensile nematic is characterized by objects pushing along their long axis and +1/2 defect moving from the tail to the head of the comet. Contractile nematic is represented by objects contracting along their long axis and +1/2 defect moving from the head to the tail of the comet. The balance between intra and intercellular stresses rules the type of active nematic the system forms.

To study a specific organization or a specific defect inside the nematic ordering, shaping the nematic ordering into the organization or defect of interest is possible. An easy way to do so is by imposing edges on the system. The objects will physically sense the edges and align their long axis along them, propagating such alignment inside the system. The size and geometry of the patterns generated by the edges impact the way the nematic ordering organizes in the pattern. Patterns with a size below or similar to the correlation length $\boldsymbol{\xi}$ of the nematic ordering can generate either one specific defect or a perfectly ordered nematic along the edge. However, patterns with a size above the correlation length $\boldsymbol{\xi}$ generate nematic ordering with several defects and aligned areas. Squared patterns create +1/4 and -1/4 defects at their corners, whereas circular patterns can generate either a dipole of two +1/2 or a sole +1 defect. Edges, however, generate interactions between themselves and the objects. At the edges, objects tend to be more elongated and move faster along the edge than inside the system.

Many biological systems organize into nematic ordering, which raises the question of their biological utility. In a biological system, defects are places with specific flow fields and mechanical stresses. Such patterns can impact tissue homogeneity, regulation and differentiation, tissue morphogenesis, and spatial organization. In some extensile systems, cells accumulate at +1/2 defects and escape at -1/2 defects. In extensile nematic epithelial tissues, compressive stresses at +1/2 defects lead to cell death and extrusion. In some contractile tissues, compressive stresses inside +1 defects generate localized differentiation. When differentiation is inhibited, the spiraling flow generates protrusions at +1 defects. In whole organisms with extensile nematic covering them entirely, defects position at each morphological feature.

Chapter IV: Objectives

The most abundant cell type in tumor stroma is the cancer-associated fibroblasts (CAFs) (LeBleu and Kalluri, 2018). They are the major producers and remodelers of the extracellular matrix (ECM), including the basement membrane (Barbazán, 2019). Together with the ECM, CAFs create a capsule that envelops the tumor (Barbazan et al., 2021). This capsule can have two different topologies around the tumor called tumor-associated collagen signatures (TACS). While TACS1 is present in normal tissues, TACS-2 is present in non-invasive regions of the tumor and it is characterized by CAFs and the ECM running parallel to the tumor edge. In contrast, TACS-3 is present in invasive regions where CAF and the ECM organize perpendicular to the tumor edge. In the pre-invasive stage, the tumor cells are separated from the adjacent stroma by the basement membrane (Clark, 2015). Cancer invasion starts by breaching the basement membrane but CAFs' role in this process remains unclear. The host lab previously showed that CAFs help cancer cells to escape the tumor mass by mechanically remodeling the basement membrane (Glentis, 2017). However, by enveloping tumors, the CAFs capsule could also create a physical barrier that prevents tumor growth and cancer cell dissemination.

Due to their spindle shape, CAFs spontaneously align along their long axis in what is called nematic order. Nematic order is intrinsically linked with topological defects, where aligned areas along different directions meet. The most common defects inside 2D layers are +1/2 defects resembling comets, and -1/2 defects resembling triangles.

We hypothesize that whereas nematically ordered CAFs form a capsule that prevents tumor expansion, defects in the nematic ordering may represent the weak points where cancer cells escape. As +1/2 comet defects are usually associated with cell extrusion, it may be places where CAFs change their orientation from parallel to perpendicular to the tumor mass. As a consequence, ECM orientation will change from TACS-2 to TACS-3. On the other hand, as -1/2 triangle defects are places where cell density is lower, this may create weak spots in the CAFs/ECM capsule that allow cancer cells to escape.

To test this hypothesis, the specific aims of my thesis are:

1. Characterize defects as possible weak points in the capsule

Cancer invasion needs time and space to occur. Some defects characteristics, such as their density, size, and movement, could impact their capacity to promote cancer invasion. I will assess these characteristics to determine whether defects could indeed be places promoting cancer invasion.

2. Determine by which mechanism defects could promote cancer invasion

Once established that defects could indeed be places promoting cancer invasion, the next aim is to determine by which means. CAFs are the major ECM remodelers and producers thanks to their contractile capacity. I will assess how defects impact CAFs stress generation and interaction with fibronectin, and how this could promote cancer invasion.

3. Determine the sites of cancer invasion in the CAFs layer

Once established by which means defects could promote cancer invasion, the next aim is to decipher whether cancer invasion indeed occurs at defects. I will assess where cancer invasion occurs in the CAFs layer and how it correlates with defects position.

To address those questions, I used colorectal cancer as a model. I have isolated CAFs and normal-associated fibroblasts (NAFs) from colon cancers of a patient treated at Institut Curie Hospital. As a model of cancer cells, I used the human colorectal cancer cell line, HCT116.

Chapter V: Results

Characterization of the nematic ordering of the cancer-associated fibroblasts

The broad objective of my thesis was to determine if the CAFs' nematic ordering, and associated defects in that ordering, affect cancer cell invasion. To reach that goal, I first described the organization of CAFs at 2D substrates. I seeded human CAFs isolated from colon cancer and normal-associated fibroblasts (NAFs) isolated from adjacent healthy tissue from the same patient on 11 kPa stiff polyacrylamide (PAA) gels. The number of seeded fibroblasts ranged from 25 to 75 thousand, depending on the desired confluence and the time to form the nematic ordering. The system was let to evolve between three to six days before imaging. The CAFs were free to organize their nematic ordering as no constraints were present on the PAA gel.

Then, I imaged the large areas by stitching four-by-four individual images and identified defects in nematic ordering (Figure 31A). I also generated their orientation maps θ and superimposed them on the CAFs images using color bars to represent locally the orientation θ the CAFs areas followed (Figure 31B). As expected, we observed mainly two types of defects: +1/2 comet defects (represented with half ellipsis) and -1/2 triangle defects (represented with triangles) separated by large areas of aligned CAFs (Figure 32A). Then, I performed auto-correlation of the orientation maps θ, fitted the results with a decreasing exponential, and extracted the correlation length of the system: $\xi \sim 320$ µm (N=3 independent experiments, n=7 areas in total). By quantifying the number of defects per field of view, I found that the density of the two types of defects was similar; 1,6 defects/mm² for +1/2 defects and 1,3 defects/mm² for -1/2 defects (Figure 32B). The two types of defects were closely positioned to each other. Proximity and similar density of defects can be explained by the fact that +1/2 and -1/2 defects can only appear and disappear together (Doostmohammadi et al., 2018). The observed density of defects suggests that defects in the CAFs layer could be places where cancer cell invasion starts. Indeed, for 1x1x1 cm tumors, this would translate to about 1 700 defects and more than 15 000 defects for 3x3x3 cm tumors, thus many possible starting points for cancer cell invasion.

Besides the density of defects, we also reasoned that the size of defects could determine the efficiency of cancer cell invasion. The bigger defects are, the bigger area of weakened CAFs' capsule, which would allow a higher number of cancer cells to invade. Thus, I measured the size of the defects. Comets' size was determined as the width of the comet at the transition between the end of the head and the beginning of the tail, while the size of triangles was determined as the distance between one vertex and the middle of the opposing side (Figure 32C, scheme).

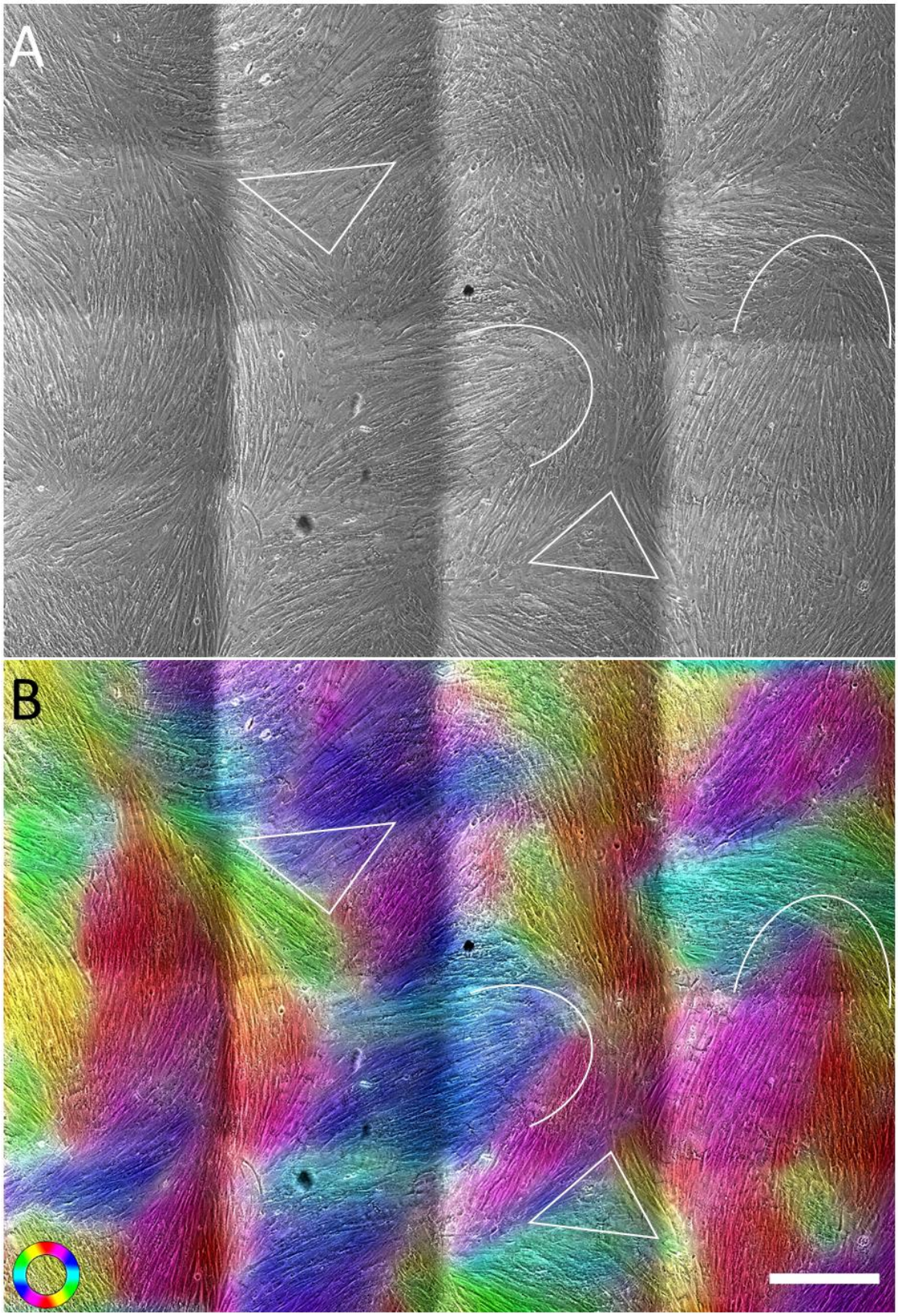

Figure 31. Nematic ordering of human colorectal CAFs.
A and B) Big field of view of four-by-four stitched images of CAF's nematic ordering with bright field (A) and CAF orientation colormap (B). White triangles and half ellipsis show an example of triangle and comet defects inside the nematic ordering. Colored circle: orientation colormap. Scale bar: 400 µm.

I found that +1/2 comet and -1/2 triangle defects had similar size, around 400 µm (Figure 32C). In comparison, defects in MDCK nematic ordering are around 100 µm (Saw et al., 2017), and defects in murine NPC nematics are around 200 µm (Kawaguchi, 2017), thus two to four times smaller than those observed here. Altogether, defects in CAFs' nematic ordering were big and frequent, which increases the possibility to stimulate cancer cell invasion.

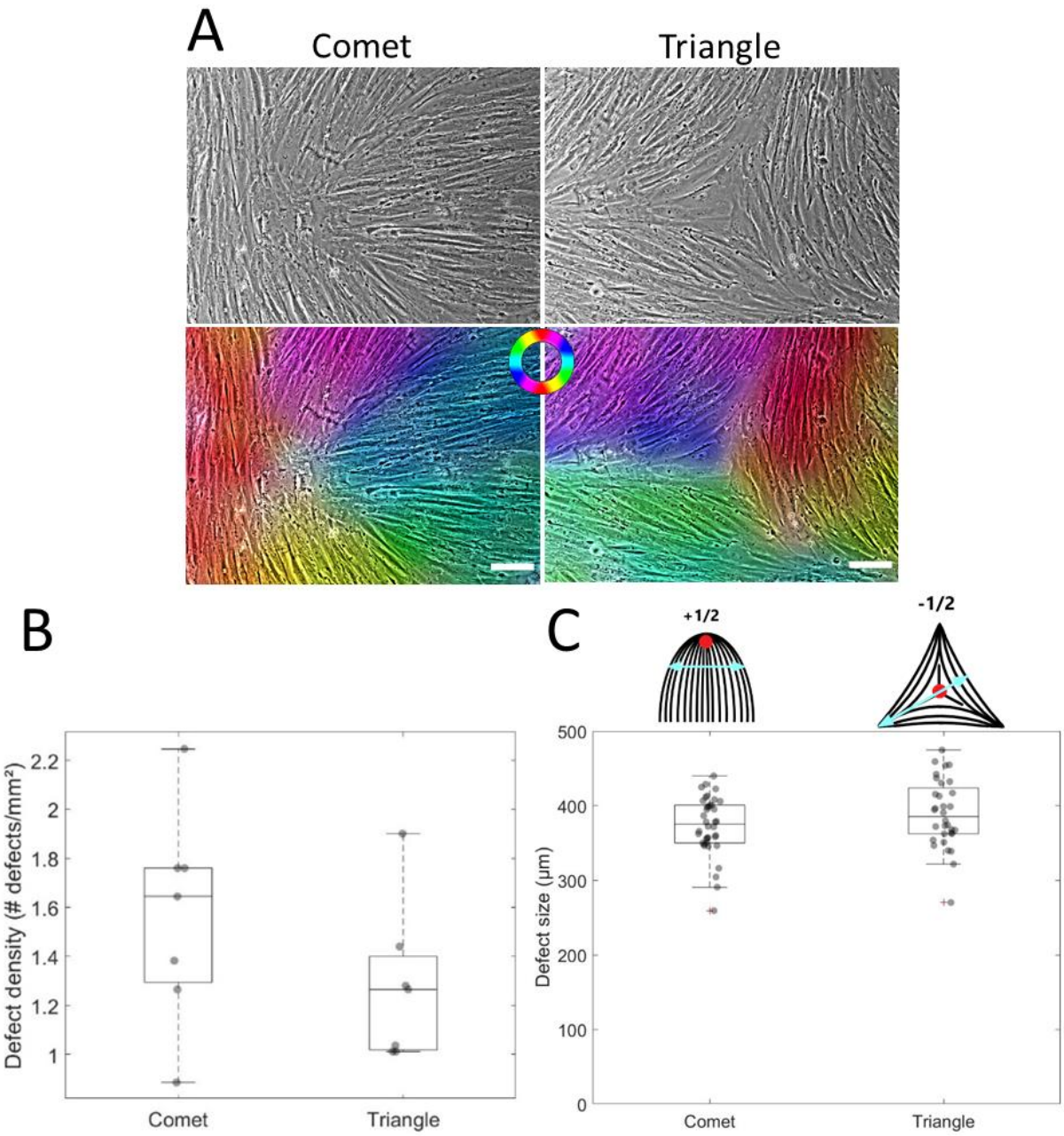

Figure 32. Density and size of defects.

A) Higher magnification of +1/2 comet defect (left) and -1/2 triangle defect (right) in CAFs' nematic ordering on the bright field (top) and CAF orientation colormap (down). Colored circle: orientation colormap. Scale bar: 100 µm.

B) Quantification of comet and triangle defects density in the CAFs' nematic ordering. Each dot represents one field of view (N=3 independent experiments, n=7 fields of view). Boxplot: middle bar= median, edges bars= 25th and 757th percentiles, whiskers= extent of data.

C) Quantification of defects' size in CAFs nematic ordering. Blue arrows on comet and triangle schemes represent where the size of each type of defect is measured. Each dot represents one defect (N=3 independent experiment, comet n=38, triangle n=32). Boxplot: middle bar= median, edges bars= 25th and 757th percentiles, whiskers= extent of data, red cross= outliers.

Cell density and fibronectin depositions are lower at defects compared to the aligned area

As discussed in chapter III, another feature to describe the nematic ordering is the potential heterogeneous repartition of cell density inside the system. Indeed, nematic ordering can impact cell density (Kawaguchi, 2017), with defects consisting of different cell numbers compared to aligned regions. Differences in cell density between each type of defect and aligned areas could have different impacts on cancer cell invasion. Places with higher density could be more efficient at acting as a physical barrier preventing invasion. In contrast, areas with lower density could act as weak spots where invasion could be facilitated. To observe if such heterogeneity in cell density exists inside the nematic ordering of CAFs, I stained CAFs (F-actin and DNA) and quantified cell density at each type of defect and aligned areas (Figure 33A and B). For defects, I focused on nuclei present in circular masks centered in the defect core. I used the same circular masks for aligned regions. I found that both +1/2 comet and -1/2 triangle defects contained fewer cells than aligned areas. This is strikingly visible in Figure 33A, with only a few cells at the defect cores. There were about 20 cells at each type of defect and twice as many in aligned regions, approximately 50 cells. Thus, cell density was lower at defects compared to aligned areas.

Because CAFs can produce and remodel the extracellular matrix (ECM), particularly fibronectin, the differences in cell density at defects compared to aligned areas could impact fibronectin deposition. Sparser CAFs could deposit less fibronectin than more densely packed CAFs. This could also affect cancer cell invasion - the more fibronectin deposition in one area, the better physical barrier it could be preventing cancer invasion. In contrast, less fibronectin deposited could be easier for cancer cells to overcome, thus favoring cancer invasion. Thus, I stained samples for fibronectin (Figure 33C) and quantified the amount of fibronectin deposition at defects and aligned regions (Figure 33D). I used the same circular masks as before and compared the amount of fluorescence intensity inside masks. As expected, quantification of fibronectin deposits showed that both +1/2 comet and -1/2 triangle defects contain less fibronectin than aligned areas (Figure 33C, note darker holes at the defect's cores). Thus, fibronectin was less dense at defects compared to aligned areas.

Lower cell and fibronectin density at defects suggested that +1/2 comet and -1/2 triangle defects could be places where the physical barrier of the CAFs layer is reduced. Compared to aligned areas, this weaker barrier at defects could potentially facilitate cancer cell invasion.

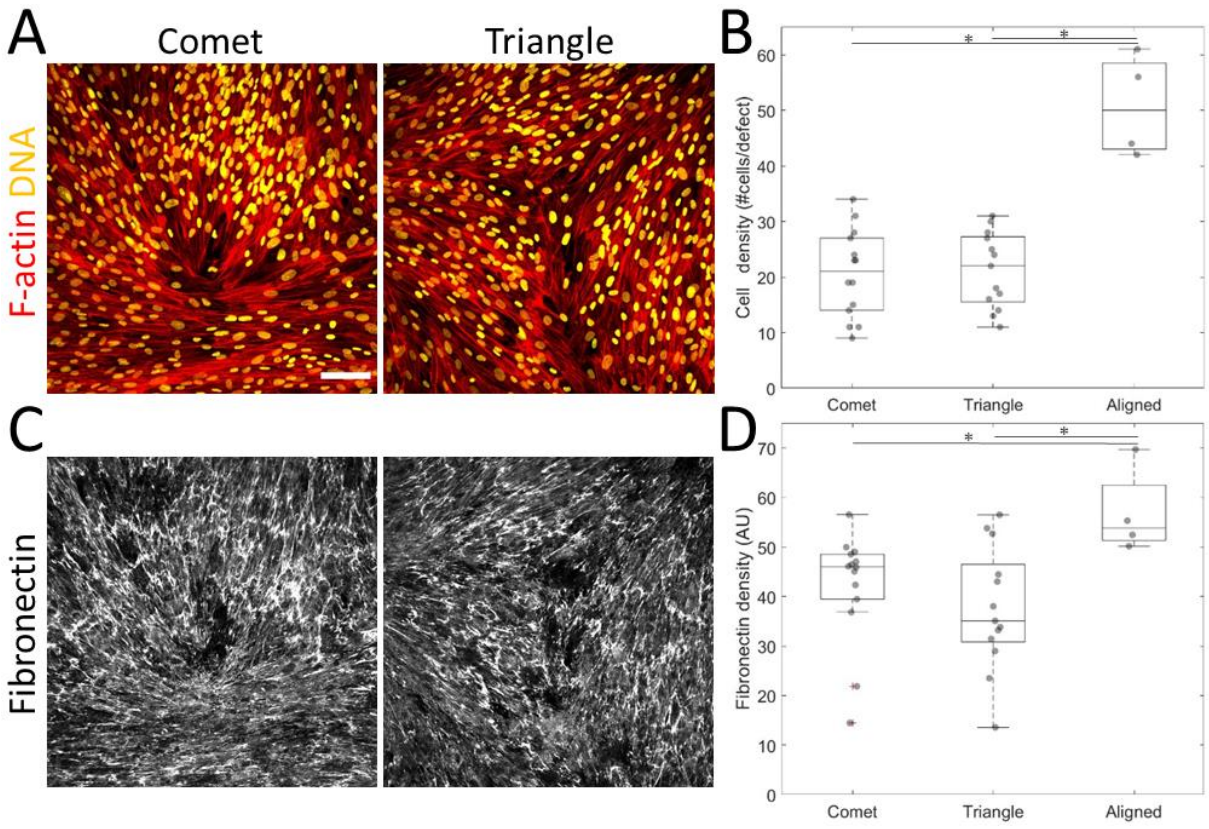

Figure 33. Cell density and fibronectin deposition at defects.
A and C) Representative examples of the comet (left) and triangle (right) defects in CAFs culture stained for F-actin (phalloidin, red), DNA (DAPI, yellow) (A), and fibronectin (C). Scale bar: 100 µm
B and D) Quantification of the cell (B) and fibronectin (D) density at comet and triangle defects and aligned area. Each dot represents one defect (N=3 independent experiments, comet n=14, triangle n=13, aligned area n=4; Oneway Anova: cells density p-value= 2,966 .10^{-7}, fibronectin density p-value= 0.0235). Boxplot: middle bar= median, edges bars= 25th and 757th percentiles, whiskers= extent of data, red cross= outliers.

Defects in the nematic ordering of the CAFs layer don't move

In most cells' nematic ordering, defects move in the layer, particularly comets whose direction depends on whether the active nematic is contractile or extensile. However, as we observed significant fibronectin deposition in our system, we wondered if that affects dynamics of nematics dynamics. our data showed that fibronectin deposition differed between defects and aligned regions. We reasoned that this could stabilize nematics and defects. Indeed, fibronectin deposition and assembly need time. In addition, as defects move, former defects' areas should become aligned areas with thus enhanced fibronectin deposition, and former aligned areas should become part of defects with thus reduced fibronectin deposition. Movements of defects should thus homogenize fibronectin deposition in CAFs layers, which contradicts the heterogeneous fibronectin deposition observed. Moreover, cancer invasion is also a slow process (Glentis, 2017); thus, having stationary defects would facilitate invasion. To assess whether defects move in this system, I realized time-lapse imaging of defects in the nematic ordering of the CAFs layer. I then tracked their trajectories and quantified their velocity (Figure 34).

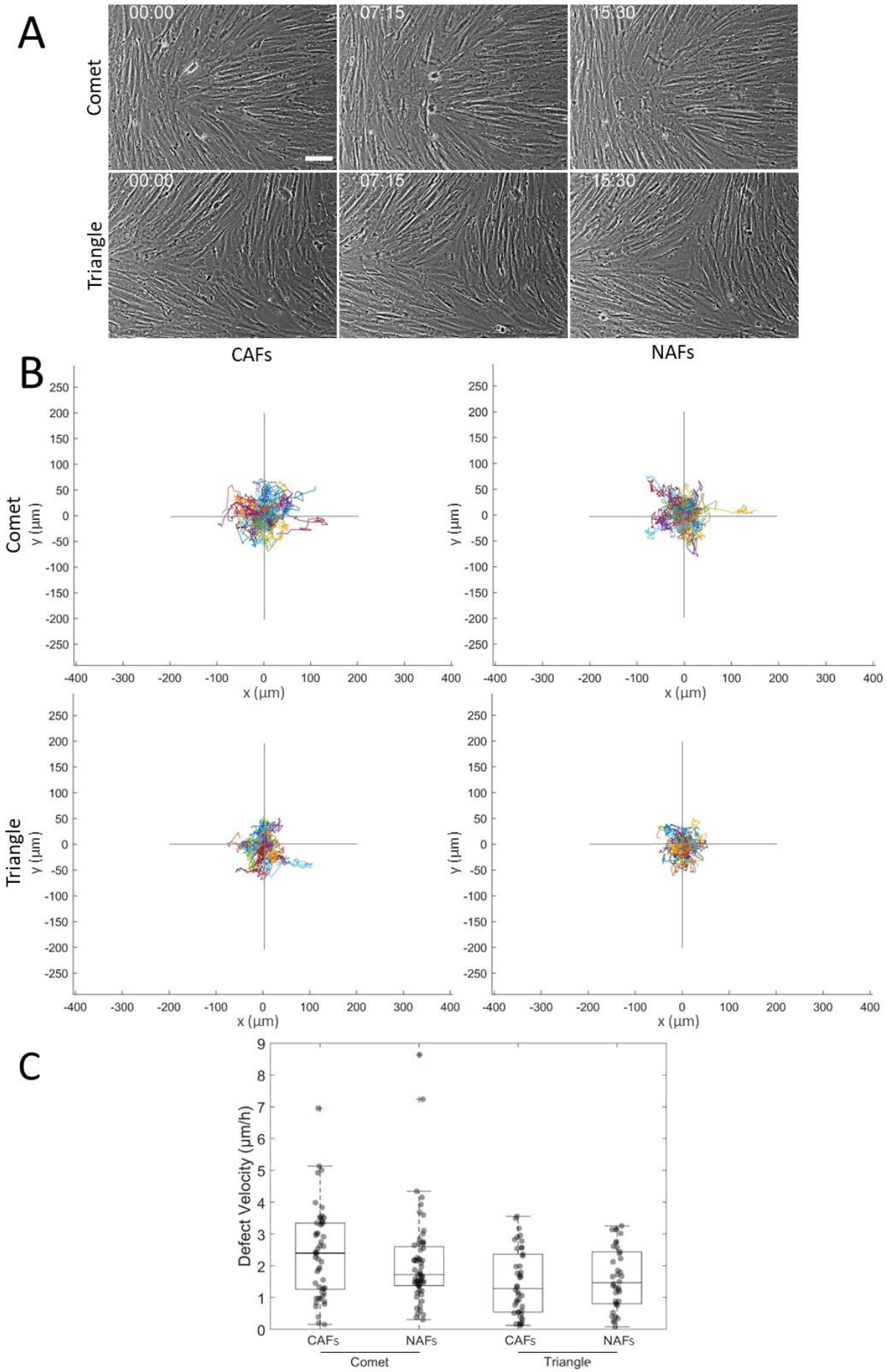
A
Comet
Triangle
00:00
07:15
15:30
CAFs
NAFs
B
Comet
Triangle
y (µm)
x (µm)
C
Defect Velocity (µm/h)
CAFs
NAFs
Comet
Triangle

Figure 34. Defects movement in the nematic ordering.
A) Time-lapse imaging of comet (top) and triangle (down) defect. Scale bar: 100 µm.
B) Defect cores trajectories in the whole field of view of comets (top) and triangles (down) for CAFs (left) and NAFs (right). Horizontal and vertical gray lines on each plot represent defect size (~ 400 µm). Each trajectory represents one defect.
C) Quantification of comet and triangle defect velocity for CAFs and NAFs. Each dot represents one defect (N=4 independent experiments, comet: CAF n=50, NAF n= 60; triangle: CAF n=42, NAF n=38). Boxplot: middle bar= median, edges bars= 25th and 757th percentiles, whiskers= extent of data, red cross= outliers.

Time-lapse images of +1/2 comet and -1/2 triangle defects showed no difference in defect position and shape over 15 h (Figure 34A). Moreover, tracking defects' trajectory showed that defects didn't move; they just slightly jiggled around their position. These movements were small compared to the size of the defect (Figure 34B, note the size of the defects represented by gray lines). Finally, quantification of defect velocity showed that defect speed for both +1/2 comet and -1/2 triangle defects was around 2 µm/h (Figure 34C). Similar results were obtained for NAFs. Such speed was two to five slower than reported in the literature for other cell types: 3,7 µm/h for NPC (Kawaguchi, 2017) and 9,7 µm/h for MDCK (Saw et al., 2017), with NPC defects movements described as slow. Thus, both +1/2 comet and -1/2 triangle defects do not move except for jiggling around their position. This defect stability over time could allow the cancer cell invasion to start at defects.

Most CAFs in the nematic ordering do not move

Defect movement in the nematic ordering can be linked to cell movement inside the CAFs layer. The cell direction would depend on extensile or contractile active nematic. As we observed that defects do not move in this system, we wondered whether CAFs move or are also static. Stationary CAFs would facilitate the fibronectin deposition and in aligned regions, allow CAFs assembly and coordination. We reason that such coordination could either prevent cancer invasion by forming an impenetrable physical barrier or opposite, favor cancer invasion by multiplying CAFs' capacities to remodel the ECM. To assess whether CAFs move in this system, I transfected CAFs and NAFs with LifeAct-GFP and I mixed a small proportion of those labeled CAFs with unlabeled CAFs. Using time-lapse imaging, I then tracked the LifeAct-expressing CAFs to extract their trajectories and calculate their velocity (Figure 35). I found that CAFs almost did not change their position during 16 h (Figure 35A). However, CAFs' velocity quantification revealed that, even if most CAFs had a speed of around 1 µm/h corresponding to no CAFs movement over time, some CAFs were much faster moving with a velocity of about 6 µm/h (Figure 35B). Moreover, by tracking CAFs' trajectories we found that even if most CAFs were just jiggling around their position, some CAFs had straight trajectories and moved in the CAFs layer (Figure 35C). Similar results were obtained for NAFs. Altogether, these data show that both defects and CAFs do not move. We further hypothesize that this could facilitate the coordinated contractility of CAFs.

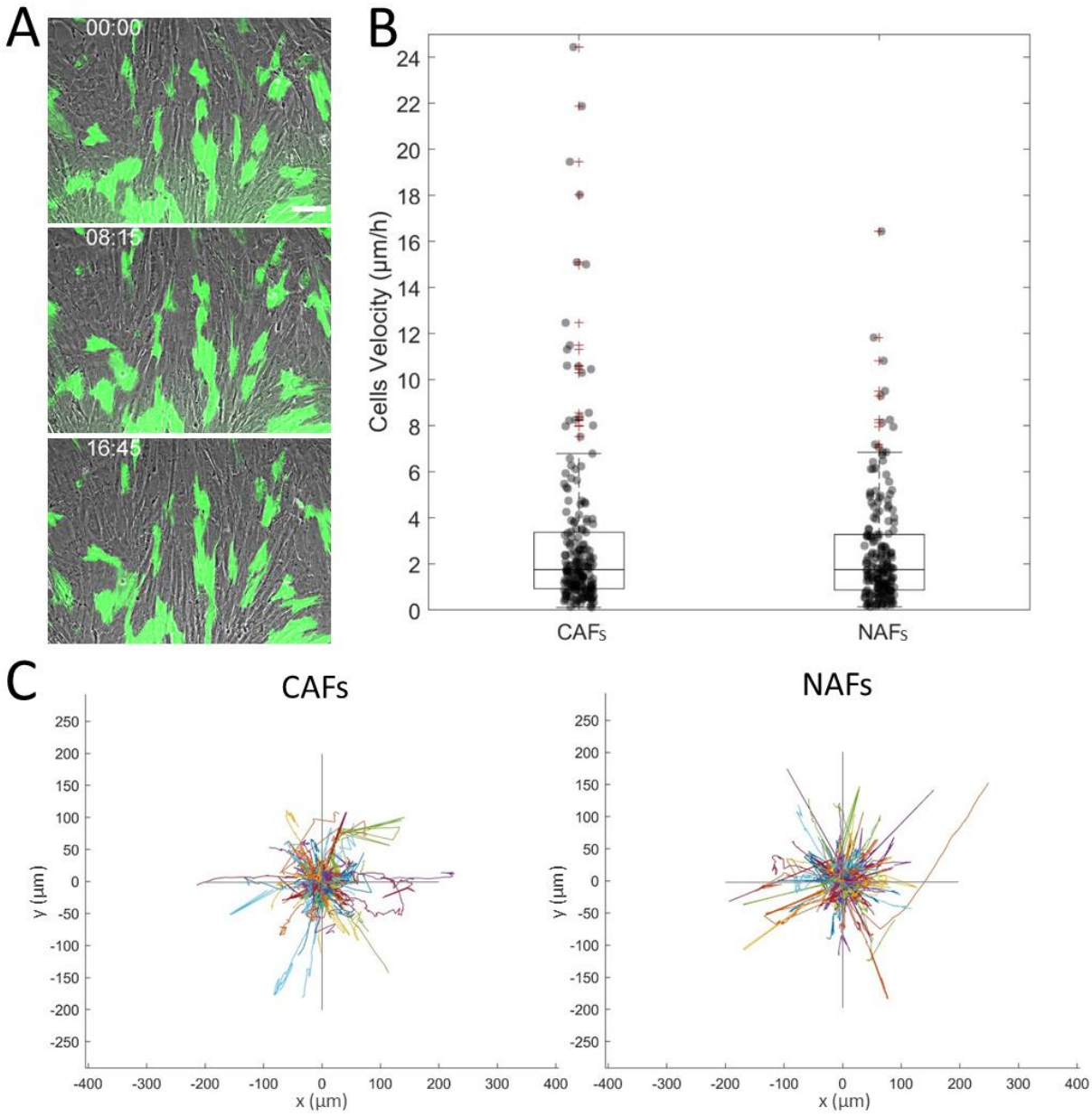

Figure 35. Cells movement in the CAFs layer.

A) Time-lapse imaging of LifeAct-expressing CAFs (green) mixed with unlabeled CAFs. Scale bar: 100 µm.

B) Quantification of cell velocity for CAFs and NAFs. Each dot represents one cell (N=2 independent experiments, CAFs n=200, NAFs n=194). Boxplot: middle bar= median, edges bars= 25th and 757th percentiles, whiskers= extent of data, red cross= outliers.

C) Cells trajectories in the whole field of view for CAFs (left) and NAFs (right). Horizontal and vertical gray lines on each plot represent defect size (~ 400 µm). Each trajectory represents one cell.

CAFs contractility is governed by RhoA/ROCK pathway

One of the major characteristics of CAFs is their contractile ability. There are two contractility pathways in cells: the Ca2+/calmodulin pathway linked with rapid and transient contraction characteristic of muscle cells, and the RhoA/ROCK pathway linked with slow and persistent contraction characteristic of ECM remodeling (Figure 36B).

To test which contractility pathway predominates in CAFs, together with Damien Bradelle, the student that I have supervised, I inhibited those two contractility pathways using specific drugs and performed time-lapse traction force microscopy. We used para-nitro blebbistatin, which inhibits myosin II, and calyculin A, which enhances contraction, affecting both contractility pathways; Y27632, which inhibits ROCK, affecting only the RhoA/ROCK pathway; and forskolin, which inhibits calmodulin, affecting only the Ca2+/calmodulin pathway (Figure 36B). For each drug, we used several concentrations to assess the extent of drug action.

We observed that these drugs affected the force magnitude but not its direction, meaning that only contractility is impaired not CAFs behaviors (Figure 36A). Traction forces almost disappeared after the addition of blebbistatin and Y2763. In contrast, Calyculin A slightly increased traction forces, whereas forskolin slightly decreased traction forces. I then quantified the fraction of the mean traction forces still present after the addition of drugs (Figure 36C): values below 100 % signify a decrease in traction force, whereas values above 100 % signify an increase in traction force upon treatment. We found that blebbistatin decreased traction force, down to only 10% of magnitude left. In contrast, calyculin A increased tractions up to 20 %. The decrease in traction forces magnitude observed at 5 µM was an artifact because CAFs contracted so much under this condition that they tore themselves out of the substrate, and consequently tractions disappeared. The addition of Y27632, even at its lowest concentration, decreased traction forces down to only 10% of magnitude left. In contrast, forskolin, even at its highest concentration, had a minimal effect with 80% of the magnitude of traction forces left. Altogether, these data show that the RhoA/ROCK pathway was predominant in CAFs suggesting that CAFs should be able to remodel the ECM and generate persistent forces that could favor cancer invasion.

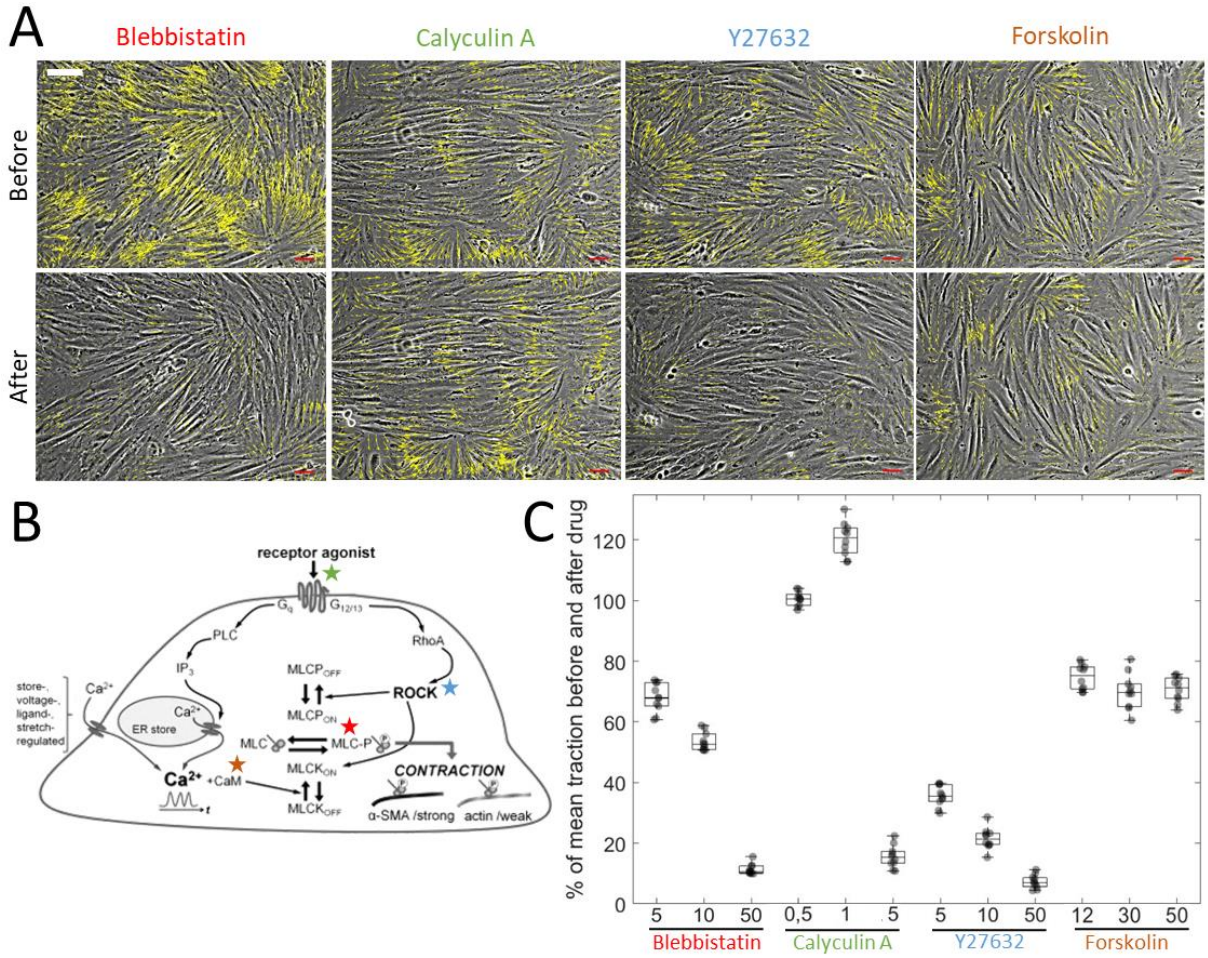

Figure 36. Impact of contractility pathways for force generation by CAFs

A) Traction force in the CAFs layer before (top) and after (down) the addition of drugs: 50 µM para-nitro Blebbistatin, 1 nM Calyculin A, 5 µM Y27632, and 50 µM Forskolin. Yellow vectors represent the direction (direction of the arrow) and the magnitude (size of the arrow) of force. Red scale bar: 400 Pa, white scale bar: 100 µm.

B) Scheme representing the two contractility pathways: Calcium/Calmodulin pathway (left) and RhoA/ROCK pathway (right). Colored stars show respectively where each drug act in the contractility pathways: red for para-nitro Blebbistatin, green for Calyculin A, blue for Y27632, and brown for Forskolin.

C) Quantification of change in the mean traction after the addition of each drug at several concentrations (in nM for Calyculin A, µM for the others), 100% being the mean traction before the addition of drugs. Each dot represents one field of view (for each concentration for each drug N=1 independent experiment, n=10 positions). Boxplot: middle bar= median, edges bars= 25th and 757th percentiles, whiskers= extent of data

Defects in CAFs nematic ordering show higher traction and specific organization

Because contractility is a major ability of CAFs, and we just saw that using the RhoA/ROCk pathway, CAFs should be able to generate persistent forces over time; we wondered how the nematic ordering would impact the distribution of traction forces in the CAFs layer, in particular, at defects. We reasoned that the specific topology of defects could impact force distribution, and consequently impact the CAFs layer capacity to either favor or prevent cancer invasion at defects compared to aligned areas. Defects could generate more forces or shape forces to favor cancer cell invasion at those positions. Moreover, forces transmitted within the CAFs layer, called internal stress, can also be affected by nematic

ordering and defects, generating places, with either enhanced compression or tension. Such changes in stresses could impact cancer cell invasion: for example, places with enhanced tension could more easily tear the CAFs layer, thus generating a hole in the capsule and allowing cancer cells to escape.

To assess how defects impact traction forces and internal stresses, I realized time-lapse traction force and internal stress microscopy (Figure 37). I collaborated with Xavier Trepat's lab (IBEC, Barcelona) and Benoît Ladoux's lab (IJM, Paris), who respectively taught me traction force and internal stress microscopy and provided me with scripts to respectively extract traction forces and internal stresses from the raw data. I rotated and cropped all images to align the orientation and core position of each type of defect (Figure 37A). Then I averaged the maps of traction forces, magnitudes, and vectors (Figure 37B) and the internal stresses (Figure 37C) for each type of defect and aligned regions.

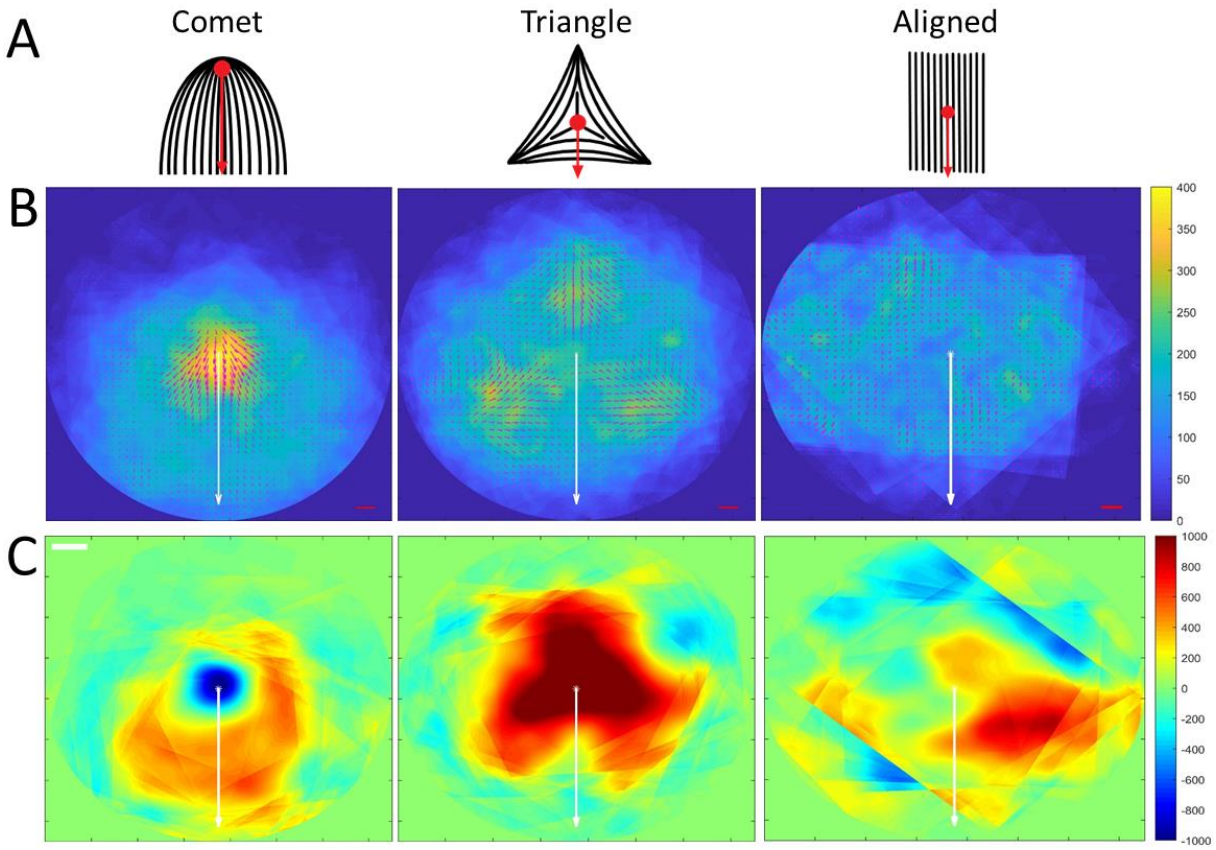

Figure 37. Traction force and internal stress maps in defects and aligned areas.
A) *Schemes representing the core and the direction used to average +1/2 comet defects, -1/2 triangle defects, and aligned areas.*
B and C) Average of traction force magnitude maps and vectors (B) and internal stress maps (A) for +1/2 comet defects (left), -1/2 triangle defects (middle), and aligned areas (right). White stars and vectors correspond to the red dot and vectors of the scheme. Color bars in Pa, red scale bar: 400 Pa, white scale bar: 100 µm. (N = 4 independent experiments, comets n=50, triangles n=42, aligned areas n=18)

I found that for +1/2 comet defects, the peak of traction forces was at the head of the comet core with forces directions pointing toward the comet tail (Figure 37B). The comet head was compressed,

whereas the tail was under tension (Figure 37C). Such a pattern correlates with cell extrusion at the compressed comet heads (Saw et al., 2017). If the same occurs here, extruded CAFs could then align perpendicularly to the tumor and thus induce a switch from TACS-2 to TACS-3, creating highways in the stroma to facilitate the dissemination of cancer cells.

For -1/2 triangle defects, I found that the peaks of traction forces were at each triangle vertex with forces pointing towards the triangle core (Figure 37B). The center of the triangle was under tension (Figure 37C). Such a pattern could pinch the extracellular matrix (e.g. basement membrane) and cancer cells localized below the CAFs' layer. In that scenario, cancer cells in the pinched area (the triangle core) could push and tear the CAFs layer, creating a hole, which would allow them to escape the capsule and disseminate.

In the aligned areas, traction forces were low compared to defects and aligned with CAFs orientation but with no preferred direction. Internal stresses didn't have any pattern. Thus, compared to aligned areas, both types of defects in the nematic ordering showed higher traction forces and internal stresses as well as specific forces and stresses organization depending on the type of defects. These distinct force and stress patterns could potentially enhance cancer cell invasion at defects.

Defects core are under more stress and can be reshaped by laser ablation

We saw that the specific forces patterns at defects could favor cancer cell invasion. Such an invasion would generate holes at defects to allow the passage of cancer cells. This hole generation could happen before the invasion with tearing of the CAFs layer due to enhanced tension, like in -1/2 triangle defects. It could also happen as CAFs get extruded at +1/2 comet defects due to enhanced compression. The size of tearing at defects could thus be bigger at defects than elsewhere. It could also disturb their specific forces patterns, like the position of the force peaks, potentially leading to more invasion. We thus wondered how tearing in defects could impact recoils and the force organization at defects.

To further assess if stress differences could impact the tearing at defects and how this tearing could impact the traction force pattern of each type of defect, Clément Hallopeau and I combined laser ablation and traction force microscopy. We ablated cells at different positions in +1/2 comet defects and -1/2 triangle defects and measured traction forces before and after the ablations. To quantify recoil, we generated kymographs on lines perpendicular to the ablation. For +1/2 comet defect, we ablated cells either in the comet tail behind the peak of traction forces (Figure 38A) or at the comet head where tractions are highest (Figure 39A).

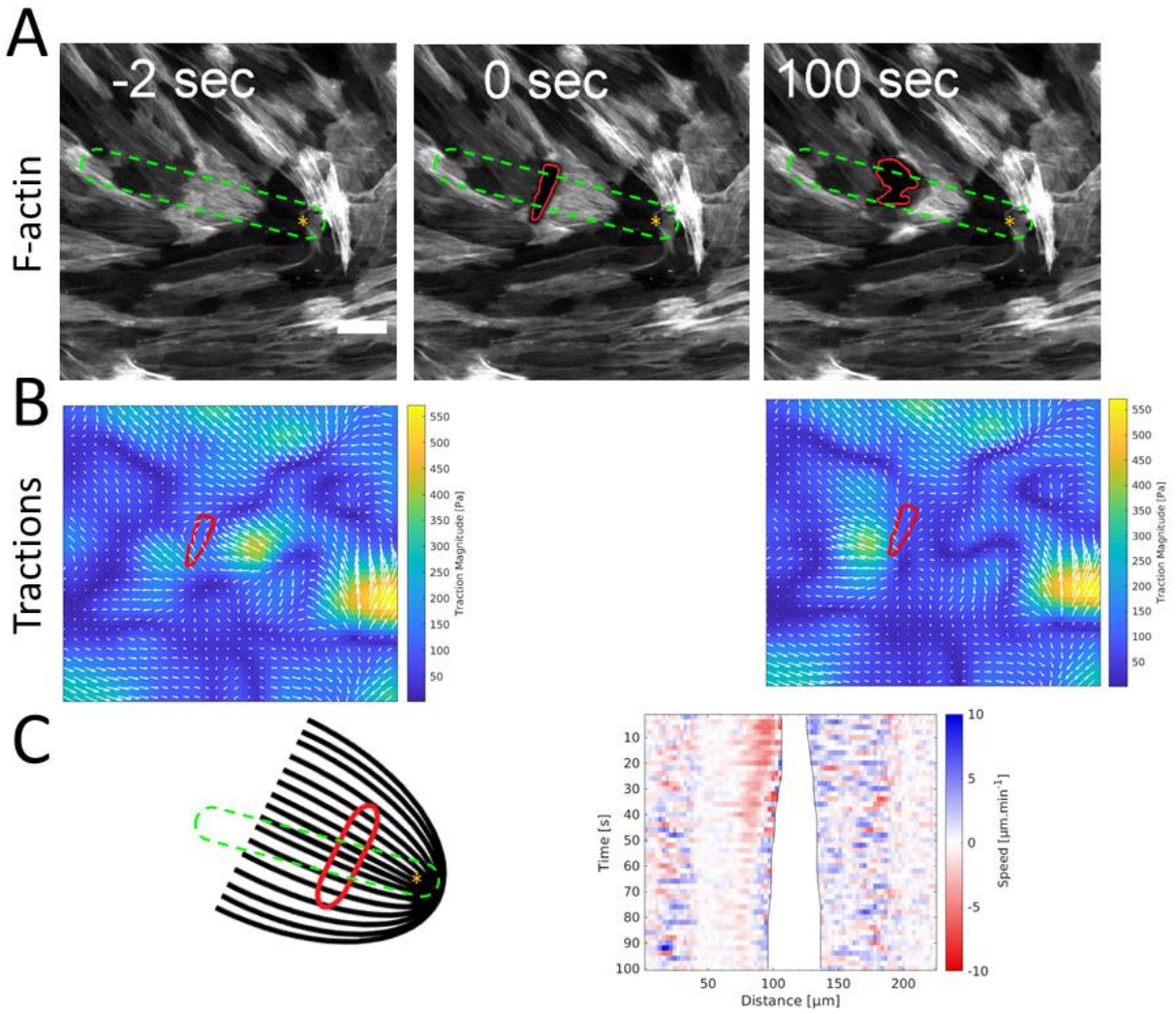

Figure 38. Laser ablation coupled with traction force microscopy at +1/2 comet defect: line ablation in the tail of the comet.
A) Time lapse of laser ablation with ablation occurring at time 0. White lines show the border of the ablated area; green dashed lines represent the area where kymographs were plotted, and yellow stars represent the starting point in the kymographs. Scale bar: 50 µm.
B) Magnitude and vector maps of traction force before (left) and after (right) laser ablation. Red lines represent the position and shape of the ablation done. Color bars in Pa.
C) Scheme representing the orientation of the +1/2 comet defect in the experiment. The Red line shows the shape and area where ablation is done in the experiment; the green dashed line represents the area where kymographs are plotted, and the yellow star represents the starting point in the kymographs (left). Kymograph of the recoil of the ablated area with the speed of recoil. Color bars in µm/min, speed sign corresponds to the speed direction, positive value signifies speed along the kymograph direction, negative value signifies speed in the opposite direction.

In both cases, the ablations of cells modified the peaks of traction forces. For ablation at the comet tail, the traction peak switched from the comet head to just behind the ablated area as if it was the new head of the comet (Figure 38B). For ablation at the comet head, the peak of traction didn't move but split into two peaks at each side of the ablated area as if the ablation cut the comet into two comets (Figure 39B). We also observed that recoil was bigger at the comet head than at the comet tail; about 40 µm upon ablation in the comet tail (Figure 38C) and about 65 µm upon ablation at the comet head (Figure 39C). Because compression is highest at comet heads, we expected less recoil than at the

comet tail that is under tension. The reason for this unexpected result could be the difference in cell density. As cell density at comet heads is lower than at tails, ablation at the comet head affected a higher number of cells, which could explain bigger recoil. The alternative explanation could be that ablation did not hit the head but just behind it, where tension was rising. I need to perform more experiments to conclude.

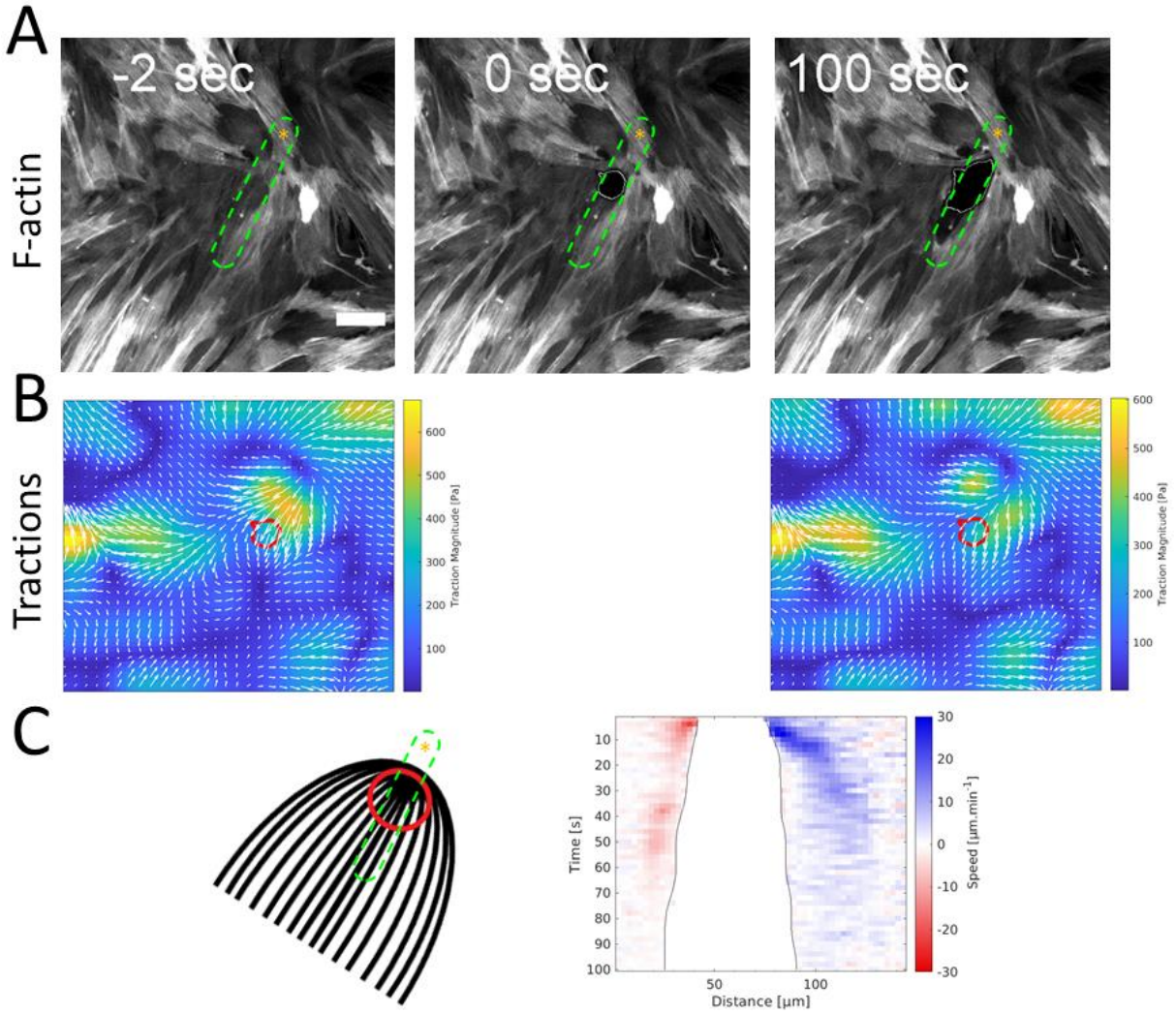

Figure 39. Laser ablation coupled with traction force microscopy at +1/2 comet defect: circle ablation in the head of the comet.

A) Time lapse of laser ablation with ablation occurring at time 0. White lines show the border of the ablated area; green dashed lines represent the area where kymographs were plotted, and yellow stars represent the starting point in the kymographs. Scale bar: 50 µm.

B) Magnitude and vector maps of traction force before (left) and after (right) laser ablation. Red lines represent the position and shape of the ablation done. Color bars in Pa.

C) Scheme representing the orientation of the +1/2 comet defect in the experiment. The Red line shows the shape and area where ablation is done in the experiment; the green dashed line represents the area where kymographs are plotted, and the yellow star represents the starting point in the kymographs (left). Kymograph of the recoil of the ablated area with the speed of recoil. Color bars in µm/min, speed sign corresponds to the speed direction, positive value signifies speed along the kymograph direction, negative value signifies speed in the opposite direction.

For -1/2 triangle defects, we ablated cells either in the core of the triangle (Figure 40A) or at one of the vertexes (Figure 41A). We found that the ablation of cells at the triangle core didn't change the position of the peaks or their magnitude (Figure 40B). However, the ablation of cells at one of the vertexes, caused the switch of the traction peak from the vertex to behind the ablated area as if a new vertex formed there (Figure 41B). We also observed that the recoil was bigger at the triangle core than at the vertex: about 80 µm at the core (Figure 40C) and 50 µm at the vertex (Figure 41C). Because the triangle core is under enhanced tension, we expected bigger recoil than at the vertex. However, fewer cells at the core could also explain this bigger recoil.

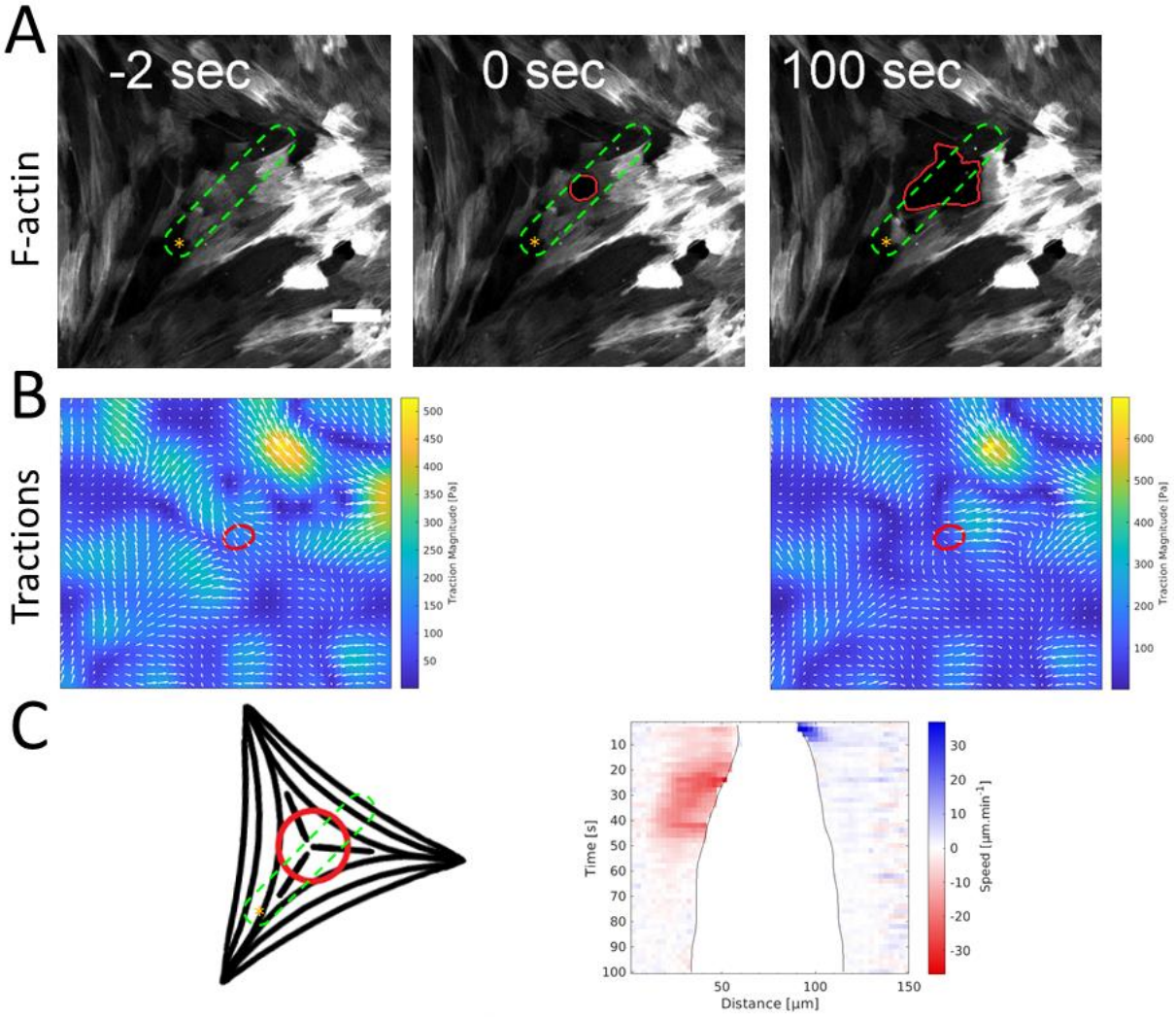

Figure 40. Laser ablation coupled with traction force microscopy at -1/2 triangle defect: Circle ablation in the center of the triangle.

A) Time lapse of laser ablation with ablation occurring at time 0. White lines show the border of the ablated area; green dashed lines represent the area where kymographs were plotted, and yellow stars represent the starting point in the kymographs. Scale bar: 50 µm.

B) Magnitude and vector maps of traction force before (left) and after (right) laser ablation. Red lines represent the position and shape of the ablation done. Color bars in Pa.

C) Scheme representing the orientation of the -1/2 triangle defect in the experiment. The red line shows the shape and area where ablation is done in the experiment; the green dashed line represents the area where kymographs are plotted, and the yellow star represents the starting point in the kymographs (left). Kymograph of the recoil of the ablated area with the speed

of recoil. Colors bar in µm/min, speed sign corresponds to the speed direction, positive value signifies speed along the kymograph direction, negative value signifies speed in the opposite direction.

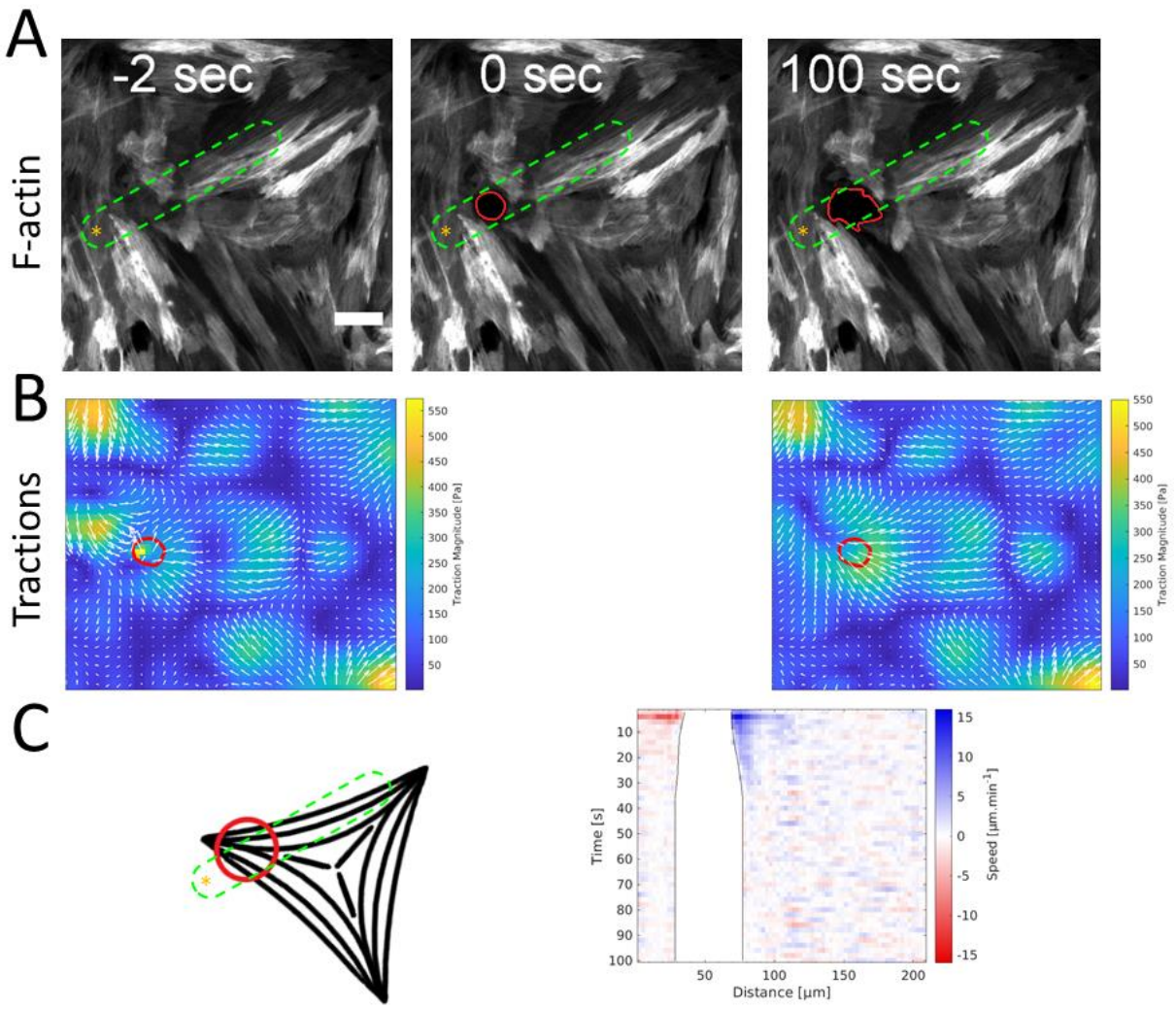

Figure 41. Laser ablation coupled with traction force microscopy at -1/2 triangle defect: circle ablation at one of the vertices of the triangle.

A) Time lapse of laser ablation with ablation occurring at time 0. White lines show the border of the ablated area; green dashed lines represent the area where kymographs were plotted, and yellow stars represent the starting point in the kymographs. Scale bar: 50 µm.

B) Magnitude and vector maps of traction force before (left) and after (right) laser ablation. Red lines represent the position and shape of the ablation done. Color bars in Pa.

C) Scheme representing the orientation of the -1/2 triangle defect in the experiment. The red line shows the shape and area where ablation is done in the experiment; the green dashed line represents the area where kymographs are plotted, and the yellow star represents the starting point in the kymographs (left). Kymograph of the recoil of the ablated area with the speed of recoil. Colors bar in µm/min, speed sign corresponds to the speed direction, positive value signifies speed along the kymograph direction, negative value signifies speed in the opposite direction.

Altogether, these data show that bigger recoil occurs in the areas of lowest cell density and not areas of highest tension. Moreover, in both +1/2 comet and -1/2 triangle defects, cell ablations around the forces' peak caused the disappearance of that peak and the appearance of a new peak behind the ablated area, preserving the force pattern of each type of defect. This could be explained by the

assembly of CAFs into supracellular units that coordinate CAFs' contractility and build up substantial traction forces at precise locations in defects. If such supracellular units are disconnected (e.g. cut by laser), the new pick of tractions is expected to appear at the end of the aligned area. Such reasoning implies that forces are transmitted directly through the cells in the aligned areas, and not on the substrate.

CAFs form supracellular units via long actin fibers and fibronectin stitch adhesions

The previous results provided several cues that CAFs could assemble into supracellular units. First, most CAFs didn't move, which would facilitate coupling together. Then, ablations of cells at defects generated a disappearance of the force peaks and their reappearance behind the ablated areas. Such reappearance at the end of the aligned areas suggested forces building up and transmission from aligned regions to defects. We thus reasoned that the low tractions forces observed in the aligned regions could imply transmission of forces through the CAFs and not the substrate.

Moreover, we speculated that the formation of CAFs' supracellular units in aligned regions could impact cancer cell invasion. We reasoned that to generate supracellular structures, CAFs should be strongly connected. This would make a better barrier for cancer cells. In contrast, CAFs misalignment at defects won't allow them to form supracellular units, and this weaker attachment would represent a weaker barrier for cancer cells.

The supracellular units are expected to transmit forces from one side of CAFs to the other side, and there from one CAF to the next one. Thus, the formation of supracellular units relies on at least two mechanical components: one operating inside cells and one between the cells. F-actin stress fibers are good candidates to transmit forces between the edges of cells. They transmit forces to the substrate via focal adhesions and give elongated shape to CAFs. N-cadherin could be a good candidate for connections between cells as it is the main cell-cell junction protein in fibroblasts (Labernadie et al., 2017). Alternatively, CAFs could be connected with stitch adhesions using fibronectin as a glue (Barbazan et al., 2021; Pankov et al., 2019). Finally, low traction forces in aligned areas suggest that forces are transmitted only through cells and not via the substrate, based on which we expect an absence of focal adhesions in aligned areas.

To assess if CAFs are connected in supracellular units I examine the presence of stress fibers, cell-cell adhesions, and focal adhesions in the nematically ordered CAFs. I stained F-actin and focal adhesion protein vinculin (Figure 42), N-cadherin (Figure 43), and fibronectin (Figures 43 and 44). In aligned regions, F-actin formed long fibers spanning several CAFs with almost no demarcation between

individual cells (Figures 42-44). These long F-actin fibers made the aligned regions look like solid united blocks, which was consistent with the presence of supracellular units. Such long F-actin fibers through CAFs could allow force transmissions from one side of aligned regions to the other.

Focal adhesions marked with vinculin were enriched in misaligned CAFs and smaller in aligned CAFs (Figure 42). The absence of focal adhesions between aligned CAFs could explain the low traction forces observed in aligned areas. With fewer cell-substrate adhesions, force transmission to the substrate is reduced, and forces are transmitted directly through the CAFs via F-actin fibers linking them into supra cellular units.

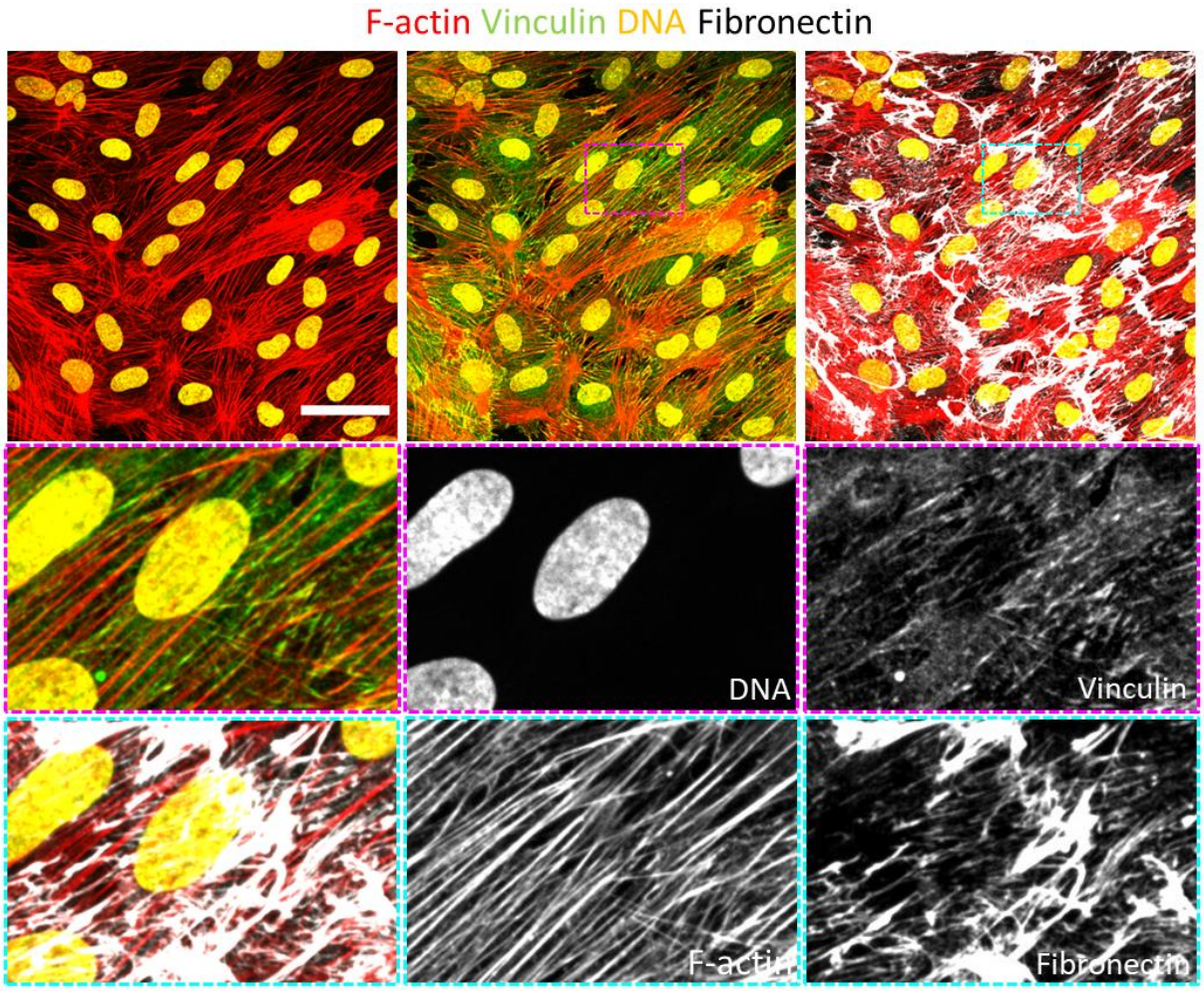

Figure 42. Observation of cell-substrate focal adhesion presence between aligned CAFs.
Immunostaining of F-actin (phalloidin, red), vinculin (green), DNA (DAPI, yellow), and fibronectin (gray), colored dashed box shows the close-up part (top). Close up on aligned CAFs with merged and separated channels of each staining. Scale bar: 50 µm.

Next, I examined cell-cell junctions between CAFs. First, I examined the localization of N-cadherin in CAFs plated at different confluences (Figure 43). N-cadherin was present at cell-cell junctions in low confluence and misaligned CAFs (Figure 43, panels on the left). However, as confluence and CAFs

alignment increased, N-cadherin disappeared from cell-cell junctions (Figure 43, panels on the right). Thus, CAFs used N-cadherin junctions in less confluent and misaligned areas but such junctions vanished for more confluent and aligned CAFs areas, suggesting that supracellular units do not rely on N-cadherin junctions.

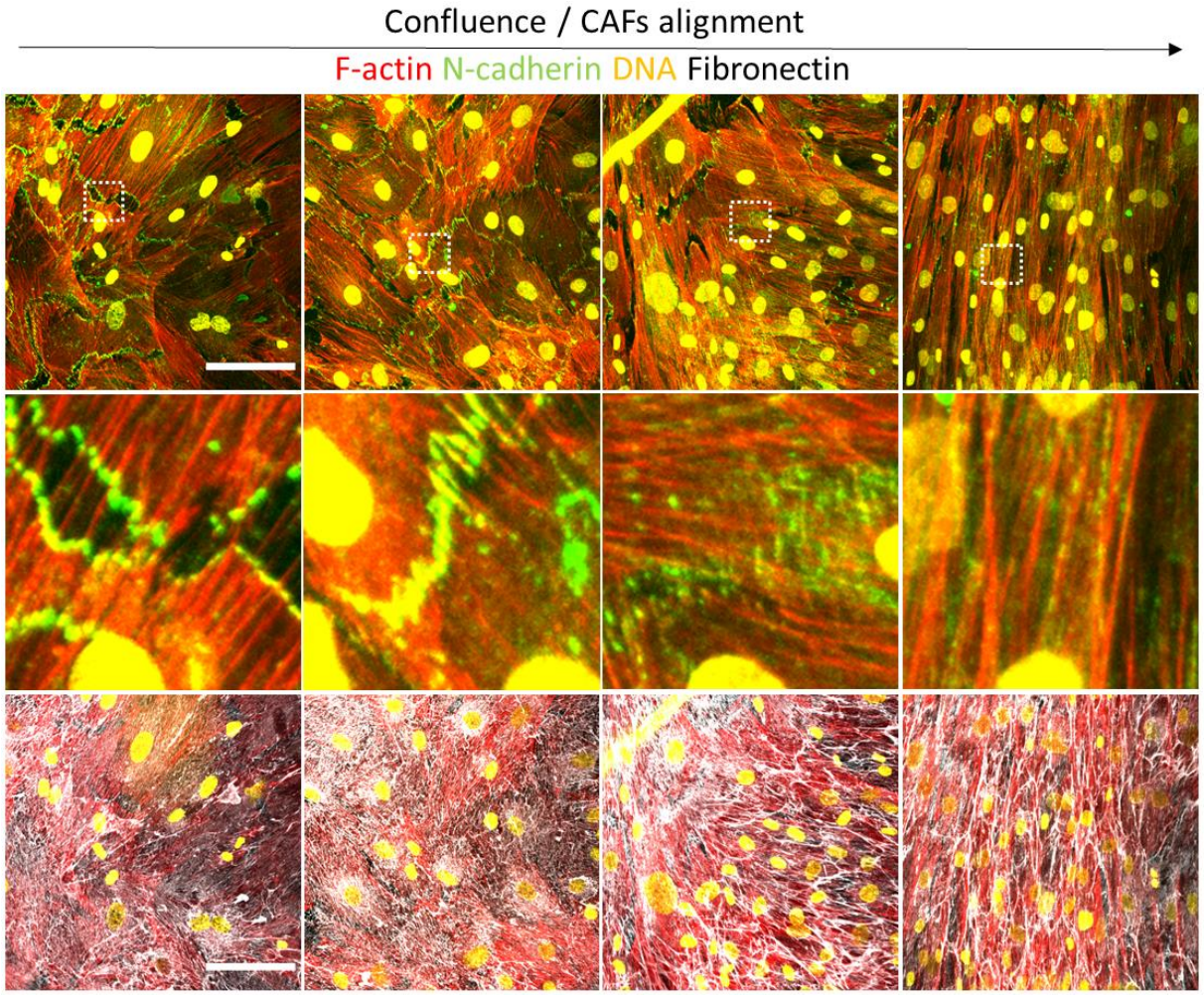

Figure 43. N-cadherin localization in CAFs as confluence and alignment increase.
N-cadherin localization in CAFs as confluence and CAFs alignment increase from left to right.
Top) Immunostainings of F-actin (phalloidin, red), N-cadherin (green), DNA (DAPI, yellow). The boxed regions are magnified below. Scale bar: 100 µm.
Middle) Higher magnification of CAF-CAF junction showing the disappearance of N-cadherin with confluence.
Bottom) Immunostainings of F-actin (red), fibronectin (gray), and DNA (yellow). Scale bar: 100 µm.

Next, I examined if CAFs could be connected indirectly via the ECM, particularly by fibronectin. CAFs deposited fibronectin mostly at focal adhesions (Figure 42) as reported in other studies (Fourriere et al., 2019). However, contrary to N-cadherin, fibronectin levels increased further at cell-cell junctions with the increase in confluence and CAFs alignment (Figure 43). Fibronectin was enriched between CAFs, likely forming stitch adhesions that connect individual cells (Figure 44). In highly aligned areas, fibronectin was also present below cells following the orientation of stress fibers (Figure 44).

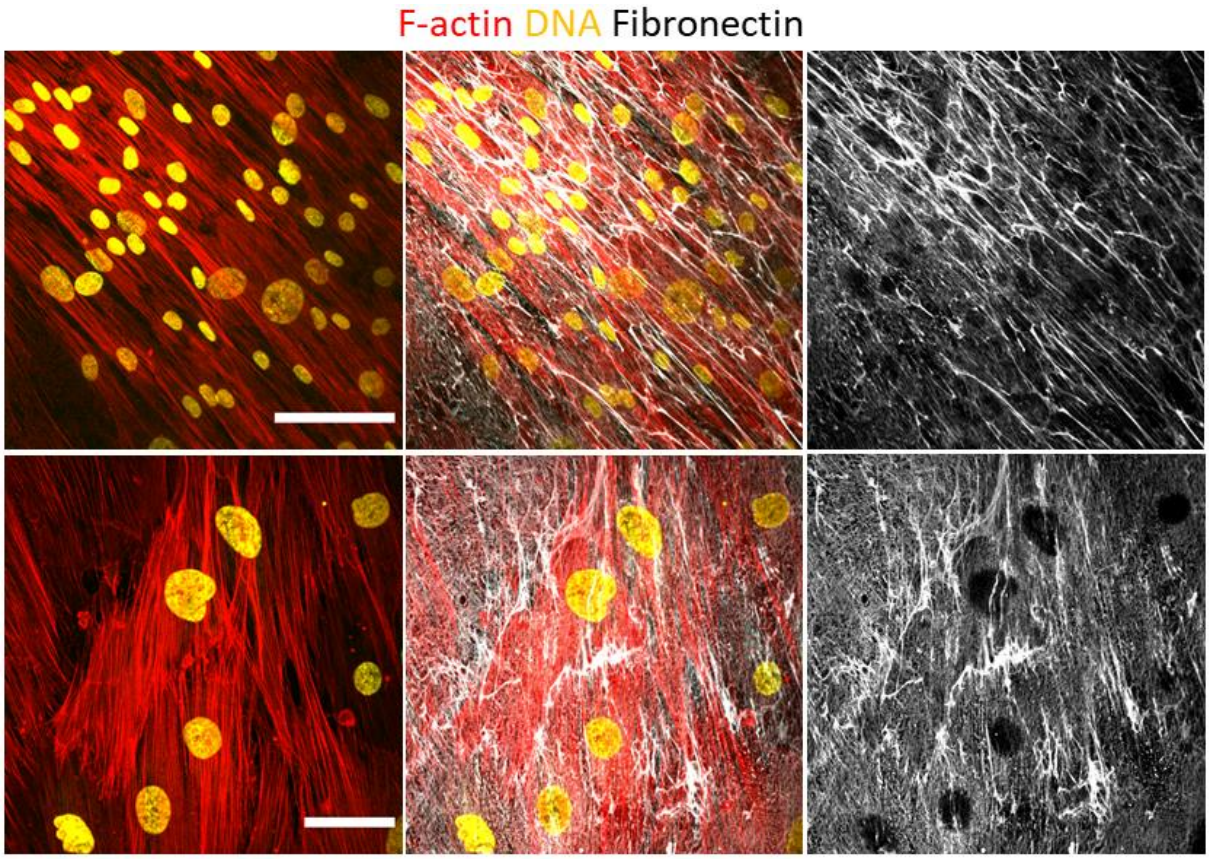

Figure 44. Fibronectin stitch adhesions between CAFs.
Staining of F-actin (phalloidin, red), DNA (DAPI, yellow), and fibronectin (gray) showing fibronectin at CAF-CAF junctions. Top scale bar: 100 µm, bottom scale bar: 50 µm.

These data suggest that CAFs formed supracellular units in aligned regions using fibronectin stitch adhesions and long F-actin stress fibers. It is possible that these supracellular units coordinated forces to transmit them to +1/2 comet defect cores or -1/2 triangle defect vertexes, resulting in force peaks at defects and low forces in aligned regions. Further, aligned CAFs and accumulated fibronectin in aligned areas may form compact and solid blocks, thus a strong barrier hard for cancer cells to get through.

Fibronectin deposition follows CAFs' orientation

Because the nematically ordered CAFs' layer was stable over time with defects and most of the CAFs not moving, we wondered if deposited fibronectin fibers follow the local CAFs alignment, reproducing the nematic ordering of CAFs.

To test whether deposited fibronectin follows the same orientation as CAFs, I stained CAFs and fibronectin on large fields of view made of stitched images. By comparing their respective orientation maps θ, I observed that fibronectin deposition followed CAFs orientation (Figure 45, note that corresponding regions in the two images had the same colors, thus matched orientations). To quantify the correlation between CAFs (looking at F-actin) and fibronectin orientation maps, I transformed orientation maps into matrixes of normalized vectors using the cosinus and sinus of each angle θ. Then, I multiplied these vector matrixes to obtain their absolute values. Values varied from 1, corresponding to parallel vectors, to 0 corresponding to perpendicular vectors. The absolute values matrix mean for each couple of images was around 0,95 (N=4 independent experiments), which confirmed that deposited fibronectin fibers followed CAFs' orientation, reproducing almost exactly the nematic ordering of the CAFs layer.

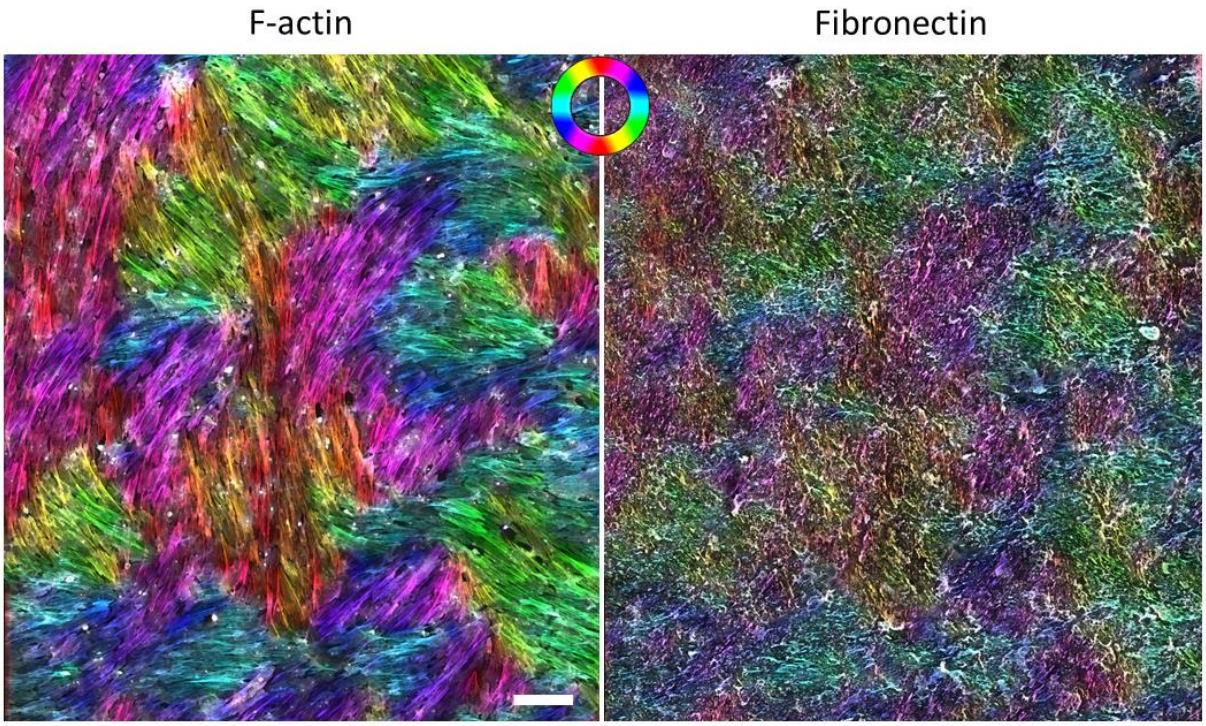

Figure 45. Comparison of the orientation of fibronectin deposition and CAFs nematic ordering orientation.
Staining F-actin (phalloidin, left) and fibronectin (right) with a color map of respectively CAF and fibronectin orientation. Colored circle: orientation color map. Scale bar: 200 µm.

Fibronectin deposition instructs nematic ordering organization and position of defects

We just saw that fibronectin deposition reproduced the nematic ordering of the CAFs layer forming the aligned regions and the defects. As CAFs can sense microtopography features, like fibronectin fibers, and then follow their orientation (Azatov et al., 2017), we wondered if fibronectin can instruct CAFs' organization.

To test whether the fibronectin deposition could instruct the nematic ordering organization, I performed the following experiment (Figure 46A). I first seeded CAFs on 11 kPa PAA gels and let them organize into nematic ordering and deposit fibronectin for three days. I removed the CAFs using NH_4OH and stained and imaged the deposited fibronectin. Then, I seeded new CAFs on top of the fibronectin patterns and let them organize for three days. Finally, I fixed and stained the CAF layer. The comparison of fibronectin patterns and the CAFs (visualized by F-actin) orientation maps θ showed that newly seeded CAFs followed the pre-existing fibronectin pattern (Figure 46B, note that the corresponding regions in the two images were in the same colors). By quantifying the correlation between the fibronectin pattern and the CAFs layer orientation maps, as explained before, I found a correlation of about 0.9 (N=4 independent experiments), confirming that the CAFs followed the fibronectin pattern they were platted on. Thus, fibronectin deposition dictated the organization of CAFs, fixing it into the initial CAFs' nematic ordering. Consequently, defects in nematic ordering were also fixed.

These results showed that fibronectin is more important than just being a glue between CAFs. During the organization of CAFs into nematic ordering, they deposit fibronectin that replicates the same organization. CAFs could then sense the fibronectin nematic ordering and align on it, thus preserving the initial CAFs nematic ordering organization. There could be a positive feedback loop: CAFs organization dictates fibronectin organization. Then fibronectin organization dictates CAFs organization, while CAFs' continuous fibronectin deposition reinforces the fibronectin nematic ordering and the initial CAFs nematic ordering organization. This positive feedback loop between the CAFs and the fibronectin organization could explain defects' stability over time. Indeed, the initial defect positions could be fixed in the CAFs' nematic ordering organization by the fibronectin deposition. The positive feedback loop stabilizes the defect positions by preserving fibronectin and CAFs' initial alignment.

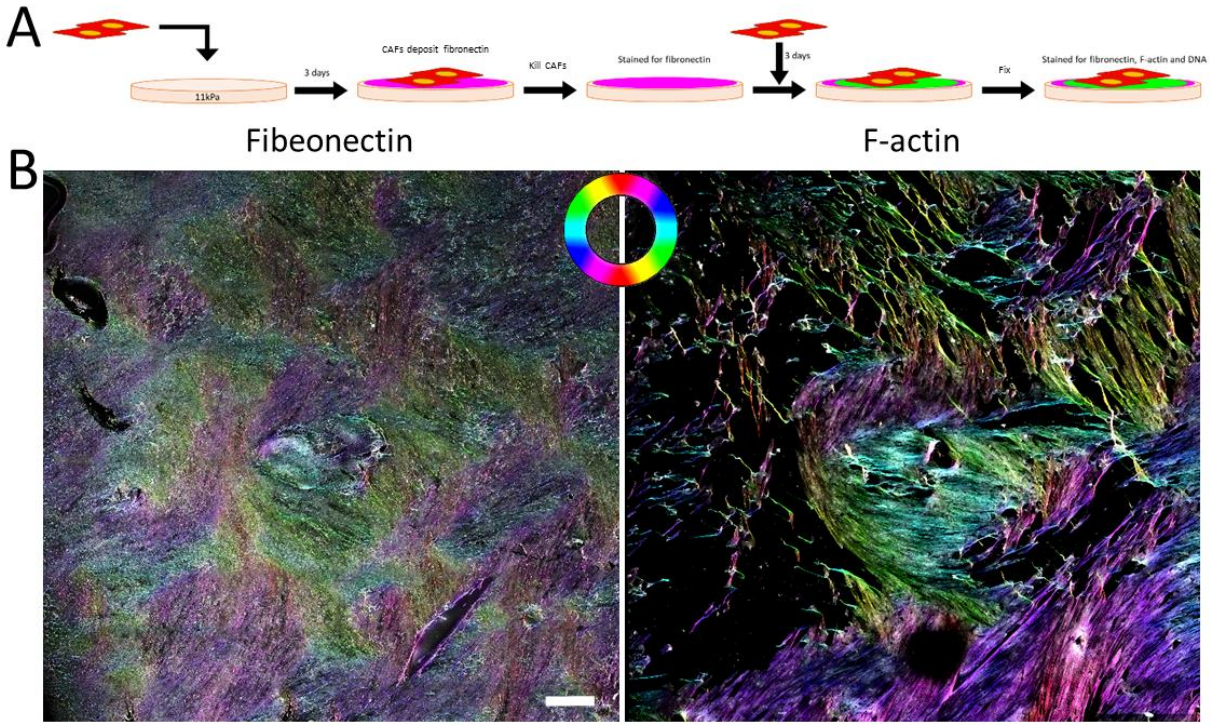

Figure 46. Comparison of the orientation of fibronectin pattern and newly seeded CAFs
A) Scheme representing the experimental design: CAFs were seeded on PAA gel and let to grow and deposit fibronectin for three days. CAFs were removed using NH_4OH, and deposited fibronectin was stained (pink). Then, new CAFs were seeded on the gel with stained fibronectin deposition and let grow for three days before being fixed. CAFs were stained for F-actin and newly deposited fibronectin (green).
B) Immunostaining of fibronectin (left) and F-actin (right) with a color map of respective fibronectin and CAFs orientation. Colored circle: orientation color map. Scale bar: 400 µm.

What is the role of fibronectin in CAFs nematics?

Our data suggest that fibronectin is a glue between CAFs and a stabilizer of nematic ordering and defects. We hypothesized that, in the absence of fibronectin, nematic ordering and associated defects should not be fixed in time and space. Without fibronectin to fix the nematic ordering organization, defects should move in the CAFs layer. In addition, CAFs should not be able to form supracellular units, potentially affecting their capacity to build up and transmit forces. Moreover, without fibronectin to connect CAFs either together or to the substrate, CAFs should be more motile, generating a more fluid system.

To test this hypothesis, we depleted fibronectin in CAFs and NAFs using siRNA. Depletion efficiency was evaluated by western blot (Figure 47A) and fibronectin immunostaining (Figure 47B). As I found that fibronectin depletion in CAFs was efficient, I used those cells to assess the impact of fibronectin on CAFs' nematics.

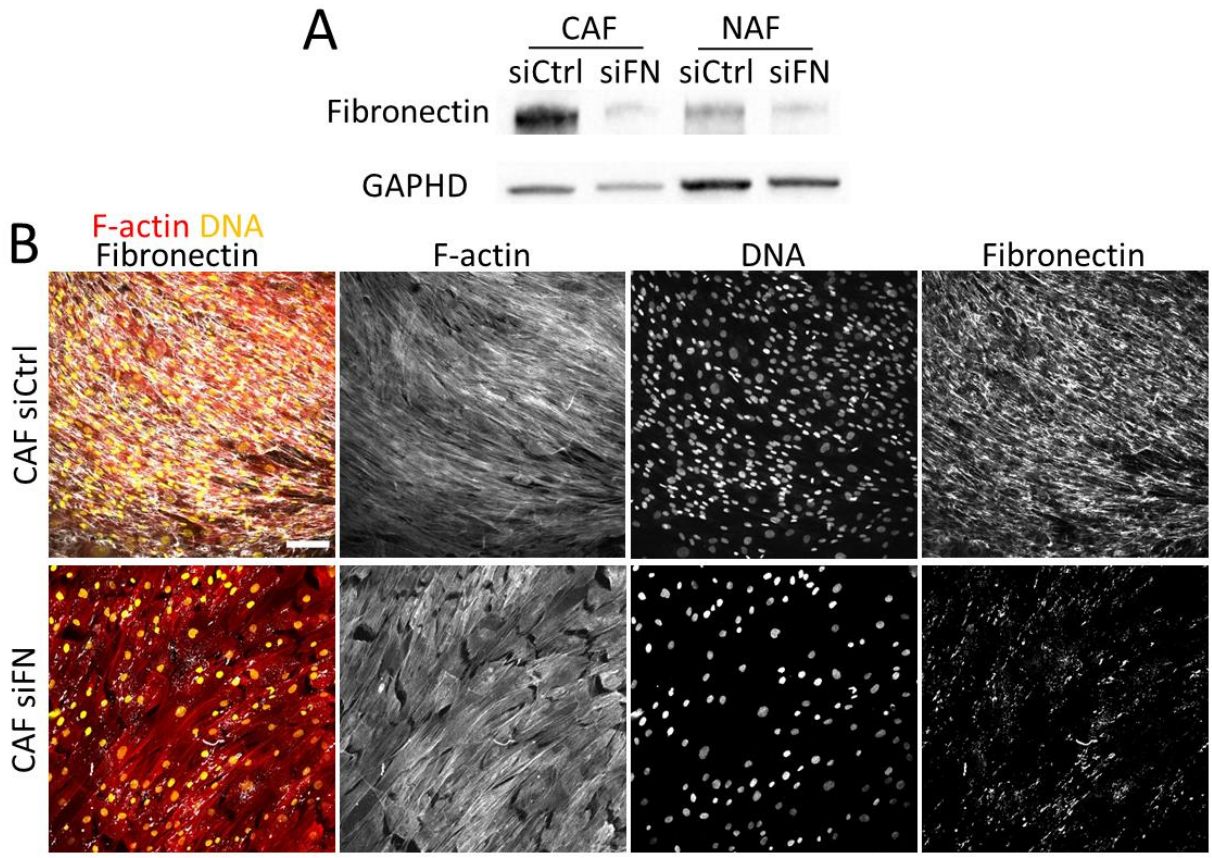

Figure 47. Depletion of fibronectin using siFN.
A) Expression level of fibronectin evaluated by Western blot in CAF and NAF transfected with either control siRNA (siCtrl) or siRNA against fibronectin (siFN). GAPHD was used as a loading control.
B) Control (siCtrl) and fibronectin-depleted CAFs (siFN). F-actin (phalloidin, red), DNA (DAPI, yellow), and fibronectin (gray) with merged and their respective separated channels. Scale bar: 100 µm.

Depletion of fibronectin reduces the traction forces of the CAFs layer

Our lab previously showed that while fibronectin depletion does not affect CAFs' capacity to exert traction forces at the single cells level (Attieh et al., 2017; Barbazan et al., 2021), fibronectin was crucial for the generation of supracellular forces (Barbazan et al., 2021). To test whether fibronectin depletion impacts CAFs' capacity to generate coordinated forces in my model, I performed time-lapse traction force microscopy using control and fibronectin-depleted CAFs. Quantification of the mean traction forces showed that fibronectin-depleted CAFs exhibit significantly lower traction forces compared to control CAFs (Figure 48). Similar results were obtained for fibronectin-depleted NAFs.

These results suggest that CAFs lose the ability to coordinate forces in the absence of fibronectin. By exerting lower tractions forces on the substrate, CAFs' capacity to remodel the ECM and basement membrane, in particular, might be diminished.

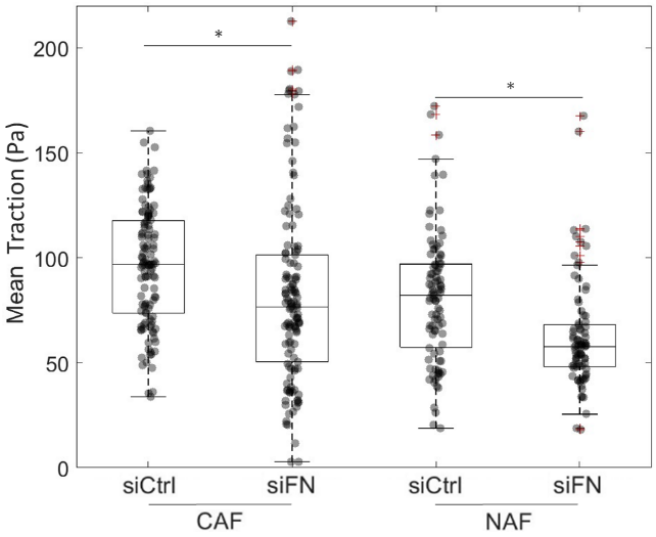

Figure 48. The impact of fibronectin depletion on the CAF layer means traction force.
Quantification of mean traction force for CAFs and NAFs transfected with either siCtrl or siFN. Each dot represents one field of view (N=8 independent experiment, CAF: siCtrl n=120, siFN n=130; NAF: siCtrl n=96, siFN n=85; CAF t-test p-value=0.0029, NAF t-test p-value=3,29.10^{-5}). Boxplot: middle bar= median, edges bars= 25th and 757th percentiles, whiskers= extent of data, red cross= outliers.

Depletion of fibronectin induces fluidization of the CAFs layer

Next, we tested if fibronectin depletion impacts the CAFs layer fluidity. As the fluidity of a system can be assessed by looking at its mean fluid flow (the higher the mean fluid flow, the more fluid system is), I performed time-lapse imaging of the fibronectin-depleted CAFs and quantified mean fluid flow using particle image velocity (PIV) on the CAFs layer (Figure 49). We found that mean fluid flow was significantly higher for fibronectin-depleted CAFs than for control CAFs. Similar results were obtained for fibronectin-depleted NAFs.

Such a fluid flow increase in the absence of fibronectin could be either caused by the increase in CAFs motility, movements of defects, or both. As they can have different consequences on cancer cell invasion, either favoring or preventing, we next tested them independently.

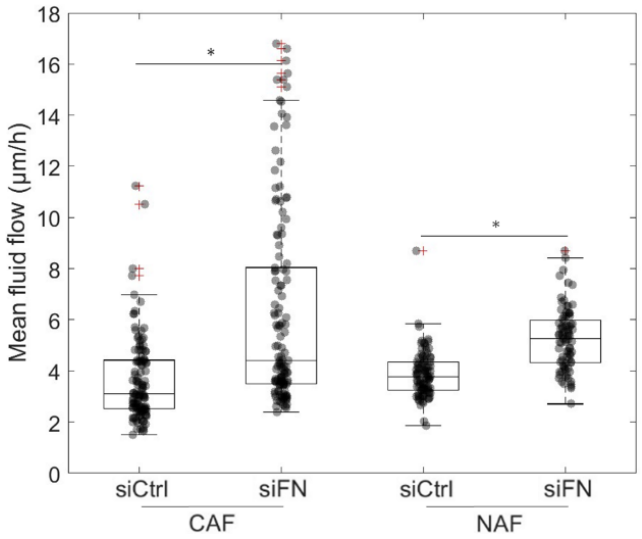

Figure 49. Mean fluid flow in control and fibronectin-depleted CAFs and NAFs.
Quantification of mean fluid flow for control (siCtrl) and fibronectin depleted (siFN) CAFs and NAFs. Each dot represents one field of view (N=8 independent experiments, CAF: siCtrl n=120, siFN n=130; NAF: siCtrl n=96, siFN n=85; CAF t-test p-value=3,45.10^{-11}, NAF t-test p-value=2,19.10^{-15}). Boxplot: middle bar= median, edges bars= 25th and 757th percentiles, whiskers= extent of data, red cross= outliers.

Depletion of fibronectin leads to enhanced CAFs movement in the CAFs layer

To assess the dynamics of CAFs upon fibronectin depletion, I imaged the fibronectin-depleted CAFs using Hoechst to mark CAFs nuclei over 17h and observed their movement (Figure 50A). Then, I tracked CAFs' trajectories and quantified their velocity (Figures 50B and C). In contrast to control CAFs that moved with a mean velocity of about 1 µm/h, the mean velocity for fibronectin-depleted CAFs was about 3 µm/h (Figure 50B). This led to a global increase in CAFs movement upon fibronectin depletion. Finally, by analyzing CAFs' trajectories, I found that most control CAFs just jiggled around their position, whereas most CAFs lacking fibronectin moved from their initial place in straight trajectories (Figure 50C).

Thus, depletion of fibronectin led to enhanced CAFs movement in the nematically ordered CAFs layer. This enhancement of CAFs' movement could be caused by the lack of fibronectin stitch adhesion to connect CAFs, or fibronectin deposition to fix CAFs on the substrate.

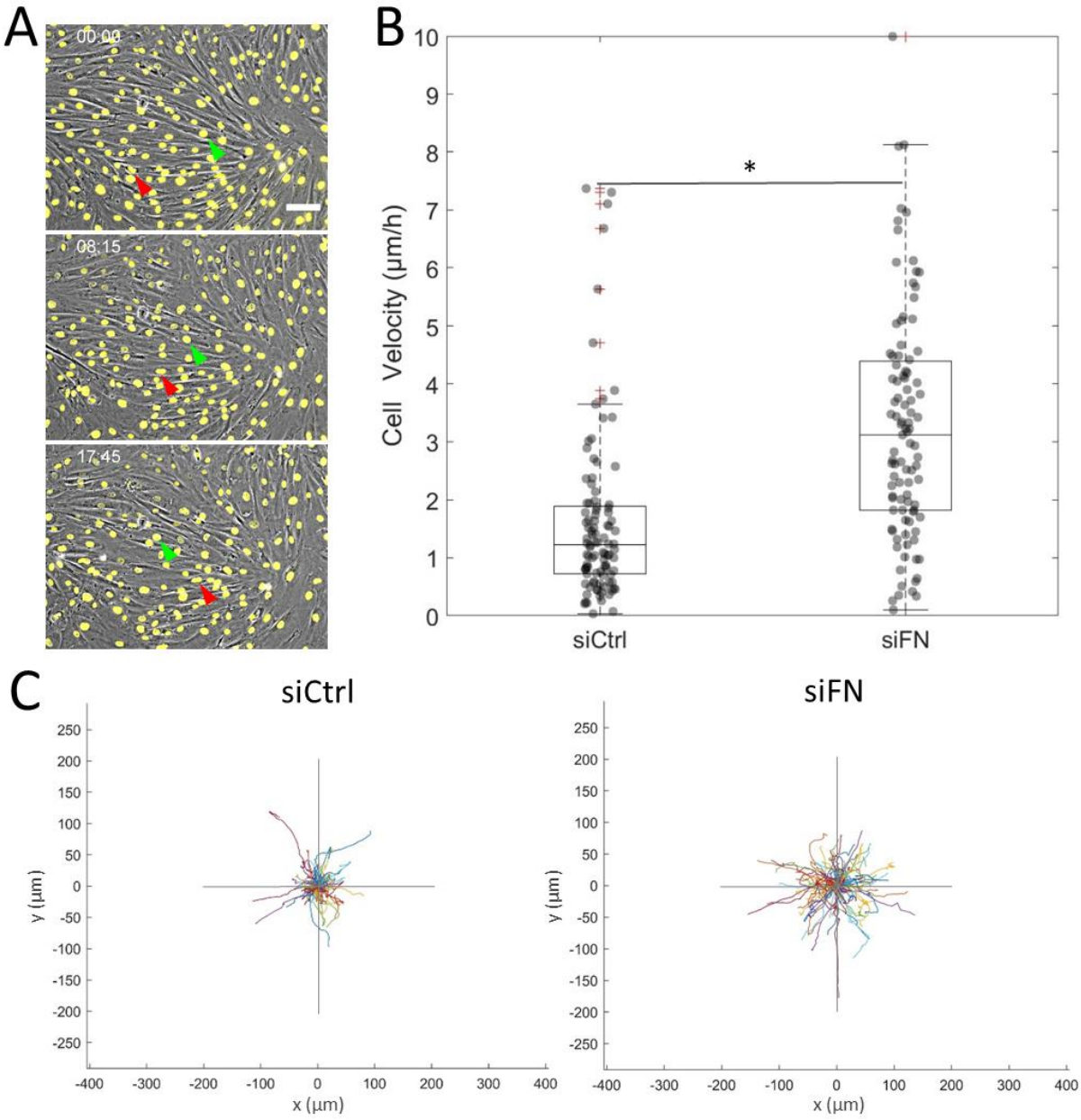

Figure 50. Impact of depleting fibronectin on CAFs movement.

A) Time-lapse imaging of CAFs labeled with Hoechst. The red and green arrows show changes in cell position at different time points. Scale bar: 100 µm.

B) Quantification of CAFs velocity. Each dot represents one field of view (N=2 independent experiments, siCtrl n=100, siFN n=100, t-test p-value=5,297.10^{-10}). Boxplot: middle bar= median, edges bars= 25th and 757th percentiles, whiskers= extent of data, red cross= outliers.

C) Cells trajectories in the whole field of view for CAFs siCtrl (left) and siFN (right). Horizontal and vertical gray lines on each plot represent defect size (~ 400 µm). Each trajectory represents one cell.

Depletion of fibronectin triggers defects' movement

Besides enhancing CAFs' movement, another reason for increased fluid flow in the fibronectin-depleted CAFs layer could be the displacement of defects.

To assess whether fibronectin depletion affects the stability of defects, I imaged defects in the nematic ordering of the fibronectin-depleted CAFs layer, tracked their trajectories, and quantified their velocity (Figure 51). I found that both +1/2 comet and -1/2 triangle defects move in the fibronectin-depleted CAFs layer (Figure 51A). The analysis of the +1/2 comet defect movement from the head to the tail of the comet revealed that fibronectin-depleted CAFs formed a contractile active nematic.

Defect trajectories showed that defects in fibronectin-depleted CAFs layers moved away from their initial positions in a proportion similar to the defect sizes (Figure 51B). +1/2 comet defects were more motile than -1/2 triangle defects. In contrast, defects in siCtrl CAFs were immobile and just jiggled around their position similarly to untransfected CAFs (Figure 34). By quantifying defect velocity, we found that both types of defects in control CAFs had a speed of about 1 µm/h, whereas, in fibronectin-depleted CAFs, +1/2 comet defects moved with a velocity of about 5 µm/h, and -1/2 triangle defects about 3 µm/h (Figure 51C).

These data show that fibronectin depletion unfroze defects in the nematically ordered CAFs layer. This movement of defects could be due to the lack of fibronectin deposition fixing the initial nematic ordering organization.

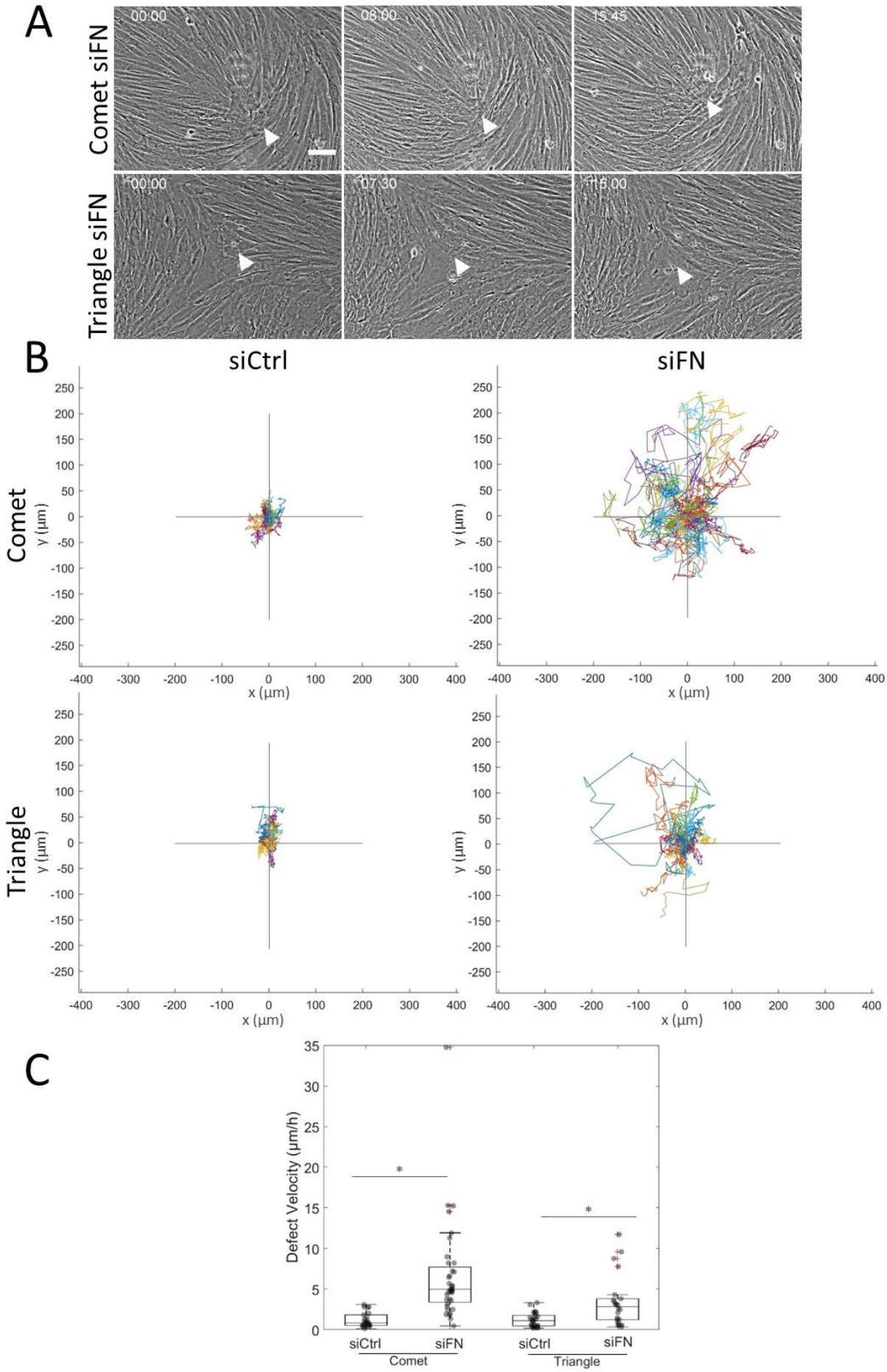
A
Comet siFN
Triangle siFN
00:00
08:00
15:45
00:00
07:30
13:00
B
siCtrl
siFN
Comet
Triangle
y (µm)
x (µm)
C
Defect Velocity (µm/h)
siCtrl
siFN
siCtrl
siFN
Comet
Triangle
*
*

Figure 51. Impact of fibronectin depletion on defects movement.
A) Time-lapse imaging of comet (top) and triangle (down) defect moving in the nematic ordering of fibronectin-depleted (siFN) CAFs. White arrows show a change of defect core position at different time points. Scale bar: 100 µm.
B) Defect cores trajectories in the whole field of view of the comet (top) and triangle (down) for control CAFs (siCtrl, left) and fibronectin-depleted (siFN, right) CAFs. Horizontal and vertical gray lines on each plot represent defect size (~ 400 µm). Each trajectory represents one defect.
C) Quantification of comet and triangle defect velocity for control (siCtrl) and fibronectin (siFN) depleted CAFs. Each dot represents one defect (N=5 independent experiments, comet: siCtrl n=22, siFN n= 36; triangle: siCtrl n=24, siFN n=22, comet t-test p-value= 0.000131, triangle t-test p-value= 0.0019). Boxplot: middle bar= median, edges bars= 25th and 757th percentiles, whiskers= extent of data, red cross= outliers.

Fibronectin patterns restore defects stability in the fibronectin-depleted CAFs layer

Upon fibronectin depletion, defects in the nematic ordering of the CAFs layer started moving. It is possible that such defects' movement was due to the lack of fibronectin deposition on the substrate to fix the initial nematic ordering organization and thus defects positions.

To test whether the lack of fibronectin deposition caused defects' movements, I first prepared fibronectin patterns using control CAFs as described above (Figure 46A). Then, I seeded siFN and siCtrl CAFs on these fibronectin patterns, imaged dynamics of defects over 15h (Figure 52A), tracked their trajectories (Figure 52B), and quantified their velocity (Figure 52C). First, I found that the shape, position, and orientation of +1/2 comet and -1/2 triangle defects matched fibronectin patterns as shown earlier for control CAFs (Figure 53A). Interestingly, both +1/2 comet and -1/2 triangle defects position inside the CAFs layer were stable over time (Figure 52A). Moreover, defects trajectories showed that both siCtrl and siFN defects didn't move and just jiggled around their position (Figure 52B). Finally, quantification of defect velocity showed that defect speed for both types of defect in both siCtrl and siFN was around 1 to 2 µm/h, which was indicative of no movement compared to the literature (Figure 52C). Thus, fibronectin patterns restore defects' stability in fibronectin-depleted CAFs layers.

Altogether, our data show that fibronectin deposition on the substrate fixes the nematic ordering via a positive feedback loop between the CAFs and fibronectin layers. The nematically ordered CAFs deposited fibronectin, reproducing the layer's initial nematic ordering organization. The nematic fibronectin deposition then dictated CAFs organization into the initial nematic ordering. Finally, CAFs deposited new fibronectin, reproducing such nematic ordering and preserving it over time.

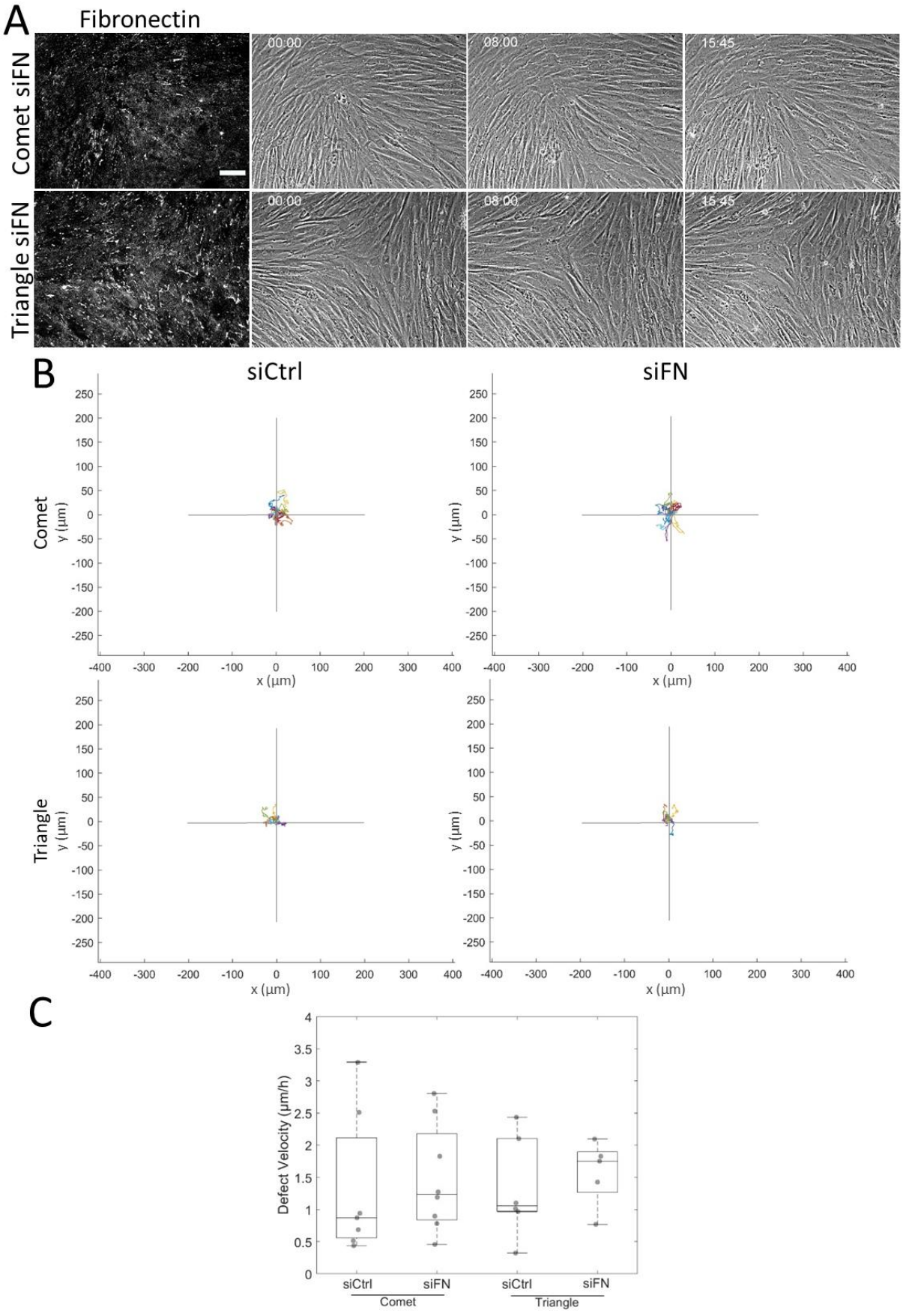

Figure 52. Impact of fibronectin depletion on defect movement in CAFs layers seeded on top of fibronectin pattern generated by control CAFs.

A) Time-lapse imaging of comet (top) and triangle (down) defect of fibronectin-depleted CAFs seeded on fibronectin patterns generated by control CAFs (left). Scale bar: 100 µm.
B) Defect cores trajectories in the field of view of the comet (top) and triangle (down) for CAFs siCtrl (left) and siFN (right). Horizontal and vertical gray lines on each plot represent defects size (~ 400 µm). Each trajectory represents one defect.
C) Quantification of comet and triangle defect velocity for CAFs siCtrl and siFN. Each dot represents one defect (N=1 independent experiment, comet: siCtrl n=7, siFN n= 8; triangle: siCtrl n=6, siFN n=5). Boxplot: middle bar= median, edges bars= 25th and 757th percentiles, whiskers= extent of data, red cross= outliers.

Fibronectin patterns restore CAFs' immobility but not their capacity to exert high traction forces

To test whether the lack of fibronectin caused the enhancement of CAFs' movement, I first prepared fibronectin patterns as described in Figure 46A. Then, I seeded siFN and siCtrl CAFs with labeled nuclei on these fibronectin patterns and imaged them over 15h. I tracked CAFs' trajectories and quantified their velocity and the mean fluid flow of the CAFs layer (Figure 53). I observed that both siCtrl and siFN CAFs mostly jiggled around their position, with some CAFs moving from their initial positions (Figure 53A). Their mean velocity was about 2 µm/h, showing that fibronectin patterns slowed down the migration of CAFs that cannot produce fibronectin (Figure 53B).

Intriguingly, mean fluid flow was slightly but significantly increased for CAFs siFN compared to siCtrl (Figure 53C): about 2.1 µm/h for CAFs siCtrl and 2.5 µm/h for CAFs siFN. However, these values were lower than the mean fluid flow for CAFs plated on gels without fibronectin patterns (Figure 49), about 3 µm/h for CAFs siCtrl and 4.5 µm/h for CAFs siFN. Together, these data show that both control and fibronectin-depleted CAFs were relatively immobile on fibronectin patterns. Thus, in addition to fixing the nematic ordering organization and its defects, fibronectin deposition also fixed the position of individual CAFs in the layer. These data also suggested that the lack of fibronectin stitch adhesions was insufficient to allow CAFs displacements in the layer in the presence of fibronectin patterns.

Because siFN CAFs were immobile on fibronectin patterns, we next wondered whether these CAFs could form supracellular units on fibronectin patterns without fibronectin stitch adhesions.

To test this, I seeded CAFs on fibronectin patterns prepared as described in Figure 46A and performed traction force microscopy. I found that siFN CAFs exerted significantly lower traction forces compared to siCtrl CAFs, showing that fibronectin patterns were unable to restore the traction forces' capacity of the CAFs that cannot produce fibronectin (Figure 53D). This indicated that fibronectin deposition on the substrate was insufficient to induce CAFs to form supracellular units. Instead, fibronectin stitch adhesions were required for CAFs to connect to build up and transmit traction forces.

Thus, fibronectin patterns restored CAFs' immobility but not their capacity to exert high traction forces.

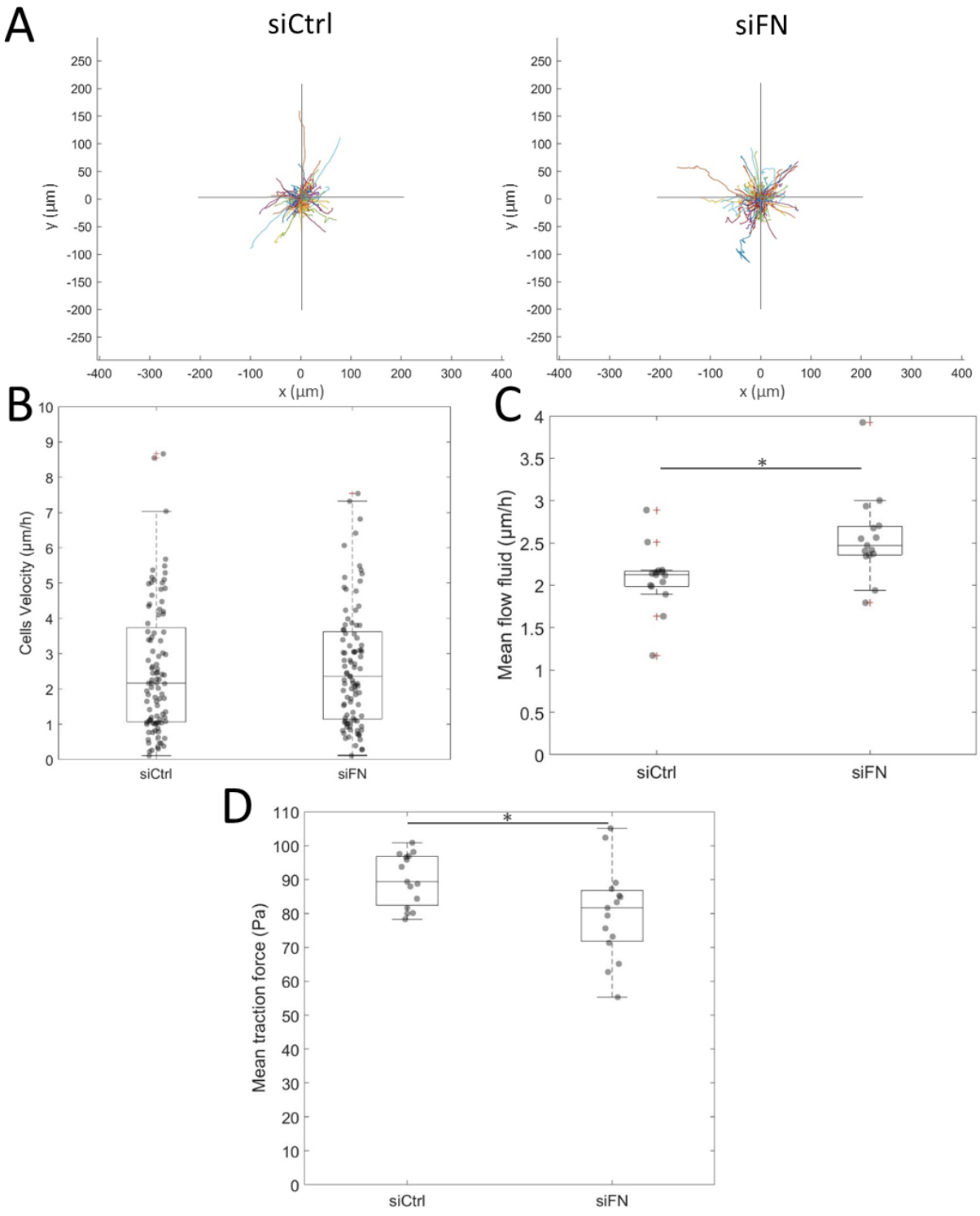

Figure 53. Impact of fibronectin depletion on CAFs movement seeded on top of fibronectin patterns.

A) Cells trajectories in the field of view for CAFs siCtrl (left) and siFN (right). Horizontal and vertical gray lines on each plot represent defect size (~ 400 µm). Each trajectory represents one cell.

B) Quantification of cells' velocity for CAFs siCtrl and siFN. Each dot represents one cell (N=1 independent experiment, siCtrl n=100, siFN n=100) Boxplot: middle bar= median, edges bars= 25th and 757th percentiles, whiskers= extent of data, red cross= outliers.

C) Quantification of mean flow fluid for CAF siCtrl and siFN. Each dot represents one field of view (N=1 independent experiment, siCtrl n=15, siFN n=15; t-test p-value=0.005). Boxplot: middle bar= median, edges bars= 25th and 757th percentiles, whiskers= extent of data, red cross= outliers.

D) Quantification of mean traction force for CAF siCtrl and siFN. Each dot represents one field of view. (N=1 independent experiment, siCtrl n=15, siFN n=15, t-test p-value=0.0205). Boxplot: middle bar= median, edges bars= 25th and 757th percentiles, whiskers= extent of data, red cross= outliers.

3D volcano-like structures can be observed at the core of +1/2 comet defect

We reasoned that the combination of high tractions and compression at the head of +1/2 comet defects could induce CAFs extrusion. To test this hypothesis, I seeded CAFs on a basement membrane, decellularized mouse mesentery, and let the system evolve for ten days before fixation and imaging (Figure 54A). We observed two +1/2 comet defects coupled by their tails (Figure 54C). On both comet heads, we observed a 3D structure resembling a volcano with CAFs going in 3D on the borders of that structure, creating a crater in the middle (Figure 54B). This suggests that CAFs can extrude from the layer at +1/2 comet defect. If embedded into a stroma, such extruded CAFs could generate highways in the ECM perpendicular to the tumor edge while grabbing cancer cells to help them migrate out of the tumor (Gaggioli et al., 2007). Thus, CAFs generate 3D volcano-like structures at +1/2 comet defects, possibly due to enhanced compression at the comet head. Those structures could potentially favor cancer cell invasion at the comet head.

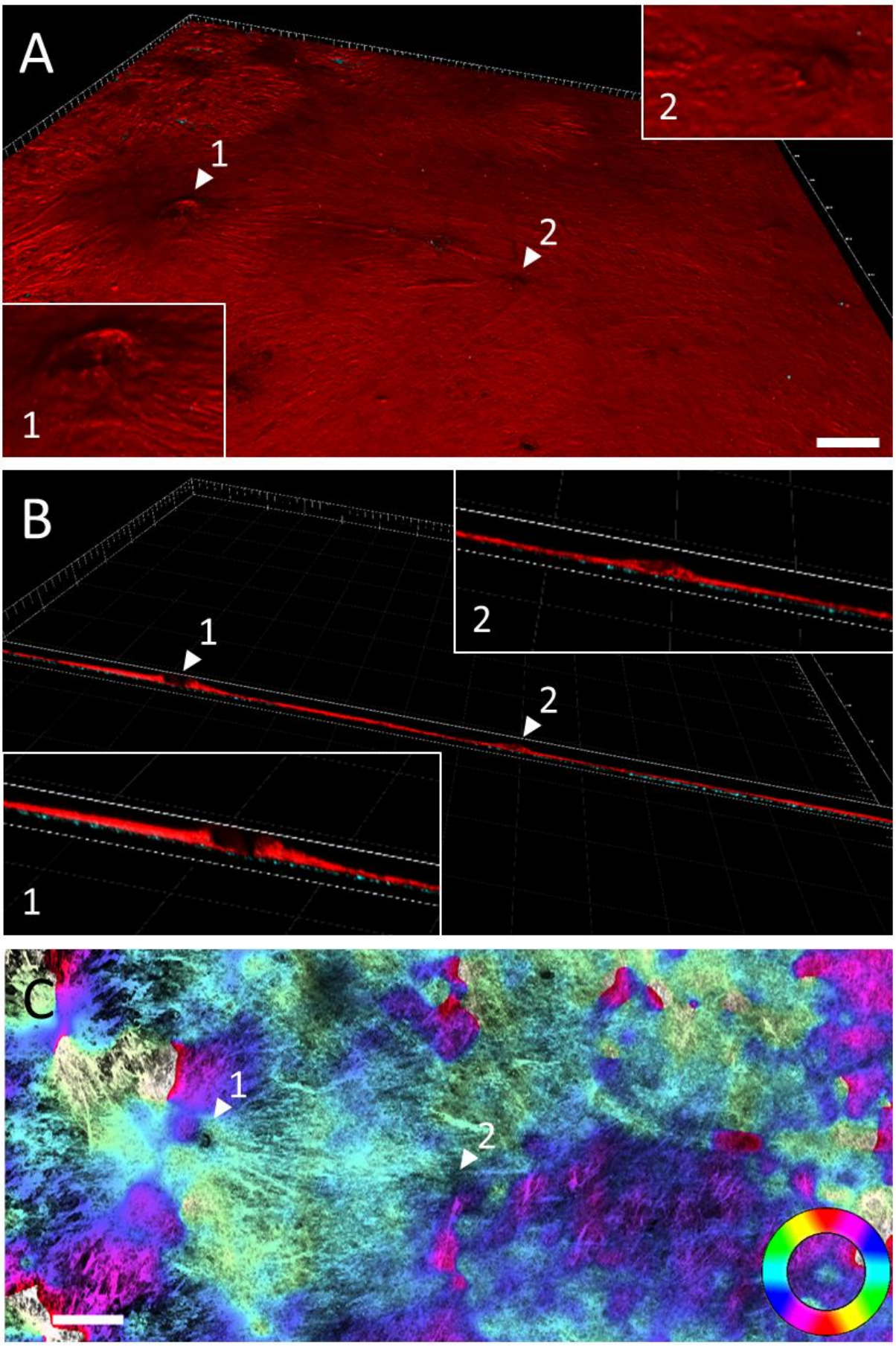
A
1
2
2
1
B
1
2
2
1
C
1
2

Figure 54. 3D structures at the +1/2 comet defect head.
A) 3D imaging of CAFs (red) on basement membrane (cyan). White arrows show where 3D structures at the head of the comet defects are. Scale bar: 400 µm.
B) Orthogonal view of the 3D imaging at the positions of the 3D structures with higher magnification on each comet head. White arrows show where 3d structures are in the orthogonal view.
C) 2D imaging of the CAFs layer with orientation color map. White arrows indicate the head of +1/2 comet defects. Colored circle: orientation color map. Scale bar: 200 µm.

Cancer cell invasion depends on the presence of defects in the CAFs layer

Until now, I only described the CAFs layer and speculated how the nematic ordering formed by the CAFs could either prevent or favor cancer cell invasion.

Based on my data, I speculate that defects in the nematic ordering could favor cancer cell invasion. First, defects were sufficiently big and frequent to impact a large number of the cancer cells below, potentially leading some of them to invade. Then, defects were made of fewer cells and fibronectin compared to aligned areas. Thus, cancer cell invasion could be more accessible at defects as the CAFs and ECM physical barriers were thinner. Moreover, fibronectin deposition on the substrate fixed the initial nematic ordering, thus, defects were stationary, allowing time for cancer cell invasion. Finally, using stitch adhesions and F-actin fibers, CAFs formed supracellular units that exerted traction forces with specific patterns at defects that could favor cancer invasion.

In contrast, I speculate that aligned regions could prevent cancer cell invasion based on my data. Aligned regions were places with a high number of cells and increased fibronectin density. Cancer cell invasion could thus be limited there as the physical barrier of the CAFs and ECM layer was thicker. Moreover, in aligned regions, the CAFs supracellular unit formation, using fibronectin stitch adhesion and F-actin fibers, created solid and compact blocks that could prevent cancer cell invasion by reinforcing the thick barrier.

To assess if and how nematic ordering and associated defects affect cancer cell invasion, I co-cultured CAFs and human colon cancer cells HCT116 on opposite sides of a basement membrane made by a decellularized mesentery. After 13 days, I quantified invasion at defects and aligned areas (Figure 55).

Observation of the CAFs layer revealed the presence of defect areas and cancer cell invasion (Figure 55A). First, I plotted the proportion of cancer cell invasion areas depending on the defect areas in the CAFs layer (Figure 55B). I found a positive correlation between cancer cell invasion and defects. In other words, the more defects in the CAFs layer, the more cancer cells were invading the basement membrane, suggesting that defects could promote cancer cell invasion.

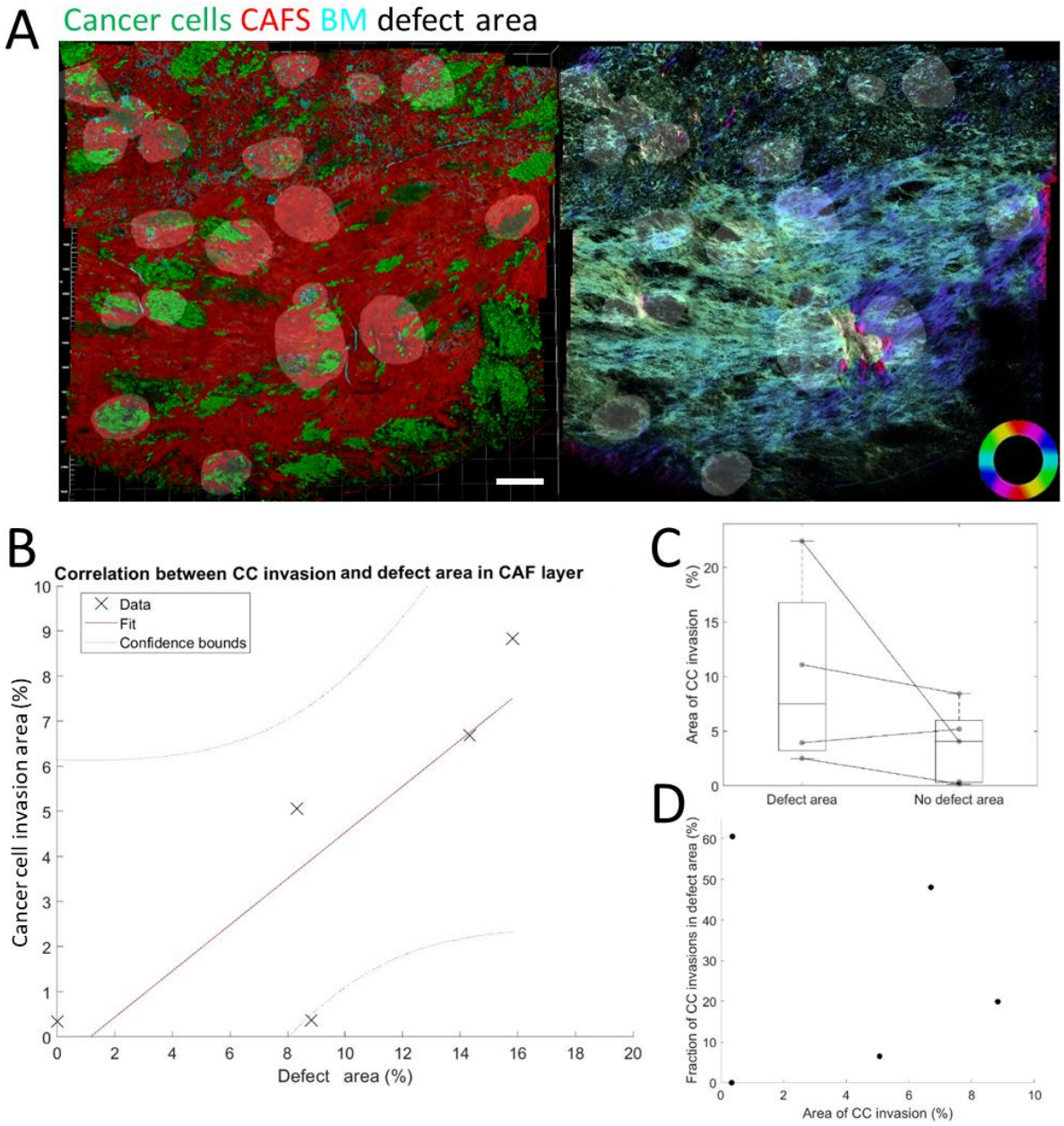

Figure 55. Cancer cells invasion through the basement membrane in the presence of the CAFs layer.
A) 3D imaging of cancer cells HCT116 (green) in CAFs (red) layer on basement membrane (cyan) (right). 2D imaging of the CAFs layer with orientation color map (left). White transparent areas show defect areas inside the CAFs layer. Each dot represents one invasion assay. Colored circle: orientation color map. Scale bar: 400 µm
B) Correlation between proportion of defect area and cancer cells invasion area inside the CAFs layer after 13 days of the invasion. Each cross represents one invasion assay.
C) Proportion of cancer cells invasion in defect area and no defect area after 13 days of the invasion. Each couple of dots represents one invasion assay. Boxplot: middle bar= median, edges bars= 25th and 757th percentiles, whiskers= extent of data.
D) Fraction of cancer cells invasion present in defect area depending on the proportion of cancer cells invasion area inside the CAFs layer after 13 days of the invasion.
.

Then, I compared the proportion of invading cancer cells at and outside the defects (Figure 55C). These preliminary data showed that for almost each invasion assay, invading cancer cells were more likely to be found at defects than outside. Indeed, cancer cell invasion covered about 7.5% of defect areas,

whereas cancer cell invasion covered about 4% of no defect areas. This suggests that cancer cell invasion happened more frequently at defects than outside.

Finally, I plotted the fraction of cancer cell invasion at the defects depending on the proportion of cancer cell invasion inside the CAFs layer (Figure 55D). This quantification showed that the more there was cancer cell invasion in the CAFs layer, the less this invasion was at the defects. This result suggested that as cancer cell invasion increases in the CAFs layer, the new points of cancer cell invasion start at other places in the CAFs layer and not only at the defects. Thus, cancer cell invasion could begin with defects, but these first points could disturb the CAFs layer, making it possible for cancer cells to invade outside the defect areas. In the end, cancer cell invasion could happen anywhere when the CAFs layer was entirely disturbed.

Summary

In this study, we aimed to decipher the role of defects in the nematic ordering of the CAFs layer in cancer cell invasion. First, we studied the CAFs layer and found cues suggesting that defects could favor cancer cell invasion while aligned regions could prevent it.

For defects favoring cancer cell invasion, we found the following results:

- Defects were sufficiently big and frequent to stimulate cancer cell invasion.
- Defects presented fewer cells density and fibronectin deposition, making them a thinner barrier to break compared to aligned regions
- Defects didn't move, which could give enough time for cancer cell invasion to occur
- Defects showed higher traction forces with specific force patterns that could either generate CAFs extrusion (+1/2 comet defect) or pinching of the tumor below (-1/2 triangle defect)

For aligned areas preventing cancer cell invasion, we found the following results:

- Aligned areas presented higher cells density and fibronectin deposition, making them a thicker barrier to break through compared to defects
- Aligned areas are made of supracellular units of CAFs connected with long F-actin fibers and fibronectin stitch adhesions, potentially making them compact and solid blocks hard to penetrate
- Aligned areas presented low traction forces without a specific pattern

Our data also highlighted the importance of fibronectin. Fibronectin deposition fixed the CAFs layer in its initial organization, so defects and individual CAFs were not moving. Fibronectin was also responsible for generating the supracellular units of CAFs via stitch adhesions.

Finally, preliminary data of invasion assays revealed the formation of 3D volcano-like structures at +1/2 defect comet. They also suggested that defects' presence could enhance cancer cell invasion. Cancer cell invasion is likely to start at defects, but once CAFs' layer is disturbed, invasion propagates to non-defect areas.

Chapter VI: Discussion

CAFs' role in cancer invasion has mainly been studied and revealed its ambiguity. Indeed, some studies show that CAFs favor invasion by stimulating cancer cell capacities (Calon et al., 2012; Dumont et al., 2013; Wei et al., 2015) or actively participate in their escape (Attieh et al., 2017; Gaggioli et al., 2007; Glentis, 2017). However, other studies show that CAFs prevent invasion by creating physical barriers (Bhattacharjee et al., 2021) or limiting cancer cell capacities (Özdemir et al., 2014; Rhim, 2014).

To better decipher CAFs' role in cancer invasion, our lab examined the CAFs layer surrounding the tumor. We showed that CAFs form a capsule around the tumor that compress the cancer cells, actively generating solid stress (Barbazan et al., 2021). Tumor compression slowed down its growth and limited cancer invasion. Tumor compression depended on CAFs aligning around the tumor and coordination of forces. However, the alignment of CAFs, nematic ordering, is associated with topological defects where CAFs are misaligned.

To understand if and how defects in nematic ordering could affect cancer cell invasion, in this study, we characterized the nematic ordering of CAFs through the prism of cancer invasion.

First, by focusing on defects, we observed that both defects were big and frequent inside the nematic ordering. Then, both defects presented fewer cells and lower fibronectin deposits. Moreover, defects and CAFs were stable inside the layer. These first observations provided clues that defects could favor invasion: there will be more than 15 000 defects around 3x3x3 cm tumors to potentially stimulate invasion. Their big sizes allow them to interact with a high number of cancer cells beneath, and lower cell density and fibronectin deposits make them thinner barriers for cancer cells to breach. Finally, as they were stable, cancer cells would have sufficient time to execute the invasion.

In addition, we also characterized the forces in defects and found specific patterns for each type. +1/2 comet defects were compressed with force peaks at the core of the comet head, whereas -1/2 triangle defects were under tension with force peaks at each vertex. Such patterns suggest that CAFs extrusion could happen at comets (Saw et al., 2017) with the extruded CAFs going perpendicularly to the tumor edge and generating highways in the stroma for cancer cells to escape. On the other hand, triangles could pinch the cancer cells below to make them pierce the CAFs layer in the triangle cores and escape. We thus envision that both defects could favor cancer invasion using different strategies.

In contrast, aligned areas presented a higher number of cells and fibronectin deposits, making them thicker barriers for cancer cells to breach. Traction forces were low in aligned areas, limiting their capacity to stimulate the cancer cells beneath. CAFs formed supracellular units in aligned areas using long F-actin stress fiber and fibronectin stitch adhesions. Such supracellular units could reinforce the already thick barrier by creating solid and compact blocks that are hard to breach and also actively

compress the tumor to limit its expansion (Barbazan et al., 2021). Thus we speculate that aligned areas should prevent cancer invasion.

Besides defects and aligned areas characterization, we also highlighted the importance of fibronectin inside the CAFs layer. We found two significant roles of fibronectin.

First, fibronectin served as a glue between CAFs to form supracellular units via stitch adhesions. Such supracellular units would allow CAFs to coordinate forces: they could build up and transmit forces to specific locations inside the layer. We saw that supracellular units could be formed in aligned areas and exert forces at the forces peaks in the defects. Upon fibronectin depletion, supracellular units seemed to be lost as traction forces were decreased in the CAFs layer, thus the importance of fibronectin as a glue between CAFs.

Second, fibronectin deposited at the substrate served as a pattern to fix the nematic ordering and its associated defects. Fibronectin deposition followed CAFs' orientation, and CAFs sensed the fibronectin deposition and aligned accordingly before depositing even more fibronectin. This creates a positive feedback loop between the fibronectin deposition layer and the CAFs which fixes the initial nematic ordering, immobilizing CAFs and defects. Upon fibronectin depletion, this feedback loop is lost along with defects and CAFs stability, showing the importance of fibronectin as a pattern to fix the nematic ordering.

Both fibronectin roles could impact the CAFs layer behavior towards cancer invasion. Fibronectin stitch adhesions allow CAFs to build up forces at defect via supracellular unit formation, thus favoring cancer invasion. However, this supracellular unit formation also creates solid and compact blocks in aligned areas, preventing invasion. Moreover, our lab also found that the CAFs capsule could use fibronectin stitch adhesions to compress the tumor, constraining it (Barbazan et al., 2021). Thus, fibronectin stitch adhesion could both prevent and favor invasion.

Fibronectin deposition fixed the nematic ordering and its associated defects, thus favoring invasion. Moreover, heterogeneous fibronectin deposition generated thin barriers in defects, favoring invasion, and thick barriers in aligned areas, preventing invasion. Thus fibronectin deposition could also both prevent and favor invasion.

Finally, preliminary data suggested that cancer invasion depended on defects in the CAFs layer. We found a positive correlation between the proportion of defects inside the CAFs layer and the proportion of cancer cell invasion. Such cancer cell invasion happened more likely inside defects. However, the more cancer cell invasion was in the CAFs layer; the less this invasion was at the defect. This suggests that, in the beginning, cancer cell invasion mainly occurs at defects. Still, as cancer cell

invasion advanced, disturbing the CAFs layer, cancer cells could start invasion everywhere, thus equalizing the proportion of cancer cell invasion at defects and other areas.

This study proposed that cancer cell invasion could mostly depend on defects in the CAFs layer.

Shaping the nematic ordering with microfabricated microtopography patterns

This study showed that the CAFs' fibronectin deposition fixed the initial nematic ordering and associated defects and CAFs at a specific position in the layer. Moreover, fibronectin patterns imposed the exact nematic ordering on newly seeded CAFs. Indeed, CAFs sensed the fibronectin patterns and aligned accordingly. Thus, CAFs-generated fibronectin patterns could be used as a new technique to shape the nematic ordering in a particular organization with a controlled position and density of each type of defect. However, there are limitations in controlling the nematic ordering organization of such fibronectin patterns. The fibronectin patterns will be random if CAFs are grown on a surface without constraint. However, suppose CAFs are grown on a surface with edges. In that case, the fibronectin pattern will adopt the exact nematic ordering as if CAFs are grown directly on the edged patterns, making the fibronectin pattern step unnecessary.

One way to control the shape of the nematic ordering would be to replace the fibronectin patterns with microfabricated microtopography patterns. Indeed, microtopography patterns can also trigger CAFs to align along drawn micro-lines (Azatov et al., 2017). Microfabricated microtopography patterns could be generated in all shapes possible, thus considerably enlarging the possibility of studying the nematic ordering and the interaction between defects. Indeed, shaping the nematic ordering is mainly done using the edges (Bade et al., 2018; Duclos et al., 2017, 2014; Guillamat et al., 2022). However, edges impose cell alignment only at their proximity, leading to two possible types of patterns: 1) "big" patterns with the controlled organization of cells at the edges but a more random distribution of cells inside the pattern, and 2) "small" patterns with controlled organization everywhere but limited to only one or two defects or even pure aligned regions.

Microtopography patterns do not have such restrictions as they allow us to draw any desired nematic ordering organization of any size. That could be used to study one particular defect in a fully nematically ordered layer of cells. Such studies would show the exchange between the chosen defect and the rest of the layer and thus extend the results obtained while studying the same defect alone on a pattern. It will also allow us to investigate how defects interact and explore the impacts of defects density or size on the cells' layer integrity, homeostasis, and functionality… However, microtopography patterns will generate fixed nematic ordering that cannot change over time. Thus, they will not allow

the study of defects' dynamics and their potential importance. Another drawback is the technical difficulty of generating such microtopography patterns due to the small, concentrated, and detailed lines to draw, limiting, for now, the nematic ordering organizations reproducible. Such technical problems could, however, be abrogated in the future with technological development like nano-precise 3D printing.

Cancer cells invasion inside the CAFs layer

This study mainly described the CAFs layer and how it could influence cancer cell invasion. I am currently performing new invasion assays to complete the preliminary data presented in the results. Nevertheless, the preliminary data show a correlation between the number of defects in the CAFs layer and the number of invading cancer cells. We also saw that cancer cell invasion was more likely to happen at defects than in aligned regions. However, as cancer cell invasion progressed and disturbed the CAFs layer, cancer cells invaded everywhere. Additional experiments are needed to confirm these preliminary data. Because cancer cell invasion seemed to start at defects before spreading to the rest of the CAFs layer, time-lapse imaging of the cancer cell invasion is required to validate this observation. This would also give cues on how cancer cells effectively invade the CAFs layer and whether the force patterns observed for each type of defect affect this process.

Concerning the strategies of cancer cell invasion at defects, we speculated that CAFs extrusions happen at +1/2 comet defects. CAFs could then go perpendicularly to the tumor and generate highways for cancer cell invasion in the stroma. Following this speculation, we observed the formation of 3D volcano-like structures at the comet heads when the CAFs layer was on a basement membrane. However, in these invasion assays, there was no extracellular matrix on top of the CAFs layer into which the extruded CAFs could migrate, limiting our conclusions on that point. To test whether extruded CAFs migrate inside the stroma and generate highways for cancer cell invasion, I attempted to add collagen I on top of the CAFs layer once confluent. However, these experiments were inconclusive because the collagen I layer detached from the basement during the fixation or imaging. I also tried to seed the CAFs mixed with collagen I. However, due to the high CAFs concentration needed to form the confluent layer, the CAFs contracted the collagen I gel, generating a ball in the middle of the construct. Thus, I will need to optimize or develop an adequate method to assess CAFs' capacity to extrude and create 3D structures at the +1/2 comet defects.

This study focused on traction forces in a 2D plane below the CAFs layer. However, we speculated that +1/2 comet defects could extrude CAFs and -1/2 triangle defects pinch the layers below it. Such strategies should generate pushing forces in 3D. To observe these potential 3D forces, I attempted to

perform 3D traction forces microscopy of the CAFs layers. However, the results were inconclusive due to the restricted field of view and noise from the small 3D deformations the CAFs layers generated on the PAA gels. Optimization of these experiments is required to draw any conclusion on 3D forces and thus assess better the forces generated at defects.

In addition to stimulating cancer cell invasion, defects could also generate the tumor-associated collagen signature (TACS) switch from parallel (TACS-2) to perpendicular to the tumor (TACS-3). Indeed, we speculated that extruded CAFs at +1/2 comet defects could go perpendicularly to the tumor edge and generate highways in the stroma. Cancer cells could then use these roads to escape the tumor. Such remodeling would correspond to the TACS-3 topology (Conklin et al., 2011; Provenzano et al., 2006).

Similarly, once -1/2 triangle defects are pinched, the resulting 3D deformations could also promote CAFs' reorientation perpendicularly to the tumor, so the switch toward the TACS-3 topology. Thus, defects in the CAFs' layer could lead to topological changes in the ECM from TACS-2 and TACS-3 at the tumor edge. Combined with other studies by (Guillamat et al., 2022; Maroudas-Sacks et al., 2020), this could reinforce the morphological role of nematic defects in biological tissues.

Intriguingly, we also observed cancer cell invasion in aligned regions of the CAFs layer. Indeed, in our preliminary data, there was one point where we observed a bit of cancer cell invasion in an only-aligned CAFs layer. For the other points, we saw cancer cell invasion mainly at defects but also in aligned areas. However, most other data suggests that aligned areas prevent cancer cell invasion. Indeed, aligned areas created solid and compact blocks via supracellular units with enhanced fibronectin deposition. We speculated that as cancer cell invasion increased, the CAFs layer was disturbed, leading to invasion in the aligned regions. We next wondered what these disruptions inside the aligned areas were and how they could lead to cancer cell invasion. One explanation could come from the CAFs' capacity to generate holes in the basement membrane, as seen before (Glentis, 2017). In that study, holes were observed everywhere in aligned CAFs layers. However, these CAFs layers were not confluent, potentially limiting CAFs' interaction with each other. Another explanation could come from the internal stresses in aligned regions. There was no specific pattern of internal stresses in the aligned area, but internal stresses could be present with either compression or tension.

Moreover, we saw that the tail of +1/2 comet defects, where aligned regions started, were under tension. We also observed that, inside the nematic ordering, +1/2 comet defects were often coupled by their tails. This suggests that internal stress, especially tension, could build up in aligned regions, particularly between two +1/2 comet defects. Such tension could potentially tear the CAFs layer, generating holes cancer cells could use to migrate through. In addition, we saw that ablation inside the

defects, which could be comparable to cancer cells breaching the CAFs layer, switched the force peaks behind the ablated areas in the continuation of aligned regions. The switch but not disappearance of the force peaks suggested that internal stresses inside aligned regions could remain and potentially be reinforced by the force peak rapprochement. Thus, inside aligned areas, there could be already existing under-tension places that could tear, leaving holes that cancer cells could use to invade. Then, as cancer invasion progress, new holes and potentially additional force peaks around aligned areas would appear. Under-tension places inside the aligned regions could increase in numbers and tension intensity, leading to more tearing and thus more cancer cell invasion.

To assess this, I performed internal stress microscopy on a large field of view of the CAFs layer. I saw strips of tension inside aligned regions between coupled +1/2 comet defects, suggesting under-tension places in aligned areas. In addition, in invasion assays I performed at the early stage of cancer cell invasion, I sometimes observed holes in aligned areas without cancer cell invasion. This suggests that aligned areas could tear themselves effectively due to internal tension. To ensure these first observations, I need to perform additional internal stress experiments on large field-of-views and time-lapse imaging to follow the hole's appearance in aligned regions during the invasion.

Fibronectin as a potential therapeutic target

In this study, we found that fibronectin plays two major roles in the nematic ordering of CAFs. When deposited on the substrate, it reproduced the nematic ordering, immobilized most of the CAFs, and fixed defects, giving enough time for cancer invasion. This stability of the nematic ordering generated heterogeneous fibronectin densities in the CAFs layer with lower fibronectin deposition at defects, which could facilitate cancer invasion, and higher fibronectin deposition in aligned areas, which could prevent cancer invasion. Fibronectin stitch adhesions contributed to forming supracellular units of CAFs, allowing CAFs to build up and transmit forces at specific positions in defects. These specific forces patterns could favor invasion at defects. Moreover, the supracellular unit formation in aligned regions generated compact and solid blocks that could prevent cancer cell invasion. Thus, fibronectin can favor or stop cancer cell invasion.

Upon fibronectin depletion, defects and CAFs started moving in the layer. As CAFs could not form fibronectin stitch adhesions and thus supracellular units, forces in the layer were reduced. CAFs' movement and incapacity to build up forces could limit the CAFs layer's ability to favor cancer cell invasion. However, the lack of supracellular units in aligned regions could also restrict the CAFs layer’s ability to prevent cancer cell invasion. These different possibilities lead us to question whether

fibronectin could be a potential target to prevent cancer cell invasion in patients and thus enhance their survival.

Moreover, CAFs' fibronectin depletion would affect the CAFs' role in breaching the basement membrane and the entire sequence of cancer invasion. Indeed, the importance of fibronectin at all steps of cancer invasion has been primarily studied (Attieh et al., 2017; Barbazan et al., 2021; Erdogan et al., 2017). Fibronectin allows CAFs to compress cancer cells, limiting their expansion, but can also cut pieces out of the tumor, favoring dissemination. Then, aligned fibronectin fibers deposition by CAFs inside the stroma is required to allow directional cancer cell migration out of the tumor. Thus, depleting fibronectin in CAFs would also affect its deposition in the stroma and tumor growth. Without squeezing, cancer could grow bigger. However, the lack of fibronectin deposition in the stroma could prevent cancer cells' migration in the stroma, restraining even more cancer cells' invasiveness. Thus, targeting fibronectin could have impactful benefits on patient survival by preventing the formation of metastasis.

In this study, fibronectin depletion changed the system behavior, potentially limiting the CAFs layer to prevent or favor cancer cell invasion. However, these observations were made in a system in which fibronectin was depleted from the beginning. In the patient's case, fibronectin depletion would start when fibronectin deposition occurred beforehand. This is more comparable to the experiment of fibronectin depletion on fibronectin patterns. Due to the fibronectin pattern, CAFs and defects were stable over time. However, the forces were reduced due to the lack of stitch adhesions. The defects' stability could still favor cancer cell invasion even though the lower forces would limit such capacity. In addition, the higher fibronectin deposition in aligned regions could still prevent cancer cell invasion, even though the lack of stitch adhesions to form compact and solid blocks would limit such capacity. This still differs from the patient because pre-existing stitched adhesions would be present at the beginning of the treatment. Thus, we speculate that supracellular units would remain as well as their capacities to build up forces and form solid blocks for a time.

Altogether, we could speculate that targeting fibronectin would not affect the system initially as already present fibronectin would maintain its function. However, with the tumor developing and thus tearing and degrading the fibronectin fibers, the prediction is that the treatment would start to affect the CAFs layer. Depletion of fibronectin could impact both capacities to prevent or favor cancer cell invasion. Experiments to determine whether fibronectin depletion leads to an imbalance towards preventing or favoring cancer cell invasion are needed to asses fibronectin as a therapeutic target.

Currently, I am performing invasive assays using fibronectin-depleted CAFs. In case of positive results, the next step would be to assess if fibronectin depletion treatment reduces cancer cell breaching of

the CAFs capsule in vivo. Using mice genetically modified to deplete fibronectin in CAFs would allow us to observe the evolution of cancer cell escape of the tumor upon fibronectin depletion treatment. In vivo experiments would also allow us to assess the impact of fibronectin depletion on the rest of the cancer invasion steps and tumor growth. Migration in the stroma could be prohibited without fibronectin to pave the way for cancer cells. However, without CAFs compressing tumors, tumor expansion could be enhanced. Thus, the need to decipher the impact of fibronectin depletion in vivo to see its potential therapeutic effects.

One issue with therapeutically targeting fibronectin would be the need to target fibronectin depletion specifically into CAFs. However, the lack of specific CAFs markers that could be used to design vehicles precisely delivering drugs to CAFs is a limiting factor in generating such treatments. Without particular targeting, the side effects of fibronectin depletion in other cell types would need to be assessed to ensure that the potential benefit from such treatment won't be undermined by a too important risk for the patient survival and well-being.

CAFs subpopulations

One aspect not examined during this study is the potential presence of CAF subpopulations (Costa et al., 2018). CAF subpopulations could lead to additional functions and possible actions to favor or prevent invasion, adding another level of complexity (Sahai et al., 2020). This study mainly focused on the contractile and matrix-producing roles of CAFs and how these capacities could modulate cancer cell invasion. However, these roles are linked to only one kind of CAF subpopulation. We thus wonder if the secretory and immune modulatory CAF subpopulations are also present and how their potential presence would affect cancer cell invasion (Park, 2020). In addition to their respective roles, different subpopulations would raise several questions, such as the repartition of such populations in the CAFs layer.

We saw that defects and aligned regions differed in cell and fibronectin density, traction forces, and stresses, potentially leading to different roles in cancer cell invasion. CAFs subpopulations may be heterogeneously repartitioned in the layer. In the aligned regions, with enhanced fibronectin deposition and supracellular units building up forces, the contractile and matrix-producing subpopulations could be enriched. At defects, with thinner physical barriers, the secretory and immune modulatory subpopulations could be more present as communication with the cancer cells could be more accessible. If such heterogeneous repartition of subpopulations exists, we could question how this heterogeneous repartition appears inside the CAFs layer.

Because CAFs and defects in the nematic ordering do not move, we could speculate that the heterogeneous repartition of subpopulations would be due to the plasticity of CAFs' phenotypes. In the beginning, the repartition of the CAFs subpopulation could be homogeneous; then, as the nematic ordering form and get fixed by the fibronectin deposition; several potential cues could trigger CAFs' convergence into different subpopulations. Such potential cues could come from known differences between defects and aligned areas, such as internal stresses, cell density, fibronectin density, or F-actin fibers alignment between CAFs. It could also arise from a potential gradient of secretive factors coming either from the CAFs or the tumor.

To assess whether different subpopulations exist and their repartition inside the nematically ordered CAFs layer, a first approach would be to perform immunostaining of already known markers specific to different subpopulations. Observation of differences in these immunostainings inside the CAFs layer could give cues on subpopulations' existence and their repartition. Single-cell RNA sequencing coupled with spatial transcriptomics on the CAFs layer would allow us to decipher the potential existence of different clusters, thus CAFs subpopulations and their relative localization, defects vs. aligned areas. Immunostaining newly identified markers would therefore allow spatially deciphering the repartition of each CAFs subpopulation inside the layer.

Once the repartition of each CAFs subpopulation inside the layer is established and if this repartition is heterogeneous, the next step would be to decipher what triggers this particular repartition. Stretching devices of the cell layers could be used to test internal stresses as triggers for phenotypic plasticity. Depletion of fibronectin and microfabricated patterns could be used to test respectively the gradient of fibronectin density and the F-actin alignment in CAFs as other potential triggers. Inhibition of potential receptors specific to each subpopulation could also be used to test specific secreted factors as triggers.

Finally, once established what triggers phenotypic plasticity in each subpopulation, the next step would be to decipher the role of each subpopulation inside the CAFs layer. To do so, each subpopulation could be isolated and studied via the same experiments performed in this study.

The potential drawback while deciphering the role of different CAF subpopulations is the loss of some subpopulations during the extraction process. Indeed, the CAFs are first extracted from the patient sample by letting them crawl out of the tissue pieces. The CAFs are then cultivated and passed several times before being immortalized. At each of these steps, some subpopulations could be lost. Even though we speculate that subpopulations could mainly arise from phenotypic plasticity between CAFs, it is still possible that lost subpopulations could not reappear as the culture conditions are not suitable for them. To assess this potential loss, a single-cell RNA sequencing of the patient preserved samples

could be performed and compared with the one done on the CAFs layer. In case of lost subpopulations, this single-cell RNA sequencing could give clues about which triggers could be used to restore these subpopulations inside the CAFs layer.

Chapter VII: Material and Method

Cell culture

CAFs were extracted from a colon cancer patient and NAFs from adjacent healthy tissue from the same patient. Fibroblasts were cultured on 30 kPa dishes (ExCellness - PrimeCoat). Dishes were plasma-treated for 30 s at 800 mTorr. Dishes were then coated with 5 µg/mL of monomeric collagen in DMEM supplemented with 2% Anti-Anti, 12.5 µg/mL Metronidazole B (Braun), and 4 µg/mL Ciprofloxacin (Panpharma). After incubation overnight at 37°C, 5% CO2, dishes were washed with some medium before adding the fibroblasts medium (DMEM 5% FBS and 1% ITS-A) and seeding approximately 1x106 cells. Cells grew for one week at 37°C 5% CO2 before being used for experiments. Colon cancer cell line, HCT116 (ATCC) expressing cytoplasmic GFP were cultured in T75 flasks with DMEM supplemented with 5% FBS.

LifeAct GFP transfection

Fibroblasts were transfected with LifeAct GFP using lentiviral infection. Lentiviruses containing the LifeAct GFP plasmid with 4 µg/mL of Polybrene were added to fibroblasts and incubated at 37°C, 5% CO_2, overnight. After incubation, fibroblasts were washed several times with media and then incubated at 37°C 5% CO_2. After a few days, the transfection success was checked using a fluorescent microscope. Once the fibroblasts population reached 15 to 20 million cells, fibroblasts were sorted to remove GFP-negative fibroblasts. Sorted fibroblasts were then cultured as described above.

PAA gel preparation

PAA gels were prepared on Glass-bottom dishes (Fluorodish, dish 35 mm Ø, Glass 23 mm Ø, WPI). First, dishes were treated with silane (Sigma) for 15min at room temperature. After three washes with MilliQwater and an air drying, dishes were treated with glutaraldehyde 0.25% in PBS for 30 min at room temperature. After three washes with MilliQ water and an air drying, 25µL drops of PAA gel preparation at the wanted stiffness (Table 1) were put in the middle of the dish and covered with 18 mm Ø glass coverslips. To allow polymerization of PAA, dishes were incubated for one hour at room temperature. Once PAA was polymerized, PBS was poured into dishes and glass coverslips were removed using a scalpel. PBS was removed and 100 µL of sulfo-sampah was added only onto PAA gels. Dishes were then treated with UV for 5 min. PAA gels were washed briefly with HEPES, followed by two washes with PBS. Dishes were then incubated with 200 µL of 100 µg/mL monomeric collagen I at 4°C overnight.

Stiffness	PBS/HEPES	Acrylamide 40%	Bis-acrylamide 2%	Beads	APS	TEMED
0,5 kPa	429,75	50	7,5	5	2,5	0,25
2 kPa	407,5	68,75	11	5	2,5	0,25
5 kPa	382,95	93,3	11	5	2,5	0,25
11 kPa	368,5	93,75	25	5	2,5	0,25
18 kPa	352,85	94,4	40	5	2,5	0,25
30 kPa	299,75	150	37,5	5	2,5	0,25

Table 1. PAA gel preparation for different stiffnesses, all volumes are in µL.
For traction force experiments fluorescent beads of the desired color were added to the solution.

2D traction force experiment

Fibroblasts. were seeded on 11 kPa PAA gel containing red beads (580/605, Invitrogen, F8810). The number of cells seeded depended on the desired cell density at the moment of imaging and the time between the seeding and the imaging. After seeding, fibroblasts were incubated in DMEM medium containing 10% FBS, 1% ITS-A, 2% Anti-Anti, 12.5 µg/mL Metronidazole (B. Braun), and 4 µg/mL Ciprofloxacin (Panpharma) at 37°C 5% CO_2. CAFs were imaged using an inverted Eclipse Ti-E microscope (NIKON) driven by Metamorph software (v.7.8.13.0) with a fully motorized stage, a 10X (NA, 0.3) objective, and an incubation system at 37°C, 5% CO_2. Beads were imaged using 562/40 nm excitation and Bright field was used to image fibroblasts. For some experiments, 472/30 nm excitation was used to image LifeAct GFP fibroblasts, while 377/50 nm excitation was used for Hoechst staining. For each region of interest, two positions were taken, one focusing on the fibroblast plane and one focusing on the beads plane. Time-lapse imaging lasted for ~15 h or ~60 h with images taken every 15 or 30 min. At the end of imaging, dishes kept on the microscope stage were carefully washed with PBS before cells were removed with Trypsin. Once cells detached from PAA gels, one-time point acquisition was performed for all positions to obtain the reference points for relaxed gel.

Laser ablation combined with 2D traction force microscopy

Fibroblasts expressing LifeAct GFP were seeded on 11 kPa PAA gel with red beads. The number of cells seeded depended on the density desired at the moment of imaging and the time between the seeding and the imaging. After seeding, fibroblasts were incubated on PAA gel in DMEM containing 10% FBS,

1% ITS-A, 2% Anti-Anti, 12.5 µg/mL Metronidazole (B. Braun), and 4 µg/mL Ciprofloxacin (Panpharma) at 37°C 5% CO_2. At desired time point, fibroblasts were imaged using an inverted laser scanning confocal microscope with spectral detection and multi-photon laser (LSM880NLO/Mai Tai laser – Zeiss/Spectra-Physics), a 25X oil immersion lens (NA, 0.8), and an incubation system to be at 37°C, 5% CO_2 to perform the ablation at 25X. Fibroblasts were imaged using a 488 nm confocal laser. Beads were imaged using a 561 nm confocal laser. Ablations were performed with a Ti: Sapphire laser (Mai Tai DeepSee, Spectra-Physics) at 800 nm with 100% laser power and two seconds time-lapse. For each position, a single fibroblasts and beads plane were acquired. Then, laser ablations were performed for each position. For each chosen position, the same fibroblasts and beads planes were acquired again after the ablation. Fibroblasts were then carefully washed with PBS and then removed with Trypsin. Once fibroblasts detached from PAA gels, all positions were imaged for beads planes.

Laser ablation analysis

Matlab was used to do the analysis. For each experiment, positions were separated between CAF and NAF and into the different types of topologies: +1/2 defects, -1/2 defects, and aligned areas. For each position, displacement within the fibroblasts layer between each time point was obtained using PIV on eight by eight pixels squares along the all images. Thanks to the known time lapse between each time point, the velocities of the displacement were also calculated for each eight-by-eight pixel. In addition, for each time point, the evolution of the recoil area was measured using a mask. The Kymograph of velocity and evolution of the recoil was then plotted along the main direction of the recoil.

3D traction force experiment

Fibroblasts lifeAct GFP were seeded on 11 kPa PAA gel containing red beads. The number of cells seeded depended on the density desired at the moment of imaging and the time between the seeding and the imaging. After seeding, fibroblasts were incubated in DMEM medium containing 10% FBS, 1% ITS-A, 2% Anti-Anti, 12.5 µg/mL Metronidazole (B. Braun), and 4 µg/mL Ciprofloxacin (Panpharma) at 37°C 5% CO2. Fibroblasts were imaged using an inverted Eclipse Ti-E microscope (NIKON) with spinning disk CSU-W1 (Yokogawa) integrated into Metamorph software (v.7.10.2.240) by Gataca Systems, a 40X water immersion lens (NA, 1.15), and an incubation system at 37°C, 5% CO2. Beads were imaged using 562/40 nm excitation and LifeAct-GFP fibroblasts with 472/30 nm excitation. At each position, a single 3D stack with 0,2 µm z steps, comprising both fibroblasts and beads, was taken. After acquisitions were done, fibroblasts were carefully washed with PBS at the microscope stage and then removed with

Trypsin. Once fibroblasts detached from PAA gels, one-time point acquisitions were done for all positions.

2D-3D traction analysis

Matlab was used to analyze traction force microscopy data. Traction force experiments are analyzed using scripts developed by Xavier Trepat's team in IBEC (Barcelona). First, data were separated into folders corresponding to each position, then positions were treated separately. For each position, all images were aligned and cropped the same way using the image of beads after trypsin treatment as reference. Using Particle Image Velocity (PIV) method, displacement of the beads between traction and trypsin images was measured on eight by eight pixels squares along all images. From the displacement and the gel settings, traction forces were calculated. The traction magnitudes' maps were plotted for each time point and traction vectors were plotted on top of the cell images. In addition, mean traction for each position over time was calculated: all mean tractions were then gathered together into boxplots for each condition. When drugs were used during the experiment, mean tractions were calculated before and after the addition of the drugs. The ratios of the mean traction after to before the addition of drugs were then calculated as percentages. All ratios were then gathered into boxplots for each condition.

Internal stress analysis

Matlab was used to do the analysis. Internal stresses of the cell layer were analyzed using Bayesian Inversion Stress Microscopy (BISM) script developed by Vincent Nier in Benoit Ladoux's team at IJM (Paris) (Nier et al., 2016). Internal stresses were calculated from the traction forces obtained previously using Bayesian inversion theory. BISM doesn't depend on the physical property of the system such as tissue rheology and doesn't need boundary conditions. However, the system needs to have a small height compared to its planar surface. BISM is based on strong statistical hypotheses such as the Gaussian distribution of the stresses. Tests performed by Vicent Nier have shown that BISM was robust and could be applied to different systems as long as they validate the height condition. The height condition was validated in this study as the fields of view are 825.6 µm by 598.56 µm and CAFs height is about 10-15 µm, so BISM can be applied.

Average of defects

Matlab was used to do the analysis. For each experiment, positions were separated between CAF and NAF and into the different types of topology: +1/2 defects, -1/2 defects, and aligned areas. Positions of each type of topology were then aligned in the same direction. To do so, the core and direction places of the defect/aligned area were pointed out of the bright field images (see Figure 2 for a visual representation of core and direction places for each type of topology). For each position and time point, core-centered circles with a radius of 800 pixels were used as masks. These circular masks were applied to traction force and internal stress results to only keep data within the masks. Rotations of these circular masks with traction force and internal stresses were then performed to align their directions (Figure 56). Finally, for each type of topology and type of fibroblasts (CAF or NAF), the averages of all the circles were done to obtain their specific force pattern organization.

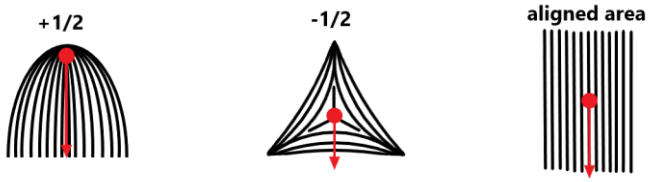

Figure 56. Representation of core and direction places for each type of topology

Immunostaining

Immunostainings of fibroblasts were performed on 11 kPa PAA gels to be in consistent conditions as traction force experiments. Cells were pre-extracted and fixed using the solutions described in Table 2. First, cells were washed with PBS and then incubated for 30 s with the extraction solution at room temperature. Cells were washed two times with the rinse solution and then incubated in the PFA solution for 20 min at room temperature. After several washes with PBS, cells were incubated with the primary antibodies for 1 h at room temperature. Cells were then washed with PBS two times with 5 min incubation and then incubated with the secondary antibodies for 1 h at room temperature. Cells were washed again twice with PBS and mounted on glass slides with AquaPolyMount. Stained cells were kept at 4°C before being imaged. All the antibodies used during this study are listed in Table 3. Cells were imaged using an inverted Eclipse Ti-E microscope (NIKON) with spinning disk CSU-W1 (Yokogawa) integrated into Metamorph software (v.7.10.2.240) by Gataca Systems, a 60X water immersion lens (NA, 1.27), a 40X water immersion lens (NA, 1.15), and a 20X (NA, 0.45) objective.

2X PEM (50 mL)	Extraction solution	Rinse solution	PFA solution
MilliQ water	0.2% Triton X-100	MilliQ water	PBS
3g PIPES	PBS	1X PEM	4% PFA
KOH, PH at 6.9	1X PEM	2 µM Phalloidin	
1M $MgCl_2$	4% PEG 35 000		
100 mM EGTA	5 µM Phalloidin		

Table 2. Solutions used for the pre-extraction fixation

Antibody	Company	Reference	Concentration	Type
Rabbit anti-Fibronectin	Sigma-Aldrich	F3648	1/400	Primary
Mouse anti-Vinculin	Home-made	/	1/10	Primary
Mouse anti-N Cadherin	Invitrogen	333900	1/400	Primary
Mouse anti-Collagen I	Sigma-Aldrich	C2456	1/400	Primary
Rabbit anti-YAP	Cell Signaling Technology	14074S	1/400	Primary
DAPI	Thermo Scientific	D1306	1/200	
Phalloidin Rhodamine	Invitrogen	R415	1/150	
Phalloidin 633	Invitrogen	A22284	1/150	
Goat anti-Rabbit AF 647	Thermo Scientific	A32733	1/200	Secondary
Goat anti-Mouse AF 488	Invitrogen	A11029	1/200	Secondary
Donkey anti-Rabbit AF 488	Invitrogen	A21206	1/200	Secondary

Table 3. The list of antibodies used in this study.
Companies, where each product has been purchased, are detailed as well as their reference. Concentrations and types of antibodies are also detailed.

Quantification of cell and fibronectin density

Matlab was used to do the analysis. After immunostaining and imaging of fibroblasts, positions are separated between CAF and NAF and into the different types of topologies: +1/2 defects, -1/2 defects, and aligned areas. First, the core for each position was pointed out and a core-centered circular mask of 400 pixels in diameter was taken from the actin staining. For each mask, the number of nuclei and the sum of pixel values inside the mask for fibronectin staining were calculated. Both were then normalized by the area to obtain the cell and fibronectin density. Data were pulled together into boxplots for each condition.

Nematically aligned fibronectin network preparation

To generate a nematically aligned fibronectin network, natural fibroblasts deposition of fibronectin was used. 5x 10^4 fibroblasts, CAFs or NAFs, were seeded on 11 kPa PAA gel with or without red beads depending on the experiment. After seeding, fibroblasts were incubated on PAA gel in DMEM with 10% FBS, 1% ITS-A, 2% Anti-Anti, 12.5 µg/mL Metronidazole (B. Braun), and 4 µg/mL Ciprofloxacin (Panpharma) for 6 days at 37°C 5% CO_2. Fibroblasts were removed by incubation with 1M NH_4OH for 20 min at room temperature. PAA gels were then washed several times with PBS. The fibronectin network was stained using the immunostaining protocol but left in PBS. Finally, PAA gels are imaged to check the fibronectin deposition. PAA gels with the fibronectin network were kept in PBS at 4°C until seeded with new fibroblasts.

Quantification of alignment correlation

Matlab and Fiji were used to do the analysis. For each experiment, the Fiji orientation J plugin was used to obtain the orientation maps θ of the CAFs and fibronectin layers. For each orientation map θ, the cosinus and sinus were calculated. The cosinus matrixes of CAFs and fibronectin were then multiplied together. Similarly, the sinus matrixes of CAFs and fibronectin were also multiplied together. Both results were summed together and the absolute value of it is taken. The mean of this absolute value matrix corresponds to the average alignment correlation between the CAFs and the fibronectin layer. All means were then pulled together into a boxplot.

Basement membrane preparation

Basement membranes were extracted from the mesentery of B6N mice females between 8 to 9 months of age. The mouse was killed by neck breaking and the gut was exteriorized to access mesentery. The mesentery was not touched directly but was manipulated by handling the gut using tweezers. The mesentery was hydrated frequently using PBS supplemented with 2% Anti-Anti during the whole procedure.

The bottom and top magnet rings were labeled using nail polish. The bottom magnet ring was then anchored to a metallic piece (Figure 57). The mesentery was placed on the bottom ring. The top magnet ring was then carefully placed above the mesentery to magnetically adhere to the bottom magnet ring. The mesentery outside the rings was cut out. The rings with the mesentery inside were then removed from the metallic piece and put in PBS containing 2% Anti-Anti. Around six mesentery constructs could be extracted from one mouse.

Mesenteries were then decellularized by incubating in 1M NH_4OH for 40 min at room temperature. Decellularized mesenteries were then quickly washed with PBS supplemented with 2% Anti-Anti and then washed for 40 min at room temperature in PBS supplemented with 2% Anti-Anti. Sulfo-sampah was applied on both sides of the mesentery and placed under a UV lamp for 5 min. Mesenteries were then washed for 3 min with 10mM HEPES and two times for 3 min with PBS supplemented with 2% Anti-Anti while shaking. Finally, mesenteries were incubated at 4°C overnight with 100 µg/mL of monomeric collagen I in PBS supplemented with 2% Anti-Anti.

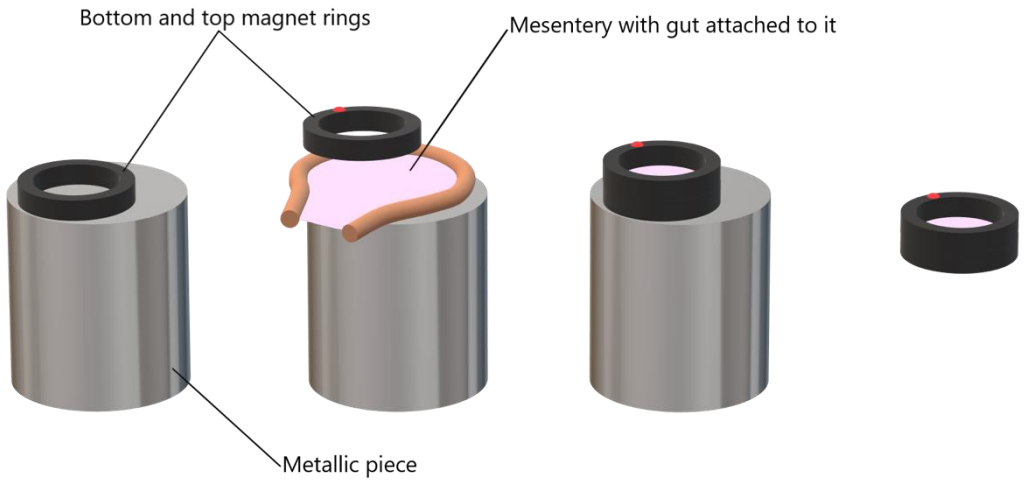

Figure 57. Representative scheme of mesentery mounting on magnet rings

Invasion assay

Invasion assays were performed on mesenteries mounted on magnetic rings and were cultivated in medium DMEM with either 10% or 1% FBS, 1% ITS-A, 2% Anti-Anti, 12.5 µg/mL Metronidazole (B. Braun), and 4 µg/mL Ciprofloxacin (Panpharma). First, mesenteries on rings were placed in 12-well plates with 700 µL medium to have the bottom part of the basement membrane immersed in the medium. $2x10^5$ fibroblasts, CAFs or NAFs, were seeded on the top part of the mesentery in 200 µL medium per ring. Rings were carefully transferred to the incubator at 37°C 5% CO_2. After 40 min, the 10% FBS medium was added into each well up to 2 mL. Two days later, rings with mesenteries were turned upside down, and $2x10^5$ HCT116 cells expressing GFP were added on the opposite side of the fibroblasts following the same process as for the fibroblasts. The day after, the medium was changed to reduce the FBS concentration from 10% to 1%. The construct was then incubated at 37°C, 5% CO_2, with half of the medium being changed every two days until the desired invasion time point. Mesenteries were then fixed with 4% PFA for 20 min at room temperature and imaged using an inverted laser scanning confocal Leica SP8 coupled to a multi-photon femtosecond Chameleon Vision II laser (680-1350 nm; Coherent) and a 25X water immersion lens (NA, 1.0).

Invasion assay analysis

Matlab and Fiji were used to do the analysis. For each experiment, the defect area and cancer invasion masks were manually drawn using Fiji. The masks obtained were transformed into 1 and 0 matrixes. The no-defect areas mask was obtained by reversing the 0 and the 1 of the defect area mask. The cancer invasion inside the defect area mask was obtained by multiplying the cancer invasion mask and the defect area mask. The cancer invasion outside the defect area was obtained by multiplying the cancer invasion mask and the no-defect area mask. For each mask, the size of the positive area was calculated. The field of view area, called the total area, is also calculated. Values of interest were then calculated as percentages by dividing the different mask sizes as listed in Table 4.

Then, the proportion of cancer invasion area toward the proportion of defect area, and the fraction of cancer invasion in the defect area toward the proportion of cancer invasion area were plotted. The proportion of cancer invasion in defect and no-defect areas were pulled together into boxplots for each condition.

	numerator	denominator
Proportion of defect area	Defect area	Total area
Proportion of cancer invasion area	Cancer invasion area	Total area
Proportion of cancer invasion in the defect area	Cancer invasion inside the defect area	Defect area
Proportion of cancer invasion in the no-defect area	Cancer invasion outside the defect area	No-defect area
Fraction of cancer invasion in the defect area	Cancer invasion inside the defect area	Cancer invasion area

Table 4. The list of the division done to obtain each value of interest.

Western Blot

Fibroblasts were seeded on 30 kPa dishes coated with 5 µg/mL of monomeric collagen. After three days, cells were scratched from the plates using PBS and transferred to a falcon. Cells were washed two times with PBS: first, cells were centrifuged for 5 min at 1200 rpm, the supernatant was removed, PBS was added and cells were re-suspended. Cells were pelleted again and pellets were re-suspended in 50 µL of Precellys and sonicated three times for 15 s. Samples were then boiled at 100°C for 10 min, then spun for 15 min at 13 000 rpm, and supernatants were collected and diluted at one to five. 10 µL of each sample was used for BCA titration using the BCA reducing agent compatible kit, Pierce. BCA samples were added to a 96-well plate and incubated at 37°C for 30 min. The plate was then read and, using the value measured, the concentration of each sample was determined. Using these concentrations, volumes needed for each condition to have the same quantity of proteins were calculated. These volumes were then taken, and mixed with colorant, and water, if necessary, to adjust the volume for all samples. Samples were then boiled at 95°C for 5 min and loaded into a 7,5% TGX gel and let migrate for about 1h. Transbloc was used to transfer the proteins from the gel to a nitrocellulose membrane. The membrane was stained with red ponceau for 5 min while shaking. The membrane was then incubated in 5% non-fat milk powder diluted in PBS on a shaker at room temperature for 1 h. The membrane was cut and then incubated at 4°C overnight with primary antibodies diluted in 1% milk/PBS solution on a shaker. The membrane was then washed three times for 5 min with PBS while shaking. The membrane was then incubated at room temperature for 1 h with

the secondary antibodies conjugated with HRP. The membrane was then washed three times for 5 min with PBS while shaking. Cut membranes were put back together and the signal was revealed using an ECL substrate and visualized using X-ray films.

Drugs and siRNA

All drugs used in this study are listed in Table 5. When drugs were added during image acquisition, a medium without drugs was first added to the cells. The acquisition was started. During two time points, the medium with drugs was added on top of the cells. Drug volumes were calculated so that drug concentrations in the final medium volumes were the ones desired. The time point at which drugs were added was saved. When drugs were added just before the start of the image acquisition, incubation time is taken into account for drugs to be effective at the start of the acquisition. Concerning Hoechst, before the acquisition, fibroblasts were washed with PBS and then incubated with Hoechst in PBS for 30 min at 37°C, 5% CO_2. After incubation, fibroblasts were washed twice with PBS, and the cell medium was added. When drugs were always present so that fibroblasts were permanently treated, cells were first cultured for three days with drugs on 30 kPa plates before being transferred on PAA gel. Fibroblasts were then incubated for three more days with drugs before launching image acquisition.

Drugs or siRNA	Company	Reference	Concentration	Method
Para-nitro Blebbistatin	Optopharma	1621326-32-6	5 / 10 / 50 µM	Added during acquisition
Calyculin A	Sigma	C5552	0.5 / 1 / 5 µM	Added during acquisition
Y27632	ATCC	ACS-3030	5 / 10 / 50 µM	Added during acquisition
Forskolin	Sigma	F6886	12 / 30 / 50 µM	Added during acquisition
AllStars Negative Control siRNA	Qiagen	1027281	100 nM	Permanently treated
Hs_FN1_6 siRNA	Qiagen	SI02664004	100 nM	Permanently treated
Hs_FN1_7 siRNA	Qiagen	SI02663997	100 nM	Permanently treated
Hoechst	Thermo Fisher	H3570	1 / 2 000	Added before acquisition

Table 5. List of the drugs and siRNA used during this study.

Companies, where each product has been purchased, are detailed as well as their reference in their companies. Concentrations and methods used for each drug or siRNA are also detailed.

Quantification of defect density

Four-by-four stitched image fields of view were used to quantify the defect densities. For each field of view, the comet and triangle defects were counted manually. For each defect, the numbers were normalized by the area. All data were then pulled together into boxplots for each condition.

Quantification of defect size

Matlab was used to do the analysis. For each experiment, positions were separated between CAF and NAF and into the different types of defect: +1/2 and -1/2 defects. For each position, defect size is taken depending on the type of defects: for the comet, size corresponds to the radius between the head and the tail of the comet, and for the triangle, size corresponds to the distance between one vortex and the middle of the opposite side (Figure 58). All sizes were then pulled together into boxplots for each condition.

Figure 58. Representation of core (red) and how size is measured (blue arrow) for each defect

Defects trajectory analysis

Matlab was used to do the analysis. For each experiment, positions are separated between CAF and NAF and into the different types of defects: +1/2 and -1/2 defects. Defect cores were chosen to follow defect trajectory. Using the bright field images, the defect core for each position was pointed out at each time point. Translations of cores trajectories coordinates were then done to have the first time point of each core at (0,0) in the (x,y) axis. From each trajectory, velocity and persistence were calculated. Finally, for each type of topology and type of fibroblasts (CAF or NAF), all trajectories were plotted together as well as boxplots for the velocities and persistence obtained.

Cells trajectory analysis

Cells' trajectory was obtained either by using Hoechst to stain nuclei or by mixing a small proportion of LifeAct-GFP expressing fibroblasts with non-labeled fibroblasts and performing time-lapse imaging. For each experiment, positions were separated between CAF and NAF and into the different types of topologies: +1/2 defects, -1/2 defects, and aligned areas. For each position, Fiji was used to apply a threshold on images with the fluorescence of interest to generate binary images where each cell was well separated from the others. Thresholded images were then uploaded into Ilastik for each position to track cell trajectories. Each cell's trajectory was saved into a file. Using Matlab, translations of cell trajectory coordinates were then done to have the first-time point of each cell at (0,0) in the (x,y) axis. From each trajectory, velocity and persistence were extracted. Finally, for each type of topology and type of fibroblasts (CAF or NAF), all cell trajectories were plotted together as well as boxplots for the velocities and persistence obtained.

Flow fluid of fibroblasts layer quantification

Matlab was used to do the analysis. For each experiment, positions are separated between CAF and NAF and into the different types of topologies: +1/2 defects, -1/2 defects, and aligned areas. For each position, displacement within the fibroblasts layer between each time point was obtained using PIV on eight by eight pixels squares along the all images. Thanks to the known time lapse between each time point, the flow fluids of the displacement were also calculated for each eight-by-eight pixel. The mean flow fluid for each position over time was then calculated. All mean velocities were then pulled together into boxplots for each condition.

Chapter VIII: Side project

During my thesis, I also collaborated with the postdoc in our team Andrew Clark on his project (Clark et al., 2022). His project aimed to decipher how the microenvironment influences cell migration, particularly their physical properties. In this study, we determined that cancer cell clusters generate local gradients of collagen density on viscoelastic collagen networks they are migrating on. Sensing this self-generated gradient, clusters migrate persistently along it. This gradient of collagen density relies on two parameters: the collagen network viscoelastic relaxation time and the cancer cell cluster size. The longer the viscoelastic relaxation time, the longer the generated gradient remains, which directs persistent migration. The bigger the cluster size is, the bigger the gradient generated is, and the better clusters sense it. Moreover, these gradient generations and resulting persistent migrations don't rely on any cluster front-back polarization but on front-back asymmetric traction forces. Finally, the collagen gradient and asymmetric traction go along with a stiffness gradient.

First, we assess that clusters migrate more persistently on collagen networks than monomeric collagen, showing the importance of the substrate viscoelastic property. Despite the persistent migration, no front-back polarization of clusters is visible. Then, using fluorescently labeled collagen, we observe the generation of a collagen gradient below the cluster with the peak density at the cluster rear. A theoretical model highlights the importance of the collagen viscoelastic relaxation time and the cluster size in the system. Modifications of the collagen viscoelastic relaxation time confirm the system dependency on this parameter: shorter relaxation time leads to less persistent migration and longer ones to more persistent migration. Changes in cluster size confirm the system dependency on this parameter: single cells and smaller clusters migrate less persistently than bigger clusters. Finally, traction forces microscopies reveal the front-back asymmetric traction forces, whereas Brillouin microscopies reveal the stiffness gradient.

In this study, I perform and analyze some of the time-lapse imaging and traction force microscopy experiments at different stiffnesses of clusters and single cells' migration on different substrates: monomeric collagen, collagen network, and crosslinked collagen networks. I also perform immunostainings such as the ones showing the no-presence of cluster front-back polarity or the no-additional ECM deposition during clusters' migration.

The article describing these data is featured in the following pages.

nature materials

ARTICLES

https://doi.org/10.1038/s41563-022-01259-5

Check for updates

Self-generated gradients steer collective migration on viscoelastic collagen networks

Andrew G. Clark[1,10,11] ✉, Ananyo Maitra[2,3] ✉, Cécile Jacques[1], Martin Bergert[4], Carlos Pérez-González[1], Anthony Simon[1], Luc Lederer[1], Alba Diz-Muñoz[4], Xavier Trepat[5,6,7,8], Raphaël Voituriez[3,9,12] and Danijela Matic Vignjevic[1,12]

Growing evidence suggests that the physical properties of the cellular microenvironment influence cell migration. However, it is not currently understood how active physical remodelling by cells affects migration dynamics. Here we report that cell clusters seeded on deformable collagen-I networks display persistent collective migration despite not showing any apparent intrinsic polarity. Clusters generate transient gradients in collagen density and alignment due to viscoelastic relaxation of the collagen networks. Combining theory and experiments, we show that crosslinking collagen networks or reducing cell cluster size results in reduced network deformation, shorter viscoelastic relaxation time and smaller gradients, leading to lower migration persistence. Traction force and Brillouin microscopy reveal asymmetries in force distributions and collagen stiffness during migration, providing evidence of mechanical cross-talk between cells and their substrate during migration. This physical model provides a mechanism for self-generated directional migration on viscoelastic substrates in the absence of internal biochemical polarity cues.

Collective cell migration is an essential process during development and tissue homoeostasis and has also been proposed to play a role in early stages of cancer metastasis[1]. In invasive carcinomas, which compose ~80% of human cancers[2], small clusters of cells can 'bud' away from the primary tumour and enter the stroma, connective tissue surrounding the tumour that comprises primarily collagen-I extracellular matrix (ECM) networks[3]. Tumour buds are associated with poor prognosis and enhanced metastatic potential[4–8]. However, the mechanisms by which small cell clusters migrate on collagen networks are not currently well understood.

Collagen networks are complex materials that undergo nonlinear strain stiffening and behave in a viscoelastic manner in response to cell-generated mechanical stress[9–14]. Large cell aggregates embedded in collagen networks in vitro can physically pull on collagen fibres, resulting in radially aligned collagen bundles that facilitate invasion of single cells into the surrounding matrix[15–17]. Such reorganization of stromal collagen networks has been associated with cancer invasiveness, and radial arrays of thick collagen bundles have been proposed to act as 'highways' for tumour cell dissemination[18,19]. Previous studies suggest that the topological properties of collagen, such as collagen fibre thickness and alignment, can act as a directional cue during cell migration[20–22]. However, it is currently unclear how active reorganization of collagen networks during collective migration can influence migration dynamics.

To address this, we combined long-term live imaging, traction force microscopy and theoretical modelling to ask how the viscoelastic properties of collagen networks affect network reorganization during collective cell migration and how these local changes in network topology can feed back on migration dynamics. Our results suggest that viscoelastic relaxation in collagen gels gives rise to local gradients in collagen organization that drive spontaneous persistent migration, even in the absence of biochemical polarity cues.

Cell clusters migrate persistently on collagen networks. To study collective migration on collagen networks, we generated small clusters of A431 cells, an epidermoid carcinoma cell line that has previously been shown to migrate collectively[23]. We seeded fluorescently labelled A431 cells or clusters on collagen networks (Fig. 1a,b). Clusters in the range of 500–5,000 μm^2 contained ~3–30 cells (Fig. 1c), around the range associated with carcinoma metastasis (~5 cells[4,7]). To investigate how interactions with collagen networks affected cluster migration, we seeded A431 clusters on soft (0.5 kPa) poly-A-acrylamide (PAA) gels coated with either a thin (~30 μm) layer of polymerized collagen-I or non-polymerized monomeric collagen-I and tracked cell migration over ~16 h (Fig. 1d and Supplementary Videos 1 and 2). During migration on collagen networks, individual cells within the cluster did not rearrange; rather, the entire cluster appeared to glide along the collagen networks as a single entity (Extended Data Fig. 1a,b).

To determine whether clusters on collagen networks migrated with higher persistence (that is, along straighter paths), we calculated the mean squared displacement (MSD) from migration trajectories (Extended Data Fig. 1c). Investigating the scaling of MSD with respect to the lag time (t), we observed higher crossover times from quadratic (MSD $\propto t^2$) to linear (MSD $\propto t$) scaling for clusters migrating on PAA plus collagen networks, suggesting more

[1]Cell Biology and Cancer Unit, Institut Curie, PSL Research University, CNRS, Paris, France. [2]Laboratoire Jean Perrin, Sorbonne Université and CNRS, Paris, France. [3]Laboratoire de Physique Théorique et Modélisation, CNRS, CY Cergy Paris Université, Cergy-Pontoise Cedex, France. [4]Cell Biology and Biophysics Unit, European Molecular Biology Laboratory, Heidelberg, Germany. [5]Institute for Bioengineering of Catalonia, The Barcelona Institute for Science and Technology (BIST), Barcelona, Spain. [6]Facultat de Medicina, University of Barcelona, Barcelona, Spain. [7]Institució Catalana de Recerca i Estudis Avançats (ICREA), Barcelona, Spain. [8]Centro de Investigación Biomédica en Red en Bioingeniería, Biomateriales y Nanomedicina, Barcelona, Spain. [9]Laboratoire de Physique Théorique de la Matière Condensée, Sorbonne Université and CNRS, Paris, France. [10]Present address: Institute of Cell Biology and Immunology, Stuttgart Research Center Systems Biology, University of Stuttgart, Stuttgart, Germany. [11]Present address: Center for Personalized Medicine, University of Tübingen, Tübingen, Germany. [12]These authors contributed equally: Raphaël Voituriez, Danijela Matic Vignjevic. ✉e-mail: andrew.clark@srcsb.uni-stuttgart.de; nyomaitra07@gmail.com

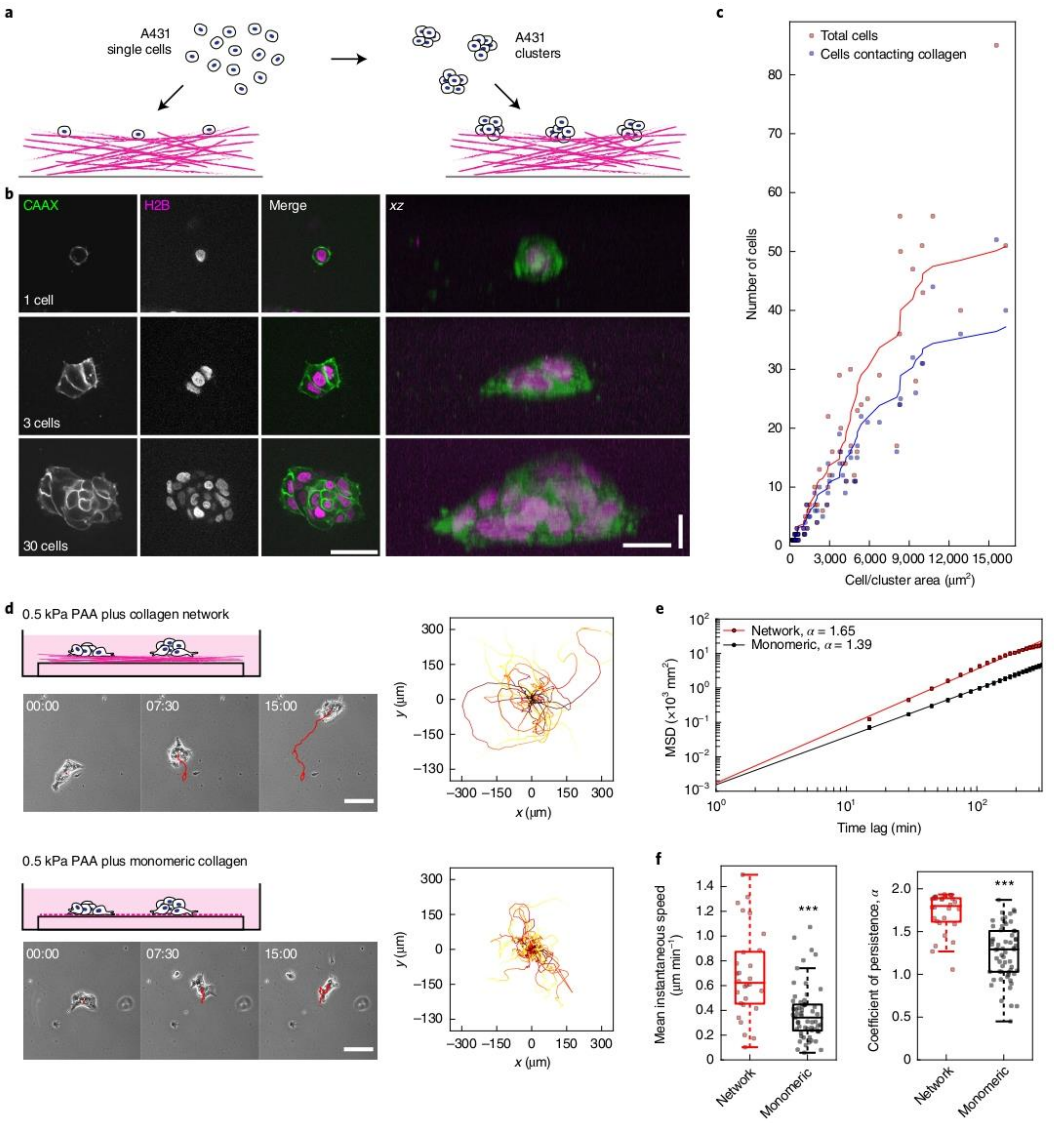

Fig. 1 | Cell clusters migrate persistently on collagen networks. a, Schematic showing plating of single cells or clusters on polymerized collagen-I networks. **b**, Micrographs from live imaging of stable A431 cells and different-sized clusters expressing GFP-CAAX (Plasma Membrane) and mCherry-H2B (DNA). Horizontal scale bars, 50 μm (left), 20 μm (right). Vertical scale bar, 100 μm. **c**, Plot of total number of cells and number of cells in contact with the collagen gel. Each dot represents one cluster or single cell. Solid lines indicate smoothed cell number versus area data. For **b** and **c**, representative images or data are from $n = 71$ clusters and $N = 2$ independent experiments. **d**, Left: schematics and montages of A431 cell clusters migrating on 0.5 kPa PAA gels coated with a thin 2 mg ml^{-1} collagen-I network (top panels) or 100 μg ml^{-1} monomeric collagen-I (bottom panels). Scale bars, 100 μm. Times are in hours:minutes. Also Supplementary Videos 1 and 2. Right: overlaid cluster migration trajectories from clusters ≥500 μm² and <5,000 μm², adjusted so that all trajectories start at the origin (0,0). **e**, MSD curves for cell clusters migrating on PAA gels coated with collagen network (red) or monomeric collagen (black). Data points represent mean ± s.e.m. Solid lines represent power-law fits for the first 300 min. **f**, Box plots of mean instantaneous speed (left) and coefficient of persistence (α, right). Coefficient of persistence was determined by fits as in **e**. Each dot represents one cluster trajectory. For **d**–**f**, representative images or data are from $n = 28, 59$ clusters and $N = 2, 3$ independent experiments. ***$P < 0.001$ for Welch's t-test ($P = 0.000148, 6.17 \times 10^{-31}$).

persistent migration on collagen networks (Extended Data Fig. 1c,d). To more easily compare the persistence across different conditions, we fit the first 300 minutes of the MSD curves with a power-law function to extract the scaling power, henceforth referred to as the 'coefficient of persistence' (α; Fig. 1e). We found that clusters migrating on PAA coated with collagen networks migrated faster and more persistently than clusters migrating on PAA coated with monomeric collagen (Fig. 1f).

We next investigated how varying collagen monomer concentration or substrate stiffness affected migration. At higher concentrations of monomeric collagen, ligand coverage was similar to collagen networks, while migration speed and persistence were reduced (Extended Data Fig. 2a–d). Mean speed and persistence peaked on 2 kPa gels (Extended Data Fig. 2e,f), consistent with previous observations[24,25]. However, even the highest migration persistence on 2 kPa PAA gels was still significantly lower than for clusters on collagen networks polymerized on PAA or glass. We next varied collagen concentration and polymerization temperature for collagen networks (Extended Data Fig. 2g,h), which are known to affect network organization[14,21,22,26]. Although migration speed and persistence varied across different collagen network conditions, migration persistence was always higher compared to cluster migration on PAA coated with monomeric collagen (Extended Data Fig. 2f,i). These data suggest that ligand density or substrate stiffness alone cannot account for the higher migration persistence on collagen networks versus monomeric collagen.

Migrating cell clusters are not front–back polarized. One potential explanation for persistent collective migration on collagen networks could be front–back biochemical polarity, a common mechanism during single cell migration. Myosin-2 typically localizes to the cell rear in front–back polarized cells, while active Rac1 localizes to leading edge protrusions[27–29]. To test for front–back polarity during cluster migration, we used a stable A431 cell line expressing a myosin-2 light chain (MLC) fused to green fluorescent protein (A431 MLC-GFP). MLC was localized to the outer 'cortex' of the cluster; however, we found no asymmetry in cortical MLC accumulation with respect to migration direction, suggesting that MLC was not polarized (Extended Data Fig. 3a and Supplementary Video 3). Similarly, Rac1 was localized at the cluster cortex and down-regulated at cell–cell junctions at the cluster interior (Extended Data Fig. 3b), consistent with previous findings[23] and suggesting that cell clusters behave as large 'super cells'. Live imaging with the Raichu-Rac biosensor for active Rac1[30] suggested that Rac1 activity was also radially symmetric during migration (Extended Data Fig. 3c). Treatment with the Rac1 inhibitor NSC23766 (ref. [31]) slightly reduced migration speed but did not affect migration persistence, suggesting that Rac1 activity is not required for persistent migration (Extended Data Fig. 3d). In addition, we found no evidence of centrosome polarization or asymmetries in cluster shape during migration, suggesting that cell clusters are radially symmetric during migration (Extended Data Fig. 4a–c). Together, these results suggest that clusters are not front–back polarized during collective migration on collagen networks.

We next tested whether adhesions or cellular ECM modification could be polarized during migration. Staining for focal adhesion markers and imaging with live focal adhesion probes revealed that clusters on collagen networks did not assemble focal adhesions (Extended Data Fig. 5a,b). Inhibition of integrin-β1 led to rapid retraction and eventual detachment of clusters, while inhibition of matrix metalloproteinases did not affect migration dynamics (Extended Data Fig. 5c,d, Supplementary Video 4 and Supplementary Discussion). Immunostaining for fibronectin, collagen-IV, laminin and collagen-I suggested that there was no additional ECM deposition during migration (Extended Data Fig. 6a–e and Supplementary Discussion). These data suggest that clusters do not form any local gradients of deposited or degraded ECM during migration.

Clusters generate collagen gradients during migration. Even without additional ECM deposition, cells and groups of cells can reorganize existing collagen networks by exerting mechanical force[15–17]. To investigate local collagen network reorganization, we imaged cell cluster migration on fluorescently labelled collagen networks and measured local filament orientation and alignment (Extended Data Fig. 7a,b). Cell clusters generated radial arrays of aligned collagen fibres around the cluster, and filament orientation was symmetric around the outside of the cluster (Extended Data Fig. 7c). In the region directly underlying the clusters, collagen was asymmetrically patterned, with a region of high collagen density offset towards the cluster rear (Fig. 2a,b and Supplementary Video 5). Analysing collagen profiles along the migration axis, we found that clusters generate inverse gradients of collagen density and alignment during cluster migration, with a density maximum and alignment minimum that are offset towards the cluster rear (Fig. 2c,d and Extended Data Fig. 7d,e).

Clusters migrating on prealigned deformable collagen networks migrated with dynamics similar to clusters migrating on isotropic collagen networks, while clusters on prealigned non-deformable collagen networks migrated preferentially along the alignment axis, but with reduced speed and persistence (Extended Data Fig. 7f–i). These data suggest that network deformability and collagen gradient formation promote persistent migration regardless of imposed collagen fibre alignment.

Fig. 2 | Local collagen topology is asymmetric during collective migration and relaxes viscoelastically. a, Pseudocolour montage of fluorescent collagen (brightest point projection, BPP). White lines indicate the cluster contour. White dots indicate the cluster centre of mass (CoM). Lower panel: zoomed in from upper panel. White arrows indicate the migration trajectory. Magenta arrows indicate the direction of collagen centre of mass. Scale bars, 25 μm. Also Supplementary Video 5. **b**, Polar histogram of angular difference between trajectory and collagen centre of mass vectors for all time points. *P* value, Rayleigh test of uniformity ($P = 2.02 \times 10^{-10}$). **c**, Segmentations from the time series in **a**, binned from the front (yellow) to the rear (violet). Colour scale indicates angle (degrees). **d**, Bar plots of collagen intensity and alignment (nematic order) over cluster regions (mean ± s.d.). Red lines, Gaussian and inverted Gaussian fits to the mean values. Red circles, centre position μ from fits. Each point represents one cluster averaged over time for $n = 34$ clusters and $N = 5$ independent experiments. **e**, Montage of bright-field and fluorescent collagen PIV vectors overlaid. The magenta line indicates the cell contour. Scale bar, 50 μm. Scale vector, 0.5 μm min^{-1}. Time is in hours:minutes after the addition of trypsin/NH_4OH. Also Supplementary Video 6. **f**, Plot of summed 3D displacements (blue) and collagen density within the cell contour (orange) for experiments in **e** and **g**. Dots indicate individual time points. Lines indicate exponential decay fit to extract relaxation time, τ_r. Colour scales in **e** and **f** indicate the out-of-plane (*z*) displacement. Negative values indicate downward displacement (towards the collagen/PAA). Times are in hours:minutes. **g**, Montage of 3D displacements of a cell cluster on a PAA gel coated with a thin collagen network, with cell removal after 0:00. Black arrows indicate in-plane (*xy*) displacements. Colour scale indicates *z* displacement (μm). Scale bar, 50 μm. Scale vector, 5 μm. Also Supplementary Video 7. **h**, Box plot of τ_r from 3D substrate displacements, collagen density and collagen PIV. Each dot represents one cluster from $n = 12, 39, 39$ clusters and $N = 3, 6, 6$ independent experiments (density and PIV measurements taken from the same data). One-way analysis of variance (ANOVA) $P = 3.62 \times 10^{-5}$. ***$P < 0.001$ for post-hoc Tukey honestly significant difference test ($P < 0.001$, < 0.001, 0.110).

Collagen networks are viscoelastic. We hypothesized that collagen gradient formation could be influenced by the viscoelastic behaviour of collagen networks during migration. To investigate collagen network viscoelasticity in response to cell-generated forces, we seeded cell clusters on collagen networks and rapidly removed the clusters by treatment with trypsin and ammonium hydroxide (NH_4OH). Following cluster removal, we measured local collagen density over time and tracked collagen network movements using particle image velocimetry (PIV; Fig. 2e,f and Supplementary Video 6). Collagen density relaxed on a timescale of $\tau_r \approx 5–10$ min. To ensure that the trypsin/NH_4OH treatment resulted in an instantaneous release of mechanical stress, we performed three-dimensional (3D) displacement microscopy using thin collagen networks polymerized on PAA gels containing fluorescent beads (Fig. 2g and Supplementary Video 7). Cell clusters initially exerted radial, inward-facing in-plane stresses and downward-facing out-of-plane stresses. Upon cell removal, substrate displacements immediately relaxed, suggesting that the cell-generated mechanical forces were nearly instantaneously released. The relaxation time of the 3D displacements was significantly shorter than the relaxation time of the collagen networks (Fig. 2f,h), suggesting that the collagen networks behave in a viscoelastic manner in response to stresses generated by cell clusters during migration.

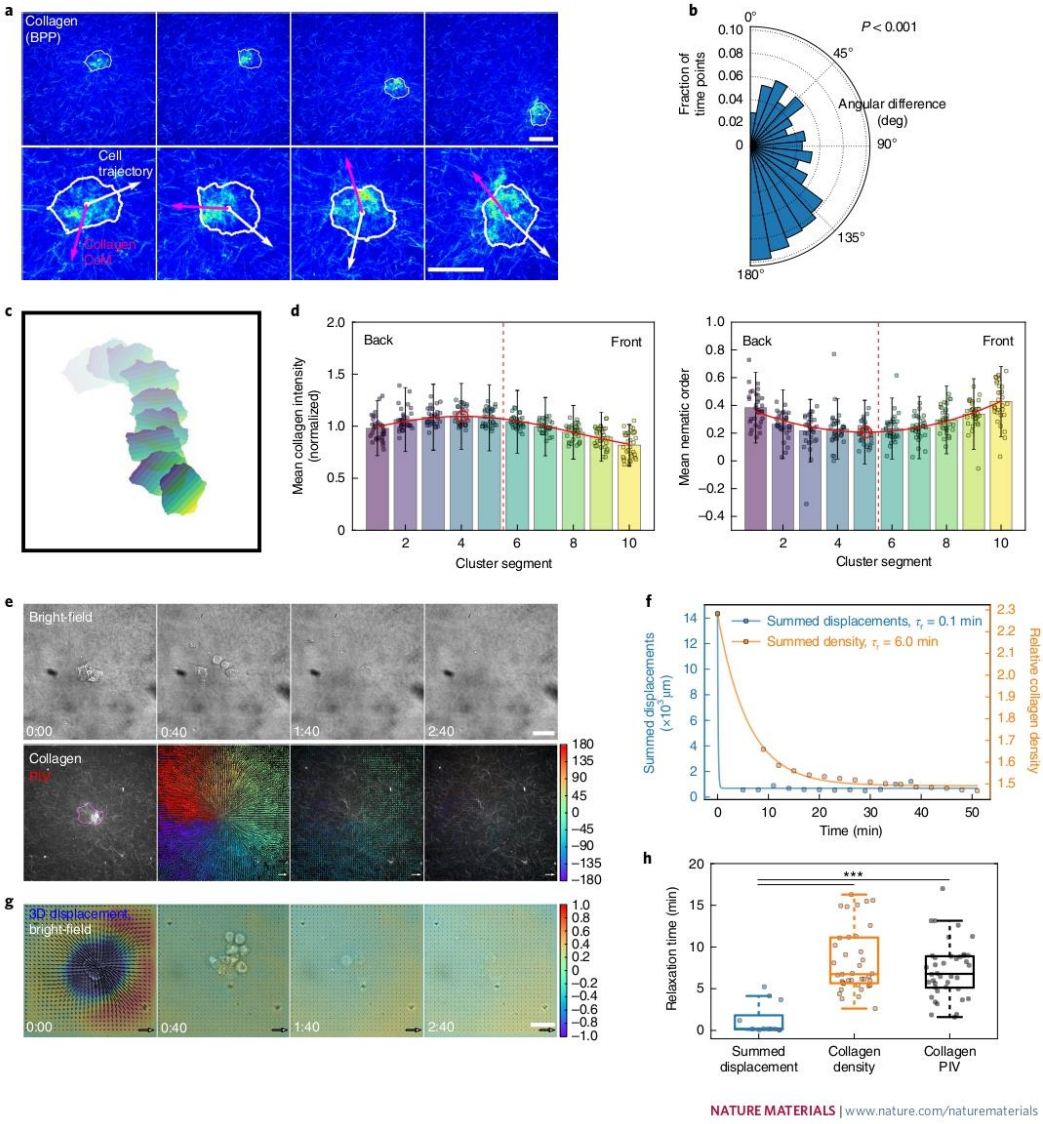

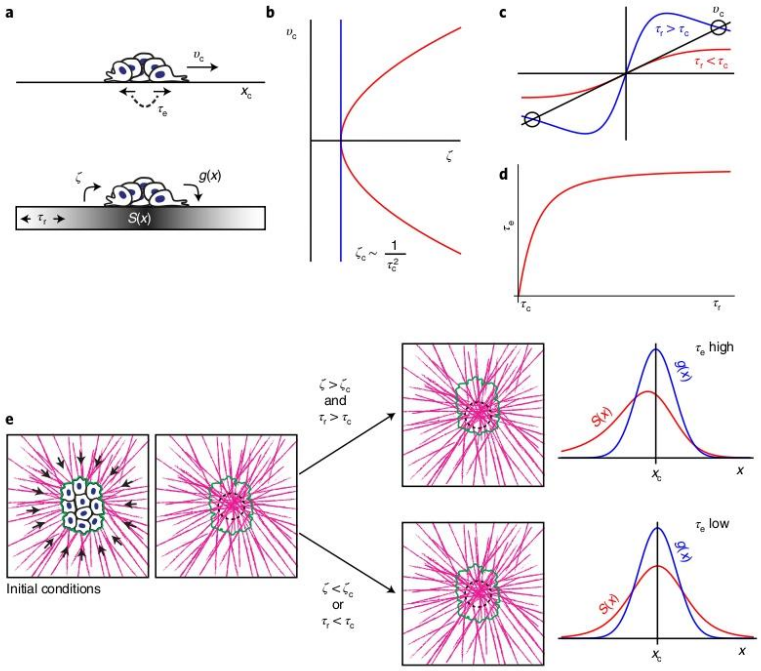

Fig. 3 | Theoretical model of persistent migration on a viscoelastic substrate. a, Schematic description of the model. A cluster of cells moves along the axis x_c with velocity v_c. The probability of switching migration direction is given by the timescale τ_e. The cell cluster interacts with the substrate according to a symmetric forcing function $g(x)$, resulting in a deformation of the substrate given by $S(x)$. The deformation in the substrate leads to a change in the activity in the cell cluster via the coupling ζ. As the substrate is viscoelastic, the relaxation is characterized by the timescale τ_r. **b**, The cell migration velocity v_c undergoes a supercritical pitchfork bifurcation at $\zeta=\zeta_c$. Here, v_c is plotted as a function of ζ for $g(\xi') = e^{-\xi'^2/2}$ (Supplementary Note 1). **c**, Solutions for migration velocity v_c for substrate relaxation times above or below the critical relaxation time. Solutions are shown by the intersection with the black line. While for $\tau_r < \tau_c$, only a stable ($v_c=0$) solution exists, a positive solution for v_c exists for $\tau_r > \tau_c$. **d**, Cluster persistence timescale τ_e as a function of the substrate relaxation timescale τ_r relative to the critical relaxation time τ_c. **e**, Interpretation of the model as it relates to experiments. Initially symmetric inward-directed tractions (left arrows) generate radially oriented collagen fibres (magenta), with a high collagen density in the centre of the cluster. After symmetry breaking, for networks with sufficient cell–substrate coupling ($\zeta > \zeta_c$) and relaxation time ($\tau_r > \tau_c$), clusters are predicted to migrate persistently (that is, τ_e is high) due to the offset between the driving function $g(x)$ and the substrate deformation $S(x)$ (top). If the coupling or relaxation times are below the critical values, $g(x)$ and $S(x)$ are both symmetric around x_c and low persistence migration (low τ_e) is predicted (bottom). Green contours, cell cluster position; black dotted circles, collagen centre of mass.

Theoretical model of migration on a viscoelastic substrate. To investigate how collagen gradients are formed and could help drive persistent migration, we developed a theoretical model of cluster migration on a viscoelastic substrate (Fig. 3a; also Supplementary Note 1 and Supplementary Figs. 1–6. The model describes the cell cluster as an isotropic active particle whose position along a one-dimensional axis is denoted by x_c. This active particle deforms an apolar viscoelastic substrate, causing a structural perturbation $S(x,t)$, whose equation of motion can be schematically written as

$$\tau_r \partial_t S = -S + \ell^2 \partial_x^2 S + \tau_r f g(x - x_c). \quad (1)$$

Here, ∂_t and ∂_x are partial derivatives with respect to time and space, respectively, τ_r is the viscoelastic relaxation time of the substrate, ℓ is a deformation length scale over which a point perturbation spreads out, f is the strength of the perturbation (proportional to the total stress exerted by the cluster on the substrate) and $g(x-x_c)$ is a normalized function that represents a spatially symmetric perturbation due to the particle's activity.

The isotropic particle actively responds to the substrate perturbation via a coupling term ζ, which parameterizes the active response of the cluster to the perturbation, giving the cluster velocity, v_c, as

$$v_c = \dot{x}_c \propto -\zeta \partial_x S|_{x_c}, \quad (2)$$

where the overdot in $\dot{x}_c$ denotes a time derivative. This simple model predicts that at a critical value of ζ_c, the particle's velocity will display a supercritical pitchfork bifurcation (Fig. 3b). For $\zeta < \zeta_c$, $v_c = 0$ and the cluster cannot migrate persistently. However, for $\zeta > \zeta_c$, $v_c \approx \pm(\zeta - \zeta_c)^{1/2}$, implying that the cluster migrates persistently in a random direction (forward or backward). Importantly, the critical value of activity scales with the relaxation time of the substrate as $\zeta_c \approx 1/(f\tau_r^2)$, implying that increasing the relaxation time beyond a critical value τ_c at a fixed coupling ζ leads to persistent motion of the cluster (Fig. 3c). In the presence of noise, the model predicts a

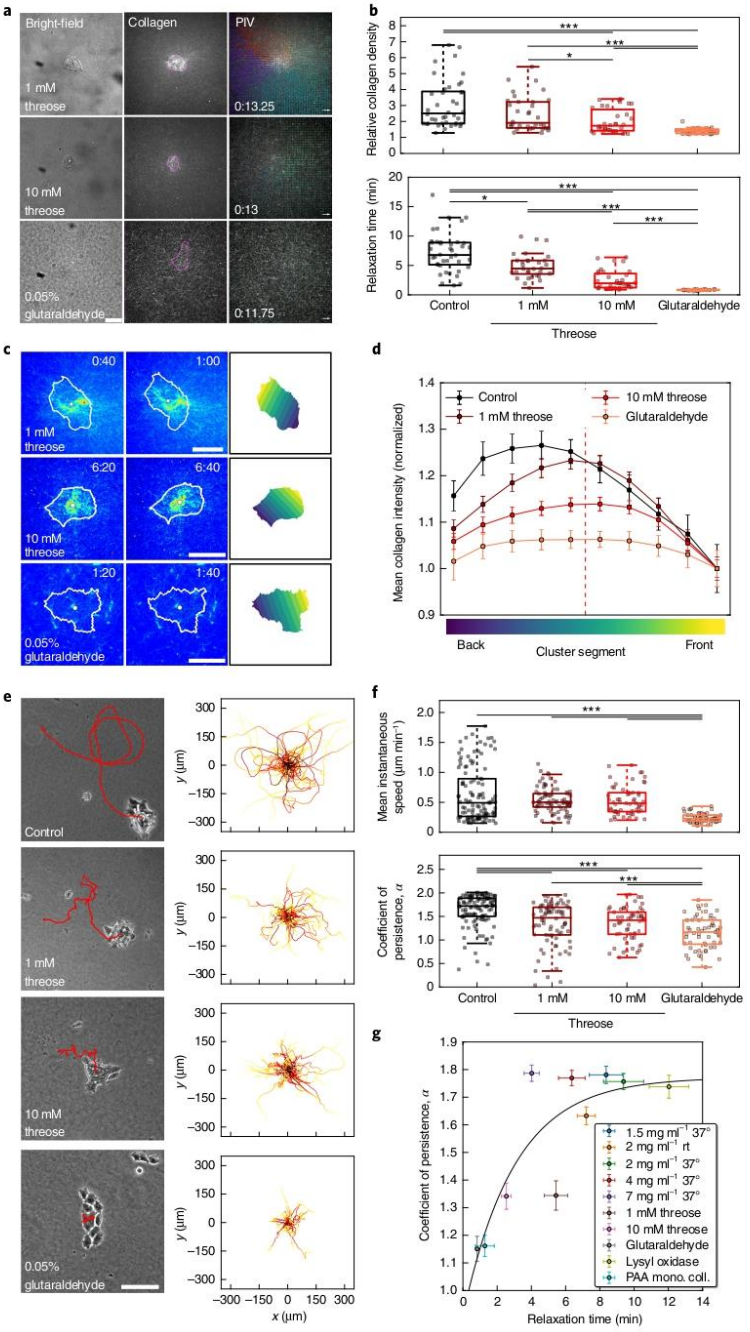
a
Bright-field
Collagen
PIV
1 mM threose
0:13.25
10 mM threose
0:13
0.05% glutaraldehyde
0:11.75
b
Relative collagen density
Relaxation time (min)
Control
1 mM
10 mM
Glutaraldehyde
Threose
c
0:40
1:00
1 mM threose
6:20
6:40
10 mM threose
1:20
1:40
0.05% glutaraldehyde
d
Control
1 mM threose
10 mM threose
Glutaraldehyde
Mean collagen intensity (normalized)
Back
Cluster segment
Front
e
Control
1 mM threose
10 mM threose
0.05% glutaraldehyde
y (μm)
x (μm)
f
Mean instantaneous speed (μm min⁻¹)
Coefficient of persistence, α
Control
1 mM
10 mM
Glutaraldehyde
Threose
g
Coefficient of persistence, α
Relaxation time (min)
1.5 mg ml⁻¹ 37°
2 mg ml⁻¹ rt
2 mg ml⁻¹ 37°
4 mg ml⁻¹ 37°
7 mg ml⁻¹ 37°
1 mM threose
10 mM threose
Glutaraldehyde
Lysyl oxidase
PAA mono. coll.

Fig. 4 | Collagen crosslinking decreases viscoelastic relaxation time and reduces migration persistence. a, Micrographs of cell clusters on fluorescent collagen networks crosslinked with threose or glutaraldehyde. Magenta lines indicate the cell contour. Scale bar, 50 μm. Scale vectors, 0.5 μm min^{-1}. Times in hours:minutes after cell removal with trypsin/NH_4OH. Also Supplementary Videos 8–10. **b**, Box plots of collagen density and relaxation time (τ_r) for conditions in **a**. Each dot represents one cluster. For **a** and **b**, representative images or data are from $n=39$, 31, 32 clusters and $N=5$, 4, 4 independent experiments. One-way ANOVA $P=8.21\times10^{-9}$, $P=3.75\times10^{-14}$, $^*P<0.05$, $^{***}P<0.001$ for Tukey honestly significant difference post-hoc test ($P=0.559$, <0.001, <0.001, 0.457, <0.001, <0.001; $P=0.0412$, <0.001, <0.001, <0.001, <0.001, <0.001). **c**, Sequential time points of cell clusters on crosslinked fluorescent collagen networks. White lines insdicate the cluster contour. White dots indicate the cluster centre of mass. Scale bars, 50 μm. Times are in hours:minutes. Right: cluster segmentation binned over the cluster length. Also Supplementary Videos 11–13. **d**, Plot of collagen intensity along the cluster length for clusters migrating on crosslinked collagen networks. For **c** and d, representative images or data are from $n=34$, 30, 17 clusters and $N=5$, 2, 3 independent experiments (mean ± s.e.m.). Control data are the same as in Fig. 2d. **e**, Bright-field micrographs from cell cluster migration on crosslinked collagen networks after 16 h of migration. Red lines indicate the cell trajectory. Scale bar, 100 μm. Right: overlaid migration trajectories for all tracked clusters, adjusted to start at the origin (0,0). Also Supplementary Videos 14–17. **f**, Box plots of mean instantaneous speed and coefficient of persistence. Each dot represents one cluster trajectory. For **e** and **f**, representative images or data are from $n=91$, 76, 57 clusters and $N=5$, 2, 2 independent experiments. One-way ANOVA $P=8.67\times10^{-12}$, 1.656×10^{-13}, $^{***}P<0.001$ for Tukey honestly significant difference post-hoc test ($P=0.073$, 0.101, <0.001, 0.881, <0.001, <0.001; $P<0.001$, <0.001, <0.001, 0.900, 0.00937, 0.00437). **g**, Plot of average coefficient of persistence versus viscoelastic relaxation time for different conditions of collagen polymerization or crosslinking or PAA gels coated with monomeric collagen (PAA mono. coll.). Mean ± s.e.m. for each condition from $n=30$, 40, 30, 20, 30, 34, 34, 29, 30, 12 clusters and $N=3$, 5, 3, 2, 3, 4, 4, 3, 3, 2 independent experiments. rt, room temperature.

Brownian-like random motion for $\zeta<\zeta_c$ or $\tau_r<\tau_c$. For $\zeta>\zeta_c$ at fixed τ_r or $\tau_r>\tau_c$ at fixed ζ, the model predicts persistent motion, whose persistence time increases with τ_r (Fig. 3d). Because traction force scales with cluster size[32], the intensity f of the perturbation likely depends on cluster size L. The coupling ζ is also likely to depend on cluster size, as clusters that are small compared to the deformation length scale ℓ would be too small to sense a collagen gradient. Our model therefore makes two important predictions: (1) migration persistence should decrease for substrates with lower relaxation times, and (2) migration persistence should be lower for small clusters (Fig. 3e).

Decreasing viscoelastic relaxation time reduces persistence. To test the prediction that reducing substrate relaxation time leads to reduced migration persistence, we crosslinked collagen networks using threose or glutaraldehyde and analysed collagen density and relaxation following rapid cell removal (Fig. 4a and Supplementary Videos 8–10). Crosslinking led to reduced initial collagen density prior to cell removal and reduced viscoelastic relaxation time following cell removal (Fig. 4b). Our theoretical model predicted that reducing τ_r would lead to a more symmetric collagen density profile. Indeed, collagen density gradients on crosslinked gels were more symmetric and had lower peak magnitudes compared with controls (Fig. 4c,d and Supplementary Videos 11–13). Clusters also migrated less persistently on crosslinked networks, while migration speed was reduced only for crosslinking with glutaraldehyde (Fig. 4e,f and Supplementary Videos 14–17). In addition, wound healing speed was significantly slower on glutaraldehyde-crosslinked collagen networks (Extended Data Fig. 8a,b), suggesting that collagen network viscoelasticity is also important for other modes of collective migration.

Treatment with the collagen-modifying enzyme lysyl oxidase led to increases in collagen viscoelastic relaxation time, migration speed and migration persistence, while collagen networks with higher collagen monomer concentrations exhibited reduced initial collagen densities and relaxation times (Extended Data Fig. 8c–e). Comparing migration persistence versus collagen relaxation time across all conditions, we found that for short relaxation times, migration persistence is low and highly dependent on relaxation time. For longer collagen relaxation times, migration persistence increases and eventually saturates, confirming the first major prediction of our model (Figs. 3d and 4g).

Migration persistence depends on cluster size. Our theoretical model predicted that migration persistence should scale with cluster size, as smaller clusters produce lower traction forces. To test this, we performed 3D displacement microscopy for differently sized clusters and single cells (Fig. 5a). Smaller clusters and single cells showed reduced substrate displacement, indicating that they indeed exert less mechanical stress on the substrate (Fig. 5b). Rapid cell removal experiments revealed that both initial collagen density and collagen relaxation time were lower for smaller clusters and single cells (Fig. 5c,d and Supplementary Video 18).

The degree of collagen reorganization by single cells is highly dependent on cell type. For cancer-associated fibroblasts (CAFs), which are known to be highly contractile and are specialized for

Fig. 5 | Collagen deformation and migration persistence depend on cluster size. a, The 3D displacement microscopy comparing clusters and single cells. Black arrows indicate *xy* displacements. Colour scale indicates *z* displacements (μm). Scale vector, 5 μm. **b**, Plot of 3D displacements versus cell or cluster area. Blue line indicates a power-law fit (all data). For **a** and **b**, representative images or data are from $n=27$, 25 clusters or cells, and $N=4$, 4 independent experiments. **c**, Micrograph of single cell on fluorescent collagen network. Magenta line indicates cell contour. Scale bar, 50 μm. Scale vector, 0.5 μm/min. Time is in hours:minutes after cell removal with trypsin/NH_4OH. Representative example from $n=22$ cells and $N=6$ independent experiments. Also Supplementary Video 18. **d**, Plot of relative collagen density and relaxation time. Each dot represents one cluster or single cell. Blue lines indicate a power-law fit (all data). Data from $n=38$, 22 clusters or single cells, and $N=6$, 6 independent experiments. Cluster data are the same as the control data in Fig. 4b. **e**, Sequential time points of a single cell on a fluorescent collagen network. White lines indicate cell contour. White dots indicate centre of mass. Scale bar, 50 μm. Times are in hours:minutes. Right: cell segmentation binned over cluster length. Lower panel: plot of collagen intensity along cell/cluster length. Mean ± s.e.m. over all time points for $n=34$, 38 clusters and $N=5$, 5 independent experiments. Cluster data are the same as in Fig. 2d. Also Supplementary Video 19. **f**, Plot of collagen gradient intensity for single cells and clusters. For **e** and **f**, representative images or data are from $n=34$, 38 clusters or single cells, and $N=5$, 5 independent experiments. **g**, Bright-field micrograph from single cell migration on collagen network after 16 h. Red indicates cell trajectory. Right: overlaid migration trajectories adjusted to start at the origin (0,0). Representative example from $n=91$ cells and $N=3$ independent experiments. Scale bar, 50 μm. Also Supplementary Video 20. **h**, Scatter plots of mean instantaneous speed and coefficient of persistence. Each dot represents one trajectory from $n=91$, 91 clusters or single cells, and $N=5$, 3 independent experiments. Cluster data are the same as the control data in Fig. 4f.

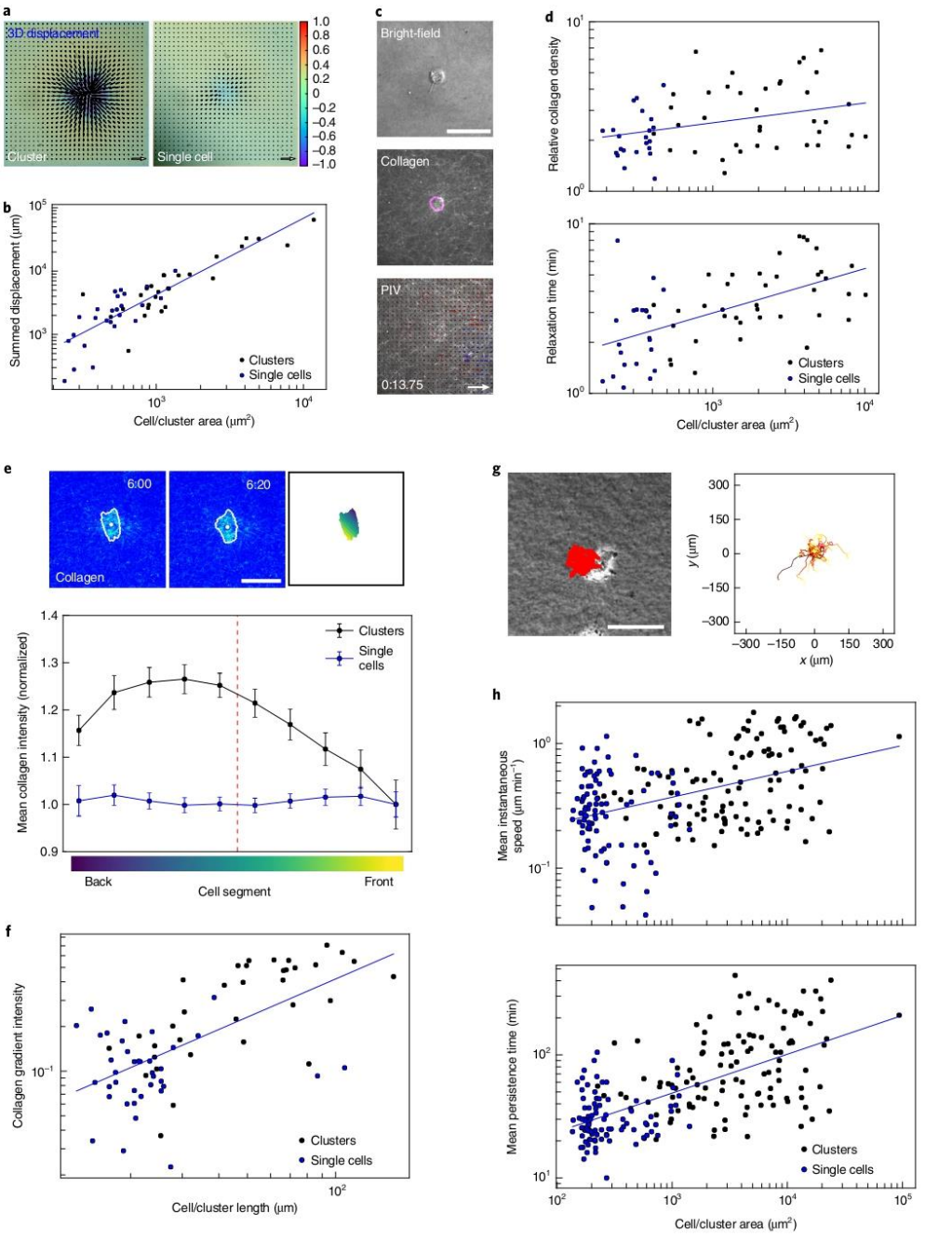
a
3D displacement
Cluster
Single cell
1.0
0.8
0.6
0.4
0.2
0
−0.2
−0.4
−0.6
−0.8
−1.0
b
Summed displacement (μm)
Cell/cluster area (μm²)
Clusters
Single cells
c
Bright-field
Collagen
PIV
0:13.75
d
Relative collagen density
Relaxation time (min)
Cell/cluster area (μm²)
Clusters
Single cells
e
6:00
6:20
Collagen
Mean collagen intensity (normalized)
Clusters
Single cells
Back
Front
Cell segment
f
Collagen gradient intensity
Cell/cluster length (μm)
Clusters
Single cells
g
y (μm)
x (μm)
h
Mean instantaneous speed (μm min⁻¹)
Mean persistence time (min)
Cell/cluster area (μm²)
Clusters
Single cells

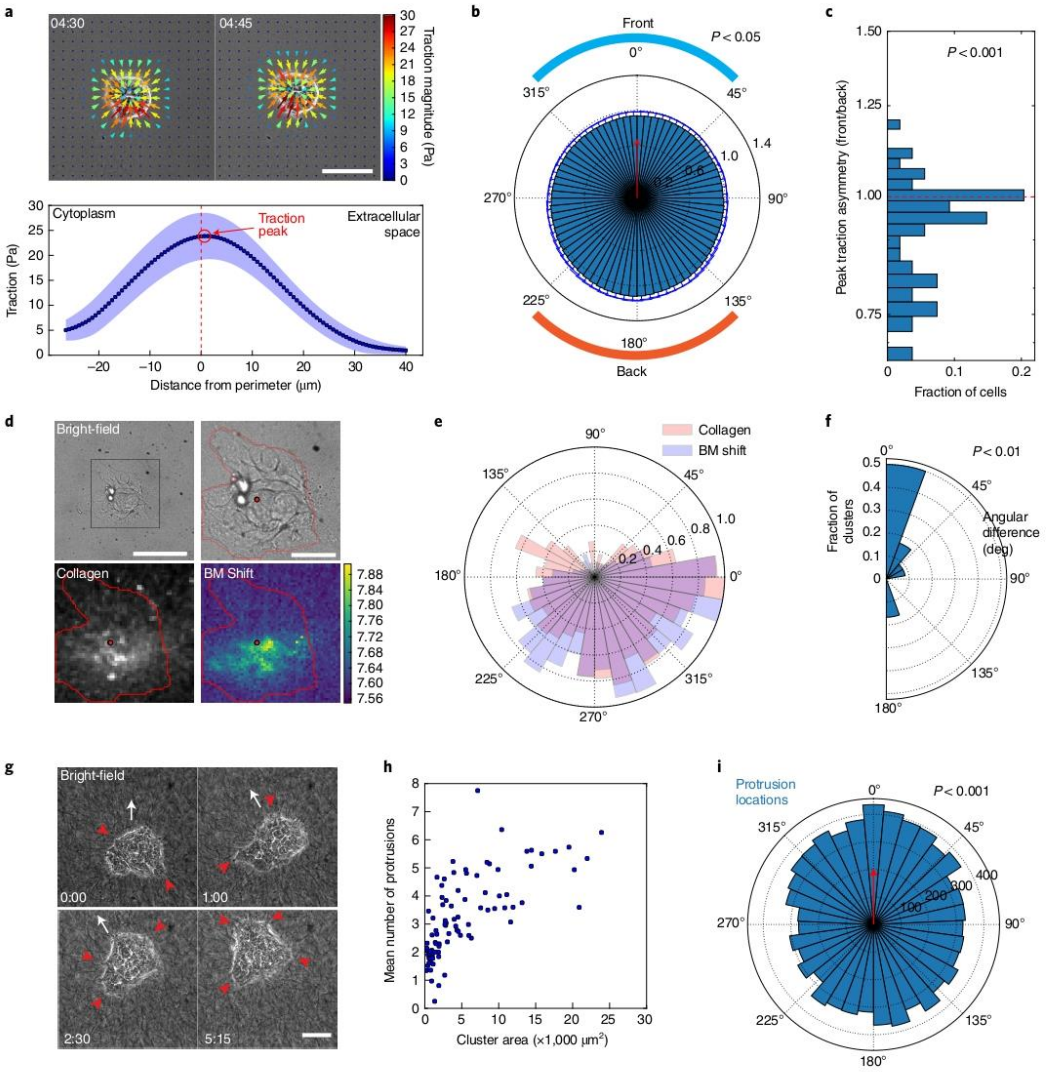

Fig. 6 | Persistent migration is associated with asymmetries in traction force distribution and collagen stiffness gradients. a, Example micrograph overlaid with traction force vectors (arrows) for a cluster on a PAA gel plus thin collagen network. Scale bar, 100 μm. Times are in hours:minutes. Lower panel: average line scan (mean ± s.d.) of traction forces around the cell cluster. Red dotted line indicates the cluster periphery. Red circle indicates the peak traction force magnitude. Also Supplementary Video 21. **b**, Polar plot of peak traction force magnitude (mean ± s.d.) with respect to migration direction (red arrow). **c**, Histogram of peak traction force asymmetry (front/back quadrants). The *y* axis is shown in log scale. For **a**–**c**, representative images or data are from $n = 27$ clusters and $N = 3$ independent experiments. *P* value, two-sided *t*-test with hypothesized mean $\mu_0 = 1$ ($P = 3.66 \times 10^{-5}$). **d**, Micrographs showing collagen density and BM shift (a proxy for stiffness). Red lines indicate cluster contour. Red dots indicate cluster centre of mass. Scale bars, 50 μm (left), 20 μm (right). Colour bar indicates Brillouin shift (GHz). **e**, Polar histogram of maximum collagen density (red) and BM shift (blue) at different angles from the centre of mass of the cluster in **d**. Data were rescaled to the range 0–1 to exemplify regional differences. **f**, Polar histogram of the angular difference between maximum collagen density and maximum Brillouin shift. *P* value, Rayleigh test of uniformity ($P = 0.00389$). For **d**–**f**, representative image or data are from $n = 13$ clusters and $N = 3$ independent experiments. **g**, Bright-field montage of a cluster migrating on a collagen network. White arrows indicate migration direction. Red arrowheads indicate protrusion locations. Scale bar, 50 μm. Times are in hours:minutes. **h**, Plot of mean number of simultaneous protrusions per clusters versus cluster area. Each dot represents one cluster. **i**, Radial histogram of protrusion location relative to the migration direction (red arrow). For **g**–**i**, representative images or data are from $n = 91$ clusters and $N = 6$ independent experiments. *P* value, Rayleigh test of uniformity ($P = 2.44 \times 10^{-11}$).

collagen modification[33], collagen densities before and after cell removal were higher for single CAFs compared to A431 clusters, and viscoelastic relaxation times were shorter following CAF removal (Extended Data Fig. 9a–c). These data suggest that CAFs can more efficiently and permanently remodel collagen compared to epithelial cell clusters (also Supplementary Discussion).

To test the prediction that single A431 cells are too small to sense collagen gradients, we performed live imaging of single cells migrating on fluorescent collagen networks. The resulting collagen density profile was constant along the length of single cells, and the intensity of the collagen gradient was lower for smaller clusters (Fig. 5e,f and Supplementary Video 19). Consistent with these data and our theoretical model, smaller clusters and single cells migrated with lower mean instantaneous speeds and lower persistence compared to larger clusters (Fig. 5g,h and Supplementary Video 20). We observed a similar difference between migration speed and persistence for clusters versus single cells for Caco2 cells, an epithelial colorectal cancer cell line (Extended Data Fig. 9d–f). This suggests that the dependence of persistence on cluster size is a general phenomenon.

To investigate whether imposed collagen alignment could increase the persistence of single cell migration in A431 cells to similar levels as that of clusters, we compared the migration dynamics of clusters and single cells on thin non-deformable aligned collagen networks. Similar to the results with clusters, single cells preferentially migrated along the collagen alignment axis, but with reduced speed and persistence compared to migration on thin isotropic collagen networks (Extended Data Fig. 9g–i). Together, these data confirm the second major prediction of our model, that small clusters and single cells migrate with lower persistence compared to larger clusters.

Traction forces are asymmetric during collective migration. To better understand the generation of mechanical force during collective migration, we performed two-dimensional (2D) traction force microscopy on cell clusters migrating on thin collagen networks polymerized on soft PAA gels (Fig. 6a, upper panels and Supplementary Video 21). Clusters generated radial inward-facing tractions around the perimeter of the cluster that peaked near the cluster contour (Fig. 6a, lower panel). Peak tractions were higher for clusters on PAA coated with monomeric collagen versus PAA coated with thin collagen networks and scaled with cluster size in both conditions (Extended Data Fig. 10a,b), suggesting that non-persistent migration on monomeric collagen is not due simply to insufficient force generation.

Treatment of clusters with blebbistatin led to a significant reduction in 3D substrate displacements, suggesting that cell-generated stresses are largely driven by myosin-2 activity (Extended Data Fig. 10c–e). Long-term treatment with blebbistatin led to a dissolution of clusters (Extended Data Fig. 10f), consistent with previous studies[23,34]. As myosin activity drives retrograde actin flow in cellular protrusions[35], we analysed actin flows along the migration direction in clusters from A431 cells stably expressing the fluorescent F-actin probe LifeAct-mCherry (Extended Data Fig. 10g and Supplementary Video 22). Clusters exhibited inward-facing actin flows with a slight overall bias towards rearward-facing flows (Extended Data Fig. 10h,i).

To investigate the distribution of traction forces during collective migration, we measured the peak traction magnitude with respect to the migration direction (Fig. 6b). The traction peak at the rear of the cluster was ~10% higher compared to the leading edge of the cluster (Fig. 6b,c). Traction peak asymmetry was lower for smaller clusters and single cells (Extended Data Fig. 10j), consistent with our observation that migration persistence also depends on cluster size. Projecting the tractions along the migration axis, we found that projected tractions were negative (rearward facing) at the front and positive (forward facing) at the rear (Extended Data Fig. 10k,l). The traction peak was slightly higher in the rear, while the tail of the traction decay at the front was slightly wider, indicating an asymmetry in the distribution of traction forces at the front versus rear of the cluster (Extended Data Fig. 10m,n). As expected from the force balance, the vectorial sum of the tractions was zero. Together, these data suggest that cell clusters exhibit asymmetric traction force profiles on collagen networks during migration.

Clusters generate stiffness gradients during migration. Previous studies have shown that networks with higher collagen concentrations are stiffer[12,14,36]. To determine whether local collagen density gradients generated during migration correlated with changes in collagen network mechanics, we performed Brillouin microscopy (BM), a purely optical technique that allows for the acquisition of 3D maps of viscoelastic properties[37,38]. We analysed the maximum collagen density and Brillouin shift in the collagen network for different angles around the cluster (Fig. 6d,e). Regions of high collagen density correlated with regions of higher Brillouin shift (Fig. 6e,f), suggesting that cell clusters generate local gradients not only in collagen density and alignment, but also in substrate stiffness, and that clusters migrate persistently down these stiffness gradients during migration.

We next asked whether the observed gradients in collagen density, stiffness and nematic order could influence protrusive activity during migration. To this end, we quantified cellular protrusions in migrating cell clusters with respect to the migration direction (Fig. 6g). Clusters typically displayed multiple simultaneous protrusions, and the average number of protrusions increased with increasing cluster area (Fig. 6h). When we compared the protrusion angles with the migration angle, we found a slight, but significant, bias in protrusion localization towards the front of migrating clusters (Fig. 6i). These data suggest that the local reorganization of the collagen network during migration could bias the protrusion location towards the leading edge of the cluster and thereby promote persistent migration.

Outlook

Here we provide a simple physical mechanism for persistent collective cell migration on ECM networks that does not depend on internal biochemical polarity and can be applied to other systems, both living and artificial (Supplementary Discussion and Supplementary Note 1). This mechanism is similar in spirit to a model showing that apolar colloidal particles can become spontaneously self-propelled and swim persistently due to hydrodynamic flows generated during particle motion[39]. The mechanism also shares similarities with a recent model of spontaneous persistent migration for cells migrating in uniform concentrations of chemokine by self-generated chemotaxis, where chemokine depletion leads to the generation of transient local gradients[40].

Several reports have shown that cells can undergo collective durotaxis, even generating stiffness gradients during migration[41–43]. Our data imply that cell clusters migrate away from regions of high collagen stiffness, suggesting that they could be undergoing 'negative' durotaxis. Migration towards softer substrates has recently been described for single cells in vitro and in vivo, namely during axonal migration[44,45]. Future studies will be required to better understand the mechanistic differences between positive and negative durotaxis. One aspect of mechanosensing during migration that has been little studied is the role of substrate viscoelaticity, which is crucial for driving persistent collective migration in our study. Other recent reports have shown that substrate viscoelasticity can impact cell spreading, migration and collective behaviour in both 2D and 3D environments[46–48], arguing that substrate viscoelasticity should also be considered alongside elastic stiffness.

Collective cell migration has emerged as a potential mechanism for tumour dissemination in early stages of metastasis. Although previous studies suggest that migrating as a group may offer advantages in cell survival or chemotaxis prowess[6,49,50], it has been unclear whether collective migration offers any specific advantage over single cell migration in stroma-like environments. The results presented here provide a mechanism for increased migration efficiency for groups of cells migrating collectively that does not require any intrinsic cell or cluster polarity, but relies simply on physical interactions with viscoelastic collagen networks. Future studies will help to uncover how this mechanism can be applied to better understand collective stromal migration during early metastasis.

Online content

Any methods, additional references, Nature Research reporting summaries, source data, extended data, supplementary information, acknowledgements, peer review information; details of author contributions and competing interests; and statements of data and code availability are available at https://doi.org/10.1038/s41563-022-01259-5.

Received: 11 July 2020; Accepted: 13 April 2022;
Published online: 30 May 2022

References

1. Friedl, P. & Gilmour, D. Collective cell migration in morphogenesis, regeneration and cancer. *Nat. Rev. Mol. Cell Biol.* **10**, 445–457 (2009).
2. *Cancer as a Disease* (US National Institutes of Health, National Cancer Institute, 2017); https://training.seer.cancer.gov/disease/
3. Prall, F. Tumour budding in colorectal carcinoma. *Histopathology* **50**, 151–162 (2007).
4. Wang, L. M. et al. Tumor budding is a strong and reproducible prognostic marker in T3N0 colorectal cancer. *Am. J. Surg. Pathol.* **33**, 134–141 (2009).
5. Ohike, N. et al. Tumor budding as a strong prognostic indicator in invasive ampullary adenocarcinomas. *Am. J. Surg. Pathol.* **34**, 1417–1424 (2010).
6. Aceto, N. et al. Circulating tumor cell clusters are oligoclonal precursors of breast cancer metastasis. *Cell* **158**, 1110–1122 (2014).
7. Koelzer, V. H., Zlobec, I. & Lugli, A. Tumor budding in colorectal cancer—ready for diagnostic practice? *Hum. Pathol.* **47**, 4–19 (2016).
8. Cho, S.-J. & Kakar, S. Tumor budding in colorectal carcinoma: translating a morphologic score into clinically meaningful results. *Arch. Pathol. Lab. Med.* **142**, 952–957 (2018).
9. Pryse, K. M., Nekouzadeh, A., Genin, G. M., Elson, E. L. & Zahalak, G. I. Incremental mechanics of collagen gels: new experiments and a new viscoelastic model. *Ann. Biomed. Eng.* **31**, 1287–1296 (2003).
10. Krishnan, L., Weiss, J. A., Wessman, M. D. & Hoying, J. B. Design and application of a test system for viscoelastic characterization of collagen gels. *Tissue Eng.* **10**, 241–252 (2004).
11. Xu, B., Li, H. & Zhang, Y. Understanding the viscoelastic behavior of collagen matrices through relaxation time distribution spectrum. *Biomatter* **3**, e24651 (2013).
12. Licup, A. J. et al. Stress controls the mechanics of collagen networks. *Proc. Natl Acad. Sci. USA* **112**, 9573–9578 (2015).
13. Nam, S., Hu, K. H., Butte, M. J. & Chaudhuri, O. Strain-enhanced stress relaxation impacts nonlinear elasticity in collagen gels. *Proc. Natl Acad. Sci. USA* **113**, 5492–5497 (2016).
14. Jansen, K. A. et al. The role of network architecture in collagen mechanics. *Biophys. J.* **114**, 2665–2678 (2018).
15. Shi, Q. et al. Rapid disorganization of mechanically interacting systems of mammary acini. *Proc. Natl Acad. Sci. USA* **111**, 658–663 (2014).
16. Kopanska, K. S., Alcheikh, Y., Staneva, R., Vignjevic, D. & Betz, T. Tensile forces originating from cancer spheroids facilitate tumor invasion. *PLoS ONE* **11**, e0156442 (2016).
17. Staneva, R. et al. A new biomimetic assay reveals the temporal role of matrix stiffening in cancer cell invasion. *Mol. Biol. Cell* **29**, 2979–2988 (2018).
18. Provenzano, P. P. et al. Collagen reorganization at the tumor-stromal interface facilitates local invasion. *BMC Med.* **4**, 38 (2006).
19. Conklin, M. W. et al. Aligned collagen is a prognostic signature for survival in human breast carcinoma. *Am. J. Pathol.* **178**, 1221–1232 (2011).
20. Riching, K. M. et al. 3D collagen alignment limits protrusions to enhance breast cancer cell persistence. *Biophys. J.* **107**, 2546–2558 (2014).
21. Fraley, S. I. et al. Three-dimensional matrix fiber alignment modulates cell migration and MT1-MMP utility by spatially and temporally directing protrusions. *Sci. Rep.* **5**, 14580 (2015).
22. Sapudom, J. et al. The phenotype of cancer cell invasion controlled by fibril diameter and pore size of 3D collagen networks. *Biomaterials* **52**, 367–375 (2015).
23. Hidalgo-Carcedo, C. et al. Collective cell migration requires suppression of actomyosin at cell–cell contacts mediated by DDR1 and the cell polarity regulators Par3 and Par6. *Nat. Cell. Biol.* **13**, 49–58 (2011).
24. Peyton, S. R. & Putnam, A. J. Extracellular matrix rigidity governs smooth muscle cell motility in a biphasic fashion. *J. Cell Physiol.* **204**, 198–209 (2005).
25. Ulrich, T. A., de Juan Pardo, E. M. & Kumar, S. The mechanical rigidity of the extracellular matrix regulates the structure, motility, and proliferation of glioma cells. *Cancer. Res.* **69**, 4167–4174 (2009).
26. Wolf, K. et al. Physical limits of cell migration: control by ECM space and nuclear deformation and tuning by proteolysis and traction force. *J. Cell Biol.* **201**, 1069–1084 (2013).
27. Ridley, A. J. et al. Cell migration: integrating signals from front to back. *Science* **302**, 1704–1709 (2003).
28. Yam, P. T. et al. Actin–myosin network reorganization breaks symmetry at the cell rear to spontaneously initiate polarized cell motility. *J. Cell Biol.* **178**, 1207–1221 (2007).
29. Allen, G. M. et al. Cell mechanics at the rear act to steer the direction of cell migration. *Cell Systems* **11**, 286–299 (2020).
30. Itoh, R. E. et al. Activation of Rac and Cdc42 video imaged by fluorescent resonance energy transfer-based single-molecule probes in the membrane of living cells. *Mol. Cell. Biol.* **22**, 6582–6591 (2002).
31. Gao, Y., Dickerson, J. B., Guo, F., Zheng, J. & Zheng, Y. Rational design and characterization of a Rac GTPase-specific small molecule inhibitor. *Proc. Natl Acad. Sci. USA* **101**, 7618–7623 (2004).
32. Mertz, A. F. et al. Scaling of traction forces with the size of cohesive cell colonies. *Phys. Rev. Lett.* **108**, 198101 (2012).
33. Gaggioli, C. et al. Fibroblast-led collective invasion of carcinoma cells with differing roles for RhoGTPases in leading and following cells. *Nat. Cell. Biol.* **9**, 1392–1400 (2007).
34. Pérez-González, C. et al. Active wetting of epithelial tissues. *Nat. Phys.* **15**, 79–88 (2019).
35. Vallotton, P., Gupton, S. L., Waterman-Storer, C. M. & Danuser, G. Simultaneous mapping of filamentous actin flow and turnover in migrating cells by quantitative fluorescent speckle microscopy. *Proc. Natl Acad. Sci. USA* **101**, 9660–9665 (2004).
36. Lee, B. et al. A three-dimensional computational model of collagen network mechanics. *PLoS ONE* **9**, e111896 (2014).
37. Scarcelli, G. & Yun, S. H. Confocal Brillouin microscopy for three-dimensional mechanical imaging. *Nat. Photon.* **2**, 39–43 (2008).
38. Prevedel, R., Diz-Muñoz, A., Ruocco, G. & Antonacci, G. Brillouin microscopy: an emerging tool for mechanobiology. *Nat. Methods* **16**, 969–977 (2019).
39. Michelin, S., Lauga, E. & Bartolo, D. Spontaneous autophoretic motion of isotropic particles. *Phys. Fluids* **25**, 061701 (2013).
40. Tweedy, L. et al. Seeing around corners: cells solve mazes and respond at a distance using attractant breakdown. *Science* **369**, eaay9792 (2020).
41. Sunyer, R. et al. Collective cell durotaxis emerges from long-range intercellular force transmission. *Science* **353**, 1157–1161 (2016).
42. Barriga, E. H., Franze, K., Charras, G. & Mayor, R. Tissue stiffening coordinates morphogenesis by triggering collective cell migration *in vivo*. *Nature* **554**, 523–527 (2018).
43. Shellard, A. & Mayor, R. Collective durotaxis along a self-generated stiffness gradient in vivo. *Nature* **600**, 690–694 (2021).
44. Thompson, A. J. et al. Rapid changes in tissue mechanics regulate cell behaviour in the developing embryonic brain. *eLife* **8**, e39356 (2019).
45. Isomursu, A. et al. Negative durotaxis: cell movement toward softer environments. Preprint at *bioRxiv* https://www.biorxiv.org/content/10.1101/2020.10.27.357178v1 (2020).
46. Chaudhuri, O., Cooper-White, J., Janmey, P. A., Mooney, D. J. & Shenoy, V. B. Effects of extracellular matrix viscoelasticity on cellular behaviour. *Nature* **584**, 535–546 (2020).
47. Mandal, K., Gong, Z., Rylander, A., Shenoy, V. B. & Janmey, P. A. Opposite responses of normal hepatocytes and hepatocellular carcinoma cells to substrate viscoelasticity. *Biomater. Sci.* **8**, 1316–1328 (2020).
48. Elosegui-Artola, A. et al. Matrix viscoelasticity controls spatio-temporal tissue organization. Preprint at *bioRxiv* https://www.biorxiv.org/content/10.1101/2022.01.19.476771v1 (2022).
49. Malet-Engra, G. et al. Collective cell motility promotes chemotactic prowess and resistance to chemorepulsion. *Curr. Biol.* **25**, 242–250 (2015).
50. Shellard, A., Szabó, A., Trepat, X. & Mayor, R. Supracellular contraction at the rear of neural crest cell groups drives collective chemotaxis. *Science* **362**, 339–343 (2018).

Methods

All research performed for this study was carried out in accordance with local ethical regulations. Experiments involving human samples were approved by the 'Committee of Protection of Patient Rights' at Institut Curie and validated by the ethics committee of the ERC STARNEL project.

Cell culture and preparation. A431 cells were cultured in DMEM medium (Gibco/Life Technologies) supplemented with 10% foetal bovine serum (FBS; Gibco). A431 wild-type cells were a gift from C. Rosse and P. Chavrier (Institut Curie) and were authenticated using the Gene Print 10 System (Promega). A431 MLC-GFP and A431 Raichu-Rac cells were a gift from T. Kato and E. Sahai (Francis Crick Institute); parental A431 lines were authenticated by short tandem repeat profiling. Stable GFP-CAAX/mCherry-H2B lines were generated following transfection using Lipofectamine 3000 (Invitrogen/Life Technologies) according to manufacturer instructions. GFP-CAAX and mCherry-H2B plasmids were obtained as a gift by E. Paluch, and selection for stable cells was performed by treatment with G418/hygromycin B. Stable LifeAct-mCherry, paxillin-GFP and zyxin-mCherry lines were generated by lentiviral infection using the pPAX2/pMD2.G packaging system in Hek293 FT cells transfected by $CaCl_2$ with help from J. Barbazan, O. Zajac and R. Bouras. The LifeAct-mCherry plasmid was a gift from G. Montagnac. The paxillin-GFP and zyxin-mCherry plasmids were designed in the lab of X. Trepat. Caco2 cells, a gift from G. Montagnac (originally American Type Culture Collection), were cultured in the same manner. All cells were passaged 2–3 times per week and tested for mycoplasma every two weeks.

Cell clusters were prepared by adding ~2×10^6 cells to a 10 cm dish that was precoated with 1% agarose in phosphate buffered saline (PBS) and filled with DMEM plus 10% FBS plus ×2 Antibiotic-Antimycotic (Gibco/LifeTechnologies). Cells were cultured in these non-adherent conditions overnight prior to being seeded on substrates for imaging. Before seeding, large clusters and single cells were removed: (1) the medium containing the clusters from the agarose-coated dish was pipetted into a 15 ml falcon tube, (2) large clusters were allowed to sediment for 1 min before all but 0.5 ml of the medium was transferred to a new 15 ml falcon tube, (3) cells were centrifuged briefly at ~140*g* and the supernatant was discarded, and (4) the pellet was resuspended in 0.5 ml medium; ~15–60 µl cluster solution was used for seeding. For single cell experiments, cells were detached, and 2×10^3 cells were seeded on collagen networks. Cells were seeded in AB+ medium (DMEM + 10% FBS + ×2 Anti/Anti + 0.125% metronidazole (w/v) + 4 µg ml^{-1} ciprofloxacin) and imaged two to three days after seeding.

Human primary fibroblasts were isolated from untreated colorectal cancer biopsies from patients treated at Institut Curie Hospital, Paris, with written consent of the patients. The project has been approved by the 'Committee of Protection of Patient Rights' at Institut Curie and validated by the ethics committee of the ERC STARNEL project.

Preparation of isotropic and aligned collagen networks. For experiments with cells or clusters on collagen networks, 3.5-cm-diameter glass-bottom dishes (WPI) were precoated with 3-amino-propyltrimethoxysilane (diluted 1:2 with water; Sigma-Aldrich/Merck) and glutaraldehyde (0.5% in PBS; Sigma-Aldrich/Merck) and washed well with water. Then 200–600 µl of neutralized rat tail collagen-I solution (2 mg ml^{-1}; Corning) was pipetted onto each dish and incubated at 37 °C with humidity for 20 min before adding 2 ml AB+ medium with cells/clusters. For experiments testing different collagen concentrations or polymerization temperatures, the same procedure was followed but with the concentration/temperature specified in the experiment.

To generate thick, deformable, aligned collagen networks, we first prepared polydimethylsiloxane (PDMS) chambers for suspending the collagen network. PDMS (Sylgard 184; Dow) components were mixed vigorously in a 1:10 ratio, degassed by centrifugation, poured into a flat aluminium boat to a thickness of ~2.5 mm and cured at 80 °C for 2 h to overnight. Thin octagonal slabs (~0.5 cm side length) were then cut out using a scalpel, and a hole was punched in the middle of the slab using a 3-mm-diameter biopsy punch (WPI). Slabs were then prestressed by inserting a sharp forceps on either side of the punched hole and stretching the PDMS slab by opening the forceps. Then, 2 mg ml^{-1} neutralized rat tail collagen-I solution was prepared, and 20 µl was pipetted into the hole. The collagen solution was incubated at room temperature for 30 min to allow for polymerization. The forceps were then removed from the PDMS slab, resulting in a relaxation to its original shape and an alignment of collagen in the direction orthogonal to the stretch. The PDMS slabs were then affixed to 3.5 cm glass-bottom dishes using vacuum grease; AB+ medium was added, and clusters were plated on the aligned collagen networks.

To generate thin, non-deformable, aligned collagen networks, 3.5 cm glass-bottom dishes precoated with silane and glutaraldehyde were affixed with Patafix (UHU) to the inner edge of a larger 10 cm Petri dish. Some 2 mg ml^{-1} neutralized rat tail collagen-I solution was then prepared and kept on ice. A 67 µl droplet of collagen solution was pipetted onto one side of each glass-bottom dish (the 'top') and incubated at room temperature for 8 min. The 10 cm Petri dish containing the glass-bottom dishes was then tipped at a ~70° angle downward, so that the collagen droplet ran down each glass-bottom dish, pulled by gravity. The excess collagen at the bottom of each glass-bottom dish was then aspirated using a micropipette. The dishes were then incubated at 37 °C to further polymerize (while remaining tipped at a ~70° angle). The dishes were then returned to room temperature and placed flat on the bench top, and the process of adding a droplet of collagen, tipping the dish and incubating was repeated two additional times. After the final collagen coating, the dishes were incubated at 37 °C for 15 min. AB+ medium was then added, and clusters were plated on the aligned collagen networks.

Preparation of PAA substrates. For experiments using coated PAA gels, PAA solutions for 0.5 kPa gels were prepared by mixing 50 µl 40% acrylamide (Bio-Rad), 7.5 µl 2% bis-acrylamide (Bio-Rad), 2.5 µl 10% ammonium peroxodisulfate (VWR) and 0.25 µl tetramethylethylenediamine (Euromedex) in PBS (full volume 500 µl). Then, 16 µl of solution was pipetted onto silane/gluteraldehye-coated glass-bottom dishes and covered with a round 18-mm-diameter coverslip. Gels were incubated for 60 min before washing with PBS and removing the coverslip. For traction force microscopy experiments, 10 µl 2% 0.5-µm-diameter green fluorescent polystyrene beads (Invitrogen/ThermoFisher) were also added.

PAA gels were coated by incubating the gel with 2 mg ml^{-1} sulfo-SANPAH (Sigma-Aldrich/Merck) under ultraviolet light (365 nm; 10 cm from source) for 10 min. The gel was then washed two times for 3 min each with 10 mM HEPES buffer and once for 3 min with PBS to remove the excess sulfo-SANPAH. For coating with thin collagen networks, 100 µl of neutralized 2 mg ml^{-1} collagen solution was added to cover the PAA gel, and all excess collagen solution was immediately removed. Collagen was allowed to polymerize at 37 °C with humidity for 20 min. For coating with monomeric collagen, the desired concentration of collagen (100 µg ml^{-1} for Fig. 1; different concentrations for Extended Data Fig. 2) was diluted in 0.2% acetic acid and pipetted to cover the PAA gel. The dish was then incubated at 37 °C with humidity for 1 h and washed briefly with PBS before adding AB+ medium and clusters.

Immunostaining. For immunostaining of Rac1 in cell clusters, dishes containing clusters on collagen networks were washed briefly with PBS and then simultaneously fixed and extracted using a solution of 4% paraformaldehyde (PFA), 5% sucrose and 0.3% Triton X-100 in PBS for 5 min at room temperature. Cells were then further fixed with 4% PFA and 5% sucrose in PBS for 40 min at room temperature before washing two times for 5 min each with PBS. Cells were stained with a primary antibody solution of 1:100 mouse–anti-Rac1 antibody (610650, BD Biosciences) in PBS overnight. The following day, cells were washed five times for 30 min each with PBS plus 0.1% Tween20 (PBS-T) and then stained with a secondary antibody solution of 1:200 goat–anti-mouse IgG–Alexa568 (ThermoFisher) plus 1:200 4′,6-diamidino-2-phenylindole (DAPI) plus 1:200 phalloidin–Alexa633 (ThermoFisher) in PBS overnight. Samples were then washed five times for 30 min each with PBS-T and incubated in PBS plus ×2 Anti/Anti until imaging. Rac1-stained clusters were imaged in 3D using an upright spinning disc confocal (Zeiss) with a ×63 dipping objective (numerical aperture (NA), 1.0) and 1 µm *z* steps driven by Metamorph software (v.7.8.13.0).

For immunostaining of centrosomes, cell clusters were washed briefly with PBS and fixed with 4% PFA in PBS for 40 min at room temperature. Samples were then washed briefly with PBS, extracted with 0.5% Triton X-100 in PBS for 5 min and then washed three times for 5 min each in PBS. Cells were stained with a primary antibody solution of 1:500 rabbit–anti-pericentrin antibody (ab4448, Abcam; gift from V. Marthiens and R. Basto) in PBS overnight. The following day, cells were washed five times for 30 min each with PBS-T and then stained with a secondary antibody solution of 1:200 goat–anti-rabbit IgG–Alexa568 (ThermoFisher) plus 1:200 DAPI plus 1:200 phalloidin–Alexa633 (ThermoFisher) in PBS overnight. Samples were then washed five times for 30 min each with PBS-T and incubated in PBS plus ×2 Anti/Anti until imaging. Pericentrin-stained clusters were imaged in 3D using an inverted Eclipse Ti-E microscope (Nikon) with spinning disc CSU-W1 (Yokogawa) integrated in Metamorph software (v.7.10.2.240) by Gataca Systems with a ×40 water immersion objective (NA, 1.15) and 1 µm *z* steps. Paxillin staining was performed using the same protocol but staining with rabbit–anti-paxillin (1:50, SC-5574, Santa Cruz) and goat–anti-rabbit–Ax647 (1:200, ThermoFisher) and imaging with a Zeiss LSM880 confocal scanning microscope with a ×40 oil objective (NA, 1.3) driven by Zeiss ZEN software (v.2.3 SP1).

For immunostaining of ECM proteins, the collagen networks were polymerized on coverslips in a six-well plate, and cell clusters were seeded on top. Two to three days after seeding, the samples were washed briefly with PBS and fixed with 4% PFA in PBS for 20 min at room temperature. Samples were then washed three times with PBS, stained with primary antibodies in PBS at room temperature for 1 h, washed three times with PBS and then stained with appropriate Alexa-conjugated secondary antibodies (ThermoFisher) in PBS at room temperature for 1 h. The samples were then washed three times with PBS and inverted into 3.5 cm glass-bottom dishes prior to imaging. The following primary antibodies were used: rabbit–anti-fibronectin (1:100, F3648, Sigma-Aldrich/Merck), mouse–anti-collagen-I (1:100, C2456, Sigma-Aldrich/Merck), mouse–anti-collagen-IV (1:100, col-94, Sigma-Aldrich/Merck) and rabbit–anti-laminin (1:100, L9393, Sigma-Aldrich/Merck). Samples were imaged using an inverted Eclipse Ti-E microscope (Nikon) with spinning disc CSU-W1 (Yokogawa) integrated in Metamorph software (v.7.10.2.240) by Gataca Systems with a ×60 water immersion

objective (NA, 1.27). For two-photon imaging (Extended Data Fig. 6e), samples were imaged using an inverted Leica SP8 microscope coupled to a femtosecond Chameleon Vision II laser (680–1,350 nm; Coherent), using a Leica ×63 oil immersion objective (NA, 1.4). Fibronectin line scans were extracted by manually segmenting clusters in FIJI in the bright-field channel and taking line scans in the fibronectin channel from points along the segmentation contour to the cluster centre of mass using custom software written in Python. For each cluster, the line scans were aligned, normalized to the contour to centre of mass length and averaged. For colocalization analysis of TAMRA-labelled collagen and collagen-I antibody staining, the Coloc 2 plugin in FIJI was used with Costes threshold regression. The colocalization value represents the Pearson's *r* value (no threshold).

Drug treatments. Clusters were treated with NSC23766 (Sigma-Aldrich/Merck) at the specified concentrations for 1 h prior to starting imaging. Cilengitide (Selleckchem) was added to a final concentration of 1 μM, 1 h prior to starting imaging. AIIB2 (MABT409, Sigma-Aldrich/Merck) was added to a final concentration of 5–10 μg ml^{-1}, 30–40 min prior to starting imaging. The matrix metalloproteinase inhibitors GM6001 (final concentration, 10 μm; Calbiochem) and BB94 (final concentration, 5 μm; Sigma-Aldrich/Merck) were added 30–40 min prior to starting imaging. For 3D displacement experiments, para-nitro-blebbistatin (Sigma-Aldrich/Merck) was added at a final concentration of 30 μM after taking the initial image. The second image was taken 10 min after adding the blebbistatin. For live imaging experiments, para-nitro-blebbistatin (30 μM) was added 1 h prior to imaging.

For crosslinking of collagen networks, threose was diluted to a final concentration of 1 μM or 10 μM in PBS and added to polymerized collagen networks. The collagen networks were incubated for 48 h at 37 °C before washing twice with ×1 PBS for 5 min. The PBS was then replaced with AB+ medium, and clusters were plated. For glutaraldehyde crosslinking, 0.05% glutaraldehyde in PBS was added to polymerized collagen networks and incubated for 1 h at room temperature, which has been shown to lead to a ×2 increase in stiffness[51]. To ensure soluble glutaraldehye was completely removed, gels were then washed three times for 5 min each with PBS, then for 1 h with PBS and then overnight with PBS, and then quickly rinsed twice with PBS. The PBS was then replaced with AB+ medium, and clusters were plated. For lysyl oxidase treatment, collagen networks were incubated with 150 ng ml^{-1} recombinant human lysyl oxidase (OriGene) in PBS plus ×2 Anti/Anti for five days at 37 °C (ref. [52]). The collagen networks were then washed twice with PBS before adding AB+ medium and plating clusters.

Imaging and analysis of migration experiments. Two to three days after seeding cells/clusters, samples were imaged using an Inverted Eclipse Ti-E microscope (Nikon) driven by Metamorph software (v.7.8.13.0) with a motorized stage and a ×10 (NA, 0.3) objective for ~16 h. Multiple cells/clusters were imaged using the Multi-Dimensional Imaging module in Metamorph. To obtain migration trajectories, cells/clusters in bright-field time-lapse images were segmented and tracked using Ilastik[53]. From the tracked segmentations, the trajectories were determined from the centre of mass of the segmentation at each time frame. Cluster fusion or fission events were not included in the analysis, and only trajectories before or after these events were considered. MSD curves were calculated using a fast Fourier transform. Crossover times were fit as in previous studies[54,55]. A linear function was fit to the log-transform of the MSD (equivalent to a power-law fit of the untransformed MSD) for the first 300 min to extract the coefficient of persistence. For experiments using aligned collagen networks, the orientational index was calculated by taking the ratio of the sum of the migration distance along the collagen alignment axis over the total sum of the migration distance, similar to the calculation of chemotactic index[56]. Analysis and plotting of the trajectories were performed using custom software written in Python.

Quantification of the number of cells for different-sized clusters and protrusion locations was performed using the CellCounter plugin (K. De Vos) in FIJI and analysed using custom software written in Python. Nuclear tracking for clusters was performed using custom software written in Python.

Preparation, imaging and analysis of wound healing experiments. Collagen networks were polymerized in glass-bottom dishes, treated with ×1 PBS or glutaraldehyde and thoroughly washed as described above. Circular PDMS slabs of ~1.5 cm diameter and ~1.5 mm thickness were prepared as described above. A scalpel was then used to cut rectangular slats 6 mm tall by 2 mm wide. The resulting PDMS stencils were then passivated by treating with 2% Pluronic F-127 (Sigma-Aldrich/Merck) in PBS for 1 h, then washed three times for 5 min each in PBS and dried using compressed air. The collagen gels were then incubated briefly in AB+ medium and dried in ambient air for 10 min, and the passivated PDMS stencils were then placed on top of the collagen gels. A431 cells were then trypsinized from their culture flask; ~200,000 cells diluted into 50 μl AB+ medium was pipetted over each rectangular slat, and the dish was incubated at 37 °C with CO_2 and humidity for 24 h to allow cells to attach. Then, 2 ml AB+ medium was added to each dish, and the stencils were removed carefully using forceps, 1 h before beginning imaging. Samples were imaged using an Inverted Eclipse Ti-E microscope (Nikon) with a motorized stage and a ×10 (NA, 0.3) objective. To capture the entire region containing the cells, a grid of *xy* positions was captured for each time point. Cells were imaged at 30 min time intervals for ~60 h.

The *xy* positions were stitched together using the Grid/Stitching plugin[57] in FIJI, rotated and cropped appropriately. To extract wound closure speed, the image stacks were filtered with a variance filter (radius = 2 pixels) and then rotated around the *x* axis by 90°, and the average intensity projected onto two dimensions to create a kymograph. From the resulting kymograph, the angle of the migrating front was measured on both sides and averaged to extract the wound closure speed.

Imaging and analysis of cortical intensities during migration. A431 MLC-GFP clusters were imaged using an inverted Eclipse Ti-E microscope (Nikon) with spinning disc CSU-W1 (Yokogawa) integrated in Metamorph software (v.7.10.2.240) by Gataca Systems with a ×40 water immersion lens (NA, 1.15) and 1 μm *z* steps for ~16 h. Multiple clusters were imaged in 3D using the Multi-Dimensional Imaging module in Metamorph. To determine cortical intensities of MLC-GFP, we first registered the 3D time-lapse images in the *z* axis using a custom macro in FIJI. We then segmented cluster time-lapse images automatically using custom software written in Python. Briefly, each image was blurred using a Gaussian filter and thresholded using Otsu's method. The segmentations were further refined using binary morphology operations to remove noise and to smooth edges. The cells were then tracked frame to frame to extract the trajectory using the centre of mass for each segmented image. Using the segmentation, we defined the cortex as the region around the cluster periphery from the outer boundary of the cluster to a contour 5 μm inside of the boundary. For each cortex pixel, we determined the angle of that pixel with respect to the cluster centre of mass. The cortex intensity around the cluster was then determined by finding the maximum cortex intensity value within angular bins of 10°. This cortical intensity was normalized to the average intensity in the region of the cluster inside of the cortex. For averaging the angular cortex intensities with respect to the angle of migration, we subtracted the trajectory angle from the angle value for each cortex pixel and determined the binned cortex intensities as described above.

For imaging A431 Raichu-Rac1 clusters, collagen networks were polymerized onto 18-mm-diameter, round, no. 1.5 coverslips pretreated with silane and glutaraldehyde and coated with 2 mg ml^{-1} collagen networks as described above. Coverslips were placed collagen side up into six-well plates, and clusters were plated on top in AB+ medium and allowed to attach for two to three days. Immediately prior to imaging, the coverslips were inverted and placed onto a 3.5-cm-diameter glass-bottom dish containing shims made from no. 1 cover glass and affixed using vacuum grease. AB+ medium was then added, and samples were transported to the microscope. Raichu-Rac1 clusters were imaged with a Zeiss LSM880 confocal scanning microscope using a ×63 oil immersion lens (NA, 1.4) driven by Zeiss ZEN software (v.2.3 SP1) using appropriate laser and filter settings for imaging yellow fluorescent protein (YFP) and cyan fluorescent protein (CFP). Images were registered, segmented and analysed as above for MLC-GFP to extract the cortical Rac1 activity with respect to the migration direction.

A431 LifeAct-mCherry clusters were imaged using an inverted Eclipse Ti-E microscope (Nikon) with spinning disc CSU-W1 (Yokogawa) integrated in Metamorph software (v.7.10.2.240) by Gataca Systems with a ×40 water immersion lens (NA, 1.15) at 10 s time intervals for ~30 min. Images were segmented, registered and rotated as described above. Actin flows were measured by PIV using the OpenPIV (www.openpiv.net) package in Python, with a window size of 22 × 22 pixel^2 (~4 × 4 μm^2) and window overlap of 11 × 11 pixel^2 (~2 × 2 μm^2). Spurious vectors were filtered out, and the gaps were filled in by local mean interpolation. PIV analysis was restricted to the cortical region of clusters (within 10 μm of the outer cluster boundary). To determine actin flows in different regions, the segmentation was split into four quadrants with respect to the migration direction (front, rear, left, right), and the vector component along the migration axis was determined. To determine the sum vector at each time point, the vectors from the entire cortical region were summed, and the angle of the resulting vector was quantified in the radial histogram (Extended Data Fig. 10i).

Imaging of paxillin-GFP and zyxin-mCherry was performed in a similar manner. Samples plated on glass substrates were plated directly on 3.5 cm glass-bottom dishes. Samples plated on collagen networks were plated on networks polymerized on coverslips and inverted into 3.5 cm glass-bottom dishes for imaging. These samples were imaged with a Zeiss LSM880 confocal scanning microscope using a ×63 oil immersion lens (NA, 1.4) driven by Zeiss ZEN software (v.2.3 SP1).

Analysis of centrosome position in cell clusters. Relative centrosome positions in cell clusters were determined by segmenting the cluster volume (phalloidin channel), nuclei (DAPI channel) and centrosomes (pericentrin channel) in three dimensions. Initially, a segmentation probability map was generated for each channel using Ilastik. Each channel was segmented by thresholding the probability map and performing binary morphology operations. Each nucleus was then paired with the closest centrosome (typically adjacent to the surface of the nucleus). Centrosome orientation was defined by a unit vector from the nucleus centre of mass to the centrosome centre of mass for each nucleus–centrosome pair.

Imaging and analysis of fluorescent collagen networks during migration. Monomeric collagen-I was labelled with TAMRA as previously described[58]. For fluorescently labelled collagen networks, TAMRA-labelled collagen was mixed with unlabelled collagen at a ratio of 1:5 and neutralized; 200 µl of collagen solution was pipetted onto silane/glutaraldehyde-coated glass-bottom dishes and polymerized as described above. Single cells or clusters were then seeded. After two to three days, the cells were labelled with CellTracker Green (ThermoFisher) at 1:2,000 in serum-free DMEM for 30 min at 37 °C with 5% CO_2 and humidity. Following incubation, the medium was replaced with fresh AB+ medium. Samples were imaged ~1 h later by 3D spinning disc microscopy using an inverted Eclipse Ti-E microscope (Nikon) with spinning disc CSU-W1 (Yokogawa) integrated in Metamorph software (v.7.10.2.240) by Gataca Systems with a ×40 water immersion lens (NA, 1.15) and 1 µm z steps at 20 min time intervals for ~16 h. Multiple cells/clusters were imaged in 3D using the Multi-Dimensional Imaging module in Metamorph.

To analyse mean collagen intensity for different collagen concentrations (monomeric or network; Extended Data Fig. 2), TAMRA-labelled collagen was used. Imaging was performed as above, and care was taken to ensure that all imaging parameters were kept constant for all conditions imaged. Mean intensity was measured using FIJI and analysed/visualized using custom software written in Python.

Segmentation and tracking were performed on the brightest point projections of CellTracker images using a custom algorithm in Python similar to those used for A431 MLC-GFP images. To determine the angular difference between clusters and the collagen centre of mass, the angle from the cluster segmentation centre of mass to the weighted centre of mass of the collagen intensity within the segmentation region was determined. The difference between this angle and the trajectory angle was taken to be the angular difference.

To measure the local nematic order outside of the cell region (Extended Data Fig. 7a–c), collagen fibre orientations were determined for a single z slice at the surface of the collagen network using CurveAlign[59] in MATLAB (v.2014b). Next, the image frame was split into a grid of square boxes, each with a side length of 120 pixel (33 µm). Within each box, we calculated the nematic order using a nematic director **n** defined by the mean filament orientation in that region. We calculated the nematic order scalar parameter considering all fibres contained within the box and not intersecting the cluster segmentation as $S(x,t) = \frac{1}{2}\langle 3\cos^2\theta_m - 1\rangle$, where θ_m is the angular difference between each fibre orientation and the nematic director **n**.

To one-dimensionalize the collagen density signature, cell segmentations at each time point were divided into ten regions of equal length from the front to the rear of the cluster, according to the angle of migration at that time step. Regions were determined by making a bounding box around the segmentation, rotated with the trajectory angle, and separating this bounding box into ten equal rectangles. The segmentation pixels intersecting these rectangles were used in determining the mean collagen intensity at each region. The nematic order for each region was determined for all fibre orientations in that region (obtained using CT-FIRE) using the migration trajectory angle as the nematic director **n**. The nematic order was only calculated for regions containing greater than three filament orientations. For each time point, the collagen density and nematic order were normalized to the mean of the ten regions. The collagen density peak was determined by fitting the averaged collagen density data with a Gaussian function and extracting the centre position, μ. The nematic order trough was determined by fitting an inverted Gaussian function. The reported peak offset for collagen density and nematic order was taken as the relative peak position multiplied by the mean segment length. Collagen gradient intensity was defined as the minimum-to-maximum range relative to mean collagen density.

Super-resolution imaging of fluorescent collagen networks was performed by polymerizing TAMRA-labelled collagen networks on round coverslips, plating clusters and inverting into 3.5 cm glass-bottom dishes, as described above. These samples were imaged with a Zeiss LSM880 confocal scanning microscope equipped with the AiryScan module using a ×40 oil immersion objective (NA, 1.3) driven by Zeiss ZEN software (v.2.3 SP1). A bright-field image was acquired initially to determine the starting position of the clusters. Then an AiryScan image of the fluorescent collagen was taken. After 30 min, a second bright-field image was acquired to determine the direction of migration. Cluster segmentation was performed as described above, and fibre orientations were determined using CT-FIRE for each imaging plane. The fibre orientations from each plane were projected onto a single 2D slice, and the nematic order was calculated as described above.

The 2D traction force microscopy. For 2D traction force experiments, cell clusters were seeded on 0.5 kPa PAA gels containing fluorescent beads and coated with a thin collagen-I network, as described above. Clusters and beads were imaged by bright-field and epifluorescence microscopy, respectively, overnight, using an inverted Eclipse Ti-E microscope (Nikon) driven by Metamorph software (v.7.8.13.0) with a fully motorized stage and a ×10 (NA, 0.3) objective. Multiple cells/clusters were imaged using the Multi-Dimensional Imaging module in Metamorph. A single z slice was acquired every 15 min for multiple stage positions and imaged overnight for ~16 h. The following day, the cells were removed by briefly rinsing with PBS and incubating for 20 min in ×0.5 TrypLE Express (ThermoFisher) and 1 N NH_4OH. The dish was then briefly rinsed with PBS, and the collagen-I network was removed by incubating for 20 min in a solution of ~50 µg ml^{-1} collagenase type 3 (Worthington Biochemical) in PBS. All incubations to remove cells and the collagen network were performed directly on the microscope, being careful not to disturb the position of the imaging dish. An additional image was then taken to serve as a reference image for measuring bead displacements. Beads displacements were extracted by PIV, and tractions were calculated from displacement fields by Fourier transform, assuming finite gel thickness, using custom software in Matlab[60] (v.2014b).

Clusters were segmented and tracked over time from bright-field images using Ilastik[53]. The migration trajectories were pooled with the cluster migration data described above. Traction force line scans were extracted by cubic spline interpolation of the traction field. The line scans ran from each contour pixel to the segmentation centre of mass and extended outward 40 µm beyond the segmentation boundary. For averaging around a single cell, line scans were aligned to the countour boundary of each line scan. The peak traction magnitude was taken as the highest traction value in the line scan between 20 µm outside of the cluster boundary and 10 µm inside the cluster boundary. To quantify the peak traction magnitude around the cluster according to the angle, each contour pixel was assigned an angle according to the vector pointing from the centre of mass of the segmentation to the contour pixel. To average over time and many clusters, the migration trajectory angle was subtracted from each contour angle (as for the MLC-GFP analysis above), and the traction peak was averaged along binned angles to achieve a mean polar plot of the peak traction magnitude with respect to migration direction. To calculate the front-to-back ratio of peak traction magnitudes, the mean peak traction from the front quadrant (315–45°) was divided by the mean of the peak tractions from the rear quadrant (135–225°).

For calculating the tractions along the axis of migration, each traction vector was projected along the migration axis, and the magnitude of this projected vector was plotted. Line scans of the projected tractions were generated by making a bounding box of 500 pixel × 500 pixel (~320 µm × 320 µm) to fit around the segmented cluster. The bounding box was then split into 500 regions from the front to the back, and the tractions (expanded to the image grid by nearest neighbour interpolation) within each segment were averaged (mean) to determine the traction value at each point along the cluster length. The raw values were smoothed using a moving window with size = 21 pixel. To include the line scan edges in the smoothed data, the line scan was padded at the start and end using the start and end values, respectively. The line scan was then cropped to start and end when the data reached 0.

The 3D deformation microscopy. The 3D deformation microscopy experiments were set up in the same way as the 2D traction force experiments. Single cells or cell clusters were seeded on 0.5 kPa PAA gels containing fluorescent beads and coated with a thin collagen-I network. Samples were imaged by 3D spinning disc microscopy using an inverted Eclipse Ti-E microscope (Nikon) with spinning disc CSU-W1 (Yokogawa) integrated in Metamorph software (v.7.10.2.240) by Gataca Systems with a ×40 water immersion lens (NA, 1.15). A single 3D stack with 1 µm z steps was collected. Then the cells and collagen network were detached as described above, and a reference image stack was collected. Bead displacements along the x, y and z axes were extracted by a custom 3D PIV algorithm in Matlab. The summed displacement was the sum of the magnitude of all xyz vectors in the imaging frame.

Collagen and stress relaxation following cell removal. To determine the collagen relaxation timescale, cells or clusters were seeded on TAMRA-labelled collagen networks as described above. A single 3D image stack was recorded by spinning disc microscopy for each cell or cluster, with 35 2 µm z steps. Cells were then removed by treatment with ×0.5 TrypLE Express and 1 N NH_4OH. Imaging was resumed as soon as possible after the sample was stable (5–10 min), noting precisely the time between cell removal and restarting imaging. Cell or cluster regions were segmented manually based on the first (pre-trypsin/NH_4OH) image. The collagen density at each time point was taken as the mean intensity of a brightest point projection of the collagen intensity within the segmentation region normalized to a reference region with the same shape as the segmentation. PIV analysis of collagen relaxation for sequential frames was performed using the OpenPIV library in Python. To determine the relaxation of stresses on the substrate following cell removal, 3D deformation microscopy was performed, as described above. A single 3D image stack of clusters or single cells and their underlying collagen network or PAA gel was recorded by spinning disc microscopy, as described above. Cells were then removed using trypsin/NH_4OH and imaging was resumed after 5–10 min. Time 0:00 refers to the frame prior to the addition of trypsin/NH_4OH. The relaxation timescale τ_r was extracted by fitting the displacement/density/PIV data over time with the exponential decay function $I = A\exp(-t/\tau_r) - C$, where A and C are constants used for fitting.

BM. BM is a purely optical technique that allows for the acquisition of 3D maps of viscoelastic properties with diffraction-limited resolution[37,38]. This technique is based on Brillouin scattering, the interaction of monochromatic laser light with thermally excited, spontaneous sound waves in the gigahertz frequency range that exists in all matter. Due to this interaction, a small amount of the laser light

exchanges energy with the sound waves and thus obtains a change in frequency. This change in frequency, termed the 'Brillouin shift', is given by

$$\nu_B = \frac{2n}{\lambda_0} V \sin\frac{\theta}{2}, \quad (3)$$

where n is the refractive index within the interaction volume, λ_0 is the wavelength of the laser in vacuum, θ is the angle between incident and scattered light and V is the speed of sound. Importantly, the speed of sound V is related to the real part of the longitudinal modulus M', a measure of stiffness, and is defined as the ratio of stress to strain in a uniaxial strain state:

$$M' = \rho V^2. \quad (4)$$

To determine the elastic modulus M', the knowledge of the refractive index n and the density ρ is required. However, it has been shown that in most biological samples, n and ρ are correlated to within an error of a few percent, thus not affecting the value of M' (refs. [61,62]). Therefore, in the absence of our own in situ measures of n and ρ, we report the Brillouin shift as the proxy for stiffness, as it is the quantity measured in our experiments. Regions within an image displaying a higher Brillouin shift are thus relatively stiffer.

Brillouin images were acquired using a custom-built confocal Brillouin microscope based on a commercial Axiovert 200 body (Zeiss) coupled with a 532 nm laser and a custom-built 2-VIPA spectrometer, as described in more detail previously[63]. The intensity of the laser light was adjusted to <10 mW on the sample to avoid photodamage. The light was focused using a ×40 water immersion objective (NA, 1.2). The images were acquired by scanning the sample with an xy step size of 2 µm and an acquisition time of 100 ms per pixel. Fluorescence confocal images of the collagen were acquired immediately before Brillouin images with an xy step size of 1 µm.

To analyse the BM shift in different regions of each cluster, we mapped rays from the cluster centre of mass to the cluster periphery at every integer degree angle (360 rays) and measured the maximum BM shift for each angle. These maximum BM shifts were then binned into 10 degree regions by taking the mean. The same approach was taken for measuring the collagen density at different angles. Then, the central angle of the bins with maximal BM shift and collagen density were compared to calculate the angular difference between the maximum BM shift and maximum collagen density.

Preprocessing, image analysis, statistics and visualization. Preprocessing of image stacks was performed using custom macros in FIJI/ImageJ[64]. For image and data analysis and visualization in Python, the Anaconda distribution of Python v.3.7 with the following packages was used: astropy (v.3.1), matplotlib (v.3.0.2), numpy (v.1.21.5), opencv (v.3.4.2), openpiv (v.0.21.2), pandas (v.0.23.4), pillow (v.5.3.0), scikit-image (v.0.17.2), scikit-learn (v.0.20.1), scipy (v.1.1.0), shapely (v.1.6.4) and tifffile (v.2020.7). For box plots, dots represent individual measurements as described in the figure legends. Boxes represent the interquartile range (Q1 to Q3), and the line represents the median. Whiskers extend to the furthest point within 1.5 times the interquartile range away from Q1 or Q3. For exact P values reported in legends, the order of values represents the pairwise combinations from left to right (for example, for 3 categories, P='1 versus 2', '1 versus 3' and '2 versus 3'). All Welch's t-tests make no assumptions of equal variance and are two sided.

Reporting summary. Further information on research design is available in the Nature Research Reporting Summary linked to this article.

Data availability

The authors declare that all data supporting the findings of this study are available within the paper and its Supplementary Information files and from the corresponding authors upon reasonable request. A minimum data set has been uploaded to the following public repository: https://doi.org/10.5281/zenodo.6390650.

Code availability

Custom software used to analyse images and data will be made available upon reasonable request.

References

51. Sherlock, B. E. et al. Nondestructive assessment of collagen hydrogel cross-linking using time-resolved autofluorescence imaging. *J. Biomed. Opt.* **23**, 036004 (2018).
52. Baker, A.-M., Bird, D., Lang, G., Cox, T. R. & Erler, J. T. Lysyl oxidase enzymatic function increases stiffness to drive colorectal cancer progression through FAK. *Oncogene* **32**, 1863–1868 (2013).
53. Berg, S. et al. ilastik: interactive machine learning for (bio)image analysis. *Nat. Methods* **16**, 1226–1232 (2019).
54. Selmeczi, D., Mosler, S., Hagedorn, P. H., Larsen, N. B. & Flyvbjerg, H. Cell motility as persistent random motion: theories from experiments. *Biophys. J.* **89**, 912–931 (2005).
55. Maiuri, P. et al. Actin flows mediate a universal coupling between cell speed and cell persistence. *Cell* **161**, 374–386 (2015).
56. Moghe, P. V., Nelson, R. D. & Tranquillo, R. T. Cytokine-stimulated chemotaxis of human neutrophils in a 3-D conjoined fibrin gel assay. *J. Immunol. Methods* **180**, 193–211 (1995).
57. Preibisch, S., Saalfeld, S. & Tomancak, P. Globally optimal stitching of tiled 3D microscopic image acquisitions. *Bioinformatics* **25**, 1463–1465 (2009).
58. Geraldo, S., Simon, A. & Vignjevic, D. M. Revealing the cytoskeletal organization of invasive cancer cells in 3D. *J. Vis. Exp.* https://doi.org/10.3791/50763 (2013).
59. Bredfeldt, J. S. et al. Computational segmentation of collagen fibers from second-harmonic generation images of breast cancer. *J. Biomed. Opt.* **19**, 16007 (2014).
60. Trepat, X. et al. Physical forces during collective cell migration. *Nat. Phys.* **5**, 426–430 (2009).
61. Scarcelli, G., Pineda, R. & Yun, S. H. Brillouin optical microscopy for corneal biomechanics. *Invest. Ophthalmol. Vis. Sci.* **53**, 185–190 (2012).
62. Schlüßler, R. et al. Mechanical mapping of spinal cord growth and repair in living zebrafish larvae by Brillouin imaging. *Biophys. J.* **115**, 911–923 (2018).
63. Bevilacqua, C., Sánchez-Iranzo, H., Richter, D., Diz-Muñoz, A. & Prevedel, R. Imaging mechanical properties of sub-micron ECM in live zebrafish using Brillouin microscopy. *Biomed. Opt. Expr.* **10**, 1420–1431 (2019).
64. Schindelin, J. et al. Fiji: an open-source platform for biological-image analysis. *Nat. Methods* **9**, 676–682 (2012).

Acknowledgements

We acknowledge the Cell and Tissue Imaging (PICT-IBiSA), Institut Curie, member of the French National Research Infractucture France-BioImaging (ANR10-INBS-04). We thank T. Kato and E. Sahai for the stable MLC-GFP and Raichu-Rac A431 cell lines and V. Marthiens and R. Basto for the pericentrin antibody. We thank J. Barbazan, O. Zajac and R. Bouras for assistance making the stable LifeAct-mCherry, paxillin-GFP and zyxin-mCherry lines. We also thank O. Zajac for designing and sharing the protocol for generating thin, aligned collagen networks. We thank N. Elkhatib and G. Montagnac for sharing reagents and protocols. We thank C. Bevilacqua and R. Prevedel, who developed the custom Brillouin microscope utilized in this work. We acknowledge M. Gómez-González and E. Latorre for developing the 3D PIV and traction force microscopy code. We thank H. Mohammadi, E. Sahai and all members of the Vignjevic lab for helpful discussions and comments on the manuscript. A.G.C. was supported by the European Moleclular Biology Organization (ALTF 1582-2014 to A.G.C.). This project also received funding from the European Research Council under the European Union Horizon 2020 research and innovation programme (grant agreement no. 772487 to D.M.V.) and Institut National du Cancer (PLBIO18-087 to D.M.V.). A.M. and R.V. were funded by PHYMAX and POLCAM grants. A.M. thanks a Talent fellowship awarded by the CY Cergy Paris University. M.B. and A.D.-M. were funded by the European Molecular Biology Laboratory and the Deutsche Forschungsgemeinschaft (DI2205/2-1 to A.D.-M.). X.T. was funded by Spanish Ministry for Science, Innovation and Universities MICCINN/FEDER (PGC2018-099645-B-I00, Severo Ochoa Award of Excellence), the Generalitat de Catalunya/CERCA programme (SGR-2017-01602), Fundació la Marató de TV3, Obra Social 'La Caixa', the European Research Council (Adv-883739) and the European Commission (H2020-FETPROACT-01-2016-731957.

Author contributions

A.G.C., A.M., R.V. and D.M.V. designed the research and wrote the manuscript; A.G.C. carried out most of the experiments and image analysis; A.M. and R.V. created the theoretical model; C.J. performed and analysed some migration and 2D traction force microscopy experiments and performed some staining experiments; A.S. performed preliminary experiments; L.L. prepared and performed some staining, migration and micropatterning experiments; M.B. and A.D.-M. performed and helped analyse the BM experiments; C.P.-G. and X.T. provided reagents, software and technical assistance for the traction force microscopy and 3D displacement experiments; C.P.-G. performed and analysed the results of the experiment measuring different monomeric collagen coatings; D.M.V. prepared and performed some staining, migration and micropatterning experiments; and all authors discussed the results and manuscript.

Competing interests

The authors declare no competing interests.

Additional information

Extended data is available for this paper at https://doi.org/10.1038/s41563-022-01259-5.

Supplementary information The online version contains supplementary material available at https://doi.org/10.1038/s41563-022-01259-5.

Correspondence and requests for materials should be addressed to Andrew G. Clark or Ananyo Maitra.

Peer review information *Nature Materials* thanks M. Lisa Manning, Giorgio Scita and the other, anonymous, reviewer(s) for their contribution to the peer review of this work.

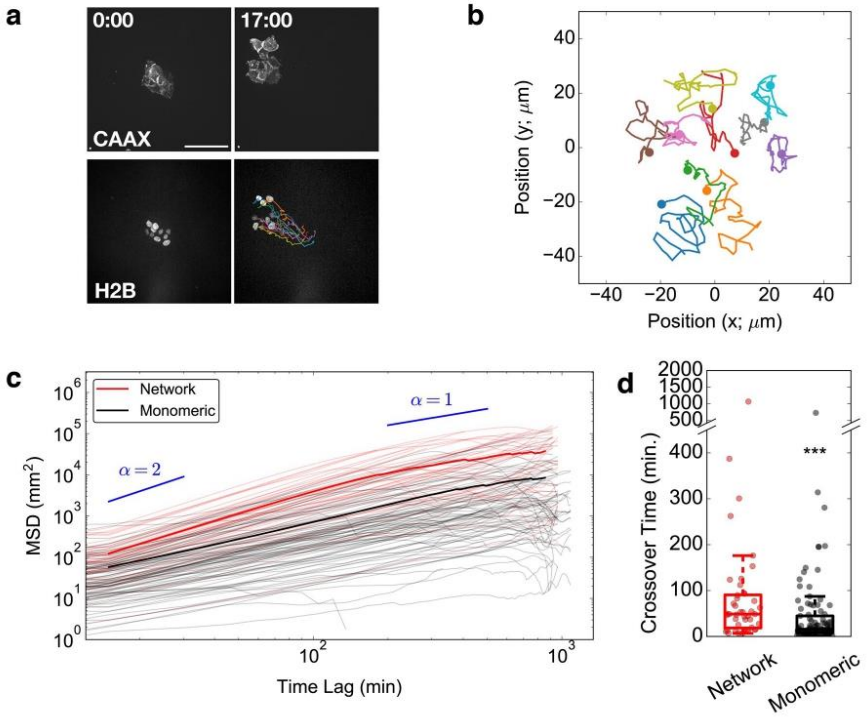

Extended Data Fig. 1 | Analysis of cell rearrangement and MSD. a. Montage from live imaging of stable A431 cells expressing GFP-CAAX (Plasma Membrane marker) and mCherry-H2B (DNA marker). Colored lines are trajectories of tracked nuclei over the course of 17 hours of imaging. Representative image from n=43 clusters imaged over N=2 independent experiments. Scale Bar: 100μm. **b**. Plot of the relative nuclear movements from *a*, registered to the migration of the whole cluster over time. **c**. Plot of the MSD curves from all trajectories of clusters migrating on PAA gels + collagen networks (red) or PAA gels + monomeric collagen (black). Individual trajectories are shown in translucent colors. Solid colored lines reflect mean MSD curves. Blue lines indicate slopes for power laws with exponents of $\alpha = 2$ or $\alpha = 1$. **d**. Crossover time from fits of individual MSD curves. For *c,d*, data from n=28,59 clusters, N=2,3 independent experiments. ***$p < 0.001$ for Tukey HSD test (p=0.0319).

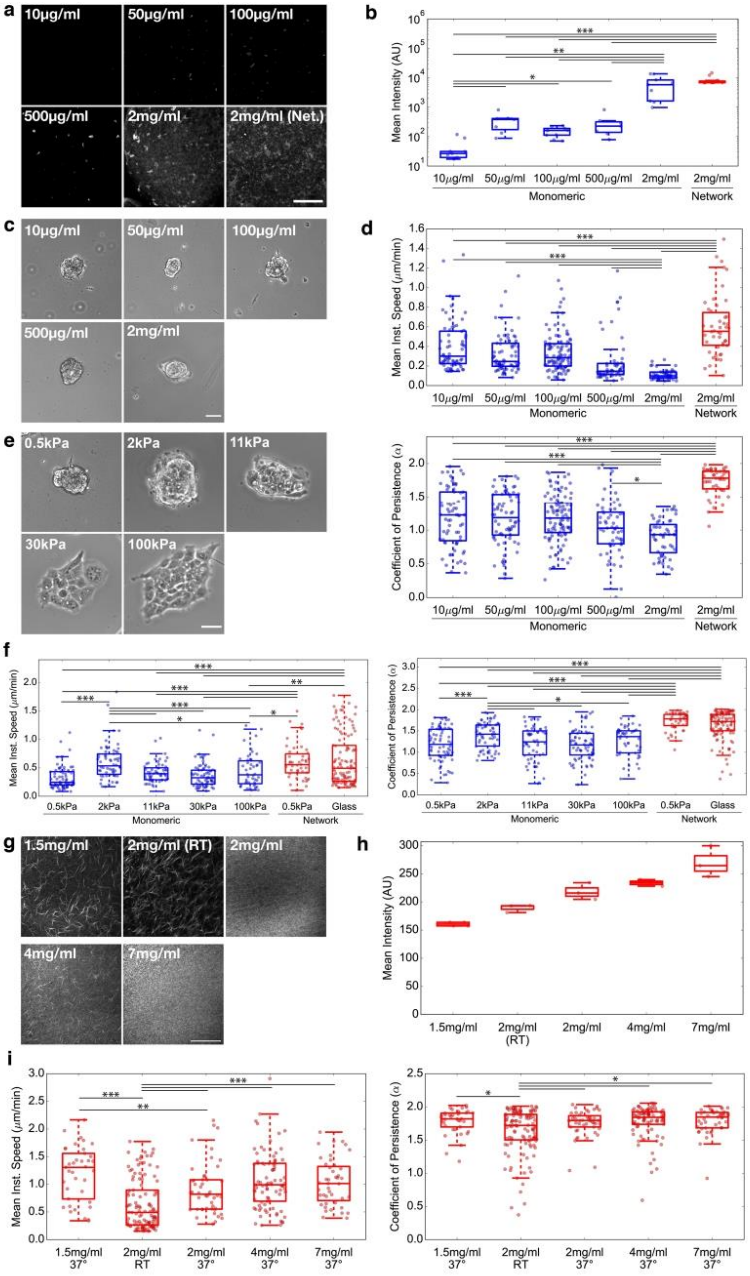

Extended Data Fig. 2 | See next page for caption.

Extended Data Fig. 2 | Analysis of PAA gel stiffness and collagen concentration. a. Representative micrographs from PAA gel coated with different concentrations of fluorescently-labeled monomeric collagen or 2mg/ml collagen networks. Scale bar: 30μm. **b**. Boxplot of mean collagen intensity for conditions shown in *a*. Each point represents one imaging field, relative to background fluorescence in areas with no coating. For *a,b*, images/data from n=5 positions per condition from one representative experiment, N=3 independent experiments. One-way ANOVA p=2.10e-11. *p < 0.05, **p < 0.01, ***p < 0.001 for Tukey HSD post-hoc test (p=0.00199, < 0.001, 0.0101, 0.00162, < 0.001, 0.0305, 0.679, 0.00717, < 0.001, 0.121, 0.00186, < 0.001, 0.00674, < 0.001, 0.248). **c**. Example micrographs of cell clusters plated on PAA gels with different concentrations of monomeric collagen. Scale bar: 50μm. **d**. Boxplots of mean instantaneous speed and coefficient of persistence for conditions in *c*. Data represents n=68, 72, 97, 56, 52, 46 clusters, N=3, 3, 3, 3, 2, 2 independent experiments. Data for collagen network and 100μg/ml monomeric collagen is the same data as presented in Fig. 1f. One-way ANOVA p=1.68e-20, 2.42e-25. *p < 0.05, **p < 0.01 for Tukey HSD post-hoc test (p=0.0304, 0.0368, 0.00153, < 0.001, 0.00795, 0.659, 0.0547, < 0.001, < 0.001, 0.0145, < 0.001, < 0.001, < 0.001, < 0.001, < 0.001; p=0.855, 0.773, 0.0490, < 0.001, < 0.001, < 0.900, 0.0518, < 0.001, < 0.001, 0.0383, < 0.001, < 0.001, 0.0253, < 0.001, < 0.001). **e**. Example micrographs of cell clusters plated on PAA gels of different stiffness (100μg/ml monomeric collagen). Scale bar: 50μm. **f**. Boxplots of mean instantaneous speed and coefficient of persistence for conditions in *e*. Data represents n=72, 62, 57, 69, 46, 46, 114 clusters, N=3, 3, 3, 3, 3, 2, 6 independent experiments. Data for collagen network and 100μg/ml monomeric collagen is the same data as presented in Fig. 1f. One-way ANOVA p=6.26e-13, 6.25e-30. *p < 0.05, **p < 0.01, ***p < 0.001 for Tukey HSD post-hoc test (p < 0.001, 0.00688, 0.238, 0.00704, < 0.001, < 0.001, < 0.001, < 0.001, 0.0122, 0.889, 0.564, 0.137, 0.504, < 0.001, < 0.001, 0.0758, < 0.001, < 0.001, 0.0143, 0.00996, 0.700; p= < 0.001, < 0.001, 0.728, 0.850, 0.233, < 0.001, < 0.001, 0.00300, < 0.001, 0.0327, < 0.001, < 0.001, 0.589,0.427, < 0.001, < 0.001, 0.158, < 0.001, < 0.001, < 0.001, < 0.001, 0.0763). **g**. Representative micrographs of fluorescently-labeled collagen networks with different collagen concentration or polymerization temperature. Scale bar: 100μm. **h**. Boxplot of mean collagen intensity for conditions shown in *g*. For *g,h*, representative images/data from n=4, 3, 3, 3, 3 positions, N=1 experiment. One-way ANOVA p=7.74e-6. **i**. Boxplots of mean instantaneous speed and coefficient of persistence for cluster migration on collagen network conditions in *g*. Data represents n=37, 114, 47, 85, 43 clusters, N=2, 3, 6, 3, 2 independent experiments. Data for 2mg/ml 37° C is the same data as presented in Fig. 1f. One-way ANOVA p=6.56e-12, 0.000609. *p < 0.05, **p < 0.01, ***p < 0.001 for Tukey HSD post-hoc test (p < 0.001, 0.00918, 0.175, 0.121, < 0.001, < 0.001, < 0.001,0.111,0.206,0.793; p=0.0134, 0.58, 0.812, 0.893, 0.0217, 0.00226, 0.00612, 0.775, 0.468, 0.705).

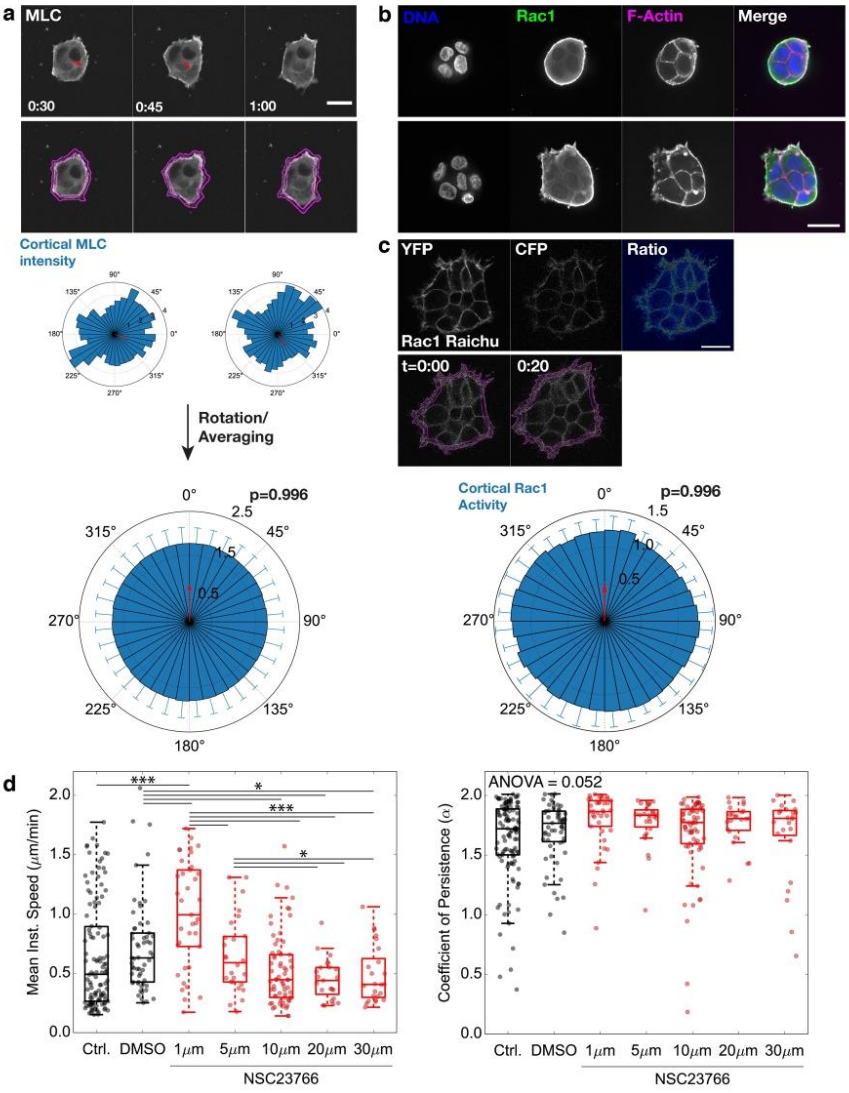

Extended Data Fig. 3 | See next page for caption.

Extended Data Fig. 3 | Clusters lack front-back polarity during migration. a. Montage from time-lapse of a myosin light chain (MLC)-GFP expressing A431 cell cluster. MLC-GFP intensity was measured in the peripheral cortical region (segmentation in magenta) around the perimeter of the cluster. See also Supplementary Video 3. At each time point, the relative cortical intensity was measured for different angles around the perimeter (blue bars) as well as the cluster trajectory (red arrow). *Lower panel*: The relative cortical intensity of myosin (mean ± SD), averaged over all time points for n=39 clusters, N=3 independent experiments. Scale bar: 25μm. p-value reflects Rayleigh test of uniformity. **b**. Fixed cell clusters plated on a collagen network and immunostained for Rac1 GTPase with DAPI (DNA) and Phalloidin (F-Actin). Shown are two representative examples from n=21 clusters and N=3 independent experiments. Scale bar: 25μm. **c**.*Upper panels*: Single time point from a live imaging experiment using Raichu-Rac1 showing YFP:CFP ratio. *Middle panels*: Micrographs of YFP:CFP ratio for two successive time points with segmentation of the cortical region (magenta lines). *Lower panel*: The cortical YFP:CFP ratio for Raichu-Rac1 (mean ± SD) with respect to the migration direction (red arrow), averaged over all time points for n=8 clusters, N=3 independent experiments. Scale bar: 25μm. **d**. Boxplots of mean instantaneous speed and coefficient of persistence for cluster migration on collagen network conditions with the Rac1 inhibitor NSC23766. Data represents n=114, 57, 37, 26, 65, 23, 24 clusters, N=6, 3, 2, 1, 3, 1, 1 independent experiments. Control data is the same data as presented in Fig. 1f. For left panel, one-way ANOVA p=9.58e-9. *p < 0.05, ***p < 0.001 for Tukey HSD post-hoc test (p=0.243, < 0.001, 0.893, 0.0858, 0.0508, 0.1155, 0.00143, 0.430, 0.00304, 0.00205, 0.00844, < 0.001, < 0.001, < 0.001, < 0.001, 0.0949, 0.0103, 0.0497, 0.238, 0.552, 0.549).

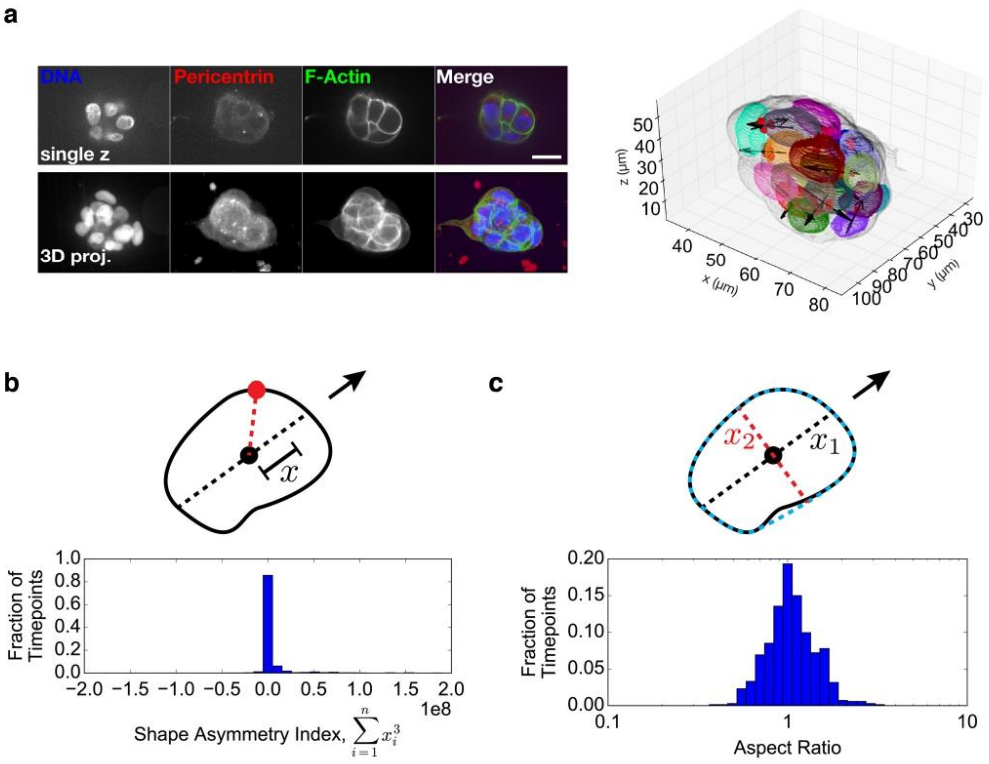

Extended Data Fig. 4 | Analysis of centrosome positioning and shape symmetry. a. Single *z*-slice and 3D projection of a cell cluster on a collagen network with pericentrin staining. Scale bar: 20μm. *Right*: Rendering of the 3D segmented nuclei (multicolor), cluster (gray) and paired centrosomes (red). Black arrows: centrosome orientation with respect to paired nucleus. Representative example from n=7 clusters, N=1 independent experiment. **b**. Shape asymmetry quantification. A center line (dotted black line) is drawn along the cluster length passing through the center of mass and parallel with the migration direction. At every pixel along the contour (red dot, for example), the distance *x* from the center of mass projected onto the center line is determined. The shape asymmetry index is calculated for each time frame as the sum of x^3 over all contour points. *Lower panel*: histogram of the shape asymmetry from n=34 cells, N=5 independent experiments. **c**. Aspect ratio quantification. Using the Hull convex of the contour (blue dotted line) to minimize shape irregularities, the major axis x_1 (dotted black line) is taken as the cluster diameter along the migration direction and passing through the center of mass (black dot). The minor axis x_2 (dotted red line) is taken as the cluster diameter perpendicular to the migration direction and passing through the contour center of mass. The aspect ratio is x_1/x_2. *Lower panel*: histogram of the aspect ratio from n=34 clusters, N=5 independent experiments.

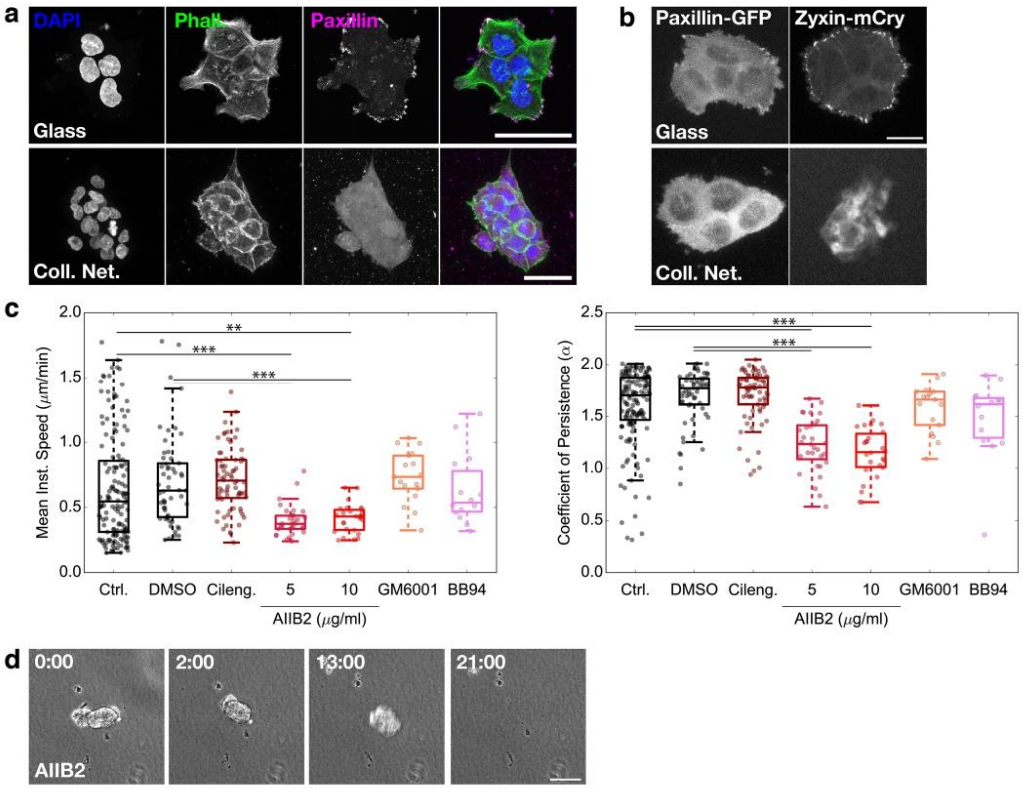

Extended Data Fig. 5 | Analysis of focal adhesions and integrins during migration. a. Fixed cell clusters plated on glass or on a collagen network and immunostained for Paxillin with DAPI (DNA) and Phalloidin (F-Actin) counterstaining. Representative examples, N=2 independent experiments. Scale bars: 50μm. **b**. Single time points from live imaging of A431 cells stably expressing Paxillin-GFP or Zyxin-mCherry, plated on glass or collagen networks. Representative examples, N=3 independent experiments. Scale bar: 50μm. **c**. Boxplots of mean instantaneous speed and coefficient of persistence for cluster migration on collagen networks with the integrin binding inhibitors Cilengitide and AIIB2 and MMP inhibitors GM6001 and BB94. Data represents n=146, 57, 72, 31, 26, 17, 14 clusters, N=8, 3, 4, 2, 2, 1, 1 independent experiments. Control data is pooled from data presented in Fig. 1f. One-way ANOVAs: p=4.36e-6, 1.76e-18. $^{**}p<0.01$, $^{***}p<0.001$ for Tukey HSD post-hoc test (p=0.268, 0.126, <0.001, 0.00492, 0.390, >0.9, 0.832, <0.001, <0.001, 0.865, 0.447, <0.001, <0.001, >0.9, 0.256, 0.537, <0.001, <0.001, <0.001, <0.001, 0.243; p=0.0788, 0.0195, <0.001, <0.001, 0.88, 0.25, 0.689, <0.001, <0.001, 0.130, 0.016, <0.001, <0.001, 0.061, 0.00522, 0.268, <0.001, 0.0148, <0.001, 0.00246, 0.354). **d**. Example micrograph from a cell cluster on a collagen network following treatment with the Integrin-β1 functional antibody AIIB2 (10μg/ml). Scale bar: 100μm. HH:MM. See also Supplementary Video 4. Representative image series from n=26 clusters, N=2 independent experiments.

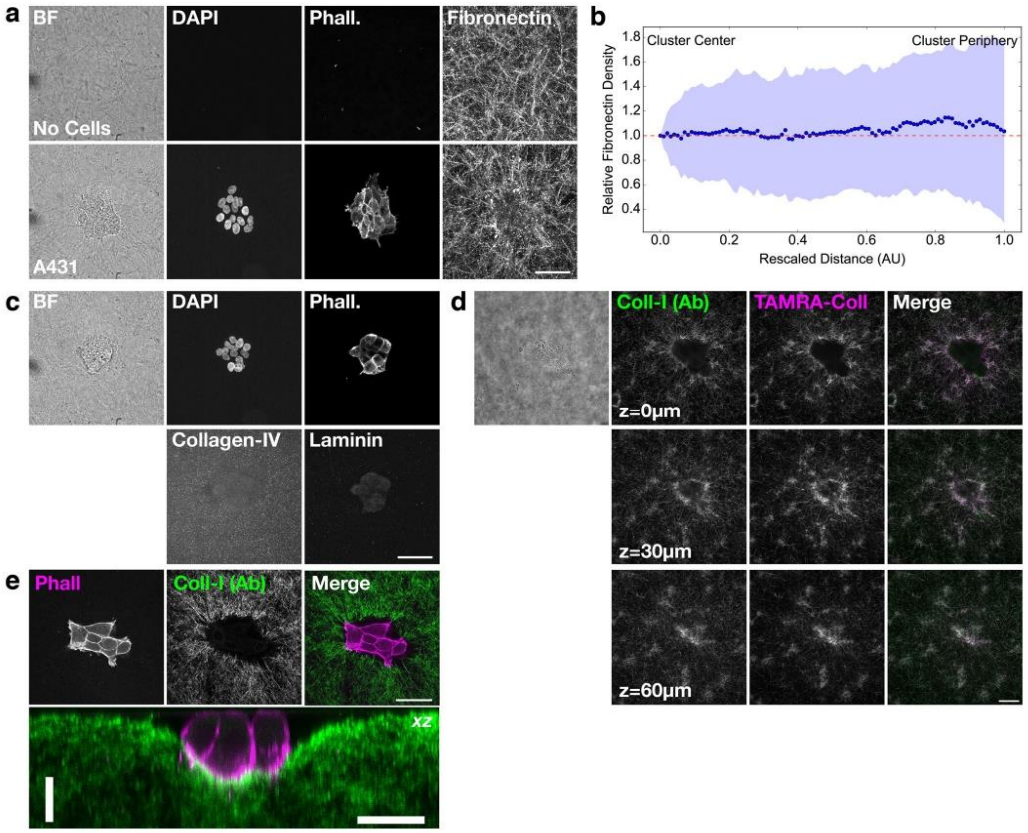

Extended Data Fig. 6 | Cell clusters do not deposit additional ECM during migration. a. Collagen networks containing no cells or A431 clusters fixed and immunostained for Fibronectin, with additional DAPI (DNA) and Phalloidin (F-Actin) staining. The Fibronectin panel represents a brightest point projection over 25μm in the z-axis to capture the network in the region directly under the cluster. Representative image from n=23 clusters, N=3 independent experiment. Scale bar: 50μm. **b**. Average radial linescan (median ± SD) of fibronectin intensity from the cluster center to the periphery from data represented in e. At all distances, $p > 0.05$ for a two-tailed t-test with $\mu_0 = 1$. **c**. Collagen networks with A431 clusters seeded on top were fixed and immunostained for Collagen-IV and Laminin, with additional DAPI (DNA) and Phalloidin (F-Actin) staining. Representative image from n=5 clusters, N=1 independent experiments. Scale bar: 50μm. **d**. Fluorescent TAMRA-collagen networks with A431 clusters plated on top were fixed and immunostained for Collagen-I. Panels reflect single confocal slices at different z-steps. Colocalization between the TAMRA-Collagen and Collagen-I Antibody signal was $R = 0.895 \pm 0.040$ (mean ± SD; $p < 0.001$) from n=15 clusters, N=2 independent experiments. Scale bar: 50μm. **e**. A431 cluster plated on a collagen network, fixed and immunostained with a Collagen-I antibody plus Phalloidin and imaged by two-photon microscopy. Representative image from n=9 clusters, N=2 experiments. Horizontal scale bars: 50μm, 25μm. Vertical scale bar: 10μm.

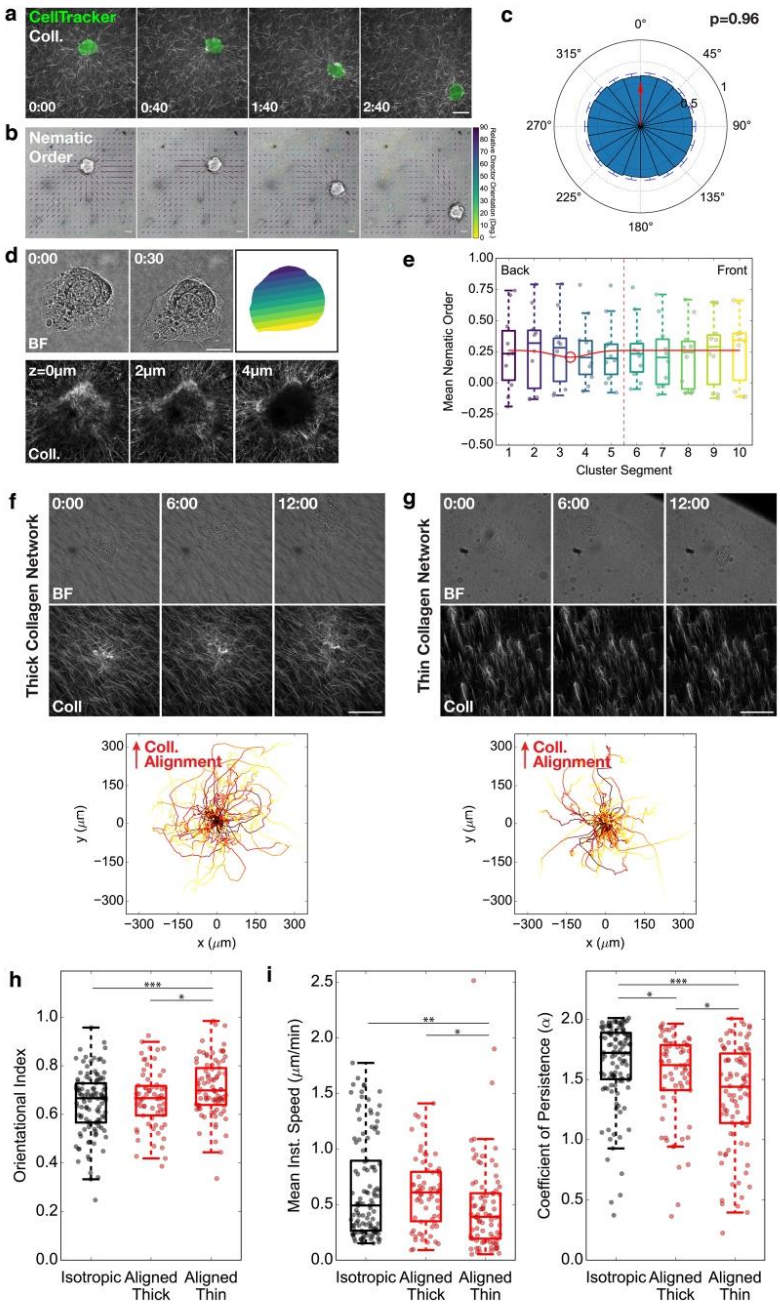

Extended Data Fig. 7 | See next page for caption.

Extended Data Fig. 7 | Analysis of collagen network alignment during collective migration. a. Montage of a cluster on a fluorescent collagen network (single *z*-slice on network surface). Scale Bar: 50μm. HH:MM. **b**. Montage of cluster in *a* overlaid with the local collagen alignment. Rods: local nematic order (orientation indicates mean collagen fiber orientation, length indicates order parameter magnitude *S*, color indicates orientation with respect to cluster center of mass (90° is oriented toward the cluster, 0° is oriented perpendicular to the cluster). Scale rod: $S=1$. Image length scale as for *a*. **c**. Polar plot of nematic order within 50μm of the cluster boundary (mean ± SD over all time points). P-value: Rayleigh test of uniformity. For *a-c*, representative images/data from n=28 cells, N=3 independent experiments. **d**. Live imaging of clusters using AiryScan super-resolution microscopy. *Upper Panels*: Brightfield images with segmentation and front-to-back regions in the direction of migration. *Lower Panels*: AiryScan images of TAMRA-labeled collagen at different z-positions. **e**. Box plot of the collagen fiber nematic order from AiryScan images. Dots represent individual clusters. For *d,e*, representative images/data from n=11 clusters, N=3 independent experiments. **f,g**. Montages of clusters migrating on thick deformable (*f*) or thin non-deformable (*g*) aligned collagen networks. *Lower Panels*: Overlaid cluster migration trajectories, adjusted to start at the origin (0,0) and rotated with respect to collagen alignment direction. Scale Bars: 100μm. HH:MM. Representative images from n=66, 86 clusters, N=4, 4 independent experiments **h**. Boxplot of orientational index along the collagen alignment direction for conditions in *f,g*. One-way ANOVA: p=0.00113. *p < 0.05, ***p < 0.001 for Tukey HSD post-hoc test (p=0.340, < 0.001, 0.0184). **i**. Boxplots of mean instantaneous speed and coefficient of persistence for conditions in *f,g*. For *h,i*, data from n=114, 66, 86 clusters, N=6, 4, 4 independent experiments. Thick isotropic data is the same as Fig. 1f. One-way ANOVAs: p=0.0180, 7.83e-6. *p < 0.05, **p < 0.01, ***p < 0.001 for Tukey HSD post-hoc test (p=0.567, 0.00919, 0.0393; p=0.0413, < 0.001, 0.0190).

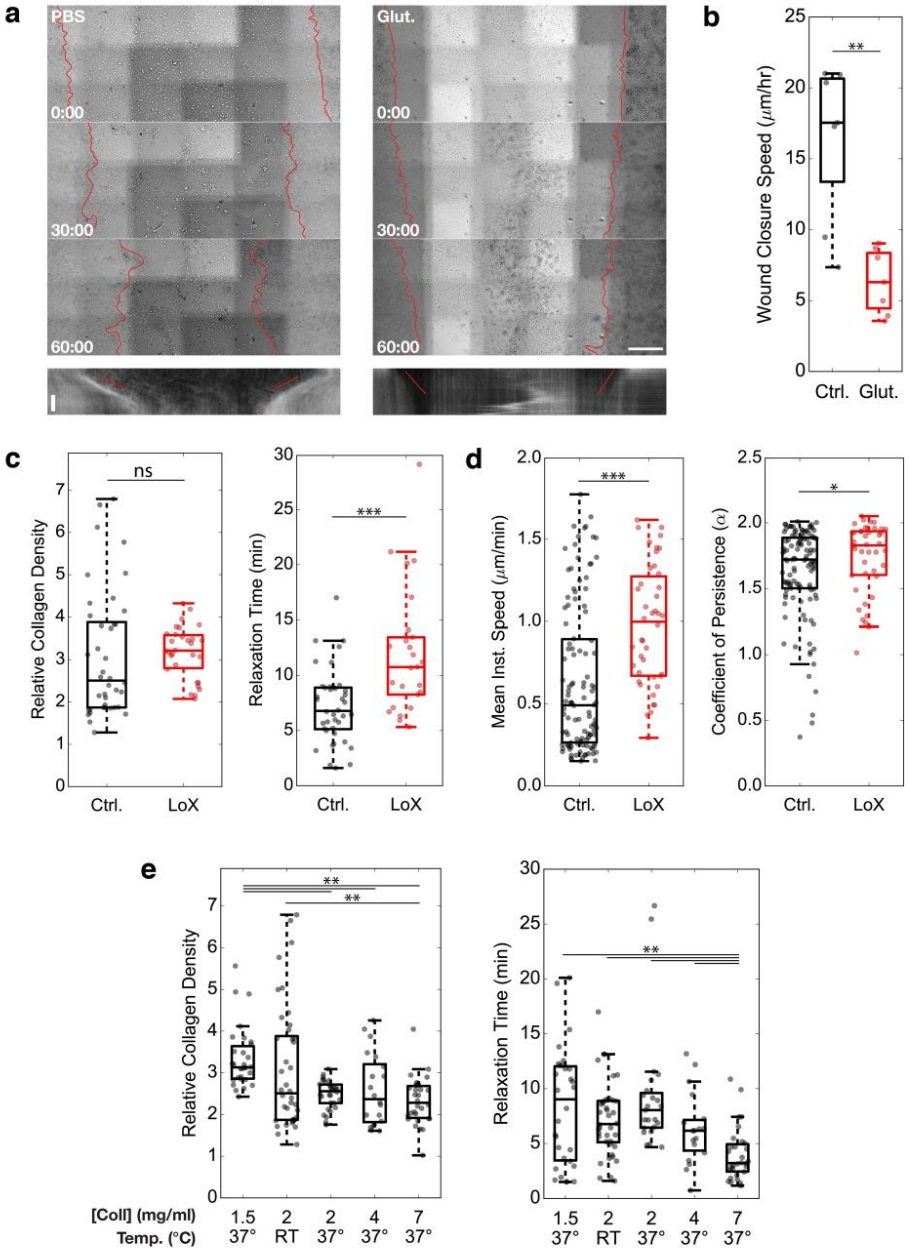

Extended Data Fig. 8 | See next page for caption.

Extended Data Fig. 8 | Role of crosslinking on different migration modes. a. Montages from wound healing assays using A431 cells plated using stencils on collagen networks pre-treated with PBS or the crosslinker glutaraldehyde. Red lines indicate the leading edge. Horizontal Scale Bar: 500μm. HH:MM. *Lower Panels*: Kymograph showing progression of the leading edge over time. Red lines indicate the velocity of wound closure on each side. Vertical Scale Bar: 20 hours. **b**. Boxplot of wound closure speed on control and crosslinked collagen gels. For *a,b*, representative images/data from n=7, 7 collagen gels, N=3,3 independent experiments. $^{**}p < 0.01$ for Welch's t-test (p=0.00258). **c**. Boxplots of relative collagen density and relaxation time (τ_r) following cluster removal using Trypsin/NH_4OH for collagen networks treated with Lysyl Oxidase (LOX). Each dot represents one cluster that was rapidly removed. Data represents n=40, 25 clusters, N=5, 3 independent experiments. ns:$p > 0.05$, $^{***}p < 0.001$ for Welch's t-test (p=0.717, 0.000550). **d**. Boxplots of mean instantaneous speed and coefficient of persistence for cluster migration on LOX-treated collagen networks. Data represents n=114, 42 clusters, N=6, 2 independent experiments. Control data is the same data as presented in Fig. 1f. $^{*}p < 0.05$, $^{***}p < 0.001$ for Welch's t-test (p=5.707e-6, 0.0472). **e**. Boxplots of relative collagen density (*left*) and relaxation time (τ_r, *right*) following cluster removal using Trypsin/NH_4OH for collagen networks using different collagen concentration or polymerization temperature. Each dot represents one cluster that was rapidly removed. Data represents n=30, 40, 23, 18, 30 clusters, N=3, 5, 3, 2, 3 independent experiments. One-way ANOVA p=8.30e-5, 5.22e-5. $^{**}p < 0.01$ for Tukey HSD post-hoc test (p=0.375, < 0.001,0.001665, < 0.001, 0.0332, 0.176,0.01, 0.539, 0.204, 0.195; p=0.27, 0.506, 0.159, < 0.001, 0.0579, 0.373, < 0.001, 0.0497, < 0.001, 0.00683).

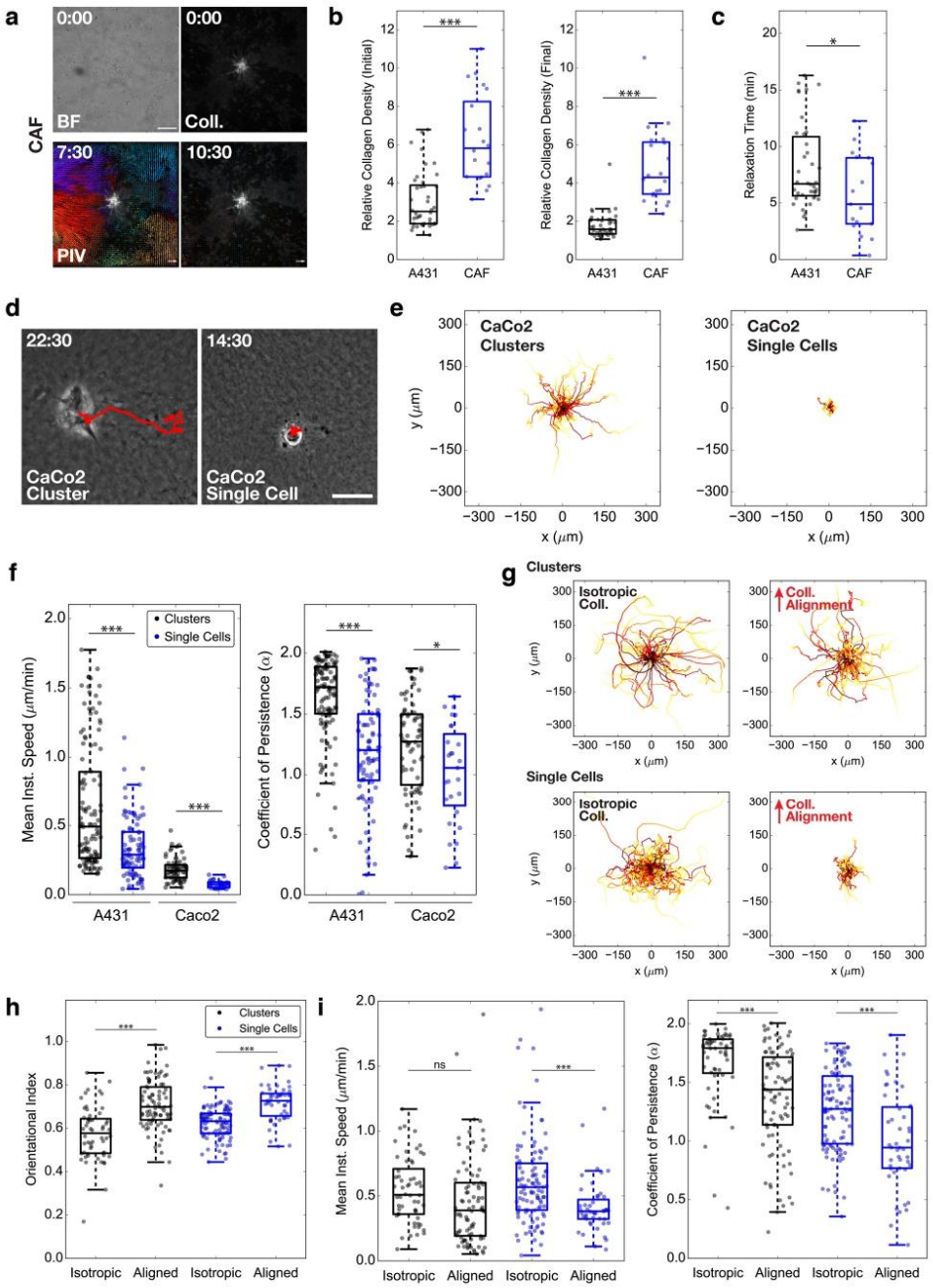

Extended Data Fig. 9 | See next page for caption.

Extended Data Fig. 9 | Single cell collagen deformation and migration. a. Micrographs of a primary human cancer associated fibroblast (CAF) on a fluorescent collagen network. Scale bar: 50μm. Scale vector: 0.5μm/min. HH:MM after addition of Trypsin/NH_4OH. Representative image from n=18 CAFs, N=2 independent experiments. **b**. Boxplots comparing relative collagen density before and after CAF removal. **c**. Boxplot of viscoelastic relaxation time (τ_r) following CAF removal. For *b,c*: each dot represents one cluster. Data from n=39, 18 clusters/CAFs, N=5 2 independent experiments. For *b,c*, *p < 0.01, ***p < 0.001 for Welch's t-test (p=6.65e-6, 1.19e-6, 0.0260). **d**. Micrographs from CaCo2 single cell or cluster on collagen networks. Red: migration trajectories. Scale Bar: 50μm. HH:MM. **e**. Overlaid migration trajectories for CaCo2 single cells and clusters, adjusted to start at the origin (0,0). **f**. Boxplots of mean instantaneous speed and coefficient of persistence for A431/CaCo2 clusters/single cells. For *c-e*, representative examples/data from n=114, 89, 69, 27 clusters/single cells, N=6, 3, 2, 2 independent experiments. A431 cluster data is same as in Fig. 1f. *p < 0.05, ***p < 0.001 for Welch's t-test (p=2.57e-9, 3.44e-15, 5.25e-13, 0.0185). **g**. Overlaid migration trajectories for clusters and single cells on thin isotropic or aligned collagen networks, adjusted to start at the origin (0, 0) and rotated with respect to the collagen alignment direction. **h**. Boxplot of orientational index along collagen alignment direction. **i**. Boxplots of mean instantaneous speed and coefficient of persistence. For *g-i*, Data represents n=56, 86, 103, 45 clusters, N=2, 4, 2, 2 independent experiments. Data for cluster migration on thin aligned networks is same as Extended Data Fig. 5g-i. For *h,i*, ns=p > 0.05, ***p < 0.001 for Welch's t-test (p=3.89e-9, 4.28e-9, 0.209, 2.30e-5, 8.74e-6, 0.000379).

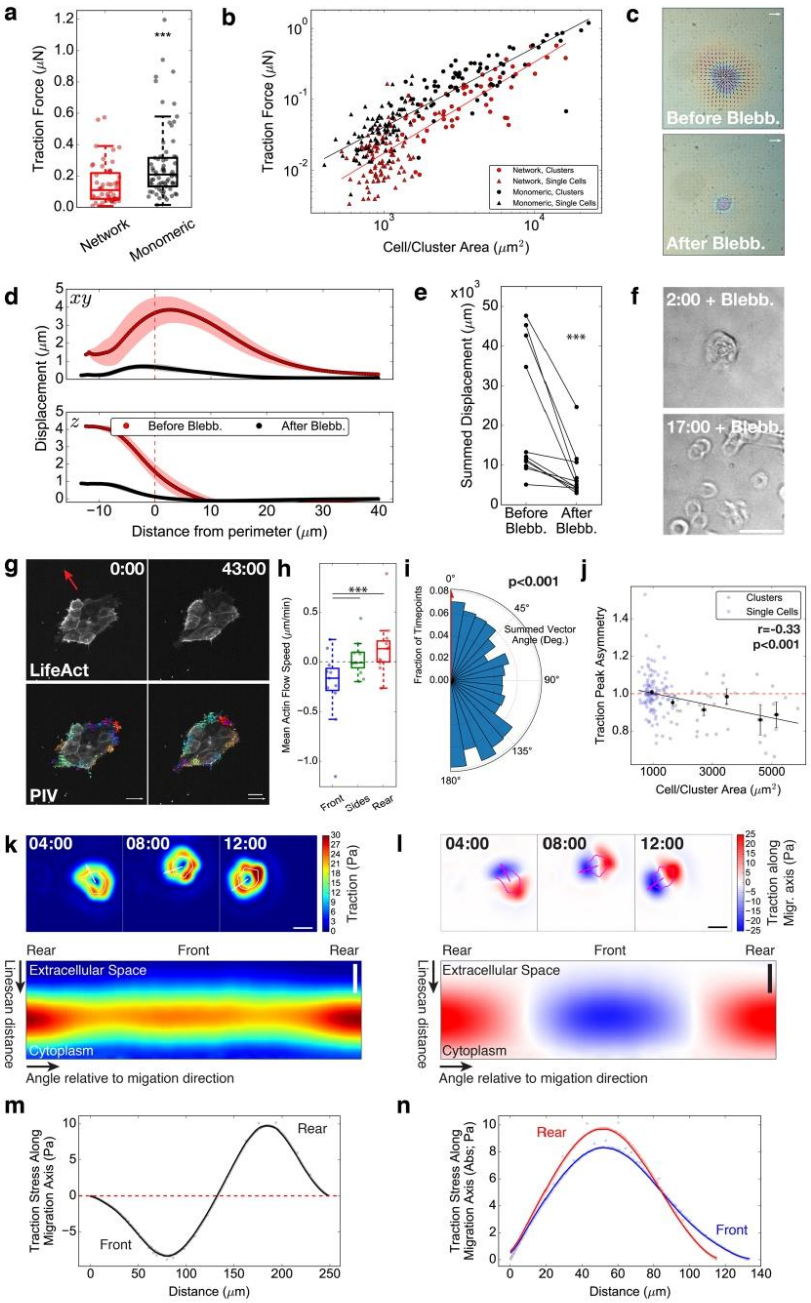

Extended Data Fig. 10 | See next page for caption.

Extended Data Fig. 10 | Traction force distributions are asymmetric and require myosin-2. a. Integrated 2D tractions from clusters on PAA + thin collagen network or monomeric collagen, n=54, 69 clusters, N=3, 3 independent experiments. ***p < 0.001 for Welch's t-test. **b**. Integrated traction force vs. cluster area on PAA + collagen network or monomeric collagen. Solid lines: power-law fits. **c**. 3D displacements of a cluster on PAA gel + thin collagen network with blebbistatin. Black arrows: *xy* displacements. Color scale: *z* displacements. **d**. Mean radial traction linescans from *c*. **e**. Summed displacements before/after blebbistatin treatment, n=11 clusters, N=1 independent experiment. ***p < 0.001 for Welch's t-test. **f**. Micrographs of clusters following blebbistatin treatment. Scale Bar: 100μm. HH:MM. **g**. Micrographs of mCherry-LifeAct A431 cells. Red arrow: migration direction. *Lower Panel*: PIV vectors of actin flows in the cortical region. Scale bar: 20μm. Scale vector: 0.05μm/min. MM:SS. See also Supplementary Video 22. **h**. Mean actin flow speeds with respect to migration direction for n=10 clusters, N=3 independent experiments. ***p < 0.001 for Welch's t-test. **i**. Radial histogram of summed PIV vector angle with respect to the migration direction (red arrow). P-value: Rayleigh test of uniformity. **j**. Plot of traction peak asymmetry (Front/Back). Solid circles: all binned data (mean ± SEM). Line: linear fit (raw data). Data represents n=54, 104 clusters/single cells, N=3, 3 independent experiments. **k,l**. Traction force magnitudes (total (*k*) or projected along migration axis (l)) for the cluster in Fig. 6a. *Lower panels*: Unfolded radial linescans with respect to the cluster front. Scale bars: 20μm. **m,n**. Linescans of tractions along migration axis (absolute values in *n*). Dots: raw values. Lines: smoothed data.

Chapter IX: References

Aceto, N., Toner, M., Maheswaran, S., Haber, D.A., 2015. En Route to Metastasis: Circulating Tumor Cell Clusters and Epithelial-to-Mesenchymal Transition. Trends Cancer 1, 44–52. https://doi.org/10.1016/j.trecan.2015.07.006

Adams, J.M., Cory, S., 2007. The Bcl-2 apoptotic switch in cancer development and therapy. Oncogene 26, 1324–1337. https://doi.org/10.1038/sj.onc.1210220

Ahmed, Z., Bicknell, R., 2009. Angiogenic signalling pathways. Methods Mol Biol 467, 3–24. https://doi.org/10.1007/978-1-59745-241-0_1

Al-Hajj, M., Wicha, M.S., Benito-Hernandez, A., Morrison, S.J., Clarke, M.F., 2003. Prospective identification of tumorigenic breast cancer cells. Proc Natl Acad Sci U S A 100, 3983–3988. https://doi.org/10.1073/pnas.0530291100

Arina, A., Idel, C., Hyjek, E.M., Alegre, M.-L., Wang, Y., Bindokas, V.P., Weichselbaum, R.R., Schreiber, H., 2016. Tumor-associated fibroblasts predominantly come from local and not circulating precursors. Proc Natl Acad Sci U S A 113, 7551–7556. https://doi.org/10.1073/pnas.1600363113

Artandi, S.E., DePinho, R.A., 2010. Telomeres and telomerase in cancer. Carcinogenesis 31, 9–18. https://doi.org/10.1093/carcin/bgp268

Attieh, Y., 2016. The hallmarks of CAFs in cancer invasion 10.

Attieh, Y., Clark, A.G., Grass, C., Richon, S., Pocard, M., Mariani, P., Elkhatib, N., Betz, T., Gurchenkov, B., Vignjevic, D.M., 2017. Cancer-associated fibroblasts lead tumor invasion through integrin-β3–dependent fibronectin assembly 12.

Auerbach, R., Lu, W.C., Pardon, E., Gumkowski, F., Kaminska, G., Kaminski, M., 1987. Specificity of adhesion between murine tumor cells and capillary endothelium: an in vitro correlate of preferential metastasis in vivo. Cancer Res 47, 1492–1496.

Azatov, M., Sun, X., Suberi, A., Fourkas, J.T., Upadhyaya, A., 2017. Topography on a subcellular scale modulates cellular adhesions and actin stress fiber dynamics in tumor associated fibroblasts. Phys. Biol. 13.

Bade, N.D., Kamien, R.D., Assoian, R.K., Stebe, K.J., 2018. Edges Impose Planar Alignment in Nematic Monolayers by Directing Cell Elongation and Enhancing Migration 11.

Baeriswyl, V., Christofori, G., 2009. The angiogenic switch in carcinogenesis. Semin Cancer Biol 19, 329–337. https://doi.org/10.1016/j.semcancer.2009.05.003

Balasubramaniam, L., Doostmohammadi, A., Saw, T.B., 2021. Investigating the nature of active forces in tissues reveals how contractile cells can form extensile monolayers 41.

Barbazán, J., 2019. Cancer associated fibroblasts: is the force the path to the dark side? Current Opinion in Cell Biology 9.

Barbazán, J., Alonso-Alconada, L., Elkhatib, N., Geraldo, S., Gurchenkov, V., Glentis, A., van Niel, G., Palmulli, R., Fernández, B., Viaño, P., Garcia-Caballero, T., López-López, R., Abal, M., Vignjevic, D.M., 2017. Liver Metastasis Is Facilitated by the Adherence of Circulating Tumor Cells to Vascular Fibronectin Deposits. Cancer Res 77, 3431–3441. https://doi.org/10.1158/0008-5472.CAN-16-1917

Barbazan, J., Pérez-González, C., Gómez-González, M., Dedenon, M., Richon, S., Latorre, E., Mariani, P., Descroix, S., Sens, P., Trepat, X., Vignjevic, D.M., 2021. Cancer-associated fibroblasts actively compress cancer cells and modulate mechanotransduction 9.

Beacham, D.A., Cukierman, E., 2005. Stromagenesis: the changing face of fibroblastic microenvironments during tumor progression. Semin Cancer Biol 15, 329–341. https://doi.org/10.1016/j.semcancer.2005.05.003

Berdasco, M., Esteller, M., 2010. Aberrant epigenetic landscape in cancer: how cellular identity goes awry. Dev Cell 19, 698–711. https://doi.org/10.1016/j.devcel.2010.10.005

Bergers, G., Benjamin, L.E., 2003. Tumorigenesis and the angiogenic switch. Nat Rev Cancer 3, 401–410. https://doi.org/10.1038/nrc1093

Bergers, G., Song, S., 2005. The role of pericytes in blood-vessel formation and maintenance. Neuro Oncol 7, 452–464. https://doi.org/10.1215/S1152851705000232

Bergfeld, S.A., DeClerck, Y.A., 2010. Bone marrow-derived mesenchymal stem cells and the tumor microenvironment. Cancer Metastasis Rev 29, 249–261. https://doi.org/10.1007/s10555-010-9222-7

Berx, G., van Roy, F., 2009. Involvement of members of the cadherin superfamily in cancer. Cold Spring Harb Perspect Biol 1, a003129. https://doi.org/10.1101/cshperspect.a003129

Bhattacharjee, S., Hamberger, F., Ravichandra, A., Miller, M., Nair, A., Affo, S., Filliol, A., Chin, L., Savage, T.M., Yin, D., Wirsik, N.M., Mehal, A., Arpaia, N., Seki, E., Mack, M., Zhu, D., Sims, P.A., Kalluri, R., Stanger, B.Z., Olive, K.P., Schmidt, T., Wells, R.G., Mederacke, I., Schwabe, R.F., 2021. Tumor restriction by type I collagen opposes tumor- promoting effects of cancer-associated fibroblasts. The Journal of Clinical Investigation 17.

Bhowmick, N.A., Neilson, E.G., Moses, H.L., 2004. Stromal fibroblasts in cancer initiation and progression. Nature 432, 332–337. https://doi.org/10.1038/nature03096

Biswas, S.K., Mantovani, A., 2010. Macrophage plasticity and interaction with lymphocyte subsets: cancer as a paradigm. Nat Immunol 11, 889–896. https://doi.org/10.1038/ni.1937

Blasco, M.A., 2005. Telomeres and human disease: ageing, cancer and beyond. Nat Rev Genet 6, 611–622. https://doi.org/10.1038/nrg1656

Bochet, L., Lehuédé, C., Dauvillier, S., Wang, Y.Y., Dirat, B., Laurent, V., Dray, C., Guiet, R., Maridonneau-Parini, I., Le Gonidec, S., Couderc, B., Escourrou, G., Valet, P., Muller, C., 2013. Adipocyte-derived fibroblasts promote tumor progression and contribute to the desmoplastic reaction in breast cancer. Cancer Res 73, 5657–5668. https://doi.org/10.1158/0008-5472.CAN-13-0530

Bonnans, C., Chou, J., Werb, Z., 2014. Remodelling the extracellular matrix in development and disease. Nat Rev Mol Cell Biol 15, 786–801. https://doi.org/10.1038/nrm3904

Boucher, Y., Baxter, L.T., Jain, R.K., 1990. Interstitial pressure gradients in tissue-isolated and subcutaneous tumors: implications for therapy. Cancer Res 50, 4478–4484.

Bronsert, P., Enderle-Ammour, K., Bader, M., Timme, S., Kuehs, M., Csanadi, A., Kayser, G., Kohler, I., Bausch, D., Hoeppner, J., Hopt, U.T., Keck, T., Stickeler, E., Passlick, B., Schilling, O., Reiss, C.P., Vashist, Y., Brabletz, T., Berger, J., Lotz, J., Olesch, J., Werner, M., Wellner, U.F., 2014. Cancer cell invasion and EMT marker expression: a three-dimensional study of the human cancer-host interface. J Pathol 234, 410–422. https://doi.org/10.1002/path.4416

Burkhart, D.L., Sage, J., 2008. Cellular mechanisms of tumour suppression by the retinoblastoma gene. Nat Rev Cancer 8, 671–682. https://doi.org/10.1038/nrc2399

Butler, T.P., Gullino, P.M., 1975. Quantitation of cell shedding into efferent blood of mammary adenocarcinoma. Cancer Res 35, 512–516.

Calon, A., Espinet, E., Palomo-Ponce, S., Tauriello, D.V.F., Iglesias, M., Céspedes, M.V., Sevillano, M., Nadal, C., Jung, P., Zhang, X.H.-F., Byrom, D., Riera, A., Rossell, D., Mangues, R., Massagué, J., Sancho, E., Batlle, E., 2012. Dependency of colorectal cancer on a TGF-β-driven program in stromal cells for metastasis initiation. Cancer Cell 22, 571–584. https://doi.org/10.1016/j.ccr.2012.08.013

Calon, A., Tauriello, D.V.F., Batlle, E., 2014. TGF-beta in CAF-mediated tumor growth and metastasis. Semin Cancer Biol 25, 15–22. https://doi.org/10.1016/j.semcancer.2013.12.008

Calvo, F., Ege, N., Grande-Garcia, A., Hooper, S., Jenkins, R.P., Chaudhry, S.I., Harrington, K., Williamson, P., Moeendarbary, E., Charras, G., Sahai, E., 2013. Mechanotransduction and YAP-dependent matrix remodelling is required for the generation and maintenance of cancer-associated fibroblasts. Nat Cell Biol 15, 637–646. https://doi.org/10.1038/ncb2756

Cancer Today [WWW Document], 2020. URL https://gco.iarc.fr/today/fact-sheets-cancers (accessed 7.8.22).

Carmeliet, P., Jain, R.K., 2000. Angiogenesis in cancer and other diseases. Nature 407, 249–257. https://doi.org/10.1038/35025220

Chang, P.-H., Hwang-Verslues, W.W., Chang, Y.-C., Chen, C.-C., Hsiao, M., Jeng, Y.-M., Chang, K.-J., Lee, E.Y.-H.P., Shew, J.-Y., Lee, W.-H., 2012. Activation of Robo1 signaling of breast cancer cells by Slit2 from stromal fibroblast restrains tumorigenesis via blocking PI3K/Akt/β-catenin pathway. Cancer Res 72, 4652–4661. https://doi.org/10.1158/0008-5472.CAN-12-0877

Cheng, N., Bhowmick, N.A., Chytil, A., Gorksa, A.E., Brown, K.A., Muraoka, R., Arteaga, C.L., Neilson, E.G., Hayward, S.W., Moses, H.L., 2005. Loss of TGF-beta type II receptor in fibroblasts promotes mammary carcinoma growth and invasion through upregulation of TGF-alpha-, MSP- and HGF-mediated signaling networks. Oncogene 24, 5053–5068. https://doi.org/10.1038/sj.onc.1208685

Cheng, N., Chytil, A., Shyr, Y., Joly, A., Moses, H.L., 2008. Transforming growth factor-beta signaling-deficient fibroblasts enhance hepatocyte growth factor signaling in mammary carcinoma cells to promote scattering and invasion. Mol Cancer Res 6, 1521–1533. https://doi.org/10.1158/1541-7786.MCR-07-2203

Cho, R.W., Clarke, M.F., 2008. Recent advances in cancer stem cells. Curr Opin Genet Dev 18, 48–53. https://doi.org/10.1016/j.gde.2008.01.017

Clark, A.G., 2015. Modes of cancer cell invasion and the role of the microenvironment. Current Opinion in Cell Biology 10.

Clark, A.G., Maitra, A., Jacques, C., Bergert, M., Pérez-González, C., Simon, A., Lederer, L., Diz-Muñoz, A., Trepat, X., Voituriez, R., Vignjevic, D.M., 2022. Self-generated gradients steer collective migration on viscoelastic collagen networks. Nat Mater. https://doi.org/10.1038/s41563-022-01259-5

Cochlin, D.L., Ganatra, R.H., Griffiths, D.F.R., 2002. Elastography in the detection of prostatic cancer. Clin Radiol 57, 1014–1020. https://doi.org/10.1053/crad.2002.0989

Colotta, F., Allavena, P., Sica, A., Garlanda, C., Mantovani, A., 2009. Cancer-related inflammation, the seventh hallmark of cancer: links to genetic instability. Carcinogenesis 30, 1073–1081. https://doi.org/10.1093/carcin/bgp127

Conklin, M.W., Eickhoff, J.C., Riching, K.M., Pehlke, C.A., Eliceiri, K.W., Provenzano, P.P., Friedl, A., Keely, P.J., 2011. Aligned collagen is a prognostic signature for survival in human breast carcinoma. Am J Pathol 178, 1221–1232. https://doi.org/10.1016/j.ajpath.2010.11.076

Costa, A., Kieffer, Y., Scholer-Dahirel, A., Pelon, F., Bourachot, B., Cardon, M., Sirven, P., Magagna, I., Fuhrmann, L., Bernard, C., Bonneau, C., Kondratova, M., Kuperstein, I., Zinovyev, A., Givel, A.-M., Parrini, M.-C., Soumelis, V., Vincent-Salomon, A., Mechta-Grigoriou, F., 2018. Fibroblast Heterogeneity and Immunosuppressive Environment in Human Breast Cancer. Cancer Cell 33, 463-479.e10. https://doi.org/10.1016/j.ccell.2018.01.011

Cox, T.R., Bird, D., Baker, A.-M., Barker, H.E., Ho, M.W.-Y., Lang, G., Erler, J.T., 2013. LOX-mediated collagen crosslinking is responsible for fibrosis-enhanced metastasis. Cancer Res 73, 1721–1732. https://doi.org/10.1158/0008-5472.CAN-12-2233

Crissman, J.D., Hatfield, J., Schaldenbrand, M., Sloane, B.F., Honn, K.V., 1985. Arrest and extravasation of B16 amelanotic melanoma in murine lungs. A light and electron microscopic study. Lab Invest 53, 470–478.

Curto, M., Cole, B.K., Lallemand, D., Liu, C.-H., McClatchey, A.I., 2007. Contact-dependent inhibition of EGFR signaling by Nf2/Merlin. J Cell Biol 177, 893–903. https://doi.org/10.1083/jcb.200703010

Darwiche, N., 2020. Epigenetic mechanisms and the hallmarks of cancer: an intimate affair. Am J Cancer Res 10, 1954–1978.

De Blander, H., Morel, A.-P., Senaratne, A.P., Ouzounova, M., Puisieux, A., 2021. Cellular Plasticity: A Route to Senescence Exit and Tumorigenesis. Cancers (Basel) 13, 4561. https://doi.org/10.3390/cancers13184561

De, P., Aske, J., Dey, N., 2021. Cancer-Associated Fibroblast Functions as a Road-Blockin Cancer Therapy 25.

De Palma, M., Murdoch, C., Venneri, M.A., Naldini, L., Lewis, C.E., 2007. Tie2-expressing monocytes: regulation of tumor angiogenesis and therapeutic implications. Trends Immunol 28, 519–524. https://doi.org/10.1016/j.it.2007.09.004

de Visser, K.E., Eichten, A., Coussens, L.M., 2006. Paradoxical roles of the immune system during cancer development. Nat Rev Cancer 6, 24–37. https://doi.org/10.1038/nrc1782

De Wever, O., Nguyen, Q.-D., Van Hoorde, L., Bracke, M., Bruyneel, E., Gespach, C., Mareel, M., 2004. Tenascin-C and SF/HGF produced by myofibroblasts in vitro provide convergent pro-invasive

signals to human colon cancer cells through RhoA and Rac. FASEB J 18, 1016–1018. https://doi.org/10.1096/fj.03-1110fje

De Wever, O., Van Bockstal, M., Mareel, M., Hendrix, A., Bracke, M., 2014. Carcinoma-associated fibroblasts provide operational flexibility in metastasis. Semin Cancer Biol 25, 33–46. https://doi.org/10.1016/j.semcancer.2013.12.009

DeBerardinis, R.J., Lum, J.J., Hatzivassiliou, G., Thompson, C.B., 2008. The biology of cancer: metabolic reprogramming fuels cell growth and proliferation. Cell Metab 7, 11–20. https://doi.org/10.1016/j.cmet.2007.10.002

DeNardo, D.G., Andreu, P., Coussens, L.M., 2010. Interactions between lymphocytes and myeloid cells regulate pro- versus anti-tumor immunity. Cancer Metastasis Rev 29, 309–316. https://doi.org/10.1007/s10555-010-9223-6

Direkze, N.C., Alison, M.R., 2006. Bone marrow and tumour stroma: an intimate relationship. Hematol Oncol 24, 189–195. https://doi.org/10.1002/hon.788

Doostmohammadi, A., Ignés-Mullol, J., Yeomans, J.M., Sagués, F., 2018. Active nematics. Nat Commun 9, 3246. https://doi.org/10.1038/s41467-018-05666-8

Duclos, G., Adkins, R., Banerjee, D., Peterson, M.S.E., Varghese, M., Kolvin, I., Baskaran, Arvind, Pelcovits, R.A., Powers, T.R., Baskaran, Aparna, Toschi, F., Hagan, M.F., Streichan, S.J., Vitelli, V., Beller, D.A., Dogic, Z., 2020. Topological structure and dynamics of three-dimensional active nematics 6.

Duclos, G., Blanch-Mercader, C., Yashunsky, V., Salbreux, G., 2018. Spontaneous shear flow in confined cellular nematics 13.

Duclos, G., Erlenkämper, C., Joanny, J.-F., Silberzan, P., 2017. Topological defects in confined populations of spindle-shaped cells. NATURE PHYSICS 13, 6.

Duclos, G., Garcia, S., Yevick, H.G., Silberzan, P., 2014. Perfect nematic order in confined monolayers of spindle-shaped cells. Soft Matter 29.

Duda, D.G., Duyverman, A.M.M.J., Kohno, M., Snuderl, M., Steller, E.J.A., Fukumura, D., Jain, R.K., 2010. Malignant cells facilitate lung metastasis by bringing their own soil. Proc Natl Acad Sci U S A 107, 21677–21682. https://doi.org/10.1073/pnas.1016234107

Dumont, N., Liu, B., Defilippis, R.A., Chang, H., Rabban, J.T., Karnezis, A.N., Tjoe, J.A., Marx, J., Parvin, B., Tlsty, T.D., 2013. Breast fibroblasts modulate early dissemination, tumorigenesis, and metastasis through alteration of extracellular matrix characteristics. Neoplasia 15, 249–262. https://doi.org/10.1593/neo.121950

Dzutsev, A., Badger, J.H., Perez-Chanona, E., Roy, S., Salcedo, R., Smith, C.K., Trinchieri, G., 2017. Microbes and Cancer. Annu Rev Immunol 35, 199–228. https://doi.org/10.1146/annurev-immunol-051116-052133

Egeblad, M., Nakasone, E.S., Werb, Z., 2010a. Tumors as organs: complex tissues that interface with the entire organism. Dev Cell 18, 884–901. https://doi.org/10.1016/j.devcel.2010.05.012

Egeblad, M., Rasch, M.G., Weaver, V.M., 2010b. Dynamic interplay between the collagen scaffold and tumor evolution. Curr Opin Cell Biol 22, 697–706. https://doi.org/10.1016/j.ceb.2010.08.015

Ekblom, P., Ekblom, M., Fecker, L., Klein, G., Zhang, H.Y., Kadoya, Y., Chu, M.L., Mayer, U., Timpl, R., 1994. Role of mesenchymal nidogen for epithelial morphogenesis in vitro. Development 120, 2003–2014. https://doi.org/10.1242/dev.120.7.2003

Erdogan, B., Ao, M., White, L.M., Means, A.L., Brewer, B.M., Yang, L., Washington, M.K., Shi, C., Franco, O.E., Weaver, A.M., Hayward, S.W., Li, D., Webb, D.J., 2017. Cancer-associated fibroblasts promote directional cancer cell migration by aligning fibronectin. J Cell Biol 216, 3799–3816. https://doi.org/10.1083/jcb.201704053

Faget, D.V., Ren, Q., Stewart, S.A., 2019. Unmasking senescence: context-dependent effects of SASP in cancer. Nat Rev Cancer 19, 439–453. https://doi.org/10.1038/s41568-019-0156-2

Fang, S., Salven, P., 2011. Stem cells in tumor angiogenesis. J Mol Cell Cardiol 50, 290–295. https://doi.org/10.1016/j.yjmcc.2010.10.024

Fearon, D.T., 2014. The carcinoma-associated fibroblast expressing fibroblast activation protein and escape from immune surveillance. Cancer Immunol Res 2, 187–193. https://doi.org/10.1158/2326-6066.CIR-14-0002

Ferrara, N., 2009. Vascular endothelial growth factor. Arterioscler Thromb Vasc Biol 29, 789–791. https://doi.org/10.1161/ATVBAHA.108.179663

Fidler, I.J., 2002. The pathogenesis of cancer metastasis: the 'seed and soil' hypothesis revisited. C ANCER 6.

Flint, T.R., Janowitz, T., Connell, C.M., Roberts, E.W., Denton, A.E., Coll, A.P., Jodrell, D.I., Fearon, D.T., 2016. Tumor-Induced IL-6 Reprograms Host Metabolism to Suppress Anti-tumor Immunity. Cell Metab 24, 672–684. https://doi.org/10.1016/j.cmet.2016.10.010

Fourriere, L., Kasri, A., Gareil, N., Bardin, S., Bousquet, H., Pereira, D., Perez, F., Goud, B., Boncompain, G., Miserey-Lenkei, S., 2019. RAB6 and microtubules restrict protein secretion to focal adhesions. J Cell Biol 218, 2215–2231. https://doi.org/10.1083/jcb.201805002

Friedl, P., Locker, J., Sahai, E., Segall, J.E., 2012. Classifying collective cancer cell invasion. Nat Cell Biol 14, 777–783. https://doi.org/10.1038/ncb2548

Friedl, P., Wolf, K., 2010. Plasticity of cell migration: a multiscale tuning model. J Cell Biol 188, 11–19. https://doi.org/10.1083/jcb.200909003

Fukumura, D., Xavier, R., Sugiura, T., Chen, Y., Park, E.C., Lu, N., Selig, M., Nielsen, G., Taksir, T., Jain, R.K., Seed, B., 1998. Tumor induction of VEGF promoter activity in stromal cells. Cell 94, 715–725. https://doi.org/10.1016/s0092-8674(00)81731-6

Gaengel, K., Genové, G., Armulik, A., Betsholtz, C., 2009. Endothelial-mural cell signaling in vascular development and angiogenesis. Arterioscler Thromb Vasc Biol 29, 630–638. https://doi.org/10.1161/ATVBAHA.107.161521

Gaggioli, C., Hooper, S., Hidalgo-Carcedo, C., Grosse, R., Marshall, J.F., Sahai, E., 2007. Fibroblast-led collective invasion of carcinoma cells with differing roles for RhoGTPases in leading and following cells 9, 19.

Gascard, P., Tlsty, T.D., 2016. Carcinoma-associated fibroblasts: orchestrating the composition of malignancy. Genes Dev 30, 1002–1019. https://doi.org/10.1101/gad.279737.116

Gay, L.J., Malanchi, I., 2017. The sleeping ugly: Tumour microenvironment's act to make or break the spell of dormancy. Biochim Biophys Acta Rev Cancer 1868, 231–238. https://doi.org/10.1016/j.bbcan.2017.05.002

Gennes, P.G. de, Prost, J., 1993. The Physics of Liquid Crystals. Clarendon Press.

Gerhardt, H., Semb, H., 2008. Pericytes: gatekeepers in tumour cell metastasis? J Mol Med (Berl) 86, 135–144. https://doi.org/10.1007/s00109-007-0258-2

Giaccia, A.J., Schipani, E., 2010. Role of carcinoma-associated fibroblasts and hypoxia in tumor progression. Curr Top Microbiol Immunol 345, 31–45. https://doi.org/10.1007/82_2010_73

Glentis, A., 2017. Cancer-associated fibroblasts induce metalloprotease-independent cancer cell invasion of the basement membrane. NATURE COMMUNICATIONS 13.

Glentis, A., Gurchenkov, V., Vignjevic, D.M., 2014. Assembly, heterogeneity, and breaching of the basement membranes 8, 11.

Gopal, S., Veracini, L., Grall, D., Butori, C., Schaub, S., Audebert, S., Camoin, L., Baudelet, E., Radwanska, A., Beghelli-de la Forest Divonne, S., Violette, S.M., Weinreb, P.H., Rekima, S., Ilie, M., Sudaka, A., Hofman, P., Van Obberghen-Schilling, E., 2017. Fibronectin-guided migration of carcinoma collectives. Nat Commun 8, 14105. https://doi.org/10.1038/ncomms14105

Goreczny, G.J., Forsythe, I.J., Turner, C.E., 2018. Hic-5 regulates fibrillar adhesion formation to control tumor extracellular matrix remodeling through interaction with tensin1. Oncogene 37, 1699–1713. https://doi.org/10.1038/s41388-017-0074-2

Goreczny, G.J., Ouderkirk-Pecone, J.L., Olson, E.C., Krendel, M., Turner, C.E., 2017. Hic-5 remodeling of the stromal matrix promotes breast tumor progression. Oncogene 36, 2693–2703. https://doi.org/10.1038/onc.2016.422

Grivennikov, S.I., Greten, F.R., Karin, M., 2010. Immunity, inflammation, and cancer. Cell 140, 883–899. https://doi.org/10.1016/j.cell.2010.01.025

Guillamat, P., Blanch-Mercader, C., Kruse, K., Roux, A., 2022. Integer topological defects organize stresses driving tissue morphogenesis 43.
Hajdu, S.I., 2011. A note from history: landmarks in history of cancer, part 1. Cancer 117, 1097–1102. https://doi.org/10.1002/cncr.25553
Hanahan, D., 2022. Hallmarks of Cancer: New Dimensions 16.
Hanahan, D., 2011. Hallmarks of Cancer: The Next Generation 29.
Hanahan, D., Coussens, L.M., 2012. Accessories to the crime: functions of cells recruited to the tumor microenvironment. Cancer Cell 21, 309–322. https://doi.org/10.1016/j.ccr.2012.02.022
Hanahan, D., Weinberg, R.A., 2000. The hallmarks of cancer. Cell 100, 57–70. https://doi.org/10.1016/s0092-8674(00)81683-9
Harper, J., Sainson, R.C.A., 2014. Regulation of the anti-tumour immune response by cancer-associated fibroblasts. Semin Cancer Biol 25, 69–77. https://doi.org/10.1016/j.semcancer.2013.12.005
Hematti, P., 2012. Mesenchymal stromal cells and fibroblasts: a case of mistaken identity? Cytotherapy 14, 516–521. https://doi.org/10.3109/14653249.2012.677822
Hotary, K.B., Yana, I., Sabeh, F., Li, X.-Y., Holmbeck, K., Birkedal-Hansen, H., Allen, E.D., Hiraoka, N., Weiss, S.J., 2002. Matrix metalloproteinases (MMPs) regulate fibrin-invasive activity via MT1-MMP-dependent and -independent processes. J Exp Med 195, 295–308. https://doi.org/10.1084/jem.20010815
Hsu, P.P., Sabatini, D.M., 2008. Cancer cell metabolism: Warburg and beyond. Cell 134, 703–707. https://doi.org/10.1016/j.cell.2008.08.021
Hugo, H., Ackland, M.L., Blick, T., Lawrence, M.G., Clements, J.A., Williams, E.D., Thompson, E.W., 2007. Epithelial--mesenchymal and mesenchymal--epithelial transitions in carcinoma progression. J Cell Physiol 213, 374–383. https://doi.org/10.1002/jcp.21223
Irianto, J., Xia, Y., Pfeifer, C.R., Athirasala, A., Ji, J., Alvey, C., Tewari, M., Bennett, R.R., Harding, S.M., Liu, A.J., Greenberg, R.A., Discher, D.E., 2017. DNA Damage Follows Repair Factor Depletion and Portends Genome Variation in Cancer Cells after Pore Migration. Curr Biol 27, 210–223. https://doi.org/10.1016/j.cub.2016.11.049
Ito, S., Nakanishi, H., Ikehara, Y., Kato, T., Kasai, Y., Ito, K., Akiyama, S., Nakao, A., Tatematsu, M., 2001. Real-time observation of micrometastasis formation in the living mouse liver using a green fluorescent protein gene-tagged rat tongue carcinoma cell line. Int J Cancer 93, 212–217. https://doi.org/10.1002/ijc.1318
Jain, R.K., 2013. Normalizing tumor microenvironment to treat cancer: bench to bedside to biomarkers. J Clin Oncol 31, 2205–2218. https://doi.org/10.1200/JCO.2012.46.3653
Johansson, M., Denardo, D.G., Coussens, L.M., 2008. Polarized immune responses differentially regulate cancer development. Immunol Rev 222, 145–154. https://doi.org/10.1111/j.1600-065X.2008.00600.x
Jones, R.G., Thompson, C.B., 2009. Tumor suppressors and cell metabolism: a recipe for cancer growth. Genes Dev 23, 537–548. https://doi.org/10.1101/gad.1756509
Junttila, M.R., Evan, G.I., 2009. p53--a Jack of all trades but master of none. Nat Rev Cancer 9, 821–829. https://doi.org/10.1038/nrc2728
Kalluri, R., 2016. The biology and function of fibroblasts in cancer 17.
Kang, S.-G., Ha, Y.-R., Ko, Y.-H., Kang, S.-H., Joo, K.-J., Cho, H.-Y., Park, H.-S., Kim, C.-H., Kwon, S.-Y., Kim, J.-J., Cheon, J., Lee, J.-G., 2013. Effect of laminin 332 on motility and invasion in bladder cancer. Kaohsiung J Med Sci 29, 422–429. https://doi.org/10.1016/j.kjms.2012.12.003
Kaplan, R.N., Riba, R.D., Zacharoulis, S., Bramley, A.H., Vincent, L., Costa, C., MacDonald, D.D., Jin, D.K., Shido, K., Kerns, S.A., Zhu, Z., Hicklin, D., Wu, Y., Port, J.L., Altorki, N., Port, E.R., Ruggero, D., Shmelkov, S.V., Jensen, K.K., Rafii, S., Lyden, D., 2005. VEGFR1-positive haematopoietic bone marrow progenitors initiate the pre-metastatic niche. Nature 438, 820–827. https://doi.org/10.1038/nature04186
Kawaguchi, K., 2017. Topological defects control collective dynamics in neural progenitor cell cultures 16.

Kessenbrock, K., Plaks, V., Werb, Z., 2010. Matrix metalloproteinases: regulators of the tumor microenvironment. Cell 141, 52–67. https://doi.org/10.1016/j.cell.2010.03.015

Klymkowsky, M.W., Savagner, P., 2009. Epithelial-mesenchymal transition: a cancer researcher's conceptual friend and foe. Am J Pathol 174, 1588–1593. https://doi.org/10.2353/ajpath.2009.080545

Krog, B.L., Henry, M.D., 2018. Biomechanics of the Circulating Tumor Cell Microenvironment. Adv Exp Med Biol 1092, 209–233. https://doi.org/10.1007/978-3-319-95294-9_11

Krzyszczyk, P., Acevedo, A., Davidoff, E.J., Timmins, L.M., Marrero-Berrios, I., Patel, M., White, C., Lowe, C., Sherba, J.J., Hartmanshenn, C., O'Neill, K.M., Balter, M.L., Fritz, Z.R., Androulakis, I.P., Schloss, R.S., Yarmush, M.L., 2018. The growing role of precision and personalized medicine for cancer treatment. Technology (Singap World Sci) 6, 79–100. https://doi.org/10.1142/S2339547818300020

Labernadie, A., Kato, T., Brugués, A., Serra-Picamal, X., Derzsi, S., Arwert, E., Weston, A., González-Tarragó, V., Elosegui-Artola, A., Albertazzi, L., Alcaraz, J., Roca-Cusachs, P., Sahai, E., Trepat, X., 2017. A mechanically active heterotypic E-cadherin/N-cadherin adhesion enables fibroblasts to drive cancer cell invasion. Nat Cell Biol 19, 224–237. https://doi.org/10.1038/ncb3478

Lamagna, C., Bergers, G., 2006. The bone marrow constitutes a reservoir of pericyte progenitors. J Leukoc Biol 80, 677–681. https://doi.org/10.1189/jlb.0506309

Lane, D.P., 1992. Cancer. p53, guardian of the genome. Nature 358, 15–16. https://doi.org/10.1038/358015a0

LeBleu, V.S., Kalluri, R., 2018. A peek into cancer-associated fibroblasts: origins, functions and translational impact 9.

Lee, H.-O., Mullins, S.R., Franco-Barraza, J., Valianou, M., Cukierman, E., Cheng, J.D., 2011. FAP-overexpressing fibroblasts produce an extracellular matrix that enhances invasive velocity and directionality of pancreatic cancer cells. BMC Cancer 11, 245. https://doi.org/10.1186/1471-2407-11-245

Leight, J.L., Wozniak, M.A., Chen, S., Lynch, M.L., Chen, C.S., 2012. Matrix rigidity regulates a switch between TGF-β1-induced apoptosis and epithelial-mesenchymal transition. Mol Biol Cell 23, 781–791. https://doi.org/10.1091/mbc.E11-06-0537

Lowe, S.W., Cepero, E., Evan, G., 2004. Intrinsic tumour suppression. Nature 432, 307–315. https://doi.org/10.1038/nature03098

Madar, S., Goldstein, I., Rotter, V., 2013. 'Cancer associated fibroblasts'--more than meets the eye. Trends Mol Med 19, 447–453. https://doi.org/10.1016/j.molmed.2013.05.004

Mantovani, A., 2010. Molecular pathways linking inflammation and cancer. Curr Mol Med 10, 369–373. https://doi.org/10.2174/156652410791316968

Maris, P., Blomme, A., Palacios, A.P., Costanza, B., Bellahcène, A., Bianchi, E., Gofflot, S., Drion, P., Trombino, G.E., Di Valentin, E., Cusumano, P.G., Maweja, S., Jerusalem, G., Delvenne, P., Lifrange, E., Castronovo, V., Turtoi, A., 2015. Asporin Is a Fibroblast-Derived TGF-β1 Inhibitor and a Tumor Suppressor Associated with Good Prognosis in Breast Cancer. PLoS Med 12, e1001871. https://doi.org/10.1371/journal.pmed.1001871

Maroudas-Sacks, Y., Garion, L., Shani-Zerbib, L., Livshits, A., Braun, E., Keren, K., 2020. Topological defects in the nematic order of actin fibers as organization centers of Hydra morphogenesis 42.

Mattiuzzi, C., Lippi, G., 2019. Current Cancer Epidemiology. Journal of Epidemiology and Global Health 6.

Merino, M.M., Levayer, R., Moreno, E., 2016. Survival of the Fittest: Essential Roles of Cell Competition in Development, Aging, and Cancer. Trends Cell Biol 26, 776–788. https://doi.org/10.1016/j.tcb.2016.05.009

Merrell, A.J., Stanger, B.Z., 2016. Adult cell plasticity in vivo: de-differentiation and transdifferentiation are back in style. Nat Rev Mol Cell Biol 17, 413–425. https://doi.org/10.1038/nrm.2016.24

Mohammadi, H., Sahai, E., 2018. Mechanisms and impact of altered tumour mechanics. Nat Cell Biol 20, 766–774. https://doi.org/10.1038/s41556-018-0131-2

Morales-Valencia, J., David, G., 2022. The origins of cancer cell dormancy. Curr Opin Genet Dev 74, 101914. https://doi.org/10.1016/j.gde.2022.101914

Mottram, N.J., Newton, C.J.P., 2014. Introduction to Q-tensor theory 20.

Mougiakakos, D., Choudhury, A., Lladser, A., Kiessling, R., Johansson, C.C., 2010. Regulatory T cells in cancer. Adv Cancer Res 107, 57–117. https://doi.org/10.1016/S0065-230X(10)07003-X

Mu, P., Zhang, Z., Benelli, M., Karthaus, W.R., Hoover, E., Chen, C.-C., Wongvipat, J., Ku, S.-Y., Gao, D., Cao, Z., Shah, N., Adams, E.J., Abida, W., Watson, P.A., Prandi, D., Huang, C.-H., de Stanchina, E., Lowe, S.W., Ellis, L., Beltran, H., Rubin, M.A., Goodrich, D.W., Demichelis, F., Sawyers, C.L., 2017. SOX2 promotes lineage plasticity and antiandrogen resistance in TP53- and RB1-deficient prostate cancer. Science 355, 84–88. https://doi.org/10.1126/science.aah4307

Murdoch, C., Muthana, M., Coffelt, S.B., Lewis, C.E., 2008. The role of myeloid cells in the promotion of tumour angiogenesis. Nat Rev Cancer 8, 618–631. https://doi.org/10.1038/nrc2444

Nagy, J.A., Chang, S.-H., Shih, S.-C., Dvorak, A.M., Dvorak, H.F., 2010. Heterogeneity of the tumor vasculature. Semin Thromb Hemost 36, 321–331. https://doi.org/10.1055/s-0030-1253454

Negrini, S., Gorgoulis, V.G., Halazonetis, T.D., 2010. Genomic instability--an evolving hallmark of cancer. Nat Rev Mol Cell Biol 11, 220–228. https://doi.org/10.1038/nrm2858

Nejman, D., Livyatan, I., Fuks, G., Gavert, N., Zwang, Y., Geller, L.T., Rotter-Maskowitz, A., Weiser, R., Mallel, G., Gigi, E., Meltser, A., Douglas, G.M., Kamer, I., Gopalakrishnan, V., Dadosh, T., Levin-Zaidman, S., Avnet, S., Atlan, T., Cooper, Z.A., Arora, R., Cogdill, A.P., Khan, M.A.W., Ologun, G., Bussi, Y., Weinberger, A., Lotan-Pompan, M., Golani, O., Perry, G., Rokah, M., Bahar-Shany, K., Rozeman, E.A., Blank, C.U., Ronai, A., Shaoul, R., Amit, A., Dorfman, T., Kremer, R., Cohen, Z.R., Harnof, S., Siegal, T., Yehuda-Shnaidman, E., Gal-Yam, E.N., Shapira, H., Baldini, N., Langille, M.G.I., Ben-Nun, A., Kaufman, B., Nissan, A., Golan, T., Dadiani, M., Levanon, K., Bar, J., Yust-Katz, S., Barshack, I., Peeper, D.S., Raz, D.J., Segal, E., Wargo, J.A., Sandbank, J., Shental, N., Straussman, R., 2020. The human tumor microbiome is composed of tumor type-specific intracellular bacteria. Science 368, 973–980. https://doi.org/10.1126/science.aay9189

Nia, H.T., Munn, L.L., Jain, R.K., 2021. Physical traits of cancer 23.

Nicolson, G.L., 1982. Metastatic tumor cell attachment and invasion assay utilizing vascular endothelial cell monolayers. J Histochem Cytochem 30, 214–220. https://doi.org/10.1177/30.3.7061823

Nier, V., Jain, S., Lim, C.T., Ishihara, S., Ladoux, B., Marcq, P., 2016. Inference of Internal Stress in a Cell Monolayer. Biophys J 110, 1625–1635. https://doi.org/10.1016/j.bpj.2016.03.002

Öhlund, D., Elyada, E., Tuveson, D., 2014. Fibroblast heterogeneity in the cancer wound. J Exp Med 211, 1503–1523. https://doi.org/10.1084/jem.20140692

Öhlund, D., Handly-Santana, A., Biffi, G., Elyada, E., Almeida, A.S., Ponz-Sarvise, M., Corbo, V., Oni, T.E., Hearn, S.A., Lee, E.J., Chio, I.I.C., Hwang, C.-I., Tiriac, H., Baker, L.A., Engle, D.D., Feig, C., Kultti, A., Egeblad, M., Fearon, D.T., Crawford, J.M., Clevers, H., Park, Y., Tuveson, D.A., 2017. Distinct populations of inflammatory fibroblasts and myofibroblasts in pancreatic cancer. J Exp Med 214, 579–596. https://doi.org/10.1084/jem.20162024

Onfroy-Roy, L., Hamel, D., Malaquin, L., Ferrand, A., 2021. Colon Fibroblasts and Inflammation: Sparring Partners in Colorectal Cancer Initiation? Cancers (Basel) 13, 1749. https://doi.org/10.3390/cancers13081749

Özdemir, B.C., Pentcheva-Hoang, T., Carstens, J.L., Wu, C.-C., Simpson, T., Laklai, H., Sugimoto, H., Novitskiy, S.V., Acosta, A.D., Sharma, P., Mahmood, U., Chin, L., Moses, H., Weaver, V., Maitra, A., Allison, J.P., LeBleu, V.S., Kalluri, R., 2014. Depletion of Carcinoma-Associated Fibroblasts and Fibrosis Induces Immunosuppression and Accelerates Pancreas Cancer with Diminished Survival 30.

Padera, T.P., Stoll, B.R., Tooredman, J.B., Capen, D., di Tomaso, E., Jain, R.K., 2004. Pathology: cancer cells compress intratumour vessels. Nature 427, 695. https://doi.org/10.1038/427695a

Pagès, F., Galon, J., Dieu-Nosjean, M.-C., Tartour, E., Sautès-Fridman, C., Fridman, W.-H., 2010. Immune infiltration in human tumors: a prognostic factor that should not be ignored. Oncogene 29, 1093–1102. https://doi.org/10.1038/onc.2009.416

Panciera, T., Azzolin, L., Cordenonsi, M., Piccolo, S., 2017. Mechanobiology of YAP and TAZ in physiology and disease. Nat Rev Mol Cell Biol 18, 758–770. https://doi.org/10.1038/nrm.2017.87

Pankov, R., Momchilova, A., Stefanova, N., Yamada, K.M., 2019. Characterization of stitch adhesions: Fibronectin-containing cell-cell contacts formed by fibroblasts. Exp Cell Res 384, 111616. https://doi.org/10.1016/j.yexcr.2019.111616

Park, D., 2020. SnapShot: Cancer-Associated Fibroblasts 2.

Pasquale, E.B., 2010. Eph receptors and ephrins in cancer: bidirectional signalling and beyond. Nat Rev Cancer 10, 165–180. https://doi.org/10.1038/nrc2806

Pasqualini, R., Ruoslahti, E., 1996. Organ targeting in vivo using phage display peptide libraries. Nature 380, 364–366. https://doi.org/10.1038/380364a0

Patenaude, A., Parker, J., Karsan, A., 2010. Involvement of endothelial progenitor cells in tumor vascularization. Microvasc Res 79, 217–223. https://doi.org/10.1016/j.mvr.2010.01.007

Peinado, H., Zhang, H., Matei, I.R., Costa-Silva, B., Hoshino, A., Rodrigues, G., Psaila, B., Kaplan, R.N., Bromberg, J.F., Kang, Y., Bissell, M.J., Cox, T.R., Giaccia, A.J., Erler, J.T., Hiratsuka, S., Ghajar, C.M., Lyden, D., 2017. Pre-metastatic niches: organ-specific homes for metastases. Nat Rev Cancer 17, 302–317. https://doi.org/10.1038/nrc.2017.6

Perona, R., 2006. Cell signalling: growth factors and tyrosine kinase receptors. Clin Transl Oncol 8, 77–82. https://doi.org/10.1007/s12094-006-0162-1

Pickup, M.W., Mouw, J.K., Weaver, V.M., 2014. The extracellular matrix modulates the hallmarks of cancer. EMBO Rep 15, 1243–1253. https://doi.org/10.15252/embr.201439246

Pietras, K., Ostman, A., 2010. Hallmarks of cancer: interactions with the tumor stroma. Exp Cell Res 316, 1324–1331. https://doi.org/10.1016/j.yexcr.2010.02.045

Poincloux, R., Lizárraga, F., Chavrier, P., 2009. Matrix invasion by tumour cells: a focus on MT1-MMP trafficking to invadopodia. J Cell Sci 122, 3015–3024. https://doi.org/10.1242/jcs.034561

Polacheck, W.J., Charest, J.L., Kamm, R.D., 2011. Interstitial flow influences direction of tumor cell migration through competing mechanisms. Proc Natl Acad Sci U S A 108, 11115–11120. https://doi.org/10.1073/pnas.1103581108

Polyak, K., Weinberg, R.A., 2009. Transitions between epithelial and mesenchymal states: acquisition of malignant and stem cell traits. Nat Rev Cancer 9, 265–273. https://doi.org/10.1038/nrc2620

Provenzano, P.P., Eliceiri, K.W., Campbell, J.M., Inman, D.R., White, J.G., Keely, P.J., 2006. Collagen reorganization at the tumor-stromal interface facilitates local invasion. BMC Med 4, 38. https://doi.org/10.1186/1741-7015-4-38

Qian, B.-Z., Pollard, J.W., 2010. Macrophage diversity enhances tumor progression and metastasis. Cell 141, 39–51. https://doi.org/10.1016/j.cell.2010.03.014

Radisky, D.C., Kenny, P.A., Bissell, M.J., 2007. Fibrosis and cancer: do myofibroblasts come also from epithelial cells via EMT? J Cell Biochem 101, 830–839. https://doi.org/10.1002/jcb.21186

Räsänen, K., Vaheri, A., 2010. Activation of fibroblasts in cancer stroma. Exp Cell Res 316, 2713–2722. https://doi.org/10.1016/j.yexcr.2010.04.032

Raza, A., Franklin, M.J., Dudek, A.Z., 2010. Pericytes and vessel maturation during tumor angiogenesis and metastasis. Am J Hematol 85, 593–598. https://doi.org/10.1002/ajh.21745

Rhim, A.D., 2014. Stromal Elements Act to Restrain, Rather Than Support, Pancreatic Ductal Adenocarcinoma. Cancer Cell 13.

Ruhland, M.K., Loza, A.J., Capietto, A.-H., Luo, X., Knolhoff, B.L., Flanagan, K.C., Belt, B.A., Alspach, E., Leahy, K., Luo, J., Schaffer, A., Edwards, J.R., Longmore, G., Faccio, R., DeNardo, D.G., Stewart, S.A., 2016. Stromal senescence establishes an immunosuppressive microenvironment that drives tumorigenesis. Nat Commun 7, 11762. https://doi.org/10.1038/ncomms11762

Ruoslahti, E., Bhatia, S.N., Sailor, M.J., 2010. Targeting of drugs and nanoparticles to tumors. J Cell Biol 188, 759–768. https://doi.org/10.1083/jcb.200910104

Saghafinia, S., Homicsko, K., Di Domenico, A., Wullschleger, S., Perren, A., Marinoni, I., Ciriello, G., Michael, I.P., Hanahan, D., 2021. Cancer Cells Retrace a Stepwise Differentiation Program

during Malignant Progression. Cancer Discov 11, 2638–2657. https://doi.org/10.1158/2159-8290.CD-20-1637

Sahai, E., Astsaturov, I., Cukierman, E., DeNardo, D.G., Egeblad, M., Evans, R.M., Fearon, D., Greten, F.R., Hingorani, S.R., Hunter, T., Hynes, R.O., Jain, R.K., Janowitz, T., Jorgensen, C., Kimmelman, A.C., Kolonin, M.G., Maki, R.G., Powers, R.S., Puré, E., Ramirez, D.C., Scherz-Shouval, R., Sherman, M.H., Stewart, S., Tlsty, T.D., Tuveson, D.A., Watt, F.M., Weaver, V., Weeraratna, A.T., Werb, Z., 2020. A framework for advancing our understanding of cancer-associated fibroblasts. Nat Rev Cancer 20, 174–186. https://doi.org/10.1038/s41568-019-0238-1

Sahai, E., Marshall, C.J., 2003. Differing modes of tumour cell invasion have distinct requirements for Rho/ROCK signalling and extracellular proteolysis. Nat Cell Biol 5, 711–719. https://doi.org/10.1038/ncb1019

Sanchez, T., 2012. Spontaneous motion in hierarchically assembled active matter 5.

Santi, A., Kugeratski, F.G., Zanivan, S., 2017. Cancer Associated Fibroblasts: The Architects of Stroma Remodeling 15.

Saw, T.B., Doostmohammadi, A., Nier, V., Kocgozlu, L., Thampi, S., Toyama, Y., Marcq, P., Lim, C.T., Yeomans, J.M., Ladoux, B., 2017. Topological defects in epithelia govern cell death and extrusion 39.

Saw, T.B., Xi, W., Ladoux, B., Lim, C.T., 2018. Biological Tissues as Active Nematic Liquid Crystals. Adv. Mater. 12.

Schoumacher, M., Louvard, D., Vignjevic, D., 2011. Cytoskeleton networks in basement membrane transmigration. Eur J Cell Biol 90, 93–99. https://doi.org/10.1016/j.ejcb.2010.05.010

Schuppler, M., 2016. Boundaries steer the contraction of active gels. NATURE COMMUNICATIONS 10.

Sears, C.L., Garrett, W.S., 2014. Microbes, microbiota, and colon cancer. Cell Host Microbe 15, 317–328. https://doi.org/10.1016/j.chom.2014.02.007

Semenza, G.L., 2010. HIF-1: upstream and downstream of cancer metabolism. Curr Opin Genet Dev 20, 51–56. https://doi.org/10.1016/j.gde.2009.10.009

Shay, J.W., Wright, W.E., 2000. Hayflick, his limit, and cellular ageing. Nat Rev Mol Cell Biol 1, 72–76. https://doi.org/10.1038/35036093

Sherr, C.J., McCormick, F., 2002. The RB and p53 pathways in cancer. Cancer Cell 2, 103–112. https://doi.org/10.1016/s1535-6108(02)00102-2

Shimoda, M., Mellody, K.T., Orimo, A., 2010. Carcinoma-associated fibroblasts are a rate-limiting determinant for tumour progression. Semin Cell Dev Biol 21, 19–25. https://doi.org/10.1016/j.semcdb.2009.10.002

Singh, A., Settleman, J., 2010. EMT, cancer stem cells and drug resistance: an emerging axis of evil in the war on cancer. Oncogene 29, 4741–4751. https://doi.org/10.1038/onc.2010.215

Sleeman, J.P., Nazarenko, I., Thiele, W., 2011. Do all roads lead to Rome? Routes to metastasis development. Int J Cancer 128, 2511–2526. https://doi.org/10.1002/ijc.26027

Smyth, M.J., Dunn, G.P., Schreiber, R.D., 2006. Cancer immunosurveillance and immunoediting: the roles of immunity in suppressing tumor development and shaping tumor immunogenicity. Adv Immunol 90, 1–50. https://doi.org/10.1016/S0065-2776(06)90001-7

Song, J.W., Munn, L.L., 2011. Fluid forces control endothelial sprouting. Proc Natl Acad Sci U S A 108, 15342–15347. https://doi.org/10.1073/pnas.1105316108

Storm, C., Pastore, J.J., MacKintosh, F.C., Lubensky, T.C., Janmey, P.A., 2005. Nonlinear elasticity in biological gels. Nature 435, 191–194. https://doi.org/10.1038/nature03521

Stylianopoulos, T., Diop-Frimpong, B., Munn, L.L., Jain, R.K., 2010. Diffusion anisotropy in collagen gels and tumors: the effect of fiber network orientation. Biophys J 99, 3119–3128. https://doi.org/10.1016/j.bpj.2010.08.065

Thienpont, B., 2016. Tumors smother their epigenome 4.

Tomasek, J.J., Gabbiani, G., Hinz, B., Chaponnier, C., Brown, R.A., 2002. MYOFIBROBLASTS AND MECHANO- REGULATION OF CONNECTIVE TISSUE REMODELLING 15.

Toullec, A., Gerald, D., Despouy, G., Bourachot, B., Cardon, M., Lefort, S., Richardson, M., Rigaill, G., Parrini, M.-C., Lucchesi, C., Bellanger, D., Stern, M.-H., Dubois, T., Sastre-Garau, X., Delattre,

O., Vincent-Salomon, A., Mechta-Grigoriou, F., 2010. Oxidative stress promotes myofibroblast differentiation and tumour spreading. EMBO Mol Med 2, 211–230. https://doi.org/10.1002/emmm.201000073

Tse, J.M., Cheng, G., Tyrrell, J.A., Wilcox-Adelman, S.A., Boucher, Y., Jain, R.K., Munn, L.L., 2012. Mechanical compression drives cancer cells toward invasive phenotype. Proc Natl Acad Sci U S A 109, 911–916. https://doi.org/10.1073/pnas.1118910109

Tyan, S.-W., Kuo, W.-H., Huang, C.-K., Pan, C.-C., Shew, J.-Y., Chang, K.-J., Lee, E.Y.-H.P., Lee, W.-H., 2011. Breast cancer cells induce cancer-associated fibroblasts to secrete hepatocyte growth factor to enhance breast tumorigenesis. PLoS One 6, e15313. https://doi.org/10.1371/journal.pone.0015313

Wang, B., Kohli, J., Demaria, M., 2020. Senescent Cells in Cancer Therapy: Friends or Foes? Trends Cancer 6, 838–857. https://doi.org/10.1016/j.trecan.2020.05.004

Wei, S.C., Fattet, L., Tsai, J.H., Guo, Y., Pai, V.H., Majeski, H.E., Chen, A.C., Sah, R.L., Taylor, S.S., Engler, A.J., Yang, J., 2015. Matrix stiffness drives epithelial-mesenchymal transition and tumour metastasis through a TWIST1-G3BP2 mechanotransduction pathway. Nat Cell Biol 17, 678–688. https://doi.org/10.1038/ncb3157

Weigelin, B., Bakker, G.-J., Friedl, P., 2012. Intravital third harmonic generation microscopy of collective melanoma cell invasion: Principles of interface guidance and microvesicle dynamics. Intravital 1, 32–43. https://doi.org/10.4161/intv.21223

Weiss, L., 1992. Comments on hematogenous metastatic patterns in humans as revealed by autopsy. Clin Exp Metastasis 10, 191–199. https://doi.org/10.1007/BF00132751

Welch, D.R., Hurst, D.R., 2020. Defining the Hallmarks of Metastasis 36.

Witsch, E., Sela, M., Yarden, Y., 2010. Roles for growth factors in cancer progression. Physiology (Bethesda) 25, 85–101. https://doi.org/10.1152/physiol.00045.2009

Wong, A.D., Searson, P.C., 2017. Mitosis-Mediated Intravasation in a Tissue-Engineered Tumor-Microvessel Platform. Cancer Res 77, 6453–6461. https://doi.org/10.1158/0008-5472.CAN-16-3279

Yachida, S., Jones, S., Bozic, I., Antal, T., Leary, R., Fu, B., Kamiyama, M., Hruban, R.H., Eshleman, J.R., Nowak, M.A., Velculescu, V.E., Kinzler, K.W., Vogelstein, B., Iacobuzio-Donahue, C.A., 2010. Distant metastasis occurs late during the genetic evolution of pancreatic cancer. Nature 467, 1114–1117. https://doi.org/10.1038/nature09515

Yang, L., Pang, Y., Moses, H.L., 2010. TGF-beta and immune cells: an important regulatory axis in the tumor microenvironment and progression. Trends Immunol 31, 220–227. https://doi.org/10.1016/j.it.2010.04.002

Yuan, S., Norgard, R.J., Stanger, B.Z., 2019. Cellular Plasticity in Cancer. Cancer Discov 9, 837–851. https://doi.org/10.1158/2159-8290.CD-19-0015

Zhang, H., Chen, J., 2018. Current status and future directions of cancer immunotherapy. J Cancer 9, 1773–1781. https://doi.org/10.7150/jca.24577

Abstract

In the pre-invasive stage, the tumor is separated from the adjacent stroma by the basement membrane. Just beneath it, there is a network of cancer-associated fibroblasts (CAFs), the major producers and remodelers of the extracellular matrix (ECM). By enveloping tumors, CAFs create a physical barrier that prevents cancer cell invasion. However, CAFs also help cancer cells escape the tumor mass by mechanically remodeling the ECM. Due to their spindle shape, CAFs spontaneously align along their long axis into nematic ordering. Nematic ordering is intrinsically linked with topological defects, where aligned regions along different directions meet. The most common defects are +1/2 defects resembling comets and -1/2 defects resembling triangles. We hypothesize that whereas nematically ordered CAFs form a capsule that prevents tumor expansion, defects in the nematic ordering may represent weak points where cancer cells escape. Using traction and stress force microscopy coupled with time-lapse imaging, we found that defects are stationary and characterized by lower cell and ECM density. The force maps suggested two different invasion strategies: 1) CAFs extrusion at the comets that could result in the ECM reorientation, and 2) pinching of the cancer layer in triangles that could create holes. CAFs formed supra cellular units to transmit forces through actin fibers spanning several cells, using fibronectin stitch adhesions. Fibronectin deposition on the substrate also fixed the initial nematic ordering, leading to defects' stability. Preliminary data of invasion assays revealed that cancer cell invasion seemed to mostly happen at defects. Together, these data suggest that defects are the weak points in the CAFs/ECM barrier.

Keywords: Cancer-associated fibroblasts, nematic ordering, cancer invasion, fibronectin

---

Résumé

Au stade pré-invasif, la tumeur est séparée du stroma adjacent par la membrane basale. Juste en dessous, se trouve un réseau de fibroblastes associés au cancer (CAFs), les principaux producteurs et remodeleurs de la matrice extracellulaire (ECM). En enveloppant la tumeur, les CAFs créent une barrière physique empêchant l'invasion cancéreuses. Cependant, les CAFs aident également l'invasion cancéreuse en remodelant mécaniquement l'ECM. De par leur forme allongée, les CAFs s'alignent spontanément le long de leur grand axe dans un ordre nématique. L'ordre nématique est intrinsèquement lié aux défauts topologiques, là où des régions alignées dans différentes directions se rencontrent. Les défauts les plus courants sont les +1/2 ressemblant à des comètes et les -1/2 ressemblant à des triangles. Nous supposons que, alors que les CAFs ordonnés nématiquement forment une capsule empêchant l'invasion cancéreuse, les défauts dans l'ordre nématique peuvent représenter des points faibles d'où les cellules cancéreuses s'échappent. En utilisant la microscopie à force de traction et de contrainte couplées à des films de la couche de CAFs, nous avons constaté que les défauts sont stationnaires et caractérisés pat une densité cellulaire et d'ECM inférieures. Les cartes de force suggéraient deux stratégies d'invasion différentes : 1) l'extrusion des CAFs aux comètes pouvant entraîner la réorientation de l'ECM, et 2) le pincement des cellules cancéreuse aux triangles pouvant créer des trous. Les CAFs formaient des unités supracellulaires pour transmettre des forces à travers des fibres d'actine sur plusieurs cellules jointes par de la fibronectine. Le dépôt de fibronectine sur le substrat fixait également l'ordre nématique initial, conduisant à la stabilité des défauts. Les données préliminaires des tests d'invasion montraient que l'invasion cancéreuses semblait se produire principalement au niveau des défauts. Ensemble, ces données suggèrent que les défauts sont les points faibles de la barrière CAFs/ECM.

Mots-clés : fibroblastes associés au cancer, ordre nématique, invasion cancéreuse, fibronectine